

SWINBURNE UNIVERSITY OF TECHNOLOGY

Faculty of Science, Engineering and Technology

Centre for Astrophysics and Supercomputing



**Scaling relations
between the supermassive black hole mass
and the host spheroid properties**

Giulia A. D. Savorgnan

Presented in fulllment of the requirements
of the degree of Doctor of Philosophy

2016

last print: March 10, 2016

1

Introduction

In the 1790s, John Michell of England and Pierre-Simon Laplace of France independently imagined an “invisible star”, an object whose escape velocity is greater than the speed of light, and they both used Newton’s gravitational laws to calculate the mass and size of such object (Montgomery et al., 2009).

A century ago, in 1915, Albert Einstein completed his General theory of Relativity and submitted to the Prussian Academy of Sciences a seminal paper where he published the full treatment of his “field equations”. Einstein’s theory finally explained the anomalous precession of the perihelion of Mercury, and predicted the deflection of light by means of gravitational fields and the gravitational redshift of light. Albert Einstein willingly embraced these three implications of his theoretical work, and was confident about a timely verification of the last two. However, he never accepted nor demonstrated any interest in another conclusion of General Relativity, i.e. the existence of regions of the space-time where the force of gravity is so strong that not even light can escape. Ironically, while some of his colleagues were fascinated by these exotic, dark objects – first of all the American physicist John Archibald Wheeler, who coined and popularised the term “black hole” – Einstein strongly opposed and fought against the idea of those weird mathematical singularities for all his life (Thorne, 1994). In his 1939 article, Einstein derived the relativistic equations that describe a stationary cluster of particles orbiting on the surface of a sphere. He imagined to gradually reduce the radius of the sphere, forcing the particles to move faster and faster, and demonstrated that the velocity of the particles was reaching the speed of light before the cluster was small enough to become a black hole. Einstein interpreted his calculations as a proof of the fact that black holes cannot exist. He concluded the article writing

"The essential result of this investigation is a clear understanding as to why the Schwarzschild singularities do not exist in physical reality. [...] The Schwarzschild singularity does not appear for the reason that matter cannot be concentrated arbitrarily".

Today, not only their existence is unanimously taken for granted by the scientific community, but black holes are at the centre of some of the most active research fields of astronomy. We know that they come in different flavours and they occupy a wide range of masses, going from the hypothetical, minuscule, primordial black holes (e.g. Carr & Hawking 1974), generated by density fluctuations of matter during the very first moments of the Universe's expansion after the Big Bang, through the well understood stellar black holes (e.g. Shahbaz 1999), remnant products left behind after the death of a massive star, to the so called "massive black holes", occupying the centre of nuclear star clusters and galaxies. Massive black holes are further differentiated into two classes according to their mass: Intermediate Mass Black Holes (within the mass range $100 - 10^5 M_{\odot}$, e.g. Miller & Colbert 2004; van der Marel 2004), still lacking many incontrovertible direct detections (but for which we might accumulate evidence over the next years, e.g. Pasham et al. 2014), and Supermassive Black Holes (e.g. Ferrarese 2006), which are the focus of this thesis.

1.1 Supermassive black holes

An astrophysical black hole is a region of the space-time whose escape velocity is greater than the speed of light. Black holes are the simplest objects in the Universe. They are completely characterised by three properties: mass, spin (or angular momentum) and electric charge.

Supermassive black holes (SMBHs) are the most massive black holes known, with typical masses $M_{\text{BH}} \approx 10^6 - 10^9 M_{\odot}$. This class of black holes was first theorised (Lynden-Bell, 1969; Wolfe & Burbidge, 1970) after the discovery of quasars. Quasars can be as luminous as galaxies ($\approx 10^{46} \text{ erg s}^{-1}$). However, their rapid variability ($\approx \text{minutes}$) at high energies implies tiny sizes for these objects ($\approx 10^{-6} \text{ pc}$), even smaller than the Solar System. Small sizes and powerful energy outputs led to the conclusion that accreting SMBHs are the engine of quasars (Salpeter, 1964; Zel'dovich & Novikov, 1964; Lynden-Bell, 1978).

Because quasars were numerous at high redshift, the Universe should be populated with relic black holes (Soltan, 1982). Assuming that the luminosity of quasars is produced by accretion of mass onto the central black hole, Andrzej Soltan calculated a lower limit for the integrated energy density due to quasar light, derived the corresponding value of mass density of accreted material, and showed that, because this mass must be discretely distributed in today's Universe, then most, if not all, nearby galaxies host quiescent black holes in their nuclei, each black hole having a mass in the $10^8 - 10^9 M_{\odot}$ range. This realisation motivated the search of SMBHs at the centre of galaxies, i.e. at the bottom of the potential well, where dynamical friction is expected to drag compact massive objects.

The gravitational potential of a SMBH dominates over the gravitational potential of the host galaxy within the sphere-of-influence radius

$$r_h = \frac{GM_{\text{BH}}}{\sigma_*^2} \approx 0.45 \left(\frac{M_{\text{BH}}}{10^6 M_{\odot}} \right) \left(\frac{100 \text{ km s}^{-1}}{\sigma_*} \right) \text{ pc}, \quad (1.1)$$

where G is the gravitational constant and σ_* is the velocity dispersion of the stars in the host galaxy's bulge. A dynamical detection of a black hole requires the ability to resolve its sphere-of-influence. For local galaxies ($\lesssim 20$ Mpc), it demands a subarcsecond spatial resolution. It is only after the introduction of CCD on spectrographs ('80s) that stellar dynamical detections of black holes became possible (see the references in the reviews by Kormendy & Richstone 1995 and Richstone et al. 1998). The number of dynamical black hole mass measurements has increased with time and it has recently become a statistically meaningful sample with which one can study SMBH demographics. It is now generally accepted that SMBHs reside at the centre of most, if not all, massive galaxies, either quiescent or active.

1.1.1 Measuring black hole masses

Techniques to measure the mass of SMBHs can be divided into two main categories: direct and indirect methods (see Ferrarese & Ford 2005 for a thorough review). In direct methods, the mass of a black hole is determined from its gravitational imprint in the motion of the surrounding stars or gas. The spatial resolution of the observing instrument has to be smaller than the size of the black hole sphere-of-influence, which implies challenging technology and time-consuming observations. In indirect methods, one adopts approximations to the direct methods or uses a parameter of the host galaxy as a proxy to infer the black hole mass on the basis of observed

scaling relations.

Sgr A*, the radio source associated with the Galactic black hole, represents a special case study. Thanks to its proximity (8.28 ± 0.33 kpc, Genzel et al. 2010), near infrared techniques have made possible to resolve and follow each individual star orbiting around Sgr A*. From the analysis of these orbits, Ghez et al. (2008) derived a best-fit central mass of $(4.5 \pm 0.4) \times 10^6 M_{\odot}$.

When measuring black hole masses in gas-poor early-type galaxies, the primary method of choice is based on modelling the integrated kinematics of stars acquired through high spatial resolution spectroscopy. Because to a good approximation the stars in a local galaxy constitute a collisionless system, it is possible to describe their motion analytically and constrain the central gravitational potential. The best-fit model to the observed integrated stellar kinematics returns an estimate of the black hole mass and the stellar mass-to-light ratio, which are treated as free parameters. Although modelling the integrated stellar kinematics can in principle return robust black hole mass estimates, this method is not exempted from systematics and degeneracies, which are mainly caused by our poor ability to resolve the tiny black hole sphere-of-influence even in the most nearby galaxies (Valluri et al., 2004). Gebhardt & Thomas (2009) first explored the effects of including the additional contribution from a dark matter halo when modelling the central stellar kinematics of the galaxy M87. Their measurement of the black hole mass was over a factor of two larger than previous stellar dynamical measurements which did not account for dark matter. Upon deriving 10 new black hole mass measurements from the analysis of two-dimensional stellar kinematics, Rusli et al. (2013) concluded that the omission of dark matter systematically overestimates the stellar mass-to-light ratio and underestimates the black hole mass; this bias does not significantly affect the estimate of the black hole mass only if the spatial resolution of the observations is at least a factor of 10 smaller than the size of the black hole sphere-of-influence. Merritt (2013a) reminds that, among all current black hole mass measurements based on stellar-dynamics, only three cases were carried out with enough spatial resolution to detect a convincing Keplerian rise in the central stellar velocities, as expected from the presence of a central massive object. From this consideration, he raises doubts about the majority of such black hole mass detections, and pessimistically cautions that they should be interpreted as upper limits only.

When water maser clouds are present in an Active Galactic Nucleus (AGN) in the form of a thin disc (with sub-parsec size) rotating around the central engine and heated by the X-ray photons emitted by the AGN accretion disc, the gas dynamics can be studied with radio interferometric techniques (e.g. with the Very Long Baseline Array) and the central gravitational potential constrained, benefiting from a spatial resolution that can be up to ≈ 200 times higher than that allowed by the Hubble Space Telescope (e.g. the black hole mass measurement in the galaxy NGC 4258, Miyoshi et al. 1995). Water masers allow the most accurate mass measurements for SMBHs in galaxies other than the Milky Way.

More than half of massive early-type (elliptical + lenticular) galaxies and virtually all spiral galaxies have detectable warm ionised gas in their nuclei (Ho et al., 1997), whose emission lines are easier to measure than stellar absorption lines. In principle, under the assumption that the ionised gas is distributed in a rotationally-supported Keplerian disc, where the effects of stellar orbital anisotropy, triaxiality or dark matter are negligible, modelling the gas dynamics is conceptually simpler than modelling the integrated stellar kinematics. However, as Kormendy & Ho (2013) pointed out, unlike stars, gas is subject to non-gravitational perturbations (turbulence, shocks, radiation pressure, magnetic fields, etc.), hence its dynamics could be much more complicated than the ordered motion assumed within a Keplerian disc model. Kormendy & Ho (2013) compared the common black hole mass measurements obtained from gas and stellar dynamics for eight galaxies and concluded that the gas-based measurements are systematically underestimated when the modelling of the gas dynamics does not include corrections for large emission-line widths, which are speculated to imply significant random motions of gas perturbed by non-gravitational phenomena, such as radio jets.

Other black hole mass determination methods can be applied to some AGNs and quasars. These techniques rely on fitting accretion disc models to multiwavelength continua spectra (Shields, 1978; Malkan, 1983) or studying the emission line due to iron fluorescence (e.g. Fabian et al. 2000; Reynolds & Nowak 2003). Reverberation mapping (e.g. Peterson 1993) consists of modelling the structure of the broad emission-line region of an AGN, as probed by the short-term variability of the ionising continuum, and estimating the black hole mass by assuming a calibration factor that depends on an observed correlation between the black hole mass and some host

galaxy parameter¹.

Building on past catalogs of direct black hole mass measurements obtained with stellar-kinematics, gas-dynamics, or water maser techniques, Graham & Scott (2013) compiled a sample of ≈ 80 galaxies with a reliable measure of M_{BH} . The galaxy sample used in this work is based on that published by Graham & Scott (2013).

1.1.2 Scaling relations

Over the last three decades, observations have demonstrated that the black hole mass scales with a number of properties of its host spheroid (see Section 1.1.3 for the meaning of the term “spheroid”), on scales much larger than the black hole sphere-of-influence. The black hole mass has been shown to correlate with the spheroid luminosity L_{sph} (Dressler, 1989; Kormendy & Richstone, 1995), the spheroid stellar velocity dispersion σ_* (Ferrarese & Merritt, 2000; Gebhardt et al., 2000), the spheroid central radial concentration of stars (Graham et al., 2001; Graham & Driver, 2007b), the spheroid dynamical mass $M_{\text{dyn,sph}}$ (Magorrian et al., 1998; Marconi & Hunt, 2003; Häring & Rix, 2004), the spheroid gravitational binding energy (Aller & Richstone, 2007), the spheroid kinetic energy of random motion (Feoli & Mele, 2005; Feoli & Mancini, 2009), the spheroid effective radius (Sani et al., 2011), and the spheroid stellar mass (e.g. Magorrian et al. 1998; Sani et al. 2011; Beifiori et al. 2012; Scott et al. 2013). Other correlations with host galaxy parameters – as opposed to spheroid parameters – have been proposed, such as with the spiral arm pitch angle (Seigar et al., 2008; Berrier et al., 2013), the number of globular clusters (Burkert & Tremaine, 2010; Snyder et al., 2011), the dark matter halo (Ferrarese, 2002) and the velocity dispersion of the globular clusters (Sadoun & Colin, 2012; Pota et al., 2013). Very recently, Läsker et al. (2014b) claimed that the black hole mass correlates equally well with the spheroid and the total galaxy luminosity.

The astrophysical interest in black hole mass scaling relations can be summarised in three points. First, the correlations probe a strong connection between SMBHs and their host spheroids. Exploring how scaling relations have changed throughout the cosmic time could help identify the driving mechanisms of the black hole – galaxy co-evolution. Observations at

¹Typically, this scaling factor is calibrated on the $M_{\text{BH}} - \sigma_*$ relation, i.e. the observed correlation between black hole mass and host spheroid stellar velocity dispersion (e.g. Ferrarese & Merritt 2000; Gebhardt et al. 2000).

$z = 0$ are the most accurate and therefore the most important. Second, *all* of the observed scaling relations must be taken into account by any complete theory or model describing the co-evolution of galaxies and SMBHs². A fundamental, but non-trivial, requirement is that all the correlations have to be consistent with each other. Third, scaling relations can be employed to predict the masses of SMBHs in other galaxies, where a direct measure of M_{BH} would be extremely time consuming or simply impossible due to technological limitations. Many accurate M_{BH} predictions would help derive the local black hole mass function (e.g. Salucci et al. 1999; Graham et al. 2007) and space density (Graham & Driver 2007a and references therein), and aid study of SMBH demographics.

1.1.3 Spheroid

Throughout the text, the term “spheroid” will be used to indicate either a pure elliptical galaxy or the bulge component of a disc galaxy. Obviously, if a galaxy is composed of a relatively flat stellar disc embedded in a triaxial, elliptically-shaped stellar system which dominates the light at large radii (a “discy elliptical”, Michard 1984; Nieto et al. 1988), the term “spheroid” designates the latter component. Providing a self-sufficient definition of a galaxy’s “bulge” is not trivial. In Laurikainen et al. (2016), B. Madore retraces the history of the origin of this term, from its first legitimation as “Galactic bulge”, to the modern, ordinary acceptation that all extragalactic astronomers embrace when they think about lenticular or early-type spiral galaxies. A bulge can be identified photometrically, as the central component rising above the inward extrapolation of the disc’s surface brightness profile, or morphologically, as a 3-dimensional rounded swelling which emerges from the disc plane (best visible in the vast majority of massive, edge-on galaxies, e.g. Kautsch et al. 2006), or also kinematically, by distinguishing a structure with low-angular momentum and higher vertical dispersion at the centre of a high-angular momentum thin disc (e.g. Fabricius et al. 2014). It is common practice to make a distinction between *classical bulges* and *pseudobulges*. Classical bulges are merger-built, pressure-supported systems, whereas pseudobulges are disc-like, rotation-supported systems, originated from secular evolution processes such as disc or bar instabilities (Kormendy, 1982; Kormendy & Kennicutt, 2004).

²Modern semi-analytic models use the observed black hole mass scaling relations to constrain the black hole accretion rate (\dot{M}_{BH}).

1.1.4 Co-evolution and AGN feedback

The tightness (or small scatter) of the observed black hole mass correlations led to the idea that SMBHs and host galaxies have co-evolved with some sort of self-regulated growth. AGN feedback has been proposed as the process by which this occurs (e.g. Silk & Rees 1998; Fabian 1999; Ostriker & Ciotti 2005; see Fabian 2012 for a review). The AGN is believed to emit intense flux of photons and particles which can sweep the gas from the host spheroid and terminate both star formation and gas accretion onto the black hole. This idea is motivated by the fact that the black hole binding energy ($\propto M_{\text{BH}}c^2$) is much larger than the bulge binding energy ($\propto M_{\text{dyn,sph}}\sigma_*^2$). Therefore, if just a very small percentage of the AGN energy output couples to the gas, all of the gas reservoir can be blown away from the host galaxy. The current picture distinguishes between “quasar mode AGN feedback”, which takes place when the AGN energy output is close to the Eddington limit³ and whose main effect is to blow gas away from the spheroid, and “radio mode AGN feedback”, also known as “maintenance mode”, which injects energy into the interstellar gas and prevents it from cooling.

Although observational evidence is not always clear, the AGN feedback scenario is consistent with some direct observations, such as the X-ray cavities of giant ellipticals, galaxy groups and clusters, thought to be inflated by AGN jets (e.g. McNamara & Nulsen 2012), or the blue-shifted quasar absorption lines, signature of high-velocity winds (e.g. Tombesi et al. 2012), or the ionised gas outflows seen in radio galaxies (e.g. Nesvadba et al. 2006). Many mechanisms, either radiative (through photons) or mechanical (through high-energy particles, winds or jets), can be responsible for AGN feedback, but it has not yet been established which ones are dominating. For each AGN feedback mechanism, theoretical models predict how the black hole mass scales with the host spheroid properties. These predictions can be compared with the observed scalings of the empirical black hole mass correlations to constrain the models and understand which mechanisms are prevailing. Part of the popularity of the AGN feedback scenario resides in its ability to resolve some open questions in galaxy formation. For instance, AGN feedback is invoked to explain the “cooling flow problem”, which states that, in the absence of an energy input, the X-ray halos of the most massive galaxies known, Brightest Cluster Galaxies (BCGs), and galaxy clusters would cool quickly, producing cold gas and associated giant bursts of star

³The Eddington limit is the maximum luminosity at which an object can emit owing to balance between the outward radiation pressure and the inward gravitational force.

formation activity that are not observed in the predicted large amounts (e.g. Ostriker & Ciotti 2005). AGN activity is also believed to quench star formation in high-mass galaxies, explaining why the galaxy mass function (at high masses) drops more quickly than expected from our standard cosmology (e.g. Croton et al. 2006).

An alternative idea to explain the empirical black hole mass correlations without calling into play AGN feedback was explicitly proposed for the first time by Peng (2007), and similar conclusions were reached later by Gaskell (2010), Hirschmann et al. (2010) and Jahnke & Macciò (2011). These studies showed that, starting from a distribution of small progenitor {galaxy – black hole} pairs, regardless of whether or not the initial black hole masses correlate with the initial galaxy masses, and building bigger galaxies through a succession of dry mergers (where galaxy masses and black hole masses add separately), as a consequence of the central limit theorem, after several mergers one obtains a near-linear correlation between black hole mass and galaxy mass, whose scatter decreases with increasing mass. In addition to this, the central limit theorem guarantees that, regardless of the nature of the initial distributions of galaxy and black hole masses, the final distributions converge to Gaussians. However, this scenario does not fit in with the non-linear $M_{\text{BH}} - L_{\text{sph}}$ correlation found by Graham & Scott (2013), as explained in Section 1.1.5.

1.1.5 The Sérsic/core-Sérsic paradigm

For many years, the samples of galaxies with a direct measurement of their black hole mass had been dominated by early-type, high-luminosity galaxies, hosting the most massive black holes known. From these samples, the $M_{\text{BH}} - M_{\text{dyn,sph}}$ and $M_{\text{BH}} - L_{\text{sph}}$ log-linear relations had been reported to have an exponent β close to 1 (i.e. $M_{\text{BH}} \propto M_{\text{dyn,sph}}^{\beta \approx 1}$). However, Graham (2012) addressed a crucial inconsistency, that becomes clear when one considers the following points.

- 1) The $L_{\text{sph}} - \sigma_*$ log-linear relation is not described by a single power law. In fact, this correlation has a different slope if one considers only the bright core-Sérsic spheroids ($L_{\text{sph}} \propto \sigma_*^5$) rather than the fainter Sérsic spheroids ($L_{\text{sph}} \propto \sigma_*^2$). Core-Sérsic spheroids display a central deficit of light relative to the inward extrapolation of their outer Sérsic light profile, whereas Sérsic spheroids do not. The different behaviour of their central light

profile is thought to be indicative of distinct formation scenarios (see Section 1.1.6 for a digression on this topic). Davies et al. (1983) and Matković & Guzmán (2005) showed that the change in slope of the $L_{\text{sph}} - \sigma_*$ relation occurs at the B-band absolute magnitude $M_B \approx -20.5$ mag ($\sigma_* \approx 200 \text{ km s}^{-1}$) and corresponds to the division between core-Sérsic and Sérsic spheroids (e.g. Graham & Guzmán 2003).

- 2) The $M_{\text{BH}} - \sigma_*$ relation, instead, does not have a bent nature, being well described by a single power law (Graham, 2012).
- 3) The dynamical mass-to-light ratio scales with the luminosity as $(M/L)_{\text{dyn}} \propto L^{1/4}$ (e.g. Faber et al. 1987).

These three points put together led to the conclusion that the $M_{\text{BH}} - L_{\text{sph}}$ and $M_{\text{BH}} - M_{\text{dyn,sph}}$ log-linear relations could not be fit with a single power law. Core-Sérsic spheroids were expected to follow $M_{\text{BH}} \propto L_{\text{sph}}^{1.0}$ and $M_{\text{BH}} \propto M_{\text{dyn,sph}}^{1.0}$. Sérsic spheroids, instead, were predicted to define a much steeper sequence, having $M_{\text{BH}} \propto L_{\text{sph}}^{2.5}$ and $M_{\text{BH}} \propto M_{\text{dyn,sph}}^{2.0}$. Therefore, the $M_{\text{BH}} - L_{\text{sph}}$ and $M_{\text{BH}} - M_{\text{dyn,sph}}$ log-linear relations should be better described by a broken (or *bent*) power law.

Upon re-analysing the sample of ≈ 30 galaxies presented by Häring & Rix (2004), Graham (2012) derived linear regressions for Sérsic and core-Sérsic spheroids, separately, in the $M_{\text{BH}} - M_{\text{dyn,sph}}$ diagram, and reported on the bent nature of this correlation. The findings of Graham (2012) were later confirmed by Graham & Scott (2013), who expanded the galaxy sample with ≈ 40 additional objects and converted B- and K-band observed, total galaxy magnitudes of disc galaxies into dust-corrected, bulge magnitudes. Rather than do this galaxy by galaxy, which would require careful bulge/disc decompositions, they employed a mean statistical correction based on each object's morphological type and disc inclination. These mean statistical bulge-to-total ratios were derived from the results of two-component (Sérsic-bulge/exponential-disc) models taken from Graham & Worley (2008, and references therein). Graham & Scott (2013) found $M_{\text{BH}} \propto L_{\text{sph}}^{1.10 \pm 0.20}$ for their core-Sérsic subsample and $M_{\text{BH}} \propto L_{\text{sph}}^{2.73 \pm 0.55}$ for their Sérsic subsample (using K-band luminosities). Following Graham & Scott (2013), Scott et al. (2013) converted luminosities into stellar masses and found $M_{\text{BH}} \propto M_{*,\text{sph}}^{0.97 \pm 0.14}$ for core-Sérsic spheroids, and $M_{\text{BH}} \propto M_{*,\text{sph}}^{2.22 \pm 0.58}$ for Sérsic spheroids. More recently, Graham & Scott (2015) compiled a sample of ≈ 140 low-redshift ($z \leq 0.35$, with a median redshift $\langle z \rangle = 0.085$) bulges

hosting AGNs with virial black hole masses $10^5 \lesssim M_{\text{BH}}/\text{M}_{\odot} \lesssim 2 \times 10^6$ (Jiang et al., 2011), and showed that they roughly follow the near-quadratic $M_{\text{BH}} - M_{*,\text{sph}}$ relation defined by their Sérsic bulges.

The physical interpretation that Graham & Scott (2013) and Scott et al. (2013) attributed to the bent nature of the $M_{\text{BH}} - M_{*,\text{sph}}$ relation is the following. Core-Sérsic spheroids follow a near-linear $M_{\text{BH}} - M_{*,\text{sph}}$ relation because these high-mass systems grow mainly through non-dissipative (gas-poor) major merger events, where the progenitor black holes and galaxies are summed together in lock steps. Instead, the (two times) steeper relation for Sérsic galaxies implies that their central black hole must grow more rapidly than their host spheroid. Sérsic galaxies are intermediate-mass galaxies, thought to be built through wet-wet or wet-dry mergers as well as via gas accretion processes which enhance both star formation and AGN activity.

Many of the concepts treated in this and the previous Sections are extensively reviewed in Graham (2016a).

1.1.6 Sérsic and core-Sérsic spheroids

The nomenclature *Sérsic/core-Sérsic* was introduced as a consequence of an observed dichotomy in the nature of the central surface brightness profile of stellar spheroids (elliptical galaxies or the bulges of disc galaxies). The surface brightness profile of Sérsic spheroids is well described by the Sérsic (1963, 1968) model all over its radial extent, including the innermost central parsecs. Occasionally, the surface brightness profile of Sérsic spheroids can exhibit a nuclear light excess, due to the contribution of an additional stellar component (e.g. a nuclear star cluster) on top of the stellar spheroid itself. The surface brightness profile of core-Sérsic spheroids is characterised by the presence of a partially depleted core, i.e. a central deficit of stellar light not caused by dust obscuration. Beyond the region affected by the partially depleted core, the surface brightness profile of core-Sérsic spheroids is well approximated by the Sérsic (1963, 1968) model. The core-Sérsic model (Graham et al., 2003; Trujillo et al., 2004) provides an excellent description of the overall surface brightness profile of core-Sérsic spheroids. Core-Sérsic spheroids fall also into the category of “core galaxies”, as given by the Nuker definition (Lauer et al., 2007), although $\approx 20\%$ of “core galaxies” are not core-Sérsic galaxies (Dullo & Graham, 2014), i.e. they

do not have depleted cores. Figure 1.1 illustrates the dichotomy between a Sérsic and a core-Sérsic spheroid. The presence of a partially depleted core is detected in the surface brightness profile of NGC 3348, whereas the best-fit model for NGC 5831 is essentially a pure Sérsic model.

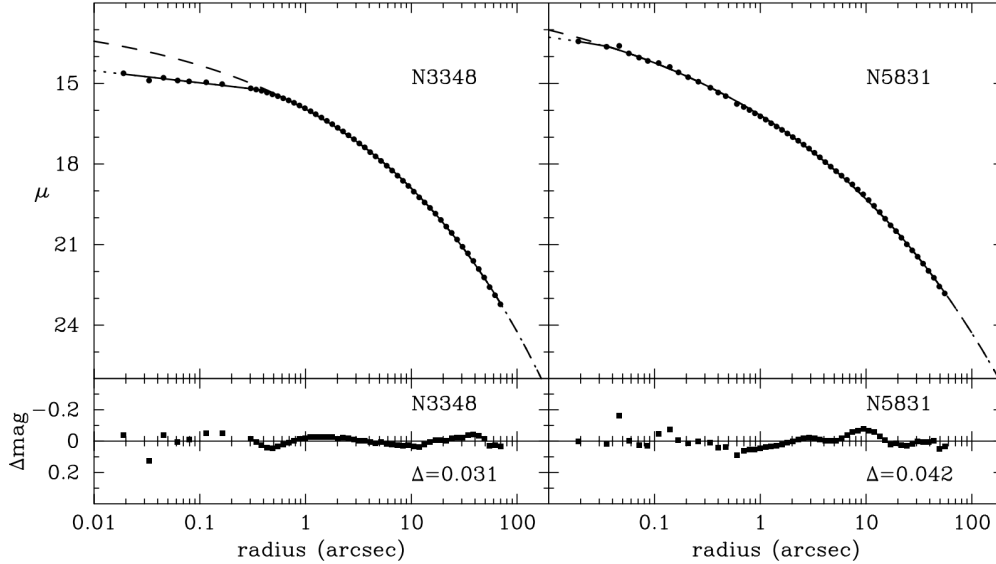


Figure 1.1: The observed major-axis surface brightness radial profiles (μ , in units of mag arcsec^{-2}) of the elliptical galaxies NGC 3348 and NGC 5831 are shown with the black points in the top left and right panels, respectively. The solid lines are fits using the empirical core-Sérsic model, and the dotted extensions are their inner and outer extrapolations. The long dashed lines indicate extrapolations of the outer Sérsic-like part of the core-Sérsic model. The residuals from the fits ($\Delta\mu = \text{data} - \text{model}$) are shown with black squares in the bottom panels, and the rms scatter Δ is given for each fit. This Figure was extracted from Graham et al. (2003).

Partially depleted cores are believed to form during dissipationless (“dry”, i.e. gas-poor) mergers (Begelman et al., 1980), where the progenitor black holes sink towards the centre of the remnant galaxy due to dynamical friction against stars, form a bound pair and further reduce their orbital separation by transferring their binding energy to the surrounding stars via a three-body scattering process also known as “gravitational slingshot” (Milosavljević & Merritt 2001; Merritt 2013b, and references therein). The scouring action of the black hole binary has the effect of lowering the galaxy’s stellar central density, in fact producing a partially depleted core (e.g. Merritt 2006a; Dotti et al. 2012; Colpi 2014). The lack of a significant amount of gas dur-

ing the merger is a necessary condition to guarantee the formation of a partially depleted core. Mayer (2009) and Colpi et al. (2009) followed the simulations of two merging Milky Way-like galaxies and reported that the time-scale for the formation of a close black hole binary system due to dynamical friction against gas is ≈ 100 times shorter than that due to dynamical friction against stars. Therefore, a black hole binary coalesces more quickly in a gas-rich (“wet”) merger than in a gas-poor (“dry”) merger, i.e. when gas is in play, the binary does not have enough time to form a partially depleted core. In addition, gas is likely to be funnelled towards the centre of the galaxy remnant, shock and induce star formation, which would act against the formation of a core by increasing the central stellar density.

1.1.7 Origin of SMBHs

As of today, the formation of SMBHs is still an unsolved puzzle. The key astrophysical questions that pertain to this open debate are: (*i*) what are the initial seeds of SMBHs and when did they form? (*ii*) how were these seeds distributed in the early universe (i.e. what is their mass distribution function and space density)? and (*iii*) what is their accretion history throughout the Universe’s first few billion years? Volonteri & Bellovary (2012) review three possible pathways – not mutually exclusive – that have been proposed as viable mechanisms to SMBH seeds formation.

The first of these three theoretical scenarios states that SMBHs originated from the remnants of Population III stars. Population III stars are the (hypothetical) first generation of stars, which formed out of zero-metallicity pristine gas. The lack of metals implies inefficient cooling and inefficient fragmentation of the gas, making possible to produce very massive stars (with initial masses $\gtrsim 100 M_{\odot}$). The fate of Population III stars mainly depends on their initial mass (Heger et al., 2003). A low-metallicity star that initially weights $\approx 25 - 140 M_{\odot}$ is predicted to directly collapse into a black hole with about half of the mass of its progenitor star. Such black hole would not be heavy enough to be dragged by dynamical friction towards the host galaxy centre, therefore it would hardly contribute to the formation of a central SMBH. Between $\approx 140 - 260 M_{\odot}$, low-metallicity stars lie within the pair instability supernova regime, where the final nuclear-powered explosion completely disrupts the star and leaves no remnant. Above $\approx 260 M_{\odot}$, the nucleus of a low-metallicity star is highly unstable and quickly (≈ 2 Myr)

collapses into a black hole that retains at least half of the initial stellar mass. For many years, these high-mass stellar black holes have been considered the most promising SMBH seeds candidates. However, as recent numerical simulations were improved thanks to the achievement of better resolution and the inclusion of more complex physics (e.g. Turk et al. 2009; Greif et al. 2011; Clark et al. 2011; Stacy et al. 2012), it became clear that fragmentation played a more important role in the formation of Population III stars, which turned into less attractive candidates for the origin of SMBHs.

A second possibility for the genesis of SMBH seeds is the formation of a supermassive star (up to $\approx 10^6 M_\odot$) at the centre of a primordial galaxy. In this scenario, low-metallicity, low-angular momentum gas infalls towards the bottom of the potential well of a dark matter halo and, due to gravitational instabilities, does not settle into a rotationally supported disc, but accumulates into a very massive star, whose core rapidly (≈ 1 Myr) collapses into a black hole and swallows the surrounding gas envelope, giving birth to a $\approx 10^3 - 10^6 M_\odot$ SMBH seed.

According to the third theoretical scenario, gas infalls towards the centre of a dark matter halo and fragments into several stars that form a dense stellar cluster. Before the first supernova explosions can occur, small stars collide with each other within the cluster and merge into a massive ($\approx 10^3 M_\odot$) star which eventually collapses into a black hole with similar mass.

The discovery of ultraluminous quasars at $z > 6$ has accentuated the urge to create very massive black hole seeds in a relatively short time (e.g. Alexander & Natarajan 2014; Madau et al. 2014; Lupi et al. 2015). To date, there have been nearly 50 claims of $z > 6$ quasars hosting $\gtrsim 10^9 M_\odot$ black holes (e.g. Fan et al. 2003; Jiang et al. 2007; Mortlock et al. 2011; Bañados et al. 2014; Trakhtenbrot et al. 2015; Wu et al. 2015). Within a Λ CDM cosmology, such early giant monsters could not have formed so quickly without the creation of anomalously massive seeds or incredibly high accretion rates, i.e. exceeding the Eddington limit (but see Melia & McClintonck 2015 for an alternative explanation). However, it is worth noting that these black hole masses are calculated with the reverberation mapping method, assuming that M_{BH} is directly proportional to the virial factor f , which is calibrated on the normalisation of the $z = 0$ observed $M_{\text{BH}} - \sigma_*$ correlation. The existence of (unknown) selection biases in the local sample of directly measured black hole masses would imply a systematic overestimation of the virial factor

and, consequently, of the black hole masses estimated with the reverberation mapping technique.

1.1.8 Monster black holes

Over the last five years, several claims of detections of *over-massive* black holes accumulated in the literature. Over-massive black holes are black holes whose mass is significantly larger than what is expected from the galaxy's spheroid stellar velocity dispersion or stellar mass, i.e. they are positive outliers in the $M_{\text{BH}} - \sigma_*$ or $M_{\text{BH}} - M_{*,\text{sph}}$ diagrams.

Using integral-field spectrographs at the Gemini North and Keck 2 telescopes, McConnell et al. (2011) targeted the BCGs (NGC 3842 and NGC 4889) of two massive galaxy clusters, the Leo and Coma clusters (Abell 1367 and Abell 1656, respectively), and reported the direct detection of the two most massive black holes ever found at that time. They claimed that these two black holes are significantly more massive than predicted by the popular $M_{\text{BH}} - \sigma_*$ and $M_{\text{BH}} - L_{\text{sph}}$ correlations, and speculated that the growth of the largest galaxies and their black holes happens by means of evolutionary processes different from what is commonly assumed for less massive elliptical galaxies.

Rusli et al. (2011) obtained SINFONI integral-field unit observations of the nuclear region of the galaxy NGC 1332 and measured a one billion solar masses black hole, consistent with the galaxy's stellar velocity dispersion, but offset from the $M_{\text{BH}} - L_{\text{sph}}$ relation by a full order of magnitude.

van den Bosch et al. (2012) combined archival Hubble Space Telescope (*HST*) high-resolution imaging and long-slit spectroscopy (obtained with the Marcario Low Resolution Spectrograph on the Hobby-Eberly Telescope, Texas) of the nuclear region of the galaxy NGC 1277, and directly measured the central black hole mass by fitting self-consistent Schwarzschild models to the integrated stellar kinematics. They found a twenty billion solar masses black hole, which they estimated to weight 59% of the host spheroid's mass (or 14% of the galaxy's total stellar mass). According to their measurement, the black hole of NGC 1277 was an order of magnitude more massive than what expected from the host spheroid's stellar velocity dispersion and two

orders of magnitude more massive than what expected from the host spheroid's stellar mass. Emsellem (2013) re-analysed van den Bosch et al.'s data and showed that their observations were consistent with a black hole mass up to an order of magnitude smaller than the extraordinary value previously reported. However, Yıldırım et al. (2015) and Scharwächter et al. (2015) confirmed van den Bosch et al.'s measurement.

Bogdán et al. (2012) reported on the unusually high $M_{\text{BH}}/M_{*,\text{sph}}$ ratio for the galaxies NGC 4342 and NGC 4291 and concluded that no co-evolution subsisted between these two galaxies and their black holes. Other reportedly over-massive black holes belong to the galaxies NGC 1271 (Walsh et al., 2015) and Mrk 1216 (Yıldırım et al., 2015).

On the basis of these claims, Ferré-Mateu et al. (2015) theorised that, while most today's massive early-type galaxies have completed their two-phase growth path ("in-situ" and "ex-situ"), the over-massive black holes hosts skipped the second ("ex-situ") phase and therefore represent an exception.

1.2 Galaxy decomposition

Galaxy decomposition is a parametric analysis that allows one to fit the surface brightness distribution of galaxies using a combination of analytic functions (usually one function per galaxy component, such as spheroid, disc, bar, nucleus, etc.). The 1D (one-dimensional) technique begins with fitting isophotes to the galaxy image. Isophotes are curves along which the intensity of light is constant and they are typically described with concentric ellipses. The 1D surface brightness radial profile is then extracted and modelled with a combination of 1D analytic functions. With the 2D (two-dimensional) technique one fits 2D analytic functions directly to digital images. Galaxy decomposition is useful to perform structural analysis of galaxies and obtain the best-fit parameters of the spheroidal component, such as the luminosity, the half-light radius and the central radial concentration of stars.

Pioneer studies that performed 1D bulge/disc decompositions of galaxies (e.g. Simien & de

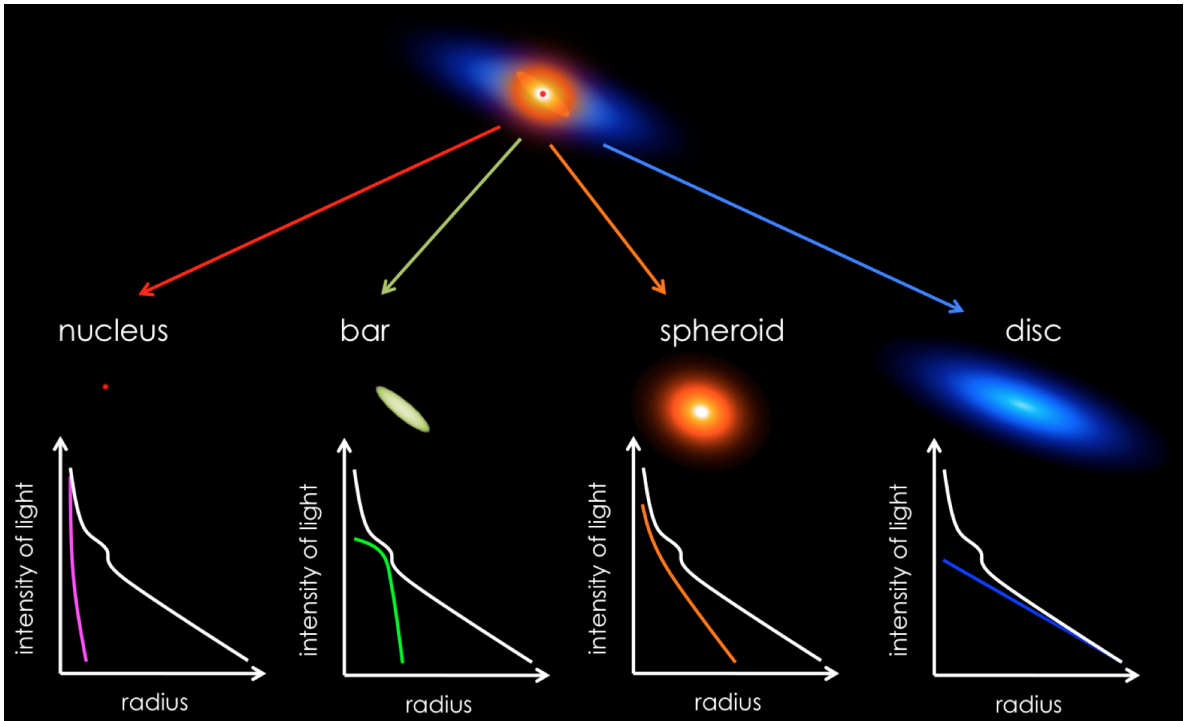


Figure 1.2: Schematic representation of one-dimensional galaxy decomposition. The mock galaxy at the top is composed of a spheroid (orange), a large-scale disc (blue), a bar (green), and a nuclear source (red). The observed surface brightness profile of the galaxy (intensity of light as a function of galactocentric radius) is the white curve. The contribution of each galaxy component to the total surface brightness profile is modelled with one analytic function, illustrated with a solid line of the same colour as the corresponding component. The sum of all analytic functions gives the total galaxy model, which is matched to the observed surface brightness profile.

Vaucouleurs 1986) described the bulge component with a de Vaucouleurs (1948) $R^{1/4}$ profile:

$$\mu_{\text{deVaucouleurs}}(\mu_e, R_e; R) = \mu_e + 8.32678 \left[\left(\frac{R}{R_e} \right)^{1/4} - 1 \right], \quad (1.2)$$

and the disc component with an exponential profile:

$$\mu_{\text{exponential}}(\mu_0, h; R) = \mu_0 + \frac{2.5}{\ln(10)} \left(\frac{R}{h} \right). \quad (1.3)$$

Here μ is the surface brightness profile, R is the projected galactic radius, i.e. the distance of the isophotes from the galaxy centre, R_e is the bulge effective radius (or half-light radius) that encloses half of the total light from the model, μ_e is the bulge surface brightness at the effective

radius, μ_0 is the disc central surface brightness, and h is the disc scale length.

However, it soon became clear to some that the fixed curvature of the two-parameter de Vaucouleurs $R^{1/4}$ law was not adequate to accommodate the variety of shapes observed in the light profiles of stellar spheroidal systems. A more ductile mathematical function was needed such as the three-parameter Sérsic (1963, 1968) $R^{1/n}$ model:

$$\mu_{\text{Sérsic}}(\mu_e, R_e, n; R) = \mu_e + \frac{2.5 b_n}{\ln(10)} \left[\left(\frac{R}{R_e} \right)^{1/n} - 1 \right], \quad (1.4)$$

where the Sérsic index n is the parameter that measures the curvature of the radial light profile, and b_n is a scalar value defined in terms of the Sérsic index (see Graham & Driver 2005 for a valuable compendium). After Caon et al. (1993) and D'Onofrio et al. (1994) demonstrated the superiority of the Sérsic model over the de Vaucouleurs law in describing the spatial distribution of light of early-type galaxies, the varying curvature of the Sérsic model became a necessity also for rendering the light profiles of the bulges of spiral galaxies (Andredakis et al., 1995; Moriondo et al., 1998; Graham & Prieto, 1999; Khosroshahi et al., 2000; Graham et al., 2001).

Thanks to the improved computational speed of machines, 2D fitting algorithms have become more and more popular over the last two decades. de Jong (1996) presented a 2D decomposition technique which allowed one to model the surface photometry of a galaxy using an exponential light profile for both the bulge and the disc. Simard (1998) developed the IRAF⁴ package GIM2D, a 2D decomposition code aimed at distant galaxies. GIM2D takes an input image and simultaneously decomposes all the objects as the sum of a Sérsic and an exponential profile.

A major breakthrough came with GALFIT, a 2D fitting algorithm released by Peng et al. (2002; the nowadays popular GALFIT3, an improved version of the original algorithm, was presented by Peng et al. 2010), which marked an important turning point for the quantitative morphological analysis of galaxies. Thanks to its capability of fitting a galaxy with an arbitrary number of components – chosen from a wide variety of analytical functions such as the Sérsic and the “Nuker” models, or the exponential, Gaussian, and Moffat profiles – and to its optimi-

⁴IRAF is the Image Reduction and Analysis Facility, distributed by the National Optical Astronomy Observatory, which is operated by the Association of Universities for Research in Astronomy (AURA) under cooperative agreement with the National Science Foundation.

sation in computational speed, GALFIT was specifically conceived for modelling large images of spatially well-resolved, nearby galaxies observed with the Hubble Space Telescope.

de Souza et al. (2004) developed BUDDA (Bulge/disc Decomposition Analysis), a code to perform 2D decomposition of galaxies using a two-component Sérsic+exponential model. The number of fitted components was intentionally limited to two (bulge+disc), with the purpose of using the residual images to study the additional substructures such as bars, lenses, rings, and inner discs.

Laurikainen et al. (2005) opted for a hybrid approach, combining the advantages of a 2D decomposition technique with the insight gained from a 1D isophotal analysis. In this exemplary study, the authors modelled the images of 24 early-type disc galaxies (S0/S0a) accounting for bulge, disc, bars, ovals/lenses⁵, and inner discs. Their decomposition method was assessed on synthetic images of galaxies composed of a bulge, a large-scale disc, and a bar. They tested the effects of the omission of the bar component from the galaxy model. While a three-component (bulge+disc+bar) model was correctly recovering the real bulge parameters, a two-component (bulge+disc) model was overestimating the bulge luminosity by up to 40% because the Sérsic model for the bulge was somehow “forced” to account also for the bar. They also experimented with a large number of different weighting maps, and concluded that the results from the fit were not significantly dependent on the choice of the weighting function, unless the signal-to-noise of the galaxy image was extremely low, or a prominent component was not included in the model. In addition, they pointed out that a fit lacking seeing correction resulted in notably biased bulge parameters. Laurikainen et al. (2005) stressed an important point about galaxy decomposition: in order to have control of the physical meaning of the different components in a galaxy, *a priori* evaluation of the existence of such components is required. This concept is opposed to the (nowadays popular) approach of repeating the fit of a galaxy by continuously increasing the number of model components until all residual structures are eliminated from the residual image. Laurikainen et al. (2005) used three different methods to identify the structural

⁵According to their nomenclature, an egg-shaped structure (with axis ratio $b/a \gtrsim 0.85$) embedded within the large-scale disc of a galaxy is dubbed lens or oval in case of a lenticular or spiral galaxy, respectively. Lenses/ovals and pseudobulges might have similar ellipticities, but the former typically have lower surface brightness and sharper outer edges than the latter (Kormendy & Kennicutt, 2004).

components of a galaxy: they inspected (*i*) the radial profiles of ellipticity and position angle of the galaxy's isophotes, whose bumps often correspond to bars, ovals/lenses, and inner discs when these components are sufficiently bright compared to the large-scale disc, (*ii*) the radial profiles of low azimuthal wavenumber Fourier amplitudes and phases, sensitive to weak bars and ovals/lenses, and (*iii*) the unsharp masks⁶, useful to reveal the innermost structures. Upon comparing the results from their three-component decompositions with those obtained from the two-component decompositions of Simien & de Vaucouleurs (1986) in the B-band and de Souza et al. (2004) in the K_S-band, Laurikainen et al. (2005) noted that their bulge-to-total ratios were considerably smaller for all Hubble types. This large discrepancy was not due to the wavelength used, but to the fact that, when a galaxy model does not account for a bar, a large fraction of the bar light erroneously goes into the bulge model, artificially increasing the bulge-to-total ratio. This sophisticated decomposition method was applied to the analysis of 175 early-type disc galaxies using deep near-infrared imaging (Laurikainen et al., 2007, 2010), and the results from these decompositions were used for a detailed study of bars, ovals/lenses and bulges. They found ovals/lenses in 70% of the S0/S0a galaxy sample, and nuclear components (bars/rings/discs) in 50% of them.

1.2.1 Photometry and kinematics

Early-type galaxies can exhibit a wide variety of kinematic features, going from the fainter rotationally-supported systems to the brighter dispersion-dominated ones (e.g. Davies et al. 1983). While the identification of stellar discs in images of spiral galaxies is generally trivial thanks to the presence of spiral arms, featureless discs in bright, early-type galaxies can be particularly hard to recognise by looking at the photometry alone, due to well-known inclination effects (e.g. Rix & White 1990; Gerhard & Binney 1996). However, this problem can be alleviated with the use of kinematic information (e.g. Carter 1987; Franx et al. 1989; Nieto et al. 1991; Rix & White 1992; Cinzano & van der Marel 1993; D'Onofrio et al. 1995; Graham et al. 1998). In particular, our understanding of the internal structure of early-type galaxies has undoubtedly improved over the past decade thanks to the introduction of integral-field spectrographs and the analysis of two-dimensional kinematic maps (e.g. the ATLAS^{3D} survey, Cappellari et al. 2011).

⁶Unsharp masks are obtained from the original images with a mathematical operation of convolution. By suppressing large-scale, low-frequency variations in the images, they act as a filter and reveal faint asymmetric structures within the galaxies (Malin & Zealey, 1979; Erwin & Sparke, 2003).

Emsellem et al. (2007) used the specific angular momentum within one effective radius ($\lambda_R = \langle R|V| \rangle / (R\sqrt{V^2 + \sigma^2})$, where R is the semimajor-axis radius, V is the mean velocity and σ is the velocity dispersion) and the ellipticity at one effective radius ($\epsilon = 1 - (b/a)$, where (b/a) is the ratio of minor-to-major axis length) to classify early-type galaxies into fast rotators and slow rotators, based on the empirical divide $\lambda_R = 0.31\sqrt{\epsilon}$.

Krajnović et al. (2006) developed “kinemetry”, a method that combines surface photometry and kinematics to recognise less obvious structures in galaxies, such as embedded discs and kinematic subcomponents. Using kinemetry, Krajnović et al. (2011) measured the regularity of velocity maps and demonstrated that fast rotators are typically nearly axisymmetric systems, whereas most slow rotators are triaxial systems. At present, the joint effort of imaging and integral-field spectroscopy is undeniably our best chance to disclose the internal structure of galaxies (e.g. Krajnović 2015).

Putting this paradigm into practice, Krajnović et al. (2013) compared photometric signatures and kinematic properties of stellar discs for the 180 unbarred early-type galaxies of the ATLAS^{3D} sample. For each galaxy, they fit the light distribution using a single bulge (Sérsic, 1963, 1968) and a bulge+disc (Sérsic+exponential) model, preferring the latter when the improvement over the single bulge model was substantial and no correlation within the residuals was observed. They found that exponential sub-components in fast rotators correspond to a genuine family of rotationally-supported discs or disc-like structures, which were identified in 83% of the unbarred early-type subsample, contributing to 40% of the total stellar mass and covering a full range of disc-to-total flux ratios. From their analysis, Krajnović et al. (2013) concluded that, when using photometry only, inclination effects do not particularly affect the identification of dominant discs, but they become much more disruptive when dealing with low-inclination, medium size discs. The use of kinematics is therefore the best approach to mitigate inclination effects. One of the key results obtained by the ATLAS^{3D} Collaboration is that the majority of early-type galaxies contain stellar discs with an essentially continuous distribution of disc-to-total flux ratios, which led Cappellari et al. (2011) to the introduction of a new classification scheme aimed at replacing the classical Hubble diagram.

1.2.2 A compendium of the previous literature

Over the past nine years, five independent studies (Graham & Driver, 2007b; Sani et al., 2011; Vika et al., 2012; Beifiori et al., 2012; Läsker et al., 2014a,b) have attempted galaxy decomposition for samples of galaxies with a direct measure of the black hole mass. The main aim of each study was to derive the parameters of the spheroidal components of their galaxies and explore correlation with the black hole mass. Table 1.1 summarises the main characteristics and findings of each work.

	GD07	S+11	V+12	B+12	L+14
Galaxies	27	57	25	19	35
Wavelength	R-band	$3.6 \mu\text{m}$	K-band	<i>i</i> -band	K-band
Decomposition	1D	2D	2D	2D	2D
Nuclei	masked	modelled	modelled	not treated	modelled
Cores	masked	masked	masked	not treated	masked
Bars	excluded	modelled	modelled	excluded	modelled
Other components	no	no	no	no	yes
Kinematics	no	no	no	no	no
<i>Conclusions</i>					
$M_{\text{BH}} - n_{\text{sph}}$	yes	no	no	no	-
$M_{\text{BH}} - L_{\text{sph}}$	-	yes	yes	yes	fundamental
$M_{\text{BH}} - M_{\text{sph,dyn}}$	-	yes	-	yes	-
$M_{\text{BH}} - M_{\text{sph,*}}$	-	yes	-	-	-
$M_{\text{BH}} - R_e$	-	secondary	-	-	-
$M_{\text{BH}} - \langle \mu_e \rangle$	-	-	-	no	-
$M_{\text{BH}} - L_{\text{gal}}$	-	-	-	secondary	fundamental

Table 1.1: Main characteristics and findings of the latest five studies that have attempted galaxy decomposition to derive and explore black hole mass scaling relations. The number of galaxies accounts only for those with a direct measurement of the black hole mass (no upper limits are considered here). GD07 = Graham & Driver (2007b); S+11 = Sani et al. (2011); V+12 = Vika et al. (2012); B+12 = Beifiori et al. (2012); L+14 = Läsker et al. (2014a,b).

Sani et al. (2011) used galaxy images obtained with the *Spitzer* satellite in the $3.6 \mu\text{m}$ wavelength-band, which currently represents the best proxy for the stellar mass, even superior

to the K-band (Sheth et al. 2010, and references therein).

There has been an ongoing debate as to whether 2D galaxy decomposition techniques should be preferred over 1D techniques. The performance of each method can vary according to different technical factors (such as the signal-to-noise of the galaxy images, the accuracy of the description of the Point Spread Function, the gradient of ellipticity and position angle of the galaxy isophotes, the fitting weighting scheme, etc.), therefore advantages and disadvantages are not absolute and depend on the individual science case. To our best knowledge, no published study has ever been conducted on a systematic comparison between 1D and 2D galaxy decomposition techniques.

Previous works have demonstrated that, when studying galaxies with a complex morphology, the accuracy of the recovery of the bulge parameters increases when all galaxy components are taken into account by the model (Laurikainen et al., 2005; Gadotti, 2008; Salo et al., 2015). Läske et al. (2014a) identified and modelled more galaxy components than any other study, but no work did it with the assistance of kinematical information.

Interestingly, the past studies all used almost the same sample of galaxies (the number of directly measured black hole masses increased with time), but they claimed some contradictory conclusions. One study obtained a good $M_{\text{BH}} - n_{\text{sph}}$ correlation, whereas three did not. Läske et al. (2014b) elected the $M_{\text{BH}} - L_{\text{gal}}$ relation as the fundamental one (likewise the $M_{\text{BH}} - L_{\text{sph}}$), as opposed to Beifiori et al. (2012), who presented it as a secondary correlation. The past studies did not converge to the same conclusions because their best-fit models for the same galaxy were often significantly different and not consistent with each other in terms of fitted components. Moreover, none of these studies attempted an individual galaxy-by-galaxy comparison of their models with the previous literature.

1.3 Thesis outline

The aim of this thesis is to refine and re-investigate several black hole mass scaling relations through the careful modelling of the spatial light distribution of a selected sample of 66 nearby galaxies. After obtaining robust structural parameters for the galaxies under study, I will explore

substructure in the correlations between these parameters and the black hole mass, and explain discrepancies in the results presented in the past literature.

In Chapter 2 (Savorgnan et al., 2013), we tackle the issue of the $M_{\text{BH}} - n_{\text{sph}}$ correlation using literature data. Four studies independently carried out photometric decompositions for similar samples of galaxies, but only one of them obtained a statistically significant $M_{\text{BH}} - n_{\text{sph}}$ relation. For each galaxy analysed by two or more studies, we compared the models used to fit the galaxy's spatial distribution of light, and found that the same galaxy was often described with remarkably different models in terms of number and type of sub-components. This was obviously resulting in significantly different best-fit parameters. We then collected the Sérsic index measurements obtained by the four studies for 54 common galaxies with a direct measure of their black hole mass, rejected the most discrepant values, and used the remaining measurements to populate the $M_{\text{BH}} - n_{\text{sph}}$ diagram. Besides recovering a statistically significant $M_{\text{BH}} - n_{\text{sph}}$ relation for all galaxies, we also explored substructure for different galaxy morphological types (elliptical galaxies versus bulges of disc galaxies) and nature of the nuclear light profile (Sérsic versus core-Sérsic).

In Chapter 3 (Savorgnan & Graham, 2016a), we present the 1D decompositions carried out by us for 66 local galaxies with a direct measure of their black hole mass. We describe the careful data reduction process through which we created the image-mosaics for these galaxies, using archival observations at $3.6 \mu\text{m}$ obtained with *Spitzer*. We detail our 1D galaxy decomposition technique and our method to estimate the uncertainties associated with the spheroid's best-fit parameters. Upon comparing the results obtained from our 1D and 2D galaxy models, we comment on the advantages and disadvantages connected with 1D and 2D decomposition techniques. The individual 1D galaxy decompositions are illustrated, along with a thorough analysis of each galaxy's structure and a scrupulous comparison with several past decompositions.

In Chapter 4 (Savorgnan et al., 2016), we use the results from our 1D galaxy decompositions to explore substructure in the $M_{\text{BH}} - L_{\text{gal}}$ and $M_{\text{BH}} - L_{\text{sph}}$ (or $M_{\text{BH}} - M_{*,\text{sph}}$) diagrams for different galaxy morphological types and nature of the nuclear light profile. Upon performing a detailed linear regression analysis using three different routines, we concluded that early-type (elliptical+lenticular) and late-type (spiral) galaxies follow two separate correlations in the $M_{\text{BH}} - L_{\text{sph}}$ (or $M_{\text{BH}} - M_{*,\text{sph}}$) diagram. In addition, we compared the level of intrinsic scatter

in the $M_{\text{BH}} - L_{\text{gal}}$ and $M_{\text{BH}} - L_{\text{sph}}$ diagrams to address the question of whether or not the $M_{\text{BH}} - L_{\text{sph}}$ correlation is more fundamental than the $M_{\text{BH}} - L_{\text{gal}}$ correlation.

In Chapter 5 (?), we use the results from our 1D galaxy decompositions to populate the $L_{\text{sph}} - n_{\text{sph}}$ and $M_{\text{BH}} - n_{\text{sph}}$ diagrams. The analysis that we performed here is essentially analogous to that presented in Chapter 4. We did not observe any significant substructure in the $M_{\text{BH}} - n_{\text{sph}}$ diagram, where all galaxies, irrespective of their morphological type, define a single tight correlation. Consistency between the $M_{\text{BH}} - n_{\text{sph}}$ and other galaxy scaling relations is discussed here.

In Chapter 6 (Savorgnan & Graham, 2015), we concentrate on the $M_{\text{BH}} - \sigma_*$ scaling relation and the presence of some outlying, “overmassive” black holes at the high-mass end of this correlation. Volonteri & Ciotti (2013) proposed a theoretical interpretation to explain why central cluster galaxies tend to appear as positive outliers in the $M_{\text{BH}} - \sigma_*$ diagram, lying above the observed $z = 0$ correlation. According to the results from their semi-analytical models, central cluster galaxies experienced more dry mergers than the “average” population of massive early-type galaxies. Dry mergers are expected to increase the black hole mass, while leaving almost unchanged the stellar velocity dispersion. We tested the interpretation offered by Volonteri & Ciotti (2013) using the latest observational data. First, we updated the $M_{\text{BH}} - \sigma_*$ diagram with a total of 89 galaxies and performed a linear regression analysis of it. Then, for each galaxy with a partially depleted core we measured the extent of dry mergers experienced by the galaxy by means of the ratio between the central stellar mass deficit and the black hole mass. We showed that no positive trend is observed between the number of dry mergers and the positive vertical offset from the $M_{\text{BH}} - \sigma_*$ correlation. A similar test using the kinematics of galaxies gave consistent results, disproving the scenario advocated by Volonteri & Ciotti (2013).

In Chapter 7 (Savorgnan & Graham, 2016b), we tackle the issue of the “overmassive” black holes in the $M_{\text{BH}} - M_{*,\text{sph}}$ diagram. Due to inaccurate decompositions that failed to take into account the correct size of the main disc component, a number of galaxies (Mrk 1216, NGC 1271, NGC 1277, and NGC 1332) had their spheroid luminosity underestimated, which made them appear as positive outliers above the $M_{\text{BH}} - M_{*,\text{sph}}$ correlation. With the aid of photometric and kinematic information, we identified the radial extent of the main disc component, and built

a galaxy model accordingly. We showed that when these galaxies are correctly modelled, they lie well within the scatter of the observed $M_{\text{BH}} - M_{*,\text{sph}}$ correlation.

Finally, Chapter 8 contains a summary of my principal findings, conclusions, and some promising directions for future research.

The recovery of the $M_{\text{BH}} - n_{\text{sph}}$ relation

Graham et al. (2001) demonstrated that the mass of SMBHs is correlated with the stellar light concentration of their host spheroid. Six years later, Graham & Driver (2007b) expanded the galaxy sample of Graham et al. (2001) and carried out 1D bulge/disc decompositions. They described the 1D surface brightness profile of spheroids with the Sérsic model, and obtained a direct measure of the central radial concentration of stars by means of the Sérsic index. Graham & Driver (2007b) confirmed the early findings of Graham et al. (2001), presenting a strong correlation between the black hole mass and the spheroid Sérsic index ($M_{\text{BH}} - n_{\text{sph}}$). They measured a small level of scatter, which made the $M_{\text{BH}} - n_{\text{sph}}$ and $M_{\text{BH}} - \sigma_*$ correlations evenly competing for the title of fundamental black hole mass scaling relation.

As the number of directly measured black hole masses increased with time and the constantly improving technology of machines allowed shorter computational times for 2D decomposition codes, more studies were dedicated to the analysis of various black hole mass scaling relations. Sani et al. (2011), Vika et al. (2012), and Beifiori et al. (2012) attempted 2D decompositions of their samples of galaxies with a direct measure of the black hole mass. Sani et al. and Vika et al. included more than two components in their galaxy models such as bars and nuclear sources, whereas Beifiori et al. excluded barred galaxies from their analysis and used simple bulge+disc models. From these decompositions, they derived and analysed several correlations. However, none of these three studies was able to obtain a strong $M_{\text{BH}} - n_{\text{sph}}$ relation from their data. This raised an obvious question: what prevented Sani et al., Vika et al., and Beifiori et al. from the recovery of a tight $M_{\text{BH}} - n_{\text{sph}}$ correlation? Imputable factors could be the decomposition technique (1D versus 2D), the use of more sophisticated models featuring a larger number

of components, the use of different wavelengths, or possibly the accuracy of the decompositions.

These circumstances motivated us to engage a preliminary study in 2012, aiming at explaining the lack of an $M_{\text{BH}} - n_{\text{sph}}$ correlation in the data of Sani et al., Vika et al., and Beifiori et al. After collecting and comparing the results from the galaxy decompositions of the aforementioned four studies (Graham & Driver, Sani et al., Vika et al., and Beifiori et al.), we immediately noticed that some galaxies had been described by these authors with significantly different models (e.g. the galaxy M60, treated as a discless elliptical galaxy by two studies, and as a lenticular galaxy by the other two studies). Different galaxy models (for the same galaxy) evidently resulted in different best-fit parameters. Not only this, but some studies obtained largely discrepant best-fit parameters for the same galaxy even when they used the same choice of decomposition (e.g. two studies described the galaxy NGC 3115 with a Sérsic-bulge + exponential-disc model, but obtained a bulge Sérsic index of 3 and 13, respectively). This confirmed our doubts about the accuracy of some decompositions.

For each galaxy, we averaged the available Sérsic index measurements and used these average values to populate the $M_{\text{BH}} - n_{\text{sph}}$ diagram. We noticed that a clear correlation was emerging from the data, although with a significant amount of scatter. We attributed the large amount of scatter to “bad” decompositions, and decided to develop a method for an impartial identification of the “bad” Sérsic index measurements. After estimating a maximum tolerable disagreement between the Sérsic index measurements of the same galaxy by taking into account the use of different decomposition methods and wavelengths, we excluded the most discrepant measurements and averaged the remaining ones. This resulted in a dramatic reduction of scatter and the recovery of a strong $M_{\text{BH}} - n_{\text{sph}}$ correlation. Finally, we explored substructure in the $M_{\text{BH}} - n_{\text{sph}}$ diagram expected for consistency with other known scaling relations.

The remainder of this chapter comprises the published version of the paper “The supermassive black hole mass – Sérsic index relations for bulges and elliptical galaxies” by G. A. D. Savorgnan et al., as it appears in Volume 434 of *Monthly Notices of the Royal Astronomical Society*.



The supermassive black hole mass–Sérsic index relations for bulges and elliptical galaxies

G. Savorgnan,¹★ A. W. Graham,¹ A. Marconi,² E. Sani,³ L. K. Hunt,³ M. Vika⁴ and S. P. Driver^{5,6}

¹Centre for Astrophysics and Supercomputing, Swinburne University of Technology, Hawthorn, Victoria 3122, Australia

²Dipartimento di Fisica e Astronomia, Università di Firenze, via G. Sansone 1, I-50019 Sesto Fiorentino, Firenze, Italy

³INAF - Osservatorio Astrofisico di Arcetri, Largo E. Fermi 5, I-50125 Firenze, Italy

⁴Carnegie Mellon University in Qatar, Education City, PO Box 24866, Doha, Qatar

⁵ICRAR - The University of Western Australia, 35 Stirling Highway, Crawley, WA 6009, Australia

⁶SUPA - School of Physics and Astronomy, University of St Andrews, North Haugh, St Andrews KY16 9SS, UK

Accepted 2013 June 6. Received 2013 April 22

ABSTRACT

Scaling relations between supermassive black hole mass, M_{BH} , and host galaxy properties are a powerful instrument for studying their co-evolution. A complete picture involving *all* of the black hole scaling relations, in which each relation is consistent with the others, is necessary to fully understand the black hole–galaxy connection. The relation between M_{BH} and the central light concentration of the surrounding bulge, quantified by the Sérsic index n , may be one of the simplest and strongest such relations, requiring only uncalibrated galaxy images. We have conducted a census of literature Sérsic index measurements for a sample of 54 local galaxies with directly measured M_{BH} values. We find a clear $M_{\text{BH}}-n$ relation, despite an appreciable level of scatter due to the heterogeneity of the data. Given the current $M_{\text{BH}}-L_{\text{sph}}$ and the $L_{\text{sph}}-n$ relations, we have additionally derived the *expected* $M_{\text{BH}}-n$ relations, which are marginally consistent at the 2σ level with the *observed* relations. Elliptical galaxies and the bulges of disc galaxies are each expected to follow two distinct *bent* $M_{\text{BH}}-n$ relations due to the Sérsic/core-Sérsic divide. For the same central light concentration, we predict that M_{BH} in the Sérsic bulges of disc galaxies are an order magnitude higher than in Sérsic elliptical galaxies if they follow the same $M_{\text{BH}}-L_{\text{sph}}$ relation.

Key words: black hole physics – galaxies: bulges – galaxies: fundamental parameters – galaxies: structure.

1 INTRODUCTION

Observations over the past decade have suggested a strong connection between supermassive black holes (SMBHs) and their host galaxies, or rather spheroids, in spite of the huge difference between their respective sizes. While it is clear that the stories of these two objects – the black hole and the galaxy – are tightly interwoven, the origin and nature of their link are still a subject of debate. The scaling relations between the SMBH mass, M_{BH} , and the host spheroid properties make the study of black hole growth an indispensable ingredient to understand the more general framework of galaxy formation and evolution. Beyond the well-known relation with the velocity dispersion σ (Ferrarese & Merritt 2000; Gebhardt et al. 2000; Graham et al. 2011), the masses of SMBHs have been shown to correlate with a wide series of properties belonging

to the spheroidal component of the host galaxy, such as the spheroid luminosity (Kormendy & Richstone 1995; McLure & Dunlop 2002; Marconi & Hunt 2003; Graham & Scott 2013) and stellar mass (Laor 2001; Scott, Graham & Schombert 2013), the spheroid dynamical mass (Magorrian et al. 1998; Marconi & Hunt 2003; Häring & Rix 2004; Scott et al. 2013) and the central stellar concentration of the spheroid (Graham et al. 2001). The connection between bulge mass and disc galaxy morphological type means that the pitch angle of a disc galaxy’s spiral arms is also related to the black hole mass (e.g. Berrier et al. 2013; Davis et al. 2013, and references therein). The old $M_{\text{BH}} \propto \sigma^4$ and $M_{\text{BH}} \propto L^{1.4}$ relations were actually inconsistent with each other (e.g. Lauer et al. 2007), and inconsistent with the curved $M_{\text{BH}}-n$ relation (Graham & Driver 2007b) given the existence of a linear $L-n$ relation (see Section 4). The first of these inconsistencies was addressed in Graham (2012; see also section 6 of Graham 2008), and we tackle the second here. The astrophysical interest in all of these empirical relations resides partly in the fact that they must *all* be taken into account by any complete theory

* E-mail: gsavorgn@astro.swin.edu.au

or model describing the co-evolution of galaxies and SMBHs, and also in their employment to predict the masses of SMBHs in other galaxies.

A decade ago Graham et al. (2001) presented evidence for a strong correlation between the stellar light concentration $C_{\text{re}}(1/3)$ of spheroids and their SMBH mass, showing that more centrally concentrated spheroids have more massive black holes. Graham & Driver (2007b) re-investigated the same relation, directly using the Sérsic (1963, 1968) index n as a measure of the radial concentration of the stars. In addition to a log-linear relation, Graham & Driver (2007b) fit a log-quadratic regression, finding that the $M_{\text{BH}}-n$ relation changed slopes at the low- and high-mass end, and had a level of scatter equivalent to the $M_{\text{BH}}-\sigma$ relation at that time (~ 0.3 dex). The advantages of using the $M_{\text{BH}}-n$ relation to predict the mass of SMBHs are several: as noted by Graham & Driver (2007b), the measurement of n requires only images (even photometrically uncalibrated); it is not heavily affected by possible kinematic substructure at the centre of a galaxy, nor by rotational velocity or the vertical velocity dispersion of an underlying disc, nor by aperture corrections; it is cheap to acquire in terms of telescope time; and it does not depend on galaxy distances.

Pastrav et al. (2013) have recently pointed out that the recent deep, wide-field photometric surveys of galaxies – e.g. the Sloan Digital Sky Survey (SDSS, York et al. 2000) and the Galaxy And Mass Assembly (GAMA, Driver et al. 2011) – are providing us with large statistically useful samples of galaxies whose major morphological components can be resolved out to $z \simeq 0.1$. Furthermore, automatic image analysis routines, such as GIM2D (Simard et al. 2002), GALFIT (Peng et al. 2002, 2010), BUDDA (Gadotti 2008) and GALPHAT (Yoon, Weinberg & Katz, in preparation), can be used to model the surface brightness distribution of the stellar components of these galaxies (e.g. Allen et al. 2006; Simard et al. 2011; Kelvin et al. 2012). A bulge/disc decomposition, along with adequate corrections to account for dust and inclination effects as provided by Pastrav et al. (2013), can provide the Sérsic index of the spheroid component of both elliptical and disc galaxies. This can then be used to predict black hole masses in large samples of galaxies to derive the local black hole mass function (e.g. Graham et al. 2007) and space density (Graham & Driver 2007a, and references therein), if a well calibrated $M_{\text{BH}}-n$ relation exists. However, in the past two years Sani et al. (2011), Vika et al. (2012) and Beifiori et al. (2012) have failed to recover a strong $M_{\text{BH}}-n$ relation.

Due to the existence of the luminosity– n relation (e.g. Young & Currie 1994; Jerjen, Binggeli & Freeman 2000; Graham 2013, and references therein) and the M_{BH} –luminosity relation (e.g. Magorrian et al. 1998), an $M_{\text{BH}}-n$ relation must exist.¹ It is important to investigate why the $M_{\text{BH}}-n$ relation may not have been recovered in the above studies. It is also important to know how it fits in with, and is consistent with, the other scaling relations. Not only does a proper and complete understanding of the SMBH–galaxy connection require this, but the central concentration of stars, reflecting the inner gradient of the gravitational potential, should be intimately related to the black hole mass. A well-determined $M_{\text{BH}}-n$ relation may also provide an easy and accurate means to predict black hole masses in other galaxies. Eventually, semi-analytic models of galaxy formation and simulations should include in their recipes *all* of the black hole mass scaling relations.

In this work, we present a census of literature Sérsic index measurements for local galaxies with directly measured SMBH mass.

¹ It is not yet established which are the primary or secondary relations.

We re-investigate and recover the $M_{\text{BH}}-n$ relation using the combined data from four past independent works. In Section 2, we describe our galaxy sample and in Section 3, we present the $M_{\text{BH}}-n$ scaling relation which is then discussed and compared with predictions in Section 4. Finally, we summarize our analysis in Section 5.

2 DATA

2.1 SMBH masses

Our SMBH galaxy sample comes from Graham & Scott (2013), who have built a catalogue of 80 galaxies with SMBH masses obtained from direct maser, stellar or gas kinematic measurements. Black hole masses for our final sample are listed in Table 1, along with their total galaxy B -band absolute magnitudes, M_{BT} , taken from the *Third Reference Catalogue of Bright Galaxies* (de Vaucouleurs et al. 1991, hereafter RC3) and also their morphological classification. The final sample consists of those galaxies for which Sérsic indices have been reported by at least one of the four studies mentioned below.

2.2 Collecting Sérsic indices

The radial light distribution of spheroidal systems (such as elliptical galaxies or the bulges of lenticular and spiral galaxies) is well described by the Sérsic (1963, 1968) $R^{1/n}$ model that parametrizes the intensity I as a function of the projected galactic radius R such that

$$I(R) = I_{\text{e}} \exp \left\{ -b_n \left[\left(\frac{R}{R_{\text{e}}} \right)^{1/n} - 1 \right] \right\}$$

(Caon, Capaccioli & D’Onofrio 1993; Andredakis et al. 1995; Graham & Driver 2005, and references therein). The quantity I_{e} is the intensity at the effective radius R_{e} that encloses half of the total light from the model, and b_n is a constant defined in terms of the Sérsic index n , which is the parameter that measures the curvature of the radial light profile.

We obtained Sérsic index measurements for our SMBH sample from the following four independent works.

(i) Graham & Driver (2007b, hereafter GD07) fit the radial light profiles from a sample of 27 elliptical and disc galaxies with SMBH masses derived from resolved dynamical studies. The light profiles they used were predominantly from Graham et al. (2001), who searched the various public archives for high-quality R -band images and fit ellipses to the isophotes with the *IRAF* task `ellipse`, allowing the position angle and ellipticity to vary with radius.² The resulting light profiles were then fit by GD07 with a seeing-convolved Sérsic $R^{1/n}$ model for elliptical galaxies, and with a combined (seeing-convolved) exponential disc and $R^{1/n}$ bulge for the disc galaxies, using the subroutine `UNCMND` from Kahaner et al. (1989). The inner couple of arcseconds of the profiles was in some instances excluded from the fit due to the potential presence of partially depleted cores or active galactic nuclei (AGNs), that would produce a biasing central deficit or excess of light relative to the inward extrapolation of their outer Sérsic profile.

(ii) Vika et al. (2012, hereafter V12) investigated the $M_{\text{BH}}-n$ and the $M_{\text{BH}}-L$ relations. They performed two-dimensional (2D) profiling with *GALFIT3* on near-IR images [from the UKIRT Infrared

² A discussion of the original galaxy light profiles can be found in Erwin, Graham & Caon (2004) and Trujillo et al. (2004).

Table 1. SMBH galaxy sample. Column (1): galaxy names; eight galaxies marked with an asterisk (*) have been excluded from the final analysis due to the large disagreement on their Sérsic index measurements, according to the criteria mentioned in Section 2.4. Column (2): morphological type as listed by Graham & Scott (2013), primarily from NED. Column (3): absolute total B -band magnitudes, from the RC3 catalogue using the galaxy distances published in Graham & Scott (2013). Column (4): black hole masses from Graham & Scott (2013). Column (5): presence of a partially depleted core as listed by Graham & Scott (2013) and such that the question mark is used when the classification has come from the velocity dispersion criteria mentioned in Section 3. Columns (6–9): galaxy decomposition performed by the four works described in Section 2.2; B = Sérsic profile, D = disc, g = Gaussian, m = central mask, b = bar, p = PSF. Columns (10–13): measured Sérsic index values.

Galaxy (1)	Type (2)	M_{B_T} (mag) (3)	M_{BH} ($10^8 M_{\odot}$) (4)	Core (5)	Decomposition				n (10)	$V12^b$ (11)	$S11^c$ (12)	$B12^d$ (13)	
					GD07 ^a (6)	$V12^b$ (7)	$S11^c$ (8)	$B12^d$ (9)					
Abell 1836-BCG	E1	-21.43	39^{+4}_{-5}	y?				BD					2.73
Circinus	Sb	-15.14	$0.011^{+0.002}_{-0.002}$	n?				BD					2.0
IC 1459	E	-21.30	24^{+10}_{-10}	y				Bg					6.0
IC 2560	SBb	-20.52	$0.044^{+0.044}_{-0.022}$	n?				BDg					2.0
MESSIER 32	S0?	-15.46	$0.024^{+0.005}_{-0.005}$	n	BD	BDm	BD		1.51	2.1	4.0		
MESSIER 59	E	-20.68	$3.9^{+0.4}_{-0.4}$	n		Bm	B			5.7	5.0		
MESSIER 60	E1	-21.26	47^{+10}_{-10}	y	B	Bm	BD	BD	6.04	3.6	3.0	1.63	
MESSIER 64	Sab	-19.96	$0.016^{+0.004}_{-0.004}$	n?				BD					1.49
MESSIER 77	SBb	-21.30	$0.084^{+0.003}_{-0.003}$	n		BDbm	BDg	BD		0.8	1.0	1.27	
MESSIER 81	Sab	-20.01	$0.74^{+0.21}_{-0.11}$	n	BD		BDg	BD	3.26		3.0	2.57	
MESSIER 84	E1	-21.17	$9^{+0.9}_{-0.8}$	y	B	Bm	Bg	B	5.60	3.5	7.0	4.10	
MESSIER 87*	E0	-21.38	$58^{+3.5}_{-3.5}$	y?	B	Bm	Bg		6.86	2.4	4.0		
MESSIER 89	E	-20.14	$4.7^{+0.5}_{-0.5}$	y		B	BDg	B		3.6	4.0	4.30	
MESSIER 96	SBab	-19.91	$0.073^{+0.015}_{-0.015}$	n			BDb					1.0	
MESSIER 104	Sa	-20.91	$6.4^{+0.4}_{-0.4}$	y			BDbg					1.5	
MESSIER 105	E1	-19.82	4^{+1}_{-1}	y	B		B		4.29			5.0	
MESSIER 106	SBbc	-20.19	$0.39^{+0.01}_{-0.01}$	n	BD	BDp	BDg		2.04	3.5	2.0		
Milky Way	SBbc		$0.043^{+0.004}_{-0.004}$	n	BD					1.32			
NGC 0524	S0	-20.54	$8.3^{+2.7}_{-1.3}$	y			BD					3.0	
NGC 0821	E	-20.18	$0.39^{+0.26}_{-0.09}$	n	B		B	B	4.00		7.0	7.70	
NGC 1023	SB0	-19.88	$0.42^{+0.04}_{-0.04}$	n	BD		BDb		2.01			3.0	
NGC 1300	SBbc	-20.47	$0.73^{+0.69}_{-0.35}$	n			BD					3.0	
NGC 1316	SB0	-21.93	$1.5^{+0.75}_{-0.8}$	y?			BDg					5.0	
NGC 1399	E	-20.89	$4.7^{+0.6}_{-0.6}$	y	B				16.8				
NGC 2549	SB0	-18.26	$0.14^{+0.02}_{-0.13}$	n			BD					7.0	
NGC 2778	SB0	-18.39	$0.15^{+0.09}_{-0.1}$	n	BD	BD	BD		1.60	2.7	2.5		
NGC 2787*	SB0	-17.50	$0.4^{+0.04}_{-0.05}$	n	BD		BDbg		1.97			3.0	
NGC 2960	Sa?	-21.25	$0.12^{+0.005}_{-0.005}$	n?		BD				4.0			
NGC 2974	E	-19.73	$1.7^{+0.2}_{-0.2}$	n			Bg					3.0	
NGC 3079	SBc	-20.04	$0.024^{+0.024}_{-0.012}$	n?			BDbg					2.0	
NGC 3115*	S0	-20.00	$8.8^{+10}_{-2.7}$	n	BD		BD		13.0			3.0	
NGC 3227	SBa	-20.44	$0.14^{+0.1}_{-0.06}$	n			BD					4.0	
NGC 3245	S0	-19.84	$2^{+0.5}_{-0.5}$	n	BD	BD	BD	BD	4.31	2.6	2.5	1.60	
NGC 3377	E5	-18.95	$0.77^{+0.04}_{-0.06}$	n	B		B	B	3.04		6.0	3.47	
NGC 3384	SB0	-19.42	$0.17^{+0.01}_{-0.02}$	n	BD		BDb	BD	1.72		2.5	2.33	
NGC 3414	S0	-19.99	$2.4^{+0.3}_{-0.3}$	n			BDb					5.0	
NGC 3489	SB0	-19.22	$0.058^{+0.008}_{-0.008}$	n			BD					1.5	
NGC 3585	S0	-20.57	$3.1^{+1.4}_{-0.6}$	n			BD					2.5	
NGC 3607	S0	-20.91	$1.3^{+0.5}_{-0.5}$	n			Bg	B				5.0	4.70
NGC 3608*	E2	-20.04	$2^{+1.1}_{-0.6}$	y			B	B				6.0	9.03
NGC 3998*	S0	-19.07	$8.1^{+2}_{-1.9}$	y?			BDg	BD				1.5	2.29
NGC 4026	S0	-18.93	$1.8^{+0.6}_{-0.3}$	n			BD					3.5	
NGC 4151	SBab	-20.01	$0.65^{+0.07}_{-0.07}$	n			BDg					3.5	
NGC 4261	E2	-21.03	5^{+1}_{-1}	y	B	Bm	BDg	B	7.30	3.5	4.0	4.31	

Table 1 – *continued*

Galaxy	Type	M_{BT} (mag)	M_{BH} ($10^8 M_{\odot}$)	Core	GD07 ^a	Decomposition			GD07 ^a	n	V12 ^b	S11 ^c	B12 ^d
						V12 ^b	S11 ^c	B12 ^d					
(1)	(2)	(3)	(4)	(5)	(6)	(7)	(8)	(9)	(10)	(11)	(12)	(13)	
NGC 4291	E2	-19.60	$3.3^{+0.9}_{-2.5}$	y	B					4.02			
NGC 4342*	S0	-18.40	$4.5^{+2.3}_{-1.5}$	n	BD	BD				5.11	1.9		
NGC 4459*	S0	-19.66	$0.68^{+0.13}_{-0.13}$	n		B	BD	B			3.9	2.5	7.44
NGC 4473	E5	-19.76	$1.2^{+0.4}_{-0.9}$	n	B	Bm	B	BD	2.73	4.3	7.0	2.23	
NGC 4486A	E2	-18.04	$0.13^{+0.08}_{-0.08}$	n		Bm	B			2.0	2.5		
NGC 4564	S0	-18.77	$0.6^{+0.03}_{-0.09}$	n	BD	BD	BD		3.15	3.7	7.0		
NGC 4596	SB0	-19.80	$0.79^{+0.38}_{-0.33}$	n		BDb	BDb	BD		3.6	3.0	4.43	
NGC 4697	E4	-20.14	$1.8^{+0.2}_{-0.1}$	n	B	B	B	B	4.00	3.8	5.0	4.96	
NGC 5077	E3	-20.69	$7.4^{+4.7}_{-3}$	y			Bg				6.0		
NGC 5128	S0	-20.06	$0.45^{+0.17}_{-0.1}$	n?			BDbg				3.5		
NGC 5252	S0	-21.03	11^{+16}_{-5}	n				BD				4.82	
NGC 5576	E3	-20.12	$1.6^{+0.3}_{-0.4}$	n		Bm	B	B		5.1	7.0	8.71	
NGC 5813	E	-21.03	$6.8^{+0.7}_{-0.7}$	y		Bm	B			8.3	6.0		
NGC 5845	E3	-18.51	$2.6^{+0.4}_{-1.5}$	n	B	B	B	B	3.22	2.6	3.0	3.45	
NGC 5846	E	-20.87	11^{+1}_{-1}	y		Bm	B			3.7	3.0		
NGC 6251*	E2	-21.46	5.9^{+2}_{-2}	y?	B		Bg			11.8	7.0		
NGC 7052	E	-20.71	$3.7^{+2.6}_{-1.5}$	y	B	BD	B		4.55	1.8	5.0		
NGC 7582	SBab	-20.34	$0.55^{+0.26}_{-0.19}$	n			BDg				4.0		

^a Graham & Driver (2007b). ^b Vika et al. (2012). ^c Sani et al. (2011). ^d Beifiori et al. (2012).

Deep Sky Survey Large Area Survey (UKIDSS-LAS); Lawrence et al. (2007)] of a sample of 25 galaxies. V12 fit the light distribution using a Sérsic function for the elliptical galaxies, the bulges and the bars of lenticular/spiral galaxies and an exponential function for the disc components. In the case of core-Sérsic galaxies with partially depleted cores, they implemented a mask for the inner region. Bright nuclei were additionally modelled as point sources using the point spread function (PSF). A relation between SMBH mass and the Sérsic index was not found by V12. They noticed that the Sérsic index can vary significantly from study to study and they suggested that such mismatch may be due to the different weighting of pixels during the fit that each study used and/or to a wavelength bias. The signal-to-noise-weighted fitting routines, such as GALFIT, can be highly sensitive to central dust obscuration, unaccounted for central excesses and deficits of light relative to the fitted model, and especially errors in the adopted PSF.

(iii) From their GALFIT3-derived 2D bulge-disc decompositions of *Spitzer*/IRAC 3.6 μm images of 57 galaxies, Sani et al. (2011, hereafter S11) investigated the scaling relations between SMBH mass and several other parameters of the host spheroids. The image decomposition was performed with a Sérsic model for the elliptical galaxies and with a Sérsic model plus an exponential model for the lenticular and spiral galaxies. A Gaussian component and a nuclear point source were added in the presence of a bar or an AGN, respectively. In an attempt to restrict the degeneracy between the effective radius and the Sérsic index, following Hunt, Pierini & Giovanardi (2004), S11 performed 2D fitting by fixing the Sérsic index to a set of constant values in the range between $n = 1$ and $n = 7$. They found tight correlations between the SMBH mass and the bulge luminosity and dynamical mass. However, the relation between the SMBH mass and the effective radius had a high intrinsic dispersion and no correlation with the Sérsic index was found.

(iv) Beifiori et al. (2012, hereafter B12) analysed SDSS *i*-band images and extracted photometric and structural parameters for a sample of 57 galaxies, for which 19 had an accurate M_{BH} measurement and the remaining 38 had only an upper limit which are not used here. They performed 2D decompositions with GASP2D (Méndez-Abreu et al. 2008), using a Sérsic profile to model the elliptical galaxies and a combination of a Sérsic plus an exponential model for the disc galaxies. Galaxies affected by poor decomposition due to either a central bar, a Freeman Type II disc profile (Freeman 1970), or just inadequately represented by the single or double component modelling were eliminated from their initial sample. Among their correlations involving the SMBH mass and the parameters of the host galaxy, the tightest was with the stellar velocity dispersion. Little or no correlation was found with the Sérsic index (see their fig. 7).

Table 1 reports the Sérsic index measurements from the above four works, along with the type of photometric decomposition performed. It comprises 62 galaxies. Each galaxy can have up to four Sérsic index estimates. 35 galaxies have multiple measurements of their Sérsic index. In the next two Sections we discuss how we compare and combine them.

2.3 Comparing Sérsic indices

There are three main points that distinguish each study: the first is the wavelength of the image.

The spatial distribution of the surface brightness of a galaxy, and hence its light profile, is a function of the observational bandpass. This means that the structural parameters, in general, may vary with wavelength due to stellar population gradients or dust obscuration. The central light concentration of a galaxy, described by the Sérsic index, is indeed a slight function of wavelength. Using reprocessed

Sloan Digital Sky Survey Data Release Seven (SDSS DR7, Abazajian et al. 2009) and UKIDSS-LAS (Lawrence et al. 2007) imaging data available from the GAMA data base, Kelvin et al. (2012) performed 2D model fits with GALFIT to $\sim 170\,000$ galaxies in the $ugrizYJHK$ bandpasses, using primarily a pure Sérsic profile, to quantify how photometric and structural parameters of a galaxy vary with wavelength. Their fig. 21 shows the mean Sérsic index as a function of the rest-frame wavelength for two subsamples: the disc-dominated and the spheroid-dominated systems. Kelvin et al. (2012) find that the spheroid-dominated population is characterized by mean Sérsic indices that remain relatively stable at all wavelengths, with n increasing by 30 per cent from g to K .

The second point is the model-fitting method: one-dimensional and two-dimensional photometric decomposition techniques, if performed on the same galaxy, can produce different values of the Sérsic index due to ellipticity gradients which the 2D models cannot accommodate. The parameters of the Sérsic model can vary if derived along the major or the minor axis, as first noted by Caon et al. (1993). Ferrari et al. (2004) quantified such discrepancy in terms of ellipticity gradients, i.e. the isophote eccentricity that varies with radius. The histogram in Fig. 1 has been created using data from Caon et al. (1993) and shows the distribution of the ratio between the ‘equivalent’ Sérsic index n_{eq} and that measured along the major axis, n_{maj} . The ‘equivalent’ axis is the geometric mean, \sqrt{ab} , of the major and the minor axis of the isophotal ellipses. The mean (and the standard deviation) of the whole sample is $\langle n_{\text{eq}}/n_{\text{maj}} \rangle = 1.10 \pm 0.27$. This tells us that the equivalent Sérsic index is on average 10 per cent higher than the major axis Sérsic index. From Fig. 1, their relative difference will be less than 40 per cent in 95 per cent of the time.

The third issue pertains to the weighting scheme used for the fits. The arrival of photons, which build up a galaxy image, is a Poissonian process ($\text{noise} \propto \sqrt{\text{signal}}$), which therefore advocates

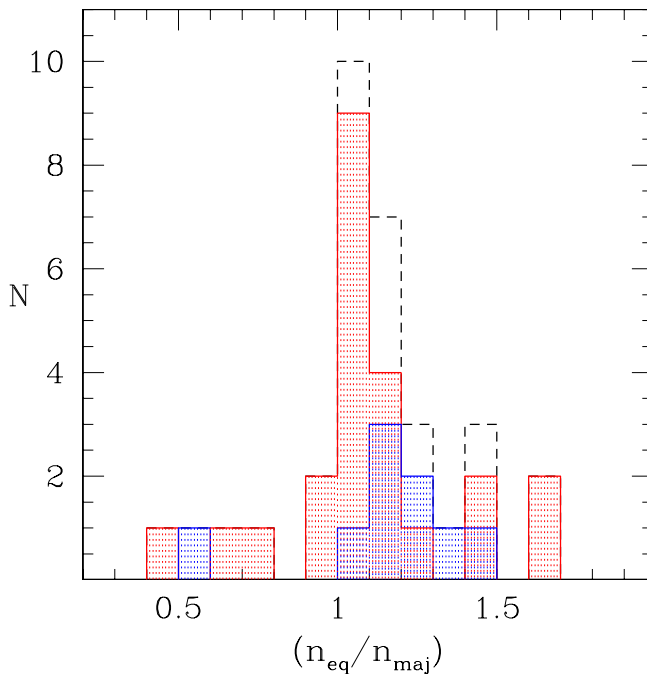


Figure 1. Distribution of the ratio between the “equivalent” Sérsic index n_{eq} and that measured along the major-axis n_{maj} . Data are taken from Caon et al. (1993). The red histogram is for elliptical galaxies, while the blue is for lenticular galaxies and the black dashed line represents the whole sample.

the need for a signal-to-noise-weighted fitting scheme. However, the presence of AGNs, nuclear star clusters, nuclear stellar discs, dust, partially depleted cores and an uncertain PSF make such a weighting prone to error unless all of these factors are taken into account.

Hence, what do we expect from our heterogeneous collection of data? First, the wavelength bias should produce a systematic effect in the Sérsic index measurements, i.e. we expect the measurements from GD07 (R band) and B12 (i band) to be slightly smaller than those from V12 (K band) and S11 (3.6 μm). Secondly, because the Sérsic index derived from a two-dimensional analysis can be approximated to the one-dimensional n_{eq} , one may expect the Sérsic index derived from one-dimensional decomposition along the major axis, as performed by GD07, to be slightly smaller than the Sérsic index derived from the two-dimensional modelling in V12, S11 and B12. However, when we compare different measurements of the Sérsic index (belonging to the same galaxy), we do not observe the previous systematic effects; moreover, for a non-negligible number of galaxies we find that multiple measurements have a relative difference³ greater than 50 per cent.

Many factors, if not properly taken into account, can affect the model fitting of the light distribution of a galaxy and hence the derivation of its structural parameters. These factors can include: additional nuclear components, the presence of a bar, a partially depleted core in high-resolution images, a bad sky subtraction, etc. Moreover, different choices of structural components for the same galaxy will produce contrasting Sérsic indices. Table 2 reports a few examples of discrepant measurements. For the first five galaxies, each study used the same type of decomposition (Sérsic or Sérsic+exponential). For the last three galaxies, each study performed a different image decomposition. M60 was modelled with a pure Sérsic profile by GD07 and V12, while S11 and B12 used an additional disc component. NGC 4459 has a bulge+disc profile according to S11, while V12 and B12 agreed in modelling the galaxy with a pure Sérsic profile. GD07 and S11 fit NGC 7052 with a pure Sérsic profile, whereas V12 chose a bulge+disc model. An exhaustive analysis of why the individual Sérsic indices differ from author to author is however beyond the scope of this work.

2.4 Combining Sérsic indices

To combine the results of these four heterogeneous works, we decided to use a method that was as simple as possible and that involved the least manipulation of the data. Our strategy consisted of looking at galaxies with multiple measurements, comparing the different Sérsic indices and excluding the most contrasting measurements before then averaging the remaining Sérsic indices.

The exclusion algorithm is the following: given a galaxy A that has been analysed by more than one study, we take each measurement n_i^A and we look for the closest one n_j^A . If the absolute difference $|\Delta n_{ij}^A| = |n_i^A - n_j^A|$ is more than 50 per cent of the minimum among the two measurements, we exclude n_i^A . Obviously, if a galaxy has only two measurements, we exclude both of them. After applying the exclusion algorithm, we compute the average logarithmic value of the remaining measurements to give us $\langle \log(n^A) \rangle$.

Figs 2 and 3 are helpful to visualize our approach. Fig. 3 is a ‘zoom’ of Fig. 2 and they both show the absolute total B -band magnitude M_{B_T} of elliptical galaxies plotted against their Sérsic

³ Given two measurements n_1 and n_2 , with $n_1 < n_2$, we define the *relative difference* as $(n_2 - n_1)/n_1$.

Table 2. Examples of outlying measurements, used to explain the crossed out data in Fig. 3. Column (1): galaxy names. Columns (2,4,6,8): literature Sérsic index measurements in ascending order; the reference is given in the superscript. Columns (3,5,7): relative differences; bold type is used for values greater than 50 per cent.

Galaxy (1)	n_1 (2)	$\frac{n_2-n_1}{n_1}$ (3)	n_2 (4)	$\frac{n_3-n_2}{n_2}$ (5)	n_3 (6)	$\frac{n_4-n_3}{n_3}$ (7)	n_4 (8)
Galaxies with same choice of decomposition							
M87	2.4 ^{V12}	0.67	4.0 ^{S11}	0.72	6.86 ^{GD07}		
NGC 0821	4.0 ^{GD07}	0.75	7.0 ^{S11}	0.10	7.70 ^{B12}		
NGC 3115	3.0 ^{S11}	3.33	13.0 ^{GD07}				
NGC 4342	1.9 ^{V12}	1.69	5.11 ^{GD07}				
NGC 4564	3.15 ^{GD07}	0.17	3.7 ^{V12}	0.89	7.0 ^{S11}		
NGC 6251	7.0 ^{S11}	0.69	11.8 ^{GD07}				
Galaxies with different choices of decomposition							
M60	1.63 ^{B12}	0.84	3.0 ^{S11}	0.20	3.6 ^{V12}	0.68	6.04 ^{GD07}
NGC 4459	2.5 ^{S11}	0.56	3.9 ^{V12}	0.91	7.44 ^{B12}		
NGC 7052	1.8 ^{V12}	1.53	4.55 ^{GD07}	0.10	5.0 ^{S11}		

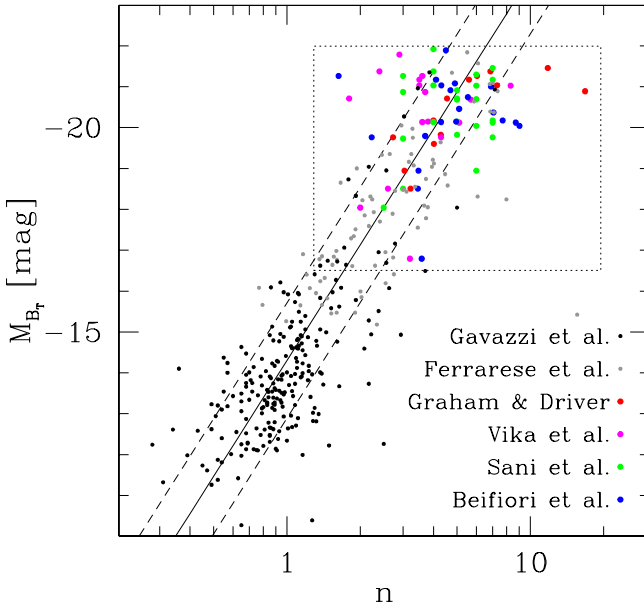


Figure 2. Absolute B -band magnitude versus Sérsic index of elliptical galaxies. Black points are measurements from Gavazzi et al. (2005); grey points are from Ferrarese et al. (2006); red points are from GD07; pink points are from V12; green points are from S11; blue points are from B12. The black points from Gavazzi et al. (2005) and the grey points from Ferrarese et al. (2006) have been plotted just for illustrative purposes, but they will be ignored in the following analysis because they are not from a black hole sample. Each galaxy can have more than one Sérsic measurement and hence may be represented more than once along the horizontal axis (with different colours). The black solid line shows the elliptical galaxy $M_{B_T} - n$ relation from Graham & Guzmán (2003), while the dashed lines are a rough ‘by eye’ estimate of the scatter from their diagram. The dotted box marks the region that is shown in Fig. 3.

index. The black solid line shows the $M_{B_T} - n$ relation from Graham & Guzmán (2003) such that $M_{B_T} = -9.4 \log(n) - 14.3$, while the dashed lines are a rough ‘by eye’ estimate of its scatter.

The horizontal solid lines in Fig. 3 connect the different Sérsic index measurements of the same galaxy. If a galaxy’s Sérsic index has been measured by more than one study, it is represented with a bigger dot. Thus, small dots refer to galaxies that have been measured by only one study. A black cross on a dot means that

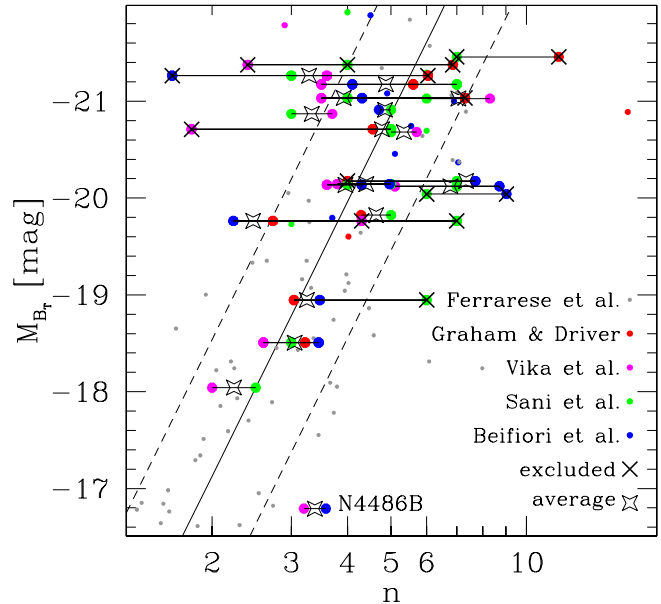


Figure 3. Absolute B -band magnitude versus Sérsic index of elliptical galaxies. This figure is a ‘zoom’ of the dotted box in Fig. 2 and it uses the same colour coding (see the previous caption). The black solid line and the dashed lines are again the $M_{B_T} - n$ relation from Graham & Guzmán (2003) and a rough ‘by eye’ estimate of the scatter in their diagram. The grey points are excluded from the following description. Horizontal solid lines connect different Sérsic measurements of the same galaxy. Bigger dots refer to galaxies with multiple measurements, while smaller dots show galaxies with only one measurement. The black crosses mark the excluded measurements, according to the algorithm described in Section 2.4 and illustrated in Table 2. Big empty stars indicate the average Sérsic index ($\langle \log(n) \rangle$) derived from the ‘good’ (not excluded) Sérsic measurements.

we intend to exclude that particular measurement because it is in strong disagreement (>50 per cent) with the other points according to our exclusion algorithm. The average ($\langle \log(n^A) \rangle$) of the logarithmic values of the remaining measurements is denoted by an empty star.

We apply the same procedure to the bulges of the lenticular and spiral galaxies, which are not shown in the $M_{B_T} - n$ plots (Figs 2 and 3), but are included in the following analysis. Our final sample consists of 54 galaxies with directly measured SMBH mass and at least one measurement of the Sérsic index; among these, 27 galaxies

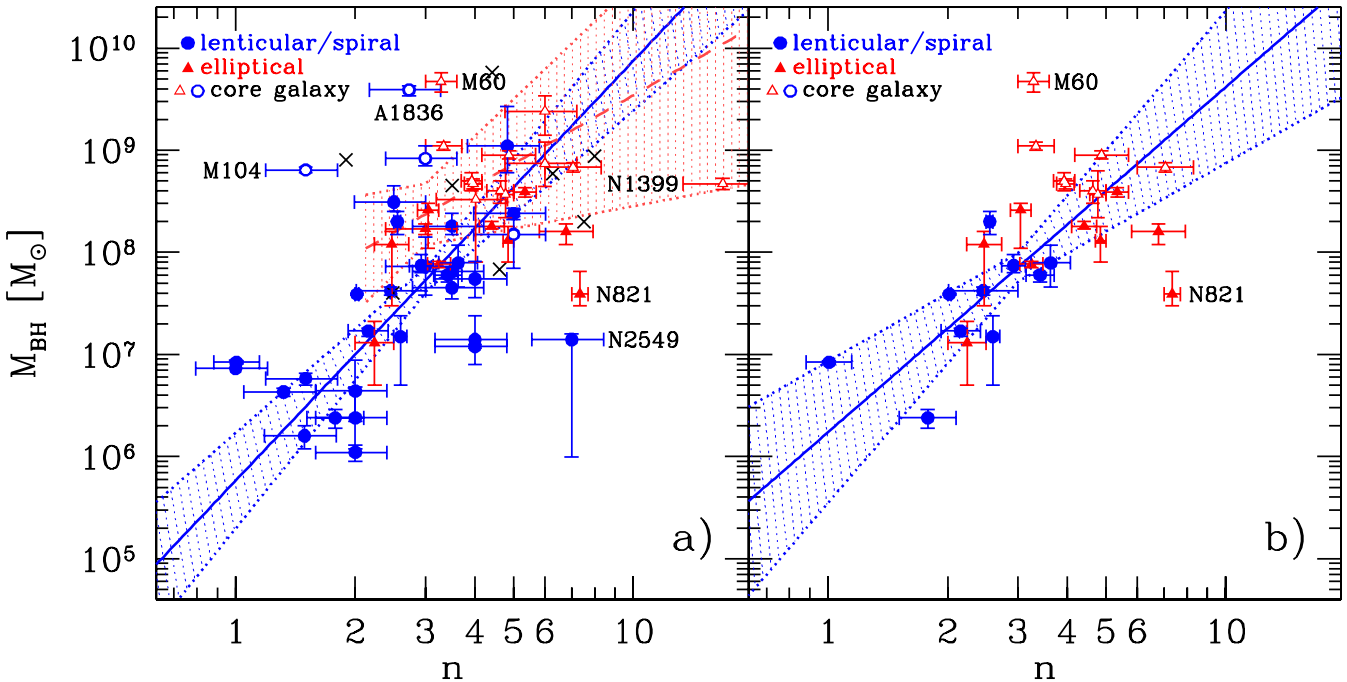


Figure 4. Black hole mass versus Sérsic index. Fig. 4(a): all galaxies with at least one measurement from GD07, V12, S11 and B12; if a galaxy has been measured by more than one study, we plot the average value of its Sérsic index as obtained in Section 2.4. The black crosses are used to show the location of the eight galaxies excluded from the initial sample of 62, due to widely varying Sérsic indices (we plot their mean Sérsic index). Fig. 4(b): only the 27 galaxies with multiple Sérsic measurements. Open symbols are used for core-Sérsic galaxies, rather than filled symbols that denote Sérsic galaxies. The solid blue line (and the blue dotted lines) shows the symmetrical bisector regression (with errors) for the Sérsic bulges of disc galaxies. The dashed red line (and the red dotted lines) shows the symmetrical bisector regression (with errors) for core-Sérsic elliptical galaxies (not shown in Fig. 4(b) due to the low number statistics). The labelled galaxies designate outliers that were excluded from the regressions.

have indices measured by more than one study. The eight galaxies excluded from the initial sample of 62 objects, due to widely varying Sérsic indices, are marked with a star in Table 1.

3 ANALYSIS

After taking galaxies with multiple Sérsic index measurements, rejecting the outlying values and averaging the remaining ones, according to the strategy discussed in Section 2.4, we build the $M_{\text{BH}}-n$ diagram. For galaxies with multiple measurements, we calculated the error on their mean Sérsic index, whereas for single-measured objects we assumed an error⁴ of 20 per cent. Fig. 4(a) includes galaxies with single and averaged-multiple Sérsic indices, whereas Fig. 4(b) only shows those with an averaged-multiple measurement and is thus more reliable.

Despite the higher level of scatter in Fig. 4(a), both diagrams display an appreciable correlation between the SMBH mass and the spheroid light concentration. That is, after excluding the discrepant Sérsic indices according to the process in Section 2.4, presumably from poor fits, we recover a clear trend between black hole mass and Sérsic index. We have visually identified six⁵ outliers in Fig. 4(a) and two⁶ outliers in Fig. 4(b); these objects are labelled in both

Table 3. Spearman's correlation coefficients $r_s(N - 2)$ and likelihood of the correlation occurring by chance P . $N - 2$ are the degrees of freedom.

Fig. 4(a) excluding outliers	$r_s(46) = 0.72$	$P < 0.1$ per cent
Fig. 4(a) including outliers	$r_s(52) = 0.53$	$P < 0.1$ per cent
Fig. 4(b) excluding outliers	$r_s(23) = 0.76$	$P < 0.1$ per cent
Fig. 4(b) including outliers	$r_s(25) = 0.60$	$P < 1$ per cent

diagrams and were excluded from the following regression analysis. The Spearman's correlation coefficients r_s and the likelihood of the correlation occurring by chance P are given in Table 3. In both panels, we have performed a symmetrical linear bisector regression using the BCES routine from Akritas & Bershady (1996), which was checked using the Bayesian linear regression code LINMIX_ERR (Kelly 2007). However, we have not lumped all the galaxy data together, as there is good reason not to do this.

Among our galaxy sample with direct M_{BH} measurements, Graham & Scott (2013) identified 'core-Sérsic' galaxies that display a central deficit of light relative to the inward extrapolation of their outer Sérsic light profile, and 'Sérsic' galaxies that do not (Graham & Guzmán 2003; Graham et al. 2003; Trujillo et al. 2004). 'Core-Sérsic' galaxies are thought to have formed from dry merger events, whereas 'Sérsic' galaxies are the result of gaseous processes. Their classification (Column 5 of Table 1) has primarily come from the inspection of high-resolution images. When no core designation was available or possible from the literature, Graham & Scott (2013) used a criteria based on the velocity dispersion σ , such that galaxies with $\sigma > 270 \text{ km s}^{-1}$ are considered likely to possess a partially depleted core, while galaxies with $\sigma < 165 \text{ km s}^{-1}$ are

⁴ The error of single-measured objects was estimated as follows. Using the 35 galaxies with multiple measurements of their Sérsic indices, we first computed the average $\langle \log(n) \rangle$ of each galaxy without applying the exclusion algorithm (see Section 2.4) and its error $\sigma_{\langle \log(n) \rangle}$; we then calculated the median value of the errors $\langle \sigma_{\langle \log(n) \rangle} \rangle = 0.08$ (20 per cent).

⁵ Abell 1836-BCG, M60, M104, NGC 1399, NGC 821, NGC 2549.

⁶ M60, NGC 821.

Table 4. Observed $M_{\text{BH}} - n$ scaling relations. M_{BH} = black hole mass, n = Sérsic index. A symmetrical bisector regression (BCES routine from Akritas & Bershady 1996) was used. The quantity n is normalized to the round median value of the distribution of the Sérsic indices for the SMBH galaxy sample ($\langle n \rangle = 3$). The total rms scatter in the $\log(M_{\text{BH}})$ direction is denoted by Δ .

Number	Type	α	β	Δdex
Fig. 4(a) $\log(M_{\text{BH}}/\text{M}_{\odot}) = \alpha + \beta \log(n/3)$				
9 Sérsic elliptical galaxies 27 Sérsic bulges 10 Core-Sérsic elliptical galaxies 2 Core-Sérsic bulges				
9	Sérsic elliptical galaxies	—	—	—
27	Sérsic bulges	7.73 ± 0.12	4.11 ± 0.72	0.62
10	Core-Sérsic elliptical galaxies	8.37 ± 0.30	2.23 ± 1.50	0.27
2	Core-Sérsic bulges	—	—	—
Fig. 4(b) $\log(M_{\text{BH}}/\text{M}_{\odot}) = \alpha + \beta \log(n/3)$				
8 Sérsic elliptical galaxies 10 Sérsic bulges 7 Core-Sérsic elliptical galaxies 0 Core-Sérsic bulges				
8	Sérsic elliptical galaxies	—	—	—
10	Sérsic bulges	7.85 ± 0.14	3.38 ± 1.16	0.44
7	Core-Sérsic elliptical galaxies	—	—	—
0	Core-Sérsic bulges	—	—	—

not. For reasons discussed in Section 4, we divided our sample into four subsamples:

- (i) the Sérsic bulges of disc galaxies;
- (ii) Sérsic elliptical galaxies;
- (iii) the core-Sérsic bulges of disc galaxies;
- (iv) core-Sérsic elliptical galaxies.

We expect a different $M_{\text{BH}} - n$ relation for each of the previous subsamples, and hence we elect not to perform a single linear regression to all the data shown in Figs 4(a) and 4(b). Our symmetrical regressions have been performed for the Sérsic bulges of disc galaxies in Figs 4(a) and 4(b) and for core-Sérsic elliptical galaxies in Fig. 4(a). Due to small numbers, the statistics were not able to provide reliable regressions for core-Sérsic elliptical galaxies in Fig. 4(b), nor for Sérsic elliptical galaxies and core-Sérsic bulges in either Figs 4(a) and 4(b). Table 4 contains the results from the symmetrical regressions. All of the outliers reside more than 3σ from the linear regressions.

4 PREDICTIONS AND DISCUSSION

The $M_{\text{BH}} - n$ relation can be predicted from two other important scaling relations: the $M_{\text{BH}} - L_{\text{sph}}$ and the $L_{\text{sph}} - n$ relations, where L_{sph} is the luminosity of the galaxy's spheroidal component.

Since at least Graham (2001, his fig. 14), we have known that the $L_{\text{sph}} - n$ relation is different for elliptical galaxies and the bulges of disc galaxies. fig. 10 from Graham & Guzmán (2003) and fig. 11 from Graham (2013) display the $L_{\text{sph}} - n$ relation for elliptical galaxies (in the B -band) and for the bulges of disc galaxies (in the K_s band), respectively. In both figures, the linear regressions had been estimated ‘by eye’. We re-analysed the data from their figures and performed a symmetrical linear bisector regression analysis using the BCES routine from Akritas & Bershady (1996).

We obtained

$$M_{B,\text{sph}} = (-18.25 \pm 0.18) + (-9.01 \pm 0.47) \log(n/3)$$

for the elliptical galaxies, and

$$M_{K_s,\text{sph}} = (-23.01 \pm 0.15) + (-5.55 \pm 0.47) \log(n/3)$$

for the bulges of the disc galaxies. Here, $M_{B,\text{sph}}$ indicates the absolute B -band magnitude of elliptical galaxies and $M_{K_s,\text{sph}}$ indicates

the dust-corrected, absolute K_s -band magnitude of the bulges of disc galaxies.

We have used the $M_{\text{BH}} - L_{\text{sph}}$ relation from Graham & Scott (2013) who derived B -band and K_s -band bulge magnitudes, from the total luminosity of lenticular and spiral galaxies, through a statistical correction that takes into account inclination effects and dust absorption. Following Graham (2012), Graham & Scott (2013) derived the $M_{\text{BH}} - L_{\text{sph}}$ relation separately for core-Sérsic and Sérsic spheroids. They observed a near-linear $M_{\text{BH}} - L_{\text{sph}}$ relation for the core-Sérsic spheroids, thought to be built in additive dry merger events, and a notably (2.5 times) steeper $M_{\text{BH}} - L_{\text{sph}}$ relation for the Sérsic spheroids considered to be products of gas-rich processes. They reported

$$\log(M_{\text{BH}}) = (9.03 \pm 0.09) + (-0.54 \pm 0.12)(M_{B,\text{sph}} + 21)$$

and

$$\log(M_{\text{BH}}) = (9.05 \pm 0.09) + (-0.44 \pm 0.08)(M_{K_s,\text{sph}} + 25)$$

for their core-Sérsic subsample, whereas

$$\log(M_{\text{BH}}) = (7.37 \pm 0.15) + (-0.94 \pm 0.16)(M_{B,\text{sph}} + 19)$$

and

$$\log(M_{\text{BH}}) = (7.39 \pm 0.14) + (-1.09 \pm 0.22)(M_{K_s,\text{sph}} + 22.5)$$

for their Sérsic galaxies.

The *bent* nature of the above $M_{\text{BH}} - L_{\text{sph}}$ relations and the *linear* nature of the two distinct $L_{\text{sph}} - n$ relations for elliptical galaxies and bulges requires that there be two distinct *bent* $M_{\text{BH}} - n$ relations for elliptical galaxies and bulges. This explains the *curved* nature of the $M_{\text{BH}} - n$ relation reported by GD07. The *predicted* $M_{\text{BH}} - n$ relations, derived from the above six equations, are reported in Table 5 and shown in Fig. 5.

The expected $M_{\text{BH}} - n$ relations for the Sérsic bulges of disc galaxies and for core-Sérsic elliptical galaxies (Table 5) are marginally consistent at the 2σ level with the results from the linear regression analysis performed in Fig. 4 (Table 4). More quality data and a wider range of Sérsic indices would be beneficial to confirm the predicted relations.

For comparison, in Fig. 5 we plot 10 additional galaxies with $M_{\text{BH}} < 10^7 \text{ M}_{\odot}$ taken from the sample of Greene et al. (2008). The horizontal offset that separates the bulges of their four disc galaxies

Table 5. Predicted $M_{\text{BH}}-n$ relations.

Type	Prediction
Sérsic elliptical galaxies	$\log(M_{\text{BH}}) = (6.66 \pm 0.26) + (8.47 \pm 1.51) \log(n/3)$
Sérsic bulges	$\log(M_{\text{BH}}) = (7.95 \pm 0.24) + (6.05 \pm 1.32) \log(n/3)$
Core-Sérsic elliptical galaxies	$\log(M_{\text{BH}}) = (7.54 \pm 0.35) + (4.87 \pm 1.11) \log(n/3)$
Core-Sérsic bulges	$\log(M_{\text{BH}}) = (8.17 \pm 0.19) + (2.44 \pm 0.49) \log(n/3)$

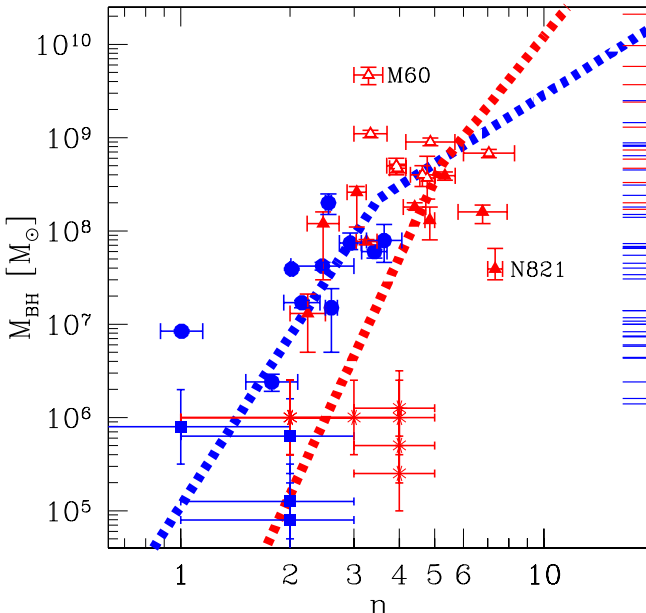


Figure 5. Same data as Fig. 4(b). For comparison, we plot four additional bulges of disc galaxies (blue squares) and six additional elliptical galaxies (red asterisks) taken from the sample of Greene, Ho & Barth (2008). The dashed lines show the predicted $M_{\text{BH}}-n$ relations for elliptical galaxies in red and for the bulges of disc galaxies in blue, given the observed $M_{\text{BH}}-L_{\text{sph}}$ and the $L_{\text{sph}}-n$ relations in the literature. The ticks on the right-hand axis indicate the black hole masses of 14 elliptical galaxies (in red) and 37 disc galaxies (in blue) that belong to the sample of Graham & Scott (2013) (and hence have a secure M_{BH} detection) but do not have multiple Sérsic index measurements.

from their six elliptical galaxies supports our predicted gap between the $M_{\text{BH}}-n$ relations for elliptical galaxies and bulges at the low-mass end of this diagram. If the bent $M_{\text{BH}}-L_{\text{sph}}$ relation is the same for all galaxies – irrespective of their morphology – this gap occurs because elliptical galaxies and the bulges of disc galaxies inhabit different regions of the $L_{\text{sph}}-n$ diagram (see fig. 14 in Graham 2001). That is, for a given light profile shape (i.e. Sérsic index n) the bulges of disc galaxies are brighter than elliptical galaxies. Fig. 5 allows one to predict that an order of magnitude gap is expected between the SMBH masses of Sérsic elliptical galaxies and the Sérsic bulges of disc galaxies having the same n .

In Fig. 5, we also show the black hole masses of 51 galaxies that belong to the sample of Graham & Scott (2013) but do not have multiple Sérsic index measurements. Among them, 13 are core-Sérsic elliptical galaxies, 5 are core-Sérsic bulges of disc galaxies, 1 is a Sérsic elliptical galaxy and 32 are Sérsic bulges of disc galaxies. We point out that measuring the Sérsic indices of these galaxies could add many useful points to the $M_{\text{BH}}-n$ diagram. In particular, the 13 extra core-Sérsic elliptical galaxies would allow one to better explore the $M_{\text{BH}}-n$ diagram in the high- M_{BH} end, between 10^8 and $10^{10} M_{\odot}$, where most galaxies are thought to

have formed from a different process, namely dry major mergers. Similarly, there are an additional 10 Sérsic bulges of disc galaxies with $M_{\text{BH}} < 10^7 M_{\odot}$ that could extend the low- M_{BH} end of the correlation.

The Sérsic index is a slight function of the observational bandpass. This dependence of galaxy structural parameters with wavelength arises due to radial gradients in the stellar population gradients and/or dust obscuration (Kelvin et al. 2012). We therefore plan to perform accurate galaxy image decompositions for all the galaxies belonging to the sample of Graham & Scott (2013) – with a directly measured SMBH mass – to explore the $M_{\text{BH}}-n$ relation and other black hole mass scaling relations in a homogeneous analysis (same observational bandpass and same light profile decomposition method).

Finally, we compare the results from this work with those from GD07, highlighting two main points. First, and similar to our sample, the galaxy sample used by GD07 was dominated (~ 80 per cent) by disc galaxies in the low-mass end ($M_{\text{BH}} < 10^8 M_{\odot}$) and by elliptical galaxies (~ 80 per cent) in the high-mass end ($M_{\text{BH}} > 10^8 M_{\odot}$). Secondly, GDO7 measured a Sérsic index greater than 10 for three spheroids with $M_{\text{BH}} \sim 10^9 M_{\odot}$, which are absent in Fig. 4(b). Combining the different galaxy types and fitting a single relation, it is easy to understand why a quadratic relation would be more appropriate than a single log-linear relation to describe their data. At $n = 3$ ($M_{\text{BH}} \sim 10^8 M_{\odot}$), their quadratic relation has a slope of 3.70 ± 0.46 , similar to that observed for our Sérsic bulges.

5 SUMMARY AND CONCLUSIONS

The $M_{\text{BH}}-n$ relation (GD07) is important for any complete theory or model to describe the co-evolution of galaxies and SMBHs. It also provides a means to estimate black hole masses in galaxies and may prove fruitful for recent and future deep, wide-field photometric surveys of galaxies which can statistically estimate the black hole masses in a large sample of galaxies up to $z \sim 0.1$. The main motivation of this work was to re-investigate the $M_{\text{BH}}-n$ relation, given a recent spate of papers which did not detect it. We have gone beyond the simple recovery of the $M_{\text{BH}}-n$ relation, and explored potential substructures in this diagram in terms of distinct relations for Sérsic and core-Sérsic galaxies, and for bulges and elliptical galaxies.

We compiled a large collection of literature Sérsic index measurements GD07, S11, V12, B12 for a sample of 62 galaxies with directly measured SMBH masses. We compared multiple Sérsic index measurements which existed for 35 galaxies, and found relative differences greater than 50 per cent in many instances. This is more than expected from a systematic bias produced by different types of light profile modelling (1D or 2D) or different observational bandpasses. We therefore excluded the outlying Sérsic indices and averaged the remaining values. This exclusion resulted in the removal of eight galaxies. Our final sample therefore consists of 54 galaxies: among them, 27 had Sérsic indices measured only by one

study and the remaining 27 have an averaged Sérsic index measurement.

Our principal conclusions are as follows.

(i) The $M_{\text{BH}} - n$ diagram (Fig. 4) displays an appreciable correlation.

(ii) The results from the symmetrical linear regressions (Fig. 4) are consistent at the 2σ level with predictions (Fig. 5) obtained by combining the $M_{\text{BH}} - L_{\text{sph}}$ relations for core-Sérsic and Sérsic galaxies with the $L_{\text{sph}} - n$ relations for elliptical galaxies and the bulges of disc galaxies.

(iii) If Sérsic bulges and Sérsic elliptical galaxies follow the same $M_{\text{BH}} - L_{\text{sph}}$ relation, then an order of magnitude gap is expected between the SMBH masses of Sérsic elliptical galaxies and the Sérsic bulges of disc galaxies having the same n .

A wider range of Sérsic indices would be beneficial to put tighter constraints on the observed slopes of the correlations. The catalogue of 80 directly measured SMBH masses compiled by Graham & Scott (2013) allows one to explore the $M_{\text{BH}} - n$ diagram in the low- and high-mass end. We recognize the need for a well-calibrated $M_{\text{BH}} - n$ relation and plan to perform accurate galaxy light profile decompositions to refine the black hole mass scaling relations.

ACKNOWLEDGEMENTS

GS thanks Dr Nicholas Scott for useful discussions. This research was supported by Australian Research Council funding through grants DP110103509 and FT110100263. AM, LKH, ES acknowledge support from grants PRIN-MIUR 2010-2011 ‘The dark Universe and the cosmic evolution of baryons: from current surveys to Euclid’ and PRIN-INAF 2011 ‘Black hole growth and AGN feedback through the cosmic time’. This research has made use of the GOLDMine data base (Gavazzi et al. 2003) and the NASA/IPAC Extragalactic Database (NED) which is operated by the Jet Propulsion Laboratory, California Institute of Technology, under contract with the National Aeronautics and Space Administration.

REFERENCES

- Abazajian K. N. et al., 2009, *ApJS*, 182, 543
 Akritas M. G., Bershady M. A., 1996, *ApJ*, 470, 706
 Allen P. D., Driver S. P., Graham A. W., Cameron E., Liske J., de Propris R., 2006, *MNRAS*, 371, 2
 Andredakis Y. C., Peletier R. F., Balcells M., 1995, *MNRAS*, 275, 874
 Beifiori A., Courteau S., Corsini E. M., Zhu Y., 2012, *MNRAS*, 419, 2497 (B12)
 Berrier J. C. et al., 2013, *ApJ*, 769, 2
 Caon N., Capaccioli M., D’Onofrio M., 1993, *MNRAS*, 265, 1013
 Davis B. L., Berrier J. C., Shields D. W., Kennefick J., Kennefick D., Seigar M. S., Lacy C. H. S., Puerari I., 2013, *ApJS*, 199, 33
 de Vaucouleurs G., de Vaucouleurs A., Corwin H. G., Jr, Buta R. J., Paturel G., Fouqué P., 1991, *Third Reference Catalogue of Bright Galaxies*. Springer, New York (RC3)
 Driver S. P. et al., 2011, *MNRAS*, 413, 971
 Erwin P., Graham A. W., Caon N., 2004, *Coevolution of Black Holes and Galaxies*, Cambridge Univ. Press, Cambridge
 Ferrarese L., Merritt D., 2000, *ApJ*, 539, L9
 Ferrarese L. et al., 2006, *ApJS*, 164, 334
 Ferrari F., Dotti H., Caon N., Nobrega A., Pavani D. B., 2004, *MNRAS*, 347, 824
 Freeman K. C., 1970, *ApJ*, 160, 811
 Gadotti D. A., 2008, *MNRAS*, 384, 420
 Gavazzi G., Boselli A., Donati A., Franzetti P., Scodellaggio M., 2003, *A&A*, 400, 451
 Gavazzi G., Donati A., Cucciati O., Sabatini S., Boselli A., Davies J., Zibetti S., 2005, *A&A*, 430, 411
 Gebhardt K. et al., 2000, *ApJ*, 539, L13
 Graham A. W., 2013, in Oswalt T. D., Keel W. C., eds, *Planets, Stars and Stellar Systems*, Volume 6. Springer, Berlin, p. 91
 Graham A. W., 2001, *AJ*, 121, 820
 Graham A. W., 2008, *ApJ*, 680, 143
 Graham A. W., 2012, *ApJ*, 746, 113
 Graham A. W., Driver S. P., 2005, *PASA*, 22, 118
 Graham A. W., Driver S. P., 2007a, *MNRAS*, 380, L15
 Graham A. W., Driver S. P., 2007b, *ApJ*, 655, 77 (GD07)
 Graham A. W., Guzmán R., 2003, *AJ*, 125, 2936
 Graham A. W., Scott N., 2013, *ApJ*, 764, 151
 Graham A. W., Erwin P., Caon N., Trujillo I., 2001, *ApJ*, 563, L11
 Graham A. W., Erwin P., Trujillo I., Asensio Ramos A., 2003, *AJ*, 125, 2951
 Graham A. W., Driver S. P., Allen P. D., Liske J., 2007, *MNRAS*, 378, 198
 Graham A. W., Onken C. A., Athanassoula E., Combes F., 2011, *MNRAS*, 412, 2211
 Greene J. E., Ho L. C., Barth A. J., 2008, *ApJ*, 688, 159
 Häring N., Rix H.-W., 2004, *ApJ*, 604, L89
 Hunt L. K., Pierini D., Giovanardi C., 2004, *A&A*, 414, 905
 Jerjen H., Binggeli B., Freeman K. C., 2000, *AJ*, 119, 593
 Kahane D., Moler C., Nash S., 1989, *Numerical Methods and Software*. Englewood Cliffs: Prentice Hall
 Kelly B. C., 2007, *ApJ*, 665, 1489
 Kelvin L. S. et al., 2012, *MNRAS*, 421, 1007
 Kormendy J., Richstone D., 1995, *ARA&A*, 33, 581
 Laor A., 2001, *ApJ*, 553, 677
 Lauer T. R., Tremaine S., Richstone D., Faber S. M., 2007, *ApJ*, 670, 249
 Lawrence A. et al., 2007, *MNRAS*, 379, 1599
 Magorrian J. et al., 1998, *AJ*, 115, 2285
 Marconi A., Hunt L. K., 2003, *ApJ*, 589, L21
 McLure R. J., Dunlop J. S., 2002, *MNRAS*, 331, 795
 Méndez-Abreu J., Aguerri J. A. L., Corsini E. M., Simonneau E., 2008, *A&A*, 478, 353
 Pastrav B. A., Popescu C. C., Tuffs R. J., Sansom A. E., 2013, *A&A*, 553, A80
 Peng C. Y., Ho L. C., Impey C. D., Rix H.-W., 2002, *AJ*, 124, 266
 Peng C. Y., Ho L. C., Impey C. D., Rix H.-W., 2010, *AJ*, 139, 2097
 Sani E., Marconi A., Hunt L. K., Risaliti G., 2011, *MNRAS*, 413, 1479 (S11)
 Scott N., Graham A. W., Schombert J., 2013, *ApJ*, 768, 76
 Sérsic J.-L., 1963, *Boletin de la Asociacion Argentina de Astronomia La Plata Argentina*, 6, 41
 Sérsic J.-L., 1968, *Atlas de Galaxias Australes*. Observatorio Astronomico. Cordoba
 Simard L. et al., 2002, *ApJS*, 142, 1
 Simard L., Mendel J. T., Patton D. R., Ellison S. L., McConnachie A. W., 2011, *ApJS*, 196, 11
 Trujillo I., Erwin P., Asensio Ramos A., Graham A. W., 2004, *AJ*, 127, 1917
 Vika M., Driver S. P., Cameron E., Kelvin L., Robotham A., 2012, *MNRAS*, 419, 2264 (V12)
 York D. G. et al., 2000, *AJ*, 120, 1579
 Young C. K., Currie M. J., 1994, *MNRAS*, 268, L11

APPENDIX A

Section 2.4 illustrates the method we used to combine multiple Sérsic index measurements of the same galaxy. These came from four different studies among which only one (GD07) reported a strong $M_{\text{BH}} - n$ relation.

To check the consistency and the robustness of our results, here we repeat the analysis excluding all the GD07 measurements. Fig. A1(a), which can be compared to Fig. 4(a), still displays a correlation, although it is more noisy at the high-mass end

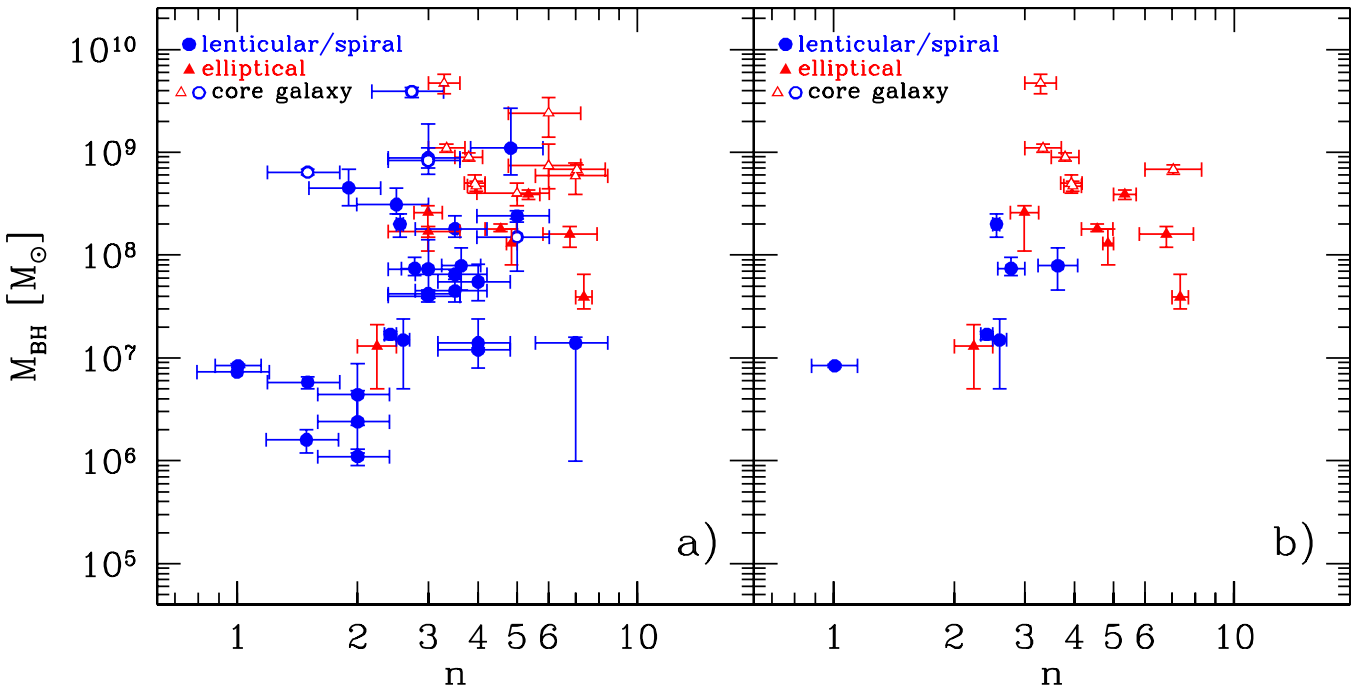


Figure A1. Same as Fig. 4 but excluding all the GD07 measurements.

(Spearman's correlation coefficient $r_s(47) = 0.38$, likelihood of the correlation occurring by chance $P < 1$ per cent). Hence, we conclude that the inclusion of the GD07 data did not force the recovery of the $M_{\text{BH}} - n$ relation(s). However, the two galaxies previously identified as outliers in Fig. 4(b) reduce the strength of the correlation vsp

in Fig. A1(b) to a likelihood of the correlation occurring by chance to $P < 5$ per cent.

This paper has been typeset from a TeX/LaTeX file prepared by the author.

3

Galaxy Vivisection

The preliminary investigation presented in Chapter 2 (Savorgnan et al., 2013) demonstrated the need for a new, systematic and homogeneous study aimed at obtaining more accurate galaxy decompositions and refining our knowledge about black hole mass scaling relations. In 2013, I visited A. Marconi, E. Sani, and L. K. Hunt (co-authors of the paper Sani et al. 2011) in Arcetri (Florence) for a short collaboration, during which I was shown their 2D galaxy decomposition method using GALFIT3 (Peng et al., 2010). This helped set the basis for the development of my own galaxy decomposition strategy.

Building on the catalog of Graham & Scott (2013) with the addition of some new black hole mass measurements later published by Rusli et al. (2013), I assembled my initial sample of 75 galaxies. For the imaging data, I chose to use *Spitzer* archival observations at $3.6\text{ }\mu\text{m}$ for three main reasons: (*i*) the $3.6\text{ }\mu\text{m}$ passband is currently the best proxy for the stellar mass (Sheth et al. 2010, and references therein); (*ii*) archival observations were publicly available for the majority of the galaxies in my initial sample; and (*iii*) within a *Spitzer* observation set of a galaxy, roughly half of the telescope pointings are dedicated to the imaging of the surrounding sky, ensuring a robust background determination during the data reduction process¹. While for each galaxy Sani et al. (2011) used only one set of *Spitzer* astronomical observations, I downloaded all the publicly available observation sets and merged them into a single mosaic with higher signal-to-noise. I paid particular attention to (and invested a consistent amount of time into) the characterisation of the 2D Point Spread Function (PSF), following the expert advice

¹These three points put together led me to prefer *Spitzer* rather than *HST* observations, albeit the lower spatial resolution.

of C. Peng.

Being aware of the importance of choosing the correct galaxy model in order to obtain reliable and meaningful structural parameters, I embraced the approach of Laurikainen et al. (2005) and planned *a priori* identification of the number and nature of the structural components in each galaxy. Given the lack of reference literature about advantages and disadvantages related to 1D and 2D decomposition techniques, I decided to experiment with both.

I wrote substantial software to perform 1D decomposition of surface brightness profiles. This code is written in Python and is based on the Levenberg-Marquardt minimisation routine of the `scipy.optimize` module. This software allows the user to build a galaxy model with any arbitrary number of analytical functions (Sérsic, exponential, Gaussian, Ferrer, etc.). Because the code is written in an object-oriented fashion, it is particularly easy to implement any new analytical function into it.

For the 2D analysis, I experimented with the codes GALFIT3 (Peng et al., 2010) and Imfit (Erwin, 2015). After checking that both codes give consistent results, I preferred the more script-oriented Imfit over GALFIT3.

The NASA/IPAC Extragalactic Database (NED) has been an invaluable resource for the structural analysis of galaxies. NED lists all the literature references contained in the SAO/NASA Astrophysics Data System (ADS) which mentioned a particular galaxy. Thanks to this functionality, I was able to search for previous photometric and kinematic analyses, structural decompositions, information about the nuclear activity, presence of dust or peculiar features, and any other detail that could be useful to the analysis of my galaxies.

The remainder of this chapter comprises the published version of the paper “Supermassive Black Holes and Their Host Spheroids. I. Disassembling Galaxies” by G. A. D. Savorgnan & A. W. Graham, as it appears in Volume 222 of the *The Astrophysical Journal Supplement Series*.



SUPERMASSIVE BLACK HOLES AND THEIR HOST SPHEROIDS. I. DISASSEMBLING GALAXIES

G. A. D. SAVORGNA AND A. W. GRAHAM

Centre for Astrophysics and Supercomputing, Swinburne University of Technology, Hawthorn, Victoria 3122, Australia; gsavorgn@astro.swin.edu.au

Received 2015 July 16; accepted 2015 November 19; published 2016 January 19

ABSTRACT

Several recent studies have performed galaxy decompositions to investigate correlations between the black hole mass and various properties of the host spheroid, but they have not converged on the same conclusions. This is because their models for the same galaxy were often significantly different and not consistent with each other in terms of fitted components. Using $3.6\text{ }\mu\text{m}$ *Spitzer* imagery, which is a superb tracer of the stellar mass (superior to the K band), we have performed state-of-the-art multicomponent decompositions for 66 galaxies with directly measured black hole masses. Our sample is the largest to date and, unlike previous studies, contains a large number (17) of spiral galaxies with low black hole masses. We paid careful attention to the image mosaicking, sky subtraction, and masking of contaminating sources. After a scrupulous inspection of the galaxy photometry (through isophotal analysis and unsharp masking) and—for the first time—2D kinematics, we were able to account for spheroids; large-scale, intermediate-scale, and nuclear disks; bars; rings; spiral arms; halos; extended or unresolved nuclear sources; and partially depleted cores. For each individual galaxy, we compared our best-fit model with previous studies, explained the discrepancies, and identified the optimal decomposition. Moreover, we have independently performed one-dimensional (1D) and two-dimensional (2D) decompositions and concluded that, at least when modeling large, nearby galaxies, 1D techniques have more advantages than 2D techniques. Finally, we developed a prescription to estimate the uncertainties on the 1D best-fit parameters for the 66 spheroids that takes into account systematic errors, unlike popular 2D codes that only consider statistical errors.

Key words: black hole physics – galaxies: bulges – galaxies: elliptical and lenticular, cD – galaxies: evolution – galaxies: structure

1. INTRODUCTION

Supermassive black holes and their host spheroids¹ have very different sizes. If the event horizon of the Galactic supermassive black hole was as big as a grain of sand in the Sahara Desert, then the black hole’s gravitational sphere of influence would be as big as the international airport of Cairo, and the Galactic bulge would be as big as the Sahara Desert itself. It is thus surprising that the masses of supermassive black holes (M_{BH}) scale with a number of properties of their host spheroid, indicating the nongravitational origin of these correlations (e.g., Dressler 1989; Yee 1992; Kormendy & Richstone 1995; Laor et al. 1997; Magorrian et al. 1998; Ferrarese & Merritt 2000; Gebhardt et al. 2000; Graham et al. 2001; Marconi & Hunt 2003; Häring & Rix 2004; Graham & Scott 2015).

The tightness of (i.e., the small scatter about) the above observed black hole mass correlations has led to the idea that black holes and host spheroids have coevolved with some sort of self-regulated growth. Exploring the evolution of this growth with cosmic time could help identify the driving mechanisms of the black hole–spheroid coevolution. Observations at $z = 0$ set the local benchmark from which to measure this evolution. Any complete theory or model describing the coevolution of spheroids and black holes must incorporate all of the observed scaling relations, which also have to be consistent with each other. Modern hydrodynamical simulations, such as EAGLE (Schaye et al. 2015), calibrate the feedback efficiencies to match the $z = 0$ black hole mass–galaxy mass relation. The observed scaling relations can also be employed to predict the

masses of black holes in other galaxies, where a direct measure of M_{BH} would be extremely time-consuming or simply impossible owing to technological limitations. Moreover, many accurate M_{BH} predictions enable one to derive the local black hole mass function (e.g., Salucci et al. 1999; Graham et al. 2007; Shankar 2009, 2013; Fontanot et al. 2015) and space density (e.g., Graham & Driver 2007b; Comastri et al. 2015). All of these examples depend on the $z = 0$ relations, and as such the recalibration of the black hole mass–spheroid stellar mass ratio ($M_{\text{BH}}/M_{*,\text{sph}}$) in large spheroids, from 0.1% to 0.2% (e.g., Marconi & Hunt 2003; Häring & Rix 2004) to 0.49% (Graham & Scott 2015), has many substantial implications.

Since the early stellar dynamical detections of black holes were carried out in the 1980s (see the references in the reviews by Kormendy & Richstone 1995; Richstone et al. 1998; Graham 2015 for pioneering papers), the number of (direct) black hole mass measurements has increased with time and it has recently become a statistically meaningful sample with which one can study SMBH demographics. It is now generally accepted that supermassive black holes reside at the center of most, if not all, massive spheroids, either quiescent or active.

Massive, early-type (E, E/S0, S0) galaxies are often composite systems. The knowledge that many “elliptical” (E) galaxies were misclassified and actually contain embedded stellar disks dates back at least three decades (Capaccioli 1987; Carter 1987; Bender 1990; Rix & White 1990, 1992; Scorz & Bender 1990, 1995; Nieto et al. 1991). After examining long-slit and integral field unit spectroscopic observations of morphologically classified elliptical galaxies in the Fornax Cluster, D’Onofrio et al. (1995), Graham et al. (1998), and Scott et al. (2014) concluded that only three bright galaxies do not harbor a disk-like component. Larger surveys with integral

¹ By the term “spheroid” we mean either an elliptical galaxy or the bulge component of a disk galaxy, with no attempt at distinguishing between classical bulges and disk-like pseudobulges.

field spectrographs of early-type galaxies, such as the ATLAS^{3D} Project (Cappellari et al. 2011), have further advanced this view of “elliptical” galaxies being all but simple and featureless pressure-supported systems. Most of the morphologically classified elliptical galaxies in the ATLAS^{3D} sample are fast rotators (Emsellem et al. 2011). Krajnović et al. (2013) showed that “fast rotators” as a class are disk galaxies or at least disk-like galaxies. In their magnitude-limited survey, systems without any signature of disk-like components (neither in the kinematics nor in the photometry) dominate only the most massive end (with stellar masses beyond $10^{11.5} M_{\odot}$) of the distribution. Given the prevalence of disks, it is clearly important to perform spheroid/disk decompositions, if one is to properly explore the black hole–spheroid connection. Indeed, separating the disk light from that of the bulge has led to the discovery of the missing population of compact, massive spheroids in the local universe (Graham et al. 2015). If we are to properly understand the evolution of galaxies, we need to understand their components.

Measuring the photometric and structural properties of a galaxy’s spheroidal component requires the ability to separate it from the rest of the galaxy. Such galaxy decomposition involves a parametric analysis that allows one to fit the surface brightness distribution of galaxies using a combination of analytic functions (usually one function per galaxy component, such as spheroids, disks, bars, nuclei, etc.). The one-dimensional (1D) technique involves fitting isophotes to the galaxy image, extracting the (1D) surface brightness radial profile, and modeling it with a combination of analytic functions. With the two-dimensional (2D) technique, one fits analytic functions directly to the 2D images.

Over the past 8 yr, five independent studies (Graham & Driver 2007a; Sani et al. 2011; Beifiori et al. 2012; Vika et al. 2012; Läsker et al. 2014a, 2014b) have attempted galaxy decomposition in order to derive the spheroid parameters and explore their relation with the black hole masses. Interestingly, the past studies used almost the same sample of galaxies, yet they claimed some contradictory conclusions. For example, one study (Graham & Driver 2007a) obtained a good $M_{\text{BH}} - n_{\text{sph}}$ correlation (the spheroid Sérsic index n_{sph} is a measure of the central radial concentration of stars; Trujillo et al. 2001), whereas the remaining four did not.² In addition, Läsker et al. (2014b) declared that M_{BH} correlates equally well with the total galaxy luminosity as it does with the spheroid luminosity, as opposed to Beifiori et al. (2012), who claimed that the spheroid mass is a better tracer of M_{BH} than the galaxy mass (see also Kormendy & Gebhardt 2001; Erwin & Gadotti 2012). The past studies did not converge to the same conclusions because their best-fit models for the same galaxy were often significantly different and not consistent with each other in terms of fitted components. Moreover, none of these studies attempted an individual galaxy-by-galaxy comparison of their models with the previous literature. We have now made this comparison and performed the optimal decompositions, using 3.6 μm *Spitzer* satellite imagery, which is an excellent proxy for the stellar mass, superior to the K band (Jun & Im 2008; Sheth et al. 2010). We will use these in a series of forthcoming papers to obtain improved black hole mass scaling relations

² Savorgnan et al. (2013) showed that, by rejecting the most discrepant Sérsic index measurements and averaging the remaining ones, a strong $M_{\text{BH}} - n_{\text{sph}}$ correlation was recovered.

using the largest sample (66) of galaxies to date with accurate spheroid properties.

This paper is structured as follows. Section 2 presents the galaxy sample and imaging data set used to conduct this study. Section 3 describes how we performed the galaxy decompositions, i.e., how we identified and modeled the subcomponents that constitute our galaxies. In Section 4 we outline the results from our analysis and discuss the error analysis. Section 5 summarizes our main conclusions. The individual galaxy decompositions are made available in the electronic version of this manuscript.

2. DATA

Our initial galaxy sample (see Table 1) consists of 75 objects for which a dynamical detection of the black hole mass had been reported in the literature at the time we started this project, and for which at least one 3.6 μm *Spitzer*/IRAC³ observation was publicly available. Black hole masses were drawn from the catalog of Graham & Scott (2013) for 70 galaxies, from Rusli et al. (2013b) for four galaxies, and from Greenhill et al. (2003) for one galaxy. As explained in Section 4, this initial sample was ultimately reduced to 66 galaxies for which useful spheroid parameters could be obtained.

2.1. Spitzer/IRAC Observations

2.1.1. Data Acquisition

For each of our 75 galaxies, we downloaded from the Spitzer Heritage Archive⁴ all the available 3.6 μm IRAC Astronomical Observation Requests (AORs). Each AOR is an individual *Spitzer* observation sequence and includes a number of data frames (the individual exposures) and the calibration data. The data frames were selected to be corrected basic calibrated data (cBCD), produced by the IRAC Level 1 pipeline. This automatic pipeline takes a single “raw” image, removes the scattered light, and performs dark subtraction, flat-fielding correction, and flux calibration (into units of MJy sr^{-1}). The final product (the BCD) is a flux-calibrated image that has had all the well-understood instrumental signatures removed. BCD frames are further processed through an “artifact correction” pipeline that mitigates the commonly found artifacts of stray light, saturation, “muxbleed,” and column pulldown.⁵ After the artifact correction has been applied, the BCD becomes a cBCD.

2.1.2. Mosaicking

We performed image mosaicking using the MOPEX package (Makovoz & Marleau 2005). This enabled the production of suitably wide field-of-view images for accurate sky background subtraction. Individual cBCD frames with exposure time of 1 s were rejected. Permanent or semipermanent bad pixels, contained in a semistatic mask (the “pmask”), were ignored. Each AOR is associated with a specific pmask. Therefore, when multiple AORs were available for the same

³ IRAC is the InfraRed Array Camera on board the *Spitzer Space Telescope*.

⁴ <http://irsa.ipac.caltech.edu/applications/Spitzer/SHA/>

⁵ Stray light includes scattered light from stars outside the array location, as well as filter ghosts from bright stars. Multiplexer bleed, or “muxbleed,” can be generated by stars, hot pixels, and particle hits. It appears as a decaying trail of pixels, repeating every fourth column. “Column pulldown” is caused by a bright pixel that triggers a bias shift within its respective column, creating a lower background value throughout the entire column than in the surrounding columns.

Table 1
Galaxy Sample

Galaxy	Distance (Mpc)	M_{BH} ($10^8 M_{\odot}$)	Ref.	Core (arcsec)	Ref.	Rot.	Vel. Map	1D Fit	2D Fit
(1)	(2)	(3)	(4)	(5)	(6)	(7)	(8)	(9)	(10)
Circinus	4.0	$0.017^{+0.004}_{-0.003}$	G+03	no?	no	no
IC 1459	28.4	24^{+10}_{-10}	GS13	yes (0.7)	R+13a	yes	yes
IC 2560	40.7	$0.044^{+0.044}_{-0.022}$	GS13	no?	yes	no
IC 4296	40.7	11^{+2}_{-2}	GS13	yes?	yes	yes
M31	0.7	$1.4^{+0.9}_{-0.3}$	GS13	no	yes	no
M32	0.8	$0.024^{+0.005}_{-0.005}$	GS13	no	no	no
M49	17.1	25^{+3}_{-1}	R+13b	yes (1.5)	DG13, R+13a	SLOW	A	yes	yes
M59	17.8	$3.9^{+0.4}_{-0.4}$	GS13	no	...	FAST	A	yes	no
M60	16.4	47^{+10}_{-10}	GS13	yes (2.7)	DG13, R+13a	FAST	A, S	no	no
M64	7.3	$0.016^{+0.004}_{-0.004}$	GS13	no?	yes	no
M77	15.2	$0.084^{+0.003}_{-0.003}$	GS13	no	no	no
M81	3.8	$0.74^{+0.21}_{-0.11}$	GS13	no	yes	no
M84	17.9	$9.0^{+0.9}_{-0.8}$	GS13	yes (1.9)	F+06	SLOW	A, S	yes	yes
M87	15.6	$58.0^{+3.5}_{-3.5}$	GS13	yes (7.2)	F+06	SLOW	A, S	yes	yes
M89	14.9	$4.7^{+0.5}_{-0.5}$	GS13	yes (0.4)	DG13, R+13a	SLOW	A	yes	no
M94	4.4	$0.060^{+0.014}_{-0.014}$	GS13	no?	yes	no
M96	10.1	$0.073^{+0.015}_{-0.015}$	GS13	no	yes	yes
M104	9.5	$6.4^{+0.4}_{-0.4}$	GS13	yes	J+11	yes	no
M105	10.3	4^{+1}_{-1}	GS13	yes (1.1)	DG13, R+13a	FAST	A	yes	yes
M106	7.2	$0.39^{+0.01}_{-0.01}$	GS13	no	yes	no
NGC 0253	3.5	$0.10^{+0.10}_{-0.05}$	GS13	no	no	no
NGC 0524	23.3	$8.3^{+2.7}_{-1.3}$	GS13	yes (0.2)	R+11	FAST	A	yes	no
NGC 0821	23.4	$0.39^{+0.26}_{-0.09}$	GS13	no	...	FAST	A, S	yes	yes
NGC 1023	11.1	$0.42^{+0.04}_{-0.04}$	GS13	no	...	FAST	A, S	yes	yes
NGC 1300	20.7	$0.73^{+0.69}_{-0.35}$	GS13	no	yes	no
NGC 1316	18.6	$1.50^{+0.75}_{-0.80}$	GS13	no	...	FAST	...	yes	no
NGC 1332	22.3	14^{+2}_{-2}	GS13	no	yes	no
NGC 1374	19.2	$5.8^{+0.5}_{-0.5}$	R+13b	no?	...	FAST	A	yes	yes
NGC 1399	19.4	$4.7^{+0.6}_{-0.6}$	GS13	yes (2.4)	DG13, R+13a	SLOW	A	yes	no
NGC 2273	28.5	$0.083^{+0.004}_{-0.004}$	GS13	no	yes	no
NGC 2549	12.3	$0.14^{+0.02}_{-0.13}$	GS13	no	...	FAST	A	yes	yes
NGC 2778	22.3	$0.15^{+0.09}_{-0.10}$	GS13	no	...	FAST	A	yes	no
NGC 2787	7.3	$0.40^{+0.04}_{-0.05}$	GS13	no	yes	no
NGC 2974	20.9	$1.7^{+0.2}_{-0.2}$	GS13	no	...	FAST	A, S	yes	yes
NGC 3079	20.7	$0.024^{+0.024}_{-0.012}$	GS13	no?	yes	no
NGC 3091	51.2	36^{+1}_{-2}	R+13b	yes (0.6)	R+13a	yes	yes
NGC 3115	9.4	$8.8^{+10.0}_{-2.7}$	GS13	no	S	yes	no
NGC 3227	20.3	$0.14^{+0.10}_{-0.06}$	GS13	no	yes	no
NGC 3245	20.3	$2.0^{+0.5}_{-0.5}$	GS13	no	...	FAST	A	yes	yes
NGC 3377	10.9	$0.77^{+0.04}_{-0.06}$	GS13	no	...	FAST	A, S	yes	yes
NGC 3384	11.3	$0.17^{+0.01}_{-0.02}$	GS13	no	...	FAST	A	yes	no
NGC 3393	55.2	$0.34^{+0.02}_{-0.02}$	GS13	no	yes	yes
NGC 3414	24.5	$2.4^{+0.3}_{-0.3}$	GS13	no	...	SLOW	A	yes	no
NGC 3489	11.7	$0.058^{+0.008}_{-0.008}$	GS13	no	...	FAST	A	yes	yes
NGC 3585	19.5	$3.1^{+1.4}_{-0.6}$	GS13	no	yes	no
NGC 3607	22.2	$1.3^{+0.5}_{-0.5}$	GS13	no	...	FAST	A	yes	yes
NGC 3608	22.3	$2.0^{+1.1}_{-0.6}$	GS13	yes (0.2)	DG13, R+13a	SLOW	A, S	yes	yes
NGC 3842	98.4	97^{+30}_{-26}	GS13	yes (0.7)	DG13, R+13a	yes	no
NGC 3998	13.7	$8.1^{+2.0}_{-1.9}$	GS13	no	...	FAST	A	yes	no
NGC 4026	13.2	$1.8^{+0.6}_{-0.3}$	GS13	no	...	FAST	A	yes	no
NGC 4151	20.0	$0.65^{+0.07}_{-0.07}$	GS13	no	yes	no
NGC 4261	30.8	5^{+1}_{-1}	GS13	yes (1.6)	R+11	SLOW	A	yes	yes
NGC 4291	25.5	$3.3^{+0.9}_{-2.5}$	GS13	yes (0.3)	DG13, R+13a	yes	yes
NGC 4342	23.0	$4.5^{+2.3}_{-1.5}$	GS13	no	...	FAST	A	no	no
NGC 4388	17.0	$0.075^{+0.002}_{-0.002}$	GS13	no?	yes	no
NGC 4459	15.7	$0.68^{+0.13}_{-0.13}$	GS13	no	...	FAST	A	yes	no

Table 1
(Continued)

Galaxy	Distance (Mpc)	M_{BH} ($10^8 M_{\odot}$)	Ref.	Core (arcsec)	Ref.	Rot.	Vel. Map	1D Fit	2D Fit
(1)	(2)	(3)	(4)	(5)	(6)	(7)	(8)	(9)	(10)
NGC 4473	15.3	$1.2^{+0.4}_{-0.9}$	GS13	no	...	FAST	A, S	yes	yes
NGC 4486A	17.0	$0.13^{+0.08}_{-0.08}$	GS13	no	...	FAST	A	no	no
NGC 4564	14.6	$0.60^{+0.03}_{-0.09}$	GS13	no	...	FAST	A	yes	no
NGC 4596	17.0	$0.79^{+0.38}_{-0.33}$	GS13	no	...	FAST	A	yes	no
NGC 4697	11.4	$1.8^{+0.2}_{-0.1}$	GS13	no	...	FAST	A, S	yes	yes
NGC 4889	103.2	210^{+160}_{-160}	GS13	yes (1.7)	F+97	yes	yes
NGC 4945	3.8	$0.014^{+0.014}_{-0.007}$	GS13	no?	yes	yes
NGC 5077	41.2	$7.4^{+4.7}_{-3.0}$	GS13	yes (0.3)	T+04	yes	yes
NGC 5128	3.8	$0.45^{+0.17}_{-0.10}$	GS13	no?	yes	no
NGC 5576	24.8	$1.6^{+0.3}_{-0.4}$	GS13	no	...	SLOW	A	yes	yes
NGC 5813	31.3	$6.8^{+0.7}_{-0.7}$	GS13	yes (0.4)	DG13, R+13a	SLOW	A	no	no
NGC 5845	25.2	$2.6^{+0.4}_{-1.5}$	GS13	no	...	FAST	A	yes	yes
NGC 5846	24.2	11^{+1}_{-1}	GS13	yes	F+97	SLOW	A, S	yes	yes
NGC 6251	104.6	5^{+2}_{-2}	GS13	yes?	yes	yes
NGC 7052	66.4	$3.7^{+2.6}_{-1.5}$	GS13	yes (0.8)	Q+00	yes	yes
NGC 7582	22.0	$0.55^{+0.26}_{-0.19}$	GS13	no	no	no
NGC 7619	51.5	25^{+8}_{-3}	R+13b	yes ^a (0.5)	DG13, R+13a	yes	no
NGC 7768	112.8	13^{+5}_{-4}	GS13	yes	G+94	yes	no
UGC 03789	48.4	$0.108^{+0.005}_{-0.005}$	GS13	no?	yes	no

Notes. Column (1): galaxy name. Column (2): distance. Column (3): black hole mass. Column (4): reference of the black hole mass reported here (G+03—Greenhill et al. 2003; GS13—Graham & Scott 2013; R+13b—Rusli et al. 2013b). Column (5): presence of a partially depleted core. The question mark is used when the classification has come from the velocity dispersion criteria mentioned in Section 2.2.3. The value of the core break radius is reported in parentheses when available. Column (6): reference of the identification of a partially depleted core (G+94—Grillmair et al. 1994; F+97—Forbes et al. 1997; Q+00—Quillen et al. 2000; T+04—Trujillo et al. 2004; F+06—Ferrarese et al. 2006; J+11—Jardel et al. 2011; R+11—Richings et al. 2011; DG13—Dullo & Graham 2013; R+13a—Rusli et al. 2013a). Column (7): kinematical classification (fast/slow rotator). Column (8): availability of velocity map (A—ATLAS^{3D}; S—SLUGGS). Column (9): completion of 1D fit. Column (10): completion of 2D fit.

^a NGC 7619 may contain an embedded disk, rather than possessing a partially depleted core (see Figure 77).

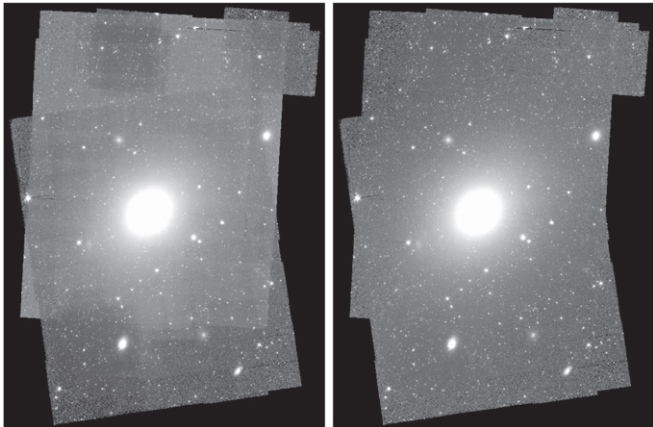


Figure 1. Example of the *overlap* correction. The image mosaic of the galaxy M49 was obtained by co-adding frames coming from eight different AORs. The evident patchiness (left image) was removed (right image) using the *overlap* module.

galaxy, we merged the different pmasks. Cosmic-ray rejection was performed with the dual outlier and multiframe techniques. The pixel size of the mosaic was set to be the same as the input cBCD frames ($1.^{\prime\prime}22 \times 1.^{\prime\prime}22$). For $3.6 \mu\text{m}$ observations with this pixel scale, the photometric zero-point magnitude is $m_{\text{zp}} = 17.26$ mag. The orientation of the mosaic was set to the average rotation angle of the input cBCD frames. Individual cBCD frames were combined together into a single mosaic with the default linear interpolation algorithm.

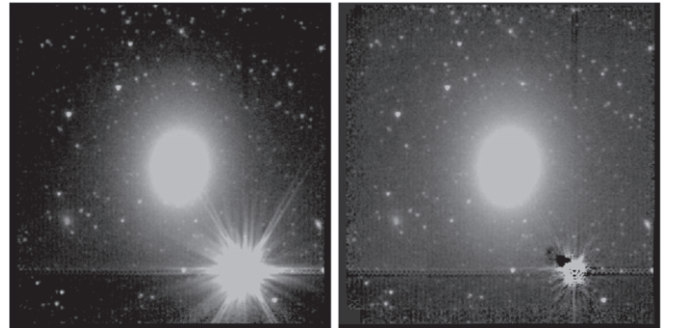


Figure 2. Example of aesthetic correction. The images show the mosaic of the galaxy NGC 4459 before (left) and after (right) the partial removal of a bright saturated star.

2.1.3. Overlap Correction

Before generating a mosaic, MOPEX can perform background matching among the individual frames by using the *overlap* module. This module calculates and applies an additive correction to the individual frames, producing a consistent background across the mosaicked image. According to the *Spitzer Data Analysis Cookbook*,⁶ the use of the *overlap* module is not particularly recommended for $3.6 \mu\text{m}$ observations. However, after a visual inspection of the mosaics

⁶ http://irsa.ipac.caltech.edu/data/SPITZER/docs/dataanalystools/cookbook/Spitzer_Data_Cookbook.pdf

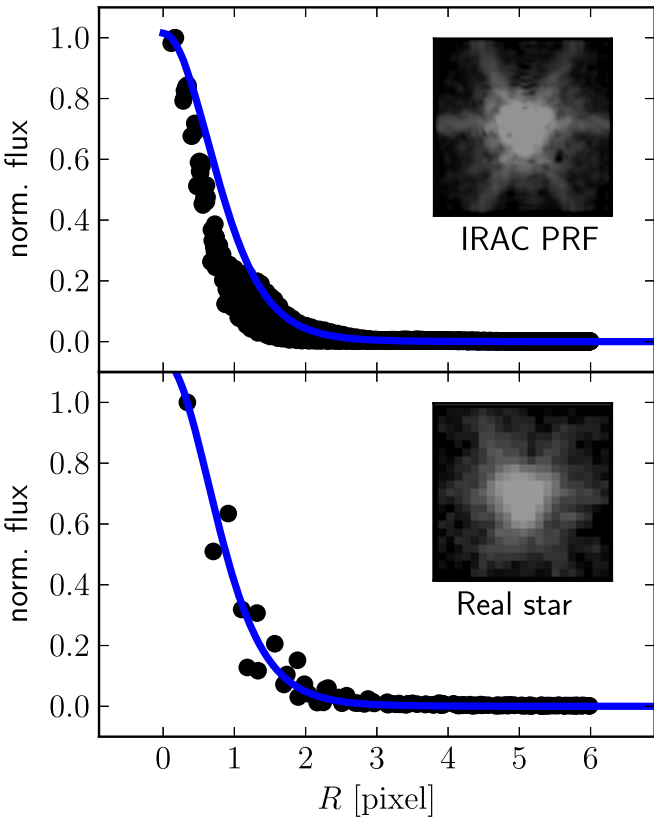


Figure 3. Normalized flux vs. radial distance from the image centroid of an observed point source (bottom panel) and of the IRAC instrument PRF (top panel). The normalized flux is given in arbitrary units, and the radial distance is in units of pixel size of the IRAC detector (1 pixel = 1''.22). The blue solid line shows our 1D Moffat PSF model, which has been normalized to intersect the data point with the largest flux. The FWHM of the IRAC PRF is clearly smaller than that of a “real” star. The inserts display the images of the observed point source and the IRAC PRF.

obtained without activating the *overlap* module, we found that all the mosaics obtained from multiple AORs were affected by patchiness, owing to bias fluctuations in the CCD array. For this reason, we regenerated the multiple-AOR mosaics by activating the *overlap* correction, which successfully removed the “chessboard” pattern (see Figure 1 for an example).

2.1.4. Sigma Mosaics

For each individual cBCD frame, the IRAC Level 1 pipeline calculates the uncertainty associated with each pixel and produces an uncertainty frame (or sigma frame). The initial uncertainty is estimated as the Poisson noise in electrons plus the readout noise added in quadrature ($\sigma^2 = \sigma_{\text{readoutnoise}}^2 + \sigma_{\text{Poisson}}^2$). This initial sigma frame is carried through the pipeline, and additional uncertainties (e.g., dark current and flat field uncertainties) are added in quadrature when appropriate. When MOPEX generates an image mosaic, it also produces the associated sigma mosaic by interpolating the individual uncertainty frames and co-adding them, following the standard assumption of additive variances.

⁷ IRAF is the Image Reduction and Analysis Facility, distributed by the National Optical Astronomy Observatory, which is operated by the Association of Universities for Research in Astronomy (AURA) under cooperative agreement with the National Science Foundation.

2.1.5. Sky Subtraction

Sky subtraction was performed manually on the image mosaics using the tasks `marksky` and `skyfit` of the IRAF⁷ package GALPHOT.⁸ The task `skyfit` also provided an estimate of the sky rms (rms_{sky}).

2.1.6. Additional Aesthetic Corrections

The image mosaics of four galaxies (NGC 0821, NGC 2974, NGC 4291, NGC 4459) were found to be affected by bright, highly saturated stars lying close to the target galaxies. These stars were modeled and subtracted using the software Galfit (Peng et al. 2010) and the extended IRAC point response function (PRF) image at 3.6 μm . This helped remove the extended wings and spikes of the saturated stars (see Figure 2 for an example).

2.1.7. Image Masking

Galactic stars and any other objects different from the target galaxy were masked through a two-step procedure. First, we created an initial mask using the IRAF task `objmasks` that identifies objects by threshold sigma detection. Then, we refined each mask by hand, using the software SAOImage DS9⁹ in conjunction with the IRAF task `mskregions`. We identified and carefully masked not only contaminating sources located in the field of the image mosaic but also objects overlapping with the target galaxy, such as foreground stars, background galaxies, globular clusters, and red giant stars.

2.1.8. 1D Point-spread Function (PSF)

A universal,¹⁰ average, 1D PSF was characterized using the IRAF task `imexamine`. A nonlinear least-squares Moffat (1969)¹¹ profile of fixed center and zero background was fit to the (background-subtracted) pixels of 20 bright stars, belonging to different image mosaics. The best-fit parameters of the 20 stars were then averaged together. Doing so, we obtained $(\alpha, \beta) = (2''.38, 4.39)$.

2.1.9. 2D PSF

The IRAC support team provides users with a 2D instrument PRF at 3.6 μm . However, while this helped remove the extended wings of saturated stars (see Section 2.1.6), we found

⁸ GALPHOT was developed in the IRAF—STSDAS environment mainly by W. Freudling, J. Salzer, and M. P. Haynes (Haynes et al. 1999).

⁹ SAOImage DS9 development has been made possible by funding from the Chandra X-ray Science Center (CXC) and the High Energy Astrophysics Science Archive Center (HEASARC).

¹⁰ Across all mosaics, the variation of the Moffat FWHM is $\pm 0''.1$, and the variation of the Moffat β is ± 2.0 . The use of a universal PSF is justified for the following reasons: (i) the PSF convolution is more sensitive to the value of the FWHM than β , i.e., having a 50% variation in β is not an issue as long as the variation in FWHM is small; (ii) the use of a non-signal-to-noise-weighted fitting scheme minimizes biases from a nonaccurate PSF description; (iii) not all mosaics have enough stars suitable for the PSF characterization: rather than having an individual PSF for each mosaic (which would have been based on only one to two stars for some mosaics), we preferred the use of a universal PSF.

¹¹ The Moffat (1969) profile has the following form:

$$\mu = \mu_0 - 2.5 \log \left[1 + \left(\frac{R}{\alpha} \right)^2 \right]^{-\beta}, \quad (1)$$

where R is the projected radius, μ_0 is the central surface brightness, and α and β regulate the width and the shape of the profile.

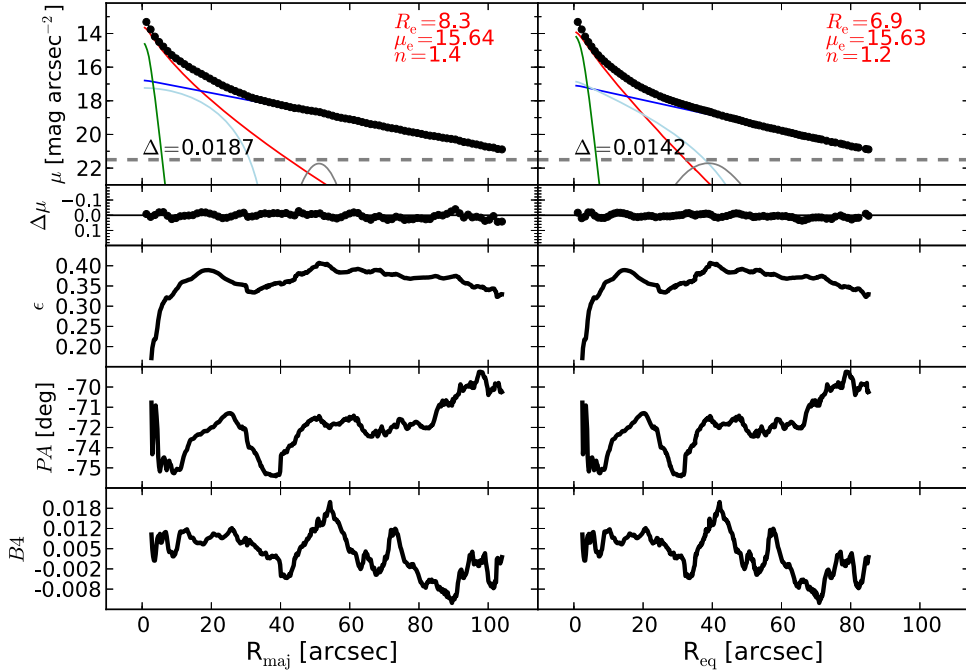


Figure 4. Best-fit model and isophotal parameters for the galaxy NGC 2974. The left panels refer to the major-axis R_{maj} , while the right panels refer to the equivalent-axis R_{eq} , i.e., the geometric mean of the major (a) and minor (b) axis ($R_{\text{eq}} = \sqrt{ab}$). The top panels display the galaxy surface brightness radial profiles obtained with a linear sampling. The black points are the observed data. The colored lines represent the individual (PSF-convolved) model components: red = Sérsic (bulge), dark blue = exponential (disk), green = Gaussian (AGN), cyan = Ferrer (bar), gray = Gaussian ring (ring). The best-fit parameters for the Sérsic bulge model are inset. The total (PSF-convolved) model is shown with a black dashed line, but it is hard to distinguish because it almost perfectly matches the data, hence the residual profile is additionally shown as $\Delta\mu$ in the second row. The horizontal gray dashed line corresponds to an intensity equal to three times the rms of the sky background fluctuations ($3 \times \text{rms}_{\text{sky}}$). Δ denotes the rms scatter of the fit in units of mag arcsec $^{-2}$. The lower six panels show the ellipticity (ϵ), position angle (PA), and fourth harmonic (B_4) radial profiles. Such profiles are available online for all other galaxies successfully modeled in 1D (see Table 2).

this PRF to be inadequate for the purposes of our modeling. In fact, the FWHM of the IRAC instrument PRF ($\sim 1.^{\circ}8$), as measured by the IRAF task `imexamine`, is systematically smaller than the average FWHM of “real” stars ($\sim 2.^{\circ}0$). Figure 3 illustrates this issue. We also tested the IRAC PRF by providing it as the input PSF for Galfit and fitting a number of stars in different image mosaics. A visual inspection of the fit residuals confirmed that the IRAC instrument PRF is narrower than “real” point sources. For this reason, we constructed our 2D PSF according to the following method (as directed by C. Peng 2013, private communication).

We provided the IRAC instrument PRF as the input PSF for Galfit and simultaneously fit seven bright stars (belonging to different mosaics), modeling the stars with Moffat profiles and constraining all the profiles to have the same (α, β), position angle, and axis ratio. The 2D PSF image was then obtained by taking the best-fit Moffat model—the same best-fit model for all seven stars, by construction—and convolving it with the IRAC instrument PRF. The advantage of this method is to obtain a 2D PSF that is wider than the instrument PRF but maintains the asymmetric features of the instrument PRF (e.g., wings and spikes). We then tested this 2D PSF on a number of stars (these stars were different from the seven stars employed to build the 2D PSF image) and verified that it correctly reproduces the shape of “real” point sources.

2.2. Additional Data

2.2.1. Kinematics

A kinematical classification (slow/fast rotator) is available for 34 of our 75 galaxies from the ATLAS^{3D} survey (Emsellem

et al. 2011) and for three additional galaxies from Scott et al. (2014). This classification (Table 1, column (7)) concerns the kinematic properties of galaxies within the spectroscopic instrument’s field of view, but does not contain additional information—crucial for our analysis—about kinematic substructures, such as embedded disks or kinematically decoupled components, which can require separate modeling. For this reason, we also visually inspected the velocity fields of our galaxies, when available from the literature. Velocity maps were taken from the ATLAS^{3D} survey for 34 galaxies (observed with SAURON by Krajnović et al. 2011), from Scott et al. (2014) for 2 galaxies (observed with WiFeS), and from the SLUGGS survey for 12 galaxies (observed with DEIMOS by Arnold et al. 2014). While the fields of view of SAURON ($33'' \times 41''$) and WiFeS ($25'' \times 38''$) reach to about one galaxy effective radius (for our local galaxies), observations taken with DEIMOS can probe the galaxy kinematics well beyond two effective radii.

2.2.2. Active Galactic Nuclei (AGNs) and Nuclear Dust

The X-ray, UV, and optical radiation emitted by the accretion disks of AGNs can stimulate infrared thermal emission from circumnuclear dust, if present. This means that if a galaxy hosts an optical AGN and a certain amount of nuclear dust, we may detect some nonstellar nuclear emission at $3.6 \mu\text{m}$. It is therefore important to identify which of our galaxies have both an optical AGN and circumnuclear dust. To help with this task, we searched NED¹² for the individual

¹² NED is the NASA/IPAC Extragalactic Database.

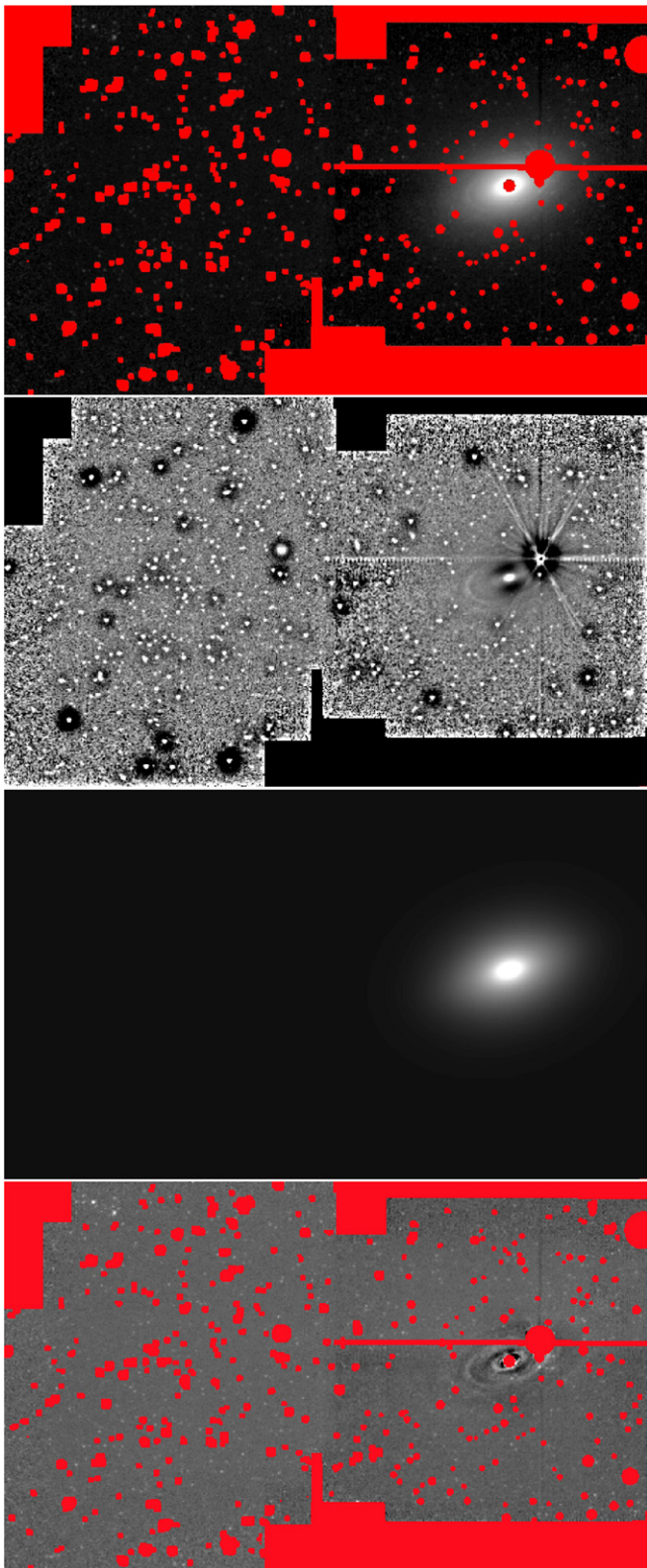


Figure 5. Image of the galaxy NGC 2974 with its mask (top panel, on a logarithmic scale), unsharp mask (second panel, on a linear scale), best-fit 2D model (third panel, on a logarithmic scale), and residual image after the subtraction of the 2D model (bottom panel, on a linear scale; the residual patterns correspond to differences between the data and the model of less than 6%). The left-hand side of the mosaic allowed an accurate determination of the sky background level.

galaxies and their associated literature. Unsurprisingly, dusty AGNs were more frequently found in late-type spiral galaxies and modeled by us with either a point source or a PSF-convolved Gaussian.

2.2.3. Sérsic/Core-Sérsic Classification

Core-Sérsic galaxies (Graham and Guzmán 2003; Graham et al. 2003; Trujillo et al. 2004) are galaxies (or spheroids) with partially depleted cores, i.e., a central deficit of light relative to the inward extrapolation of their outer Sérsic light profile. Such deficits were first noted and researched by King & Minkowski (1966). Sérsic galaxies, instead, do not exhibit such central stellar deficits. Partially depleted cores, as measured from high-resolution observations, have typical sizes of a few tens of parsecs (Rusli et al. 2013a; Dullo & Graham 2014). The majority are thus unresolved in our image mosaics. We masked these unresolved cores (identified in high-resolution images; - see Table 1) by excluding the surface brightness profile within 3 PSF's FWHM from the galaxy center. In the case of cores with sizes exceeding the PSF's FWHM, we excluded the data points within the size of the core plus 3 PSF's FWHM. The Sérsic/core-Sérsic classification presented in this work (Table 1, column (5)) comes from the compilation of Savorgnan & Graham (2015b), who identified partially depleted cores according to the same criteria used by Graham & Scott (2013). When no high-resolution image analysis was available from the literature, they inferred the presence of a partially depleted core based on the stellar velocity dispersion, σ : a galaxy is classified as core-Sérsic if $\sigma > 270 \text{ km s}^{-1}$, or as Sérsic if $\sigma < 166 \text{ km s}^{-1}$. This resulted in us assigning cores to just two galaxies using this alternative method when no high-resolution image was available.

3. ANALYSIS

3.1. Isophotal Analysis

We performed an isophotal analysis of our galaxies using the IRAF task `ellipse` (Jedrzejewski 1987), which fits elliptical isophotes to galaxy images. The center of the isophotes was held fixed, while the ellipticity (ϵ), the position angle (P.A.), and the amplitude of the fourth harmonic¹³ (B_4) were allowed to vary with radius. The step in semimajor axis length between successive ellipses was first set to increase linearly, and then geometrically in our second run.¹⁴ As a result, for each galaxy we produced respectively a “linearly sampled” and a “logarithmically sampled” surface brightness profile along the major axis. Major-axis surface brightness profiles were additionally converted into the equivalent axis, i.e., the geometric mean of the major (a) and minor (b) axis ($R_{\text{eq}} = \sqrt{ab}$), equivalent to the circularized radius. This resulted in four profiles per galaxy. Isophotes corresponding to an intensity less than three times the rms of the sky background fluctuations ($3 \times \text{rms}_{\text{sky}}$) were ignored. Some surface brightness profiles were truncated at our discretion before the $3 \times \text{rms}_{\text{sky}}$ limit, according to specific technical reasons (e.g., contamination from light of a neighboring galaxy, disturbed morphology in

¹³ The amplitude of the fourth harmonic deviations from perfect ellipses (B_4) parameterizes the diskyness ($B_4 > 0$) or boxyness ($B_4 < 0$) of the isophotes.

¹⁴ In the case of linear steps, the semimajor axis length for the next ellipse was calculated by adding 1 pixel to the current length. In the case of geometric steps, the semimajor axis length for the next ellipse was calculated as 1.1 times the current length.

Table 2
Results of Galaxy Decompositions

Galaxy (1)	1D Major Axis			1D Equivalent Axis				2D				
	R_e (2)	μ_e (3)	n (4)	R_e (5)	μ_e (6)	n (7)	m_{sph} (8)	m_{gal} (9)	Q.F. (10)	R_e (11)	n (12)	m_{sph} (13)
Circinus
IC 1459	63.1	18.49	6.6	57.3	18.59	7.0	6.11	6.11	1	87.5	8.3	6.04
IC 2560	6.1	16.58	0.8	4.5	16.48	0.6	10.77	8.29	2
IC 4296	65.9	19.32	5.8	68.1	19.48	6.2	6.70	6.70	1	82.3	6.6	6.66
M104	11.0	14.63	5.8	19.6	15.78	3.7	5.98	4.68	2
M105	57.2	17.93	5.2	50.9	17.84	5.3	5.77	5.77	2	73.6	7.0	5.62
M106	15.3	16.11	2.0	8.3	15.57	1.2	8.18	5.24	1
M31	418.6	16.80	2.2	173.6	15.63	1.3	1.61	-0.33	1
M32
M49	190.2	19.33	6.6	135.3	18.83	5.4	4.63	4.63	1	151.9	5.5	4.64
M59	48.0	18.02	5.5	90.9	19.67	8.8	6.07	5.98	1
M60
M64	3.8	13.38	0.8	4.3	13.78	1.4	7.78	5.08	1
M77
M81	31.0	15.22	1.7	33.2	15.55	2.1	4.89	3.47	3
M84	101.6	19.01	7.8	129.8	19.57	7.9	5.25	5.25	2	181.8	8.4	5.20
M87	203.0	19.87	10.0	87.1	18.26	5.9	4.97	4.97	2	88.3	4.3	5.11
M89	29.0	17.14	4.6	28.2	17.15	5.1	6.38	6.12	2
M94	11.4	13.73	0.9	8.4	13.50	1.1	6.14	4.86	1
M96	7.5	14.63	1.5	5.3	14.28	1.3	7.87	5.82	1	8.3	2.0	7.36
NGC 0253
NGC 0524	6.0	15.24	1.1	5.8	15.21	1.1	8.65	6.91	1
NGC 0821	36.5	18.40	5.3	18.9	17.83	6.1	7.85	7.59	3	33.8	2.5	7.78
NGC 1023	9.2	14.96	2.1	7.4	14.79	2.0	7.41	6.03	1	6.6	2.3	7.49
NGC 1300	9.9	17.62	3.8	8.1	17.41	3.6	9.52	7.42	2
NGC 1316	21.5	15.55	2.0	15.9	15.43	1.8	6.46	4.87	2
NGC 1332	34.7	17.44	5.1	18.0	16.47	3.7	6.85	6.79	3
NGC 1374	25.6	18.06	3.7	24.8	18.11	4.1	7.74	7.72	1	25.2	3.7	7.81
NGC 1399	405.2	21.80	10.0	338.1	21.53	10.0	5.01	4.98	1
NGC 2273	1.6	13.36	2.1	1.9	13.83	2.7	9.27	8.06	2
NGC 2549	6.1	15.57	2.3	3.1	14.54	1.5	9.20	7.85	1	5.6	2.1	8.76
NGC 2778	2.3	15.61	1.3	2.2	15.46	1.2	10.94	9.30	2
NGC 2787	4.8	14.86	1.1	3.3	14.62	1.3	9.21	7.04	2
NGC 2974	8.3	15.64	1.4	6.9	15.63	1.2	8.65	7.44	2	10.6	1.3	8.39
NGC 3079	6.8	14.47	1.3	4.3	14.48	1.1	8.57	7.13	2
NGC 3091	100.5	20.43	7.6	51.2	19.47	6.6	7.27	7.27	1	67.1	6.7	7.26
NGC 3115	43.6	16.67	4.4	34.4	16.85	5.1	5.65	5.47	1
NGC 3227	8.1	16.56	1.7	4.6	15.83	1.1	9.77	7.28	2
NGC 3245	4.4	14.96	2.9	2.4	14.00	1.7	9.11	7.66	1	1.9	1.8	9.19
NGC 3377	61.8	19.16	7.7	91.7	20.33	9.2	6.69	6.62	2	71.8	3.7	7.21
NGC 3384	5.5	14.21	1.6	5.6	14.56	1.8	7.83	6.52	1
NGC 3393	1.4	14.03	3.4	1.4	14.15	2.6	10.23	8.42	2	1.2	1.9	10.45
NGC 3414	28.0	18.10	4.8	25.5	18.08	4.5	7.60	7.53	1
NGC 3489	2.2	13.47	1.5	1.7	13.25	1.3	9.21	7.27	2	1.7	2.1	9.04
NGC 3585	105.0	19.13	5.2	86.3	19.24	6.3	5.93	5.90	2
NGC 3607	69.3	19.00	5.5	65.5	19.01	5.6	6.37	6.29	2	60.0	5.3	6.40
NGC 3608	47.5	18.93	5.2	43.4	19.00	5.7	7.25	7.25	2	62.0	7.0	7.15
NGC 3842	100.7	21.43	8.1	73.6	21.07	8.2	7.97	7.92	1
NGC 3998	5.8	15.15	1.2	4.8	14.63	1.3	8.37	7.15	3
NGC 4026	3.4	15.52	2.4	6.3	16.09	2.1	9.02	7.44	3
NGC 4151	7.6	15.50	1.4	6.8	15.26	1.9	8.10	7.06	2
NGC 4261	52.6	18.58	4.7	47.3	18.53	4.3	6.72	6.68	2	50.4	4.4	6.73
NGC 4291	15.0	17.14	4.2	15.4	17.51	5.9	7.99	7.99	2	20.8	7.7	7.91
NGC 4342
NGC 4388	4.6	15.89	0.6	4.2	15.86	1.3	9.89	7.66	3
NGC 4459	18.4	16.69	3.1	13.0	16.23	2.6	7.50	6.97	2
NGC 4473	45.9	17.93	2.3	36.9	18.10	2.9	7.04	6.82	2	49.8	3.0	7.03
NGC 4486A
NGC 4564	5.0	15.23	2.6	6.0	15.65	3.0	8.52	7.83	1
NGC 4596	6.6	15.93	2.7	9.0	16.44	3.0	8.43	6.98	1
NGC 4697	239.3	20.62	7.2	226.4	20.90	6.7	5.47	5.34	3	121.4	5.0	5.72
NGC 4889	119.7	21.01	8.1	60.8	20.11	6.8	7.53	7.53	1	104.3	7.8	7.43

Table 2
(Continued)

Galaxy (1)	1D Major Axis			1D Equivalent Axis				2D				
	R_e (2)	μ_e (3)	n (4)	R_e (5)	μ_e (6)	n (7)	m_{sph} (8)	m_{gal} (9)	Q.F. (10)	R_e (11)	n (12)	m_{sph} (13)
NGC 4945	13.9	14.95	1.4	9.5	14.78	1.7	6.94	4.11	2	16.2	0.8	7.07
NGC 5077	23.5	17.67	4.2	23.0	18.01	5.7	7.62	7.62	1	30.5	6.8	7.57
NGC 5128	61.3	15.73	1.2	60.8	16.01	2.2	4.01	2.93	3
NGC 5576	61.5	19.41	3.3	49.3	19.34	3.7	7.53	7.53	1	45.9	8.3	7.19
NGC 5813
NGC 5845	3.6	14.79	2.5	3.1	14.64	2.3	9.05	8.91	3	2.8	2.4	9.09
NGC 5846	105.1	19.67	6.4	83.4	19.28	5.7	6.10	6.10	2	85.1	5.2	6.14
NGC 6251	41.7	19.82	6.8	30.1	19.31	5.6	8.35	8.35	1	39.3	7.1	8.27
NGC 7052	59.4	19.38	4.2	37.0	19.19	5.6	7.79	7.79	1	36.2	4.0	8.09
NGC 7582
NGC 7619	63.2	19.53	5.3	58.0	19.55	5.2	7.21	7.15	2
NGC 7768	92.9	21.37	8.4	42.1	20.15	6.7	8.36	8.36	2
UGC 03789	1.8	15.26	1.9	2.4	15.39	1.4	10.65	9.22	3	-

Note. Column (1): galaxy name. Columns (2)–(4): effective radius (in units of arcsec), surface brightness at the effective radius (in units of mag arcsec $^{-2}$), and Sérsic index for 1D fits along the major axis. Columns (5)–(9): effective radius (in units of arcsec), surface brightness at the effective radius (in units of mag arcsec $^{-2}$), Sérsic index, spheroid apparent magnitude (in units of mag, Vega system), and galaxy apparent magnitude (in units of mag, Vega system) for 1D fits along the equivalent axis. Column (10): quality flag of the 1D fits (see Section 4.2). Columns (11)–(13): effective radius (in units of arcsec), Sérsic index, and spheroid apparent magnitude (in units of mag, Vega system) for 2D fits.

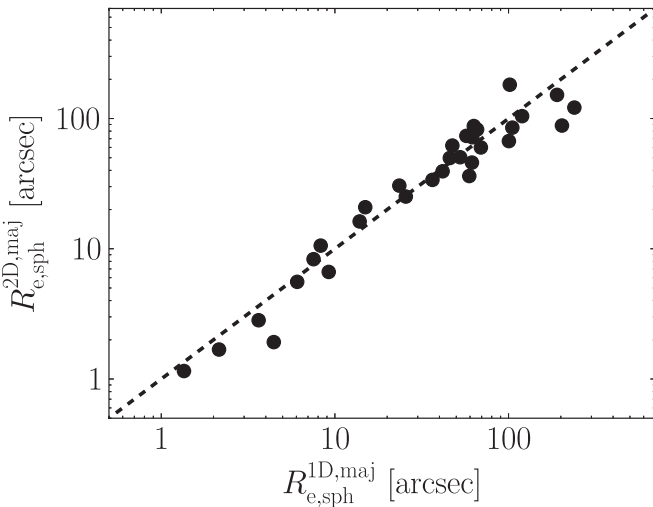


Figure 6. 2D vs. 1D major-axis measurements of the spheroid effective radii. The dashed line displays the 1:1 relation.

the galaxy outskirts, etc.). In particular, we did not attempt to fit bends or truncations of large-scale disks (e.g., Erwin et al. 2005, 2008, 2012; Gutiérrez et al. 2011; Comerón et al. 2012; Muñoz-Mateos et al. 2013; Kim et al. 2014), but instead truncated the surface brightness profiles before the occurrence of such features. Individual cases are discussed in Section 5.1.

3.2. Unsharp Masking

Unsharp masking is an image-sharpening technique that is useful to reveal asymmetric structures in galaxies, such as bars or (inclined) embedded disks. First, the original galaxy image was smoothed with a Gaussian filter. Then, the original image was divided by the smoothed one. The result of such an operation is the “unsharp mask.” The asymmetric features revealed by this technique have sizes comparable to the FWHM of the Gaussian kernel used for the smoothing. Therefore, for each galaxy, we produced a set of different

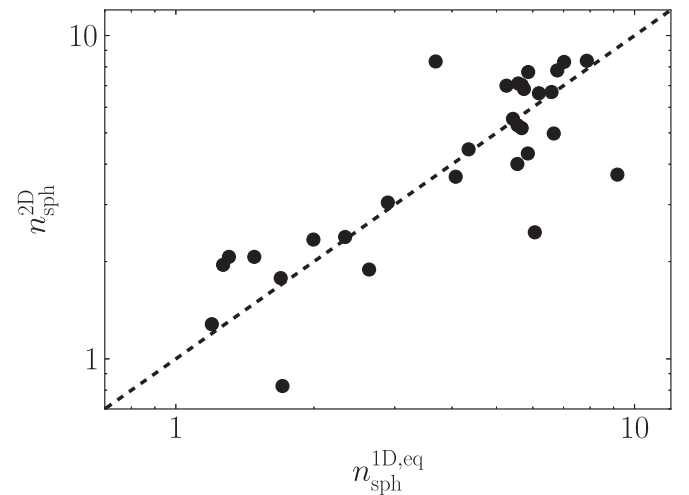


Figure 7. 2D measurements of the spheroid Sérsic indices roughly approximate the 1D equivalent-axis measurements. The dashed line displays the 1:1 relation. The four most obvious outliers are NGC 821, NGC 3377, NGC 4945, and NGC 5576. Their individual cases are discussed in the Appendix.

unsharp masks by varying the FWHM of the filter, to identify all the asymmetric features that could bias the fitting process and may therefore need to be considered during the galaxy modeling phase. This information was used in combination with kinematic and AGN information discussed in Section 2.2.

3.3. 1D Fitting Routine

The decomposition of the surface brightness profiles was performed with software written by G. Savorgnan. This software can fit an observed surface brightness profile with any linear combination of a set of analytical functions (Sérsic, exponential, Gaussian, Moffat, Ferrer, symmetric Gaussian ring, etc.; see the Appendix for a description of the analytical form of these profiles). At each iteration, the model is numerically convolved with a Moffat filter, to account for PSF effects, and then matched to the data. The minimization

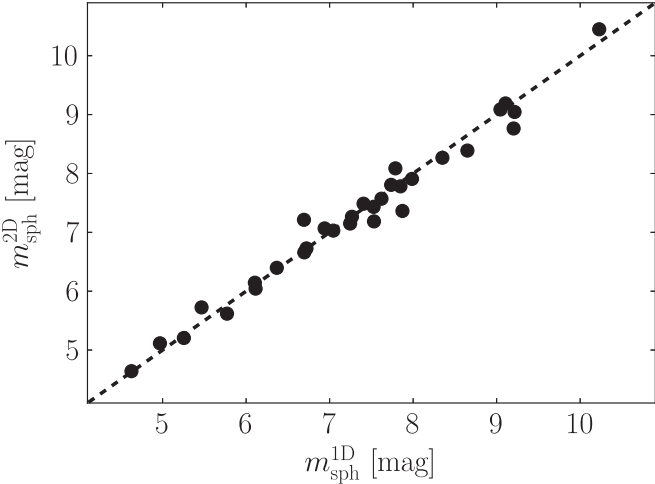


Figure 8. 2D vs. 1D measurements of the $3.6\ \mu\text{m}$ spheroid magnitudes. The dashed line displays the 1:1 relation.

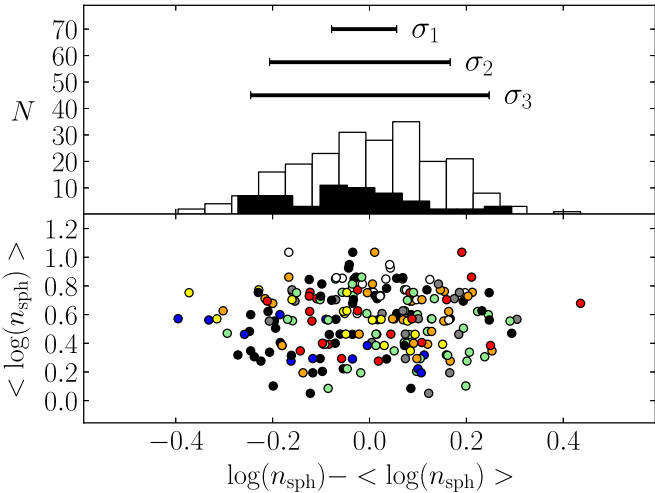


Figure 9. Bottom panel: 58 galaxies for which at least one measurement of the spheroid Sérsic index n_{sph} is available from the literature (Table 3), in addition to that measured by us. The average (logarithmic) value ($\langle \log(n_{\text{sph}}) \rangle$) is plotted against the difference between (the logarithm of) the individual measurements of a galaxy and the average (logarithmic) value for that same galaxy. Each data point corresponds to an individual measurement from Graham & Driver (2007a; red points), Laurikainen et al. (2010; blue points), Sani et al. (2011; green points), Vika et al. (2012; yellow points), Beifiori et al. (2012; gray points), Rusli (2013a; white points), and Läsker et al. (2014a; orange points). Black points are measurements obtained from the 1D fits presented in this work (using linearly sampled surface brightness profiles, along the major axis). In the top panel, the white histogram shows the distribution of $\log(n_{\text{sph}}) - \langle \log(n_{\text{sph}}) \rangle$ for all measurements, whereas the black histogram refers only to the measurements obtained by us. The (asymmetric) error bars σ_1 , σ_2 , and σ_3 enclose 38%, 78%, and 92% of the black histogram, respectively, corresponding to our quality flags 1, 2, and 3 given in Table 2 (see Section 4.2 for details). We consider these to be absolute upper limits to the uncertainty on our parameters given the care we have taken to minimize sources of systematic errors.

routine is based on the Levenberg–Marquardt algorithm. During the fit, we deliberately did not make use of any weighting scheme on the data points that constitute the surface brightness profile, although the use of a linearly and logarithmically sampled profile effectively represents a different weighting scheme. The all too often overlooked flaw with signal-to-noise ratio (S/N) based weighting schemes is that they immediately become biased weighting schemes when

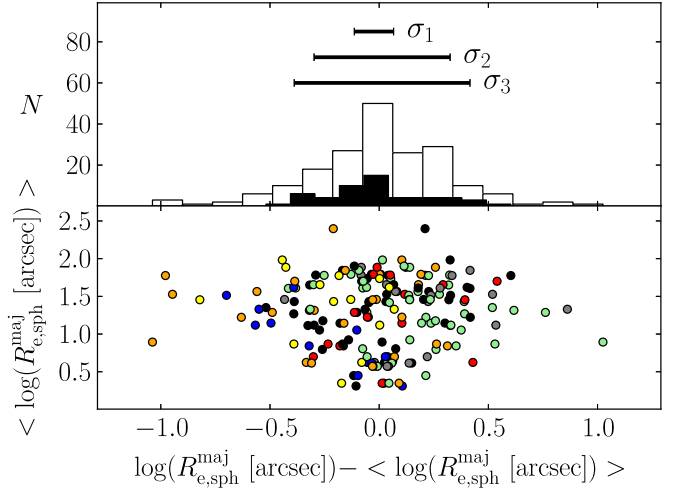


Figure 10. Bottom panel: 52 galaxies for which at least one measurement of the spheroid major-axis effective radius $R_{\text{e}}^{\text{maj}}$ is available from the literature (Table 3), in addition to that measured by us. The average (logarithmic) value ($\langle \log(R_{\text{e}}^{\text{maj}}) \rangle$) is plotted against the difference between (the logarithm of) the individual measurements of a galaxy and the average (logarithmic) value for that same galaxy. See Figure 9 for color description and explanation of the top panel.

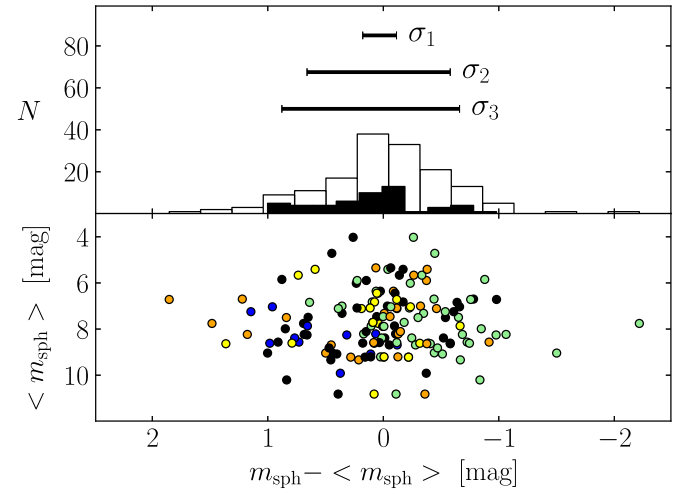


Figure 11. Bottom panel: 51 galaxies for which at least one measurement of the spheroid apparent magnitude m_{sph} —either in the K band or at $3.6\ \mu\text{m}$ —is available from the literature (Table 3), in addition to that measured by us. The $3.6\ \mu\text{m}$ magnitudes were converted into K -band magnitudes (see Section 4.2 for details). The average value ($\langle m_{\text{sph}} \rangle$) is plotted against the difference between the individual measurements of a galaxy and the average value for that same galaxy. See Figure 9 for color description and explanation of the top panel.

additional components are present but not modeled. For example, fitting only a Sérsic model to what is actually a nucleated elliptical galaxy immediately voids a S/N-based weighting scheme and results in Sérsic parameters that describe the spheroid less accurately than had no S/N-based weighting been used. While we have paid careful attention to the components in each galaxy, this is an issue that warrants the nonapplication of S/N-based weighting schemes. Overlooked partially depleted cores, or an incorrect PSF, can of course also result in S/N-weighted fitting schemes performing poorly because of the emphasis they place on matching the model to the inner data.

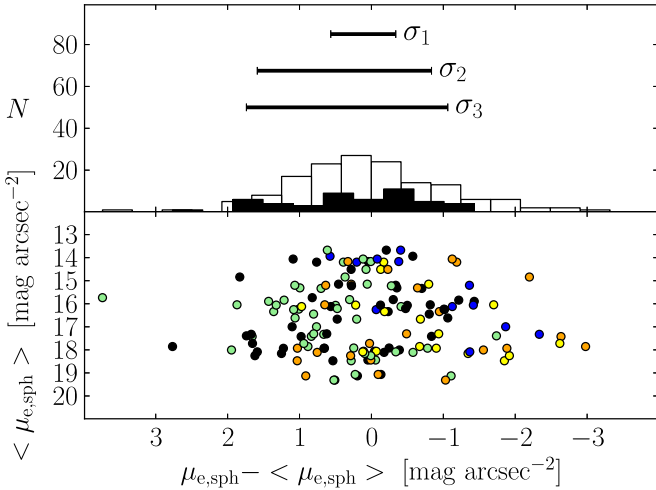


Figure 12. Bottom panel: 49 galaxies for which at least one measurement of the spheroid effective surface brightness $\mu_{e,\text{sph}}$ —either in the K band or at $3.6 \mu\text{m}$ —is available from the literature (Table 3), in addition to that measured by us. The K -band magnitudes were converted into $3.6 \mu\text{m}$ magnitudes (see Section 4.2 for details). The average value $\langle \mu_{e,\text{sph}} \rangle$ from all fits to a galaxy, not to be confused with the mean effective surface brightness within $R_{e,\text{sph}}$, is plotted against the difference between the individual measurements of a galaxy and the average value for that same galaxy. See Figure 9 for color description and explanation of the top panel.

Table 3 Summary of Previous Investigations of Black Hole Mass Scaling Relations					
	GD07	S+11	V+12	B+12	L+14
Galaxies with successful fit	27	57	25	19	35
Wavelength	R -band	$3.6 \mu\text{m}$	K -band	i -band	K -band
Decomposition	1D	2D	2D	2D	2D
Nuclear components	masked	modeled	modeled	not treated	modeled
Partially depleted cores	masked	masked	masked	not treated	masked
Bars	excluded	modeled	modeled	excluded	modeled
Other components	no	no	no	no	yes
Kinematics	no	no	no	no	yes

Note. GD07—Graham & Driver (2007a); S+11—Sani et al. (2011); V+12—Vika et al. (2012); B+12—Beifiori et al. (2012); L+14—Läsker et al. (2014a).

Table 4
Best-fit Parameters for the Spheroidal Component of IC 1459

Work	Model	$R_{e,\text{sph}}$ (arcsec)	n_{sph}
1D maj.	S-bul + m-c	63.1	6.6
1D eq.	S-bul + m-c	57.3	7.0
2D	S-bul + m-c	87.5	8.3
S+11 2D	S-bul + G-n	61.1	6.0
R+13 1D eq.	core-Sérsic	45.4	7.6
L+14 2D	S-bul + m-c	62.4	8.3

Note. Our results are shown in the upper portion of the table. See Section 5.1 for the legend key to the other authors listed in the lower portion of the table. See Table 2 for our associated surface brightnesses and magnitudes.

3.4. Smoothing Technique

Some nearby galaxies in our sample have very large apparent sizes, and for them we obtained surface brightness profiles more extended than 8 arcmin. This means that their outermost (significant) isophote corresponds to a projected galactic radius R of more than 240 times the FWHM of the instrumental PSF. Such a level of spatial resolution is

Table 5
Best-fit Parameters for the Spheroidal Component of IC 2560

Work	Model	$R_{e,\text{sph}}$ (arcsec)	n_{sph}
1D maj.	S-bul + e-d + F-bar + G-n	6.1	0.8
1D eq.	S-bul + e-d + F-bar + G-n	4.5	0.6
S+11 2D	S-bul + e-d + G-n	27.5	2.0

Note. In their model, S+11 did not account for the bar component and thus overestimated the effective radius and the Sérsic index of the bulge.

Table 6
Best-fit Parameters for the Spheroidal Component of IC 4296

Work	Model	$R_{e,\text{sph}}$ (arcsec)	n_{sph}
1D maj.	S-bul + m-c	65.9	5.8
1D eq.	S-bul + m-c	68.1	6.2
2D	S-bul + m-c	82.3	6.6
S+11 2D	S-bul + G-n	33.6	4.0
L+14 2D	S-bul + m-c	97.8	8.2

Note. S+11 obtained a small effective radius and Sérsic index because they fit a nuclear component rather than masking the core.

Table 7
Best-fit Parameters for the Spheroidal Component of M31

Work	Model	$R_{e,\text{sph}}$ (arcsec)	n_{sph}
1D maj.	S-bul + e-d + F-bar	418.6	2.2
1D eq.	S-bul + e-d + F-bar	173.6	1.3

Table 8
Best-fit Parameters for the Spheroidal Component of M49

Work	Model	$R_{e,\text{sph}}$ (arcsec)	n_{sph}
1D maj.	S-bul + m-c	190.2	6.6
1D eq.	S-bul + m-c	135.3	5.4
2D	S-bul + m-c	151.9	5.5
R+13 1D eq.	core-Sérsic	199.0	5.6

Note. The equivalent-axis effective radius estimated by R+13 is larger than that measured by us. Since their circularized light profile is almost three times more extended than ours, it is possible that their best-fit model required a larger R_e to account for the galaxy intracluster halo light.

Table 9
Best-fit Parameters for the Spheroidal Component of M59

Work	Model	$R_{\text{e,sph}}$ (arcsec)	n_{sph}
1D maj.	S-bul + m-n + e-id	48.0	5.5
1D eq.	S-bul + m-n + e-id	90.9	8.8
S+11 2D	S-bul	70.1	5.0
V+12 2D	S-bul + m-c	54.7	5.7

Table 10
Best-fit Parameters for the Spheroidal Component of M64

Work	Model	$R_{\text{e,sph}}$ (arcsec)	n_{sph}
1D maj.	S-bul + e-d + F-bar + S-id	3.8	0.8
1D eq.	S-bul + e-d + F-bar + S-id	4.3	1.4
B+12 2D	S-bul + e-d	5.0	1.5

Table 11
Best-fit Parameters for the Spheroidal Component of M81

Work	Model	$R_{\text{e,sph}}$ (arcsec)	n_{sph}
1D maj.	S-bul + e-d	31.0	1.7
1D eq.	S-bul + e-d	33.2	2.1
GD07 1D maj.	S-bul + e-d	68.1	3.3
S+11 2D	S-bul + e-d + G-n	127.3	3.0
B+12 2D	S-bul + e-d	50.0	2.6

Note. GD07 and B+12 obtained estimates of the effective radius larger than ours by a factor of two. This is not particularly surprising, given the complicated surface brightness distribution of this galaxy. The large measurement of the effective radius reported by S+11 is the most discrepant, but the reasons for this are unclear.

Table 12
Best-fit Parameters for the Spheroidal Component of M84

Work	Model	$R_{\text{e,sph}}$ (arcsec)	n_{sph}
1D maj.	S-bul + m-c	101.6	7.8
1D eq.	S-bul + m-c	129.8	7.9
2D	S-bul + m-c	181.8	8.4
GD07 1D maj.	S-bul	75.1	5.6
S+11 2D	S-bul + G-n	105.9	7.0
V+12 2D	S-bul + m-c	28.7	3.5
B+12 2D	S-bul	63.6	4.1
R+13 1D eq.	core-Sérsic	126.2	7.1
L+14 2D	S-bul + m-c	139.0	8.3

Note. B+12 did not mask the core and thus underestimated the effective radius and the Sérsic index. V+12 used the same model as R+13, L+14, and us, but the smaller radial extent of their data led them to underestimate the effective radius and the Sérsic index.

unnecessary for the purposes of our analysis, and, especially in the case of a clumpy star-forming galaxy, it results in a “noisy” surface brightness profile. Moreover, in the case of a linearly sampled light profile, it significantly prolongs the computational time of the fitting routine (because, at each iteration, the PSF convolution is performed numerically on a large array). To overcome this problem, we introduced a method to which we refer as the “smoothing technique.” This method was applied to the galaxies M31, M81, NGC 4945, and NGC 5128. For each

Table 13
Best-fit Parameters for the Spheroidal Component of M87

Work	Model	$R_{\text{e,sph}}$ (arcsec)	n_{sph}
1D maj.	S-bul + m-c	203.9	10.0
1D eq.	S-bul + m-c	87.1	5.9
2D	S-bul + m-c	88.3	4.3
GD07 1D maj.	S-bul	...	6.9
S+11 2D	S-bul + G-n	99.5	4.0
V+12 2D	S-bul + m-c	34.6	2.4
R+13 1D eq.	core-Sérsic	180.9	8.9
L+14 2D	S-bul + m-c	122.0	5.6

Note. The equivalent-axis fit of R+13 returns the largest values for $R_{\text{e,sph}}$ and n_{sph} . As in the case of M49, since their circularized light profile is almost three times more extended than ours, it is possible that their best-fit model required a larger R_{e} to account for the extra intracluster halo light. V+12 obtained the smallest estimates of $R_{\text{e,sph}}$ and n_{sph} because of the small radial extent of their data.

Table 14
Best-fit Parameters for the Spheroidal Component of M89

Work	Model	$R_{\text{e,sph}}$ (arcsec)	n_{sph}
1D maj.	S-bul + e-halo	29.0	4.6
1D eq.	S-bul + e-halo	28.2	5.1
S+11 2D	S-bul + e-d	24.3	4.0
V+12 2D	S-bul	16.7	3.6
B+12 2D	S-bul	45.2	4.3
R+13 1D eq.	S-bul + S-halo	19.8	3.8

Table 15
Best-fit Parameters for the Spheroidal Component of M94

Work	Model	$R_{\text{e,sph}}$ (arcsec)	n_{sph}
1D maj.	S-bul + e-d + F-bar	11.4	0.9
1D eq.	S-bul + e-d + F-bar	8.4	1.1

Table 16
Best-fit Parameters for the Spheroidal Component of M96

Work	Model	$R_{\text{e,sph}}$ (arcsec)	n_{sph}
1D maj.	S-bul + e-d + F-bar + S-id	7.5	1.5
1D eq.	S-bul + e-d + F-bar + S-id	5.3	1.3
2D	S-bul + e-d + G-bar + G-id	8.3	2.0
S+11 2D	S-bul + e-d + G-bar	45.6	1.0

Note. The bulge effective radius obtained by S+11 largely exceeds our estimates because their galaxy decomposition does not account for the inner component embedded in the bulge ($R_{\text{maj}} \lesssim 25''$).

of these galaxies, we took the image mosaic and convolved it with a Gaussian filter whose FWHM was larger than the FWHM of the instrumental PSF. We then ran `ellipse` on the convolved image and extracted “linearly sampled” and “logarithmically sampled” surface brightness profiles. For the “linearly sampled” profiles, we set the radial step between contiguous isophotes to be comparable to the FWHM of the smoothing Gaussian filter. Doing so, we reduced the number of fitted isophotes and also produced smoother surface brightness

Table 17
Best-fit Parameters for the Spheroidal Component of M104

Work	Model	$R_{\text{e,sph}}$ (arcsec)	n_{sph}
1D maj.	S-bul + e-d + F-bar + m-c	11.0	5.8
1D eq.	S-bul + e-d + F-bar + m-c	19.6	3.7
S+11 2D	S-bul + e-d + G-bar + G-n	66.1	1.5

Note. The bulge Sérsic index obtained by S+11 is smaller than our estimates because they fit an additional nuclear component.

Table 18
Best-fit Parameters for the Spheroidal Component of M105

Work	Model	$R_{\text{e,sph}}$ (arcsec)	n_{sph}
1D maj.	S-bul + m-c	57.2	5.2
1D eq.	S-bul + m-c	50.9	5.3
2D	S-bul + m-c	73.6	7.0
GD07 1D maj.	S-bul	58.3	4.3
S+11 2D	S-bul	46.0	5.0
R+13 1D eq.	core-Sérsic	55.1	5.8
L+14 2D	S-bul + m-c	96.3	9.3

Note. L+14 obtained the largest values of $R_{\text{e,sph}}$ and n_{sph} , possibly owing to incorrect sky subtraction (see the “upturn” of the three outermost data points in their Figure 21).

Table 19
Best-fit Parameters for the Spheroidal Component of M106

Work	Model	$R_{\text{e,sph}}$ (arcsec)	n_{sph}
1D maj.	S-bul + e-d	15.3	2.0
1D eq.	S-bul + e-d	8.3	1.2
GD07 1D maj.	S-bul + e-d	14.9	2.0
S+11 2D	S-bul + e-d + G-n	111.7	2.0
V+12 2D (1)	S-bul + e-d + PSF-n	17.0	3.5
V+12 2D (2)	S-bul + e-d + PSF-n + S-bar	6.3	2.2
L+14 2D	S-bul + e-d + PSF-n + e-id + S-bar + spiral arms	6.3	3.3

Note. The bulge effective radius obtained by S+11 largely exceeds all the other estimates, behavior noted also in NGC 3031.

Table 20
Best-fit Parameters for the Spheroidal Component of NGC 0524

Work	Model	$R_{\text{e,sph}}$ (arcsec)	n_{sph}
1D maj.	S-bul + e-d + G-r	6.0	1.1
1D eq.	S-bul + e-d + G-r	5.8	1.1
L+10 2D	S-bul + e-d + 2 F-l	8.9	2.7
S+11 2D	S-bul + e-d	26.8	3.0

Note. S+11 obtained the largest value of the effective radius because their two-component model does not account for the ring. Both L+10 and S+11 estimated a Sérsic index of ~ 3 , three times larger than the value obtained by us.

profiles. Before the software fit a smoothed light profile, the model to be fit was convolved twice: the first time to account for PSF effects, and the second time to account for the artificial Gaussian smoothing applied to the image mosaic.

Table 21
Best-fit Parameters for the Spheroidal Component of NGC 0821

Work	Model	$R_{\text{e,sph}}$ (arcsec)	n_{sph}
1D maj.	S-bul + e-id + PSF-n	36.8	5.4
1D eq.	S-bul + e-id + PSF-n	20.7	6.0
2D	S-bul + e-id + m-n	33.8	2.5
GD07 1D maj.	S-bul	44.1	4.0
S+11 2D	S-bul	63.6	7.0
B+12 2D	S-bul	111.3	7.7
L+14 2D	S-bul + e-d + S-halo	3.8	3.1

Note. L+14 obtained a tiny estimate of the spheroid effective radius and a small Sérsic index because they failed to identify the extent of the intermediate-scale disk. Inaccurate sky subtraction could be the reason why B+12 obtained a large estimate of the effective radius. We could not obtain a successful 2D model that included a nuclear component; therefore, we opted for masking the nuclear region of the galaxy. This resulted in a significantly lower Sérsic index, which we consider underestimated.

Table 22
Best-fit Parameters for the Spheroidal Component of NGC 1023

Work	Model	$R_{\text{e,sph}}$ (arcsec)	n_{sph}
1D maj.	S-bul + e-d + F-bar	9.2	2.1
1D eq.	S-bul + e-d + F-bar	7.4	2.0
2D	S-bul + e-d + G-bar	6.6	2.3
GD07 1D maj.	S-bul + e-d	17.7	2.0
S+11 2D	S-bul + e-d + G-bar	24.0	3.0
L+14 2D	S-bul + e-d + S-bar	9.6	3.1

Note. S+11 obtained the largest value of the bulge effective radius, although they accounted for the bar in their model.

Table 23
Best-fit Parameters for the Spheroidal Component of NGC 1300

Work	Model	$R_{\text{e,sph}}$ (arcsec)	n_{sph}
1D maj.	S-bul + e-(d+bar) + S-id	9.9	3.8
1D eq.	S-bul + e-(d+bar) + S-id	8.1	3.6
S+11 2D	S-bul + e-d	85.4	3.0
L+14 2D	S-bul + e-d + PSF-n + e-id + S-bar + spiral arms	10.4	4.3

Note. S+11 dramatically overestimated the bulge effective radius mainly because their model does not account for the large-scale bar.

Table 24
Best-fit Parameters for the Spheroidal Component of NGC 1316

Work	Model	$R_{\text{e,sph}}$ (arcsec)	n_{sph}
1D maj.	S-bul + e-d + F-bar + 2 G-r + G-n	21.5	2.0
1D eq.	S-bul + e-d + F-bar + 2 G-r + G-n	15.9	1.8
S+11 2D	S-bul + e-d + G-n	93.0	5.0

Note. S+11 overestimated the bulge effective radius and Sérsic index because their model does not take into account the bar.

3.5. Identifying and Modeling Subcomponents

In this section we give a general overview of the guidelines that we followed to identify and model the subcomponents that

Table 25

Best-fit Parameters for the Spheroidal Component of NGC 1332

Work	Model	$R_{\text{e,sph}}$ (arcsec)	n_{sph}
1D maj.	S-bul + S-id + m-c	34.7	5.1
1D eq.	S-bul + S-id + m-c	18.0	3.7

Table 26

Best-fit Parameters for the Spheroidal Component of NGC 1374

Work	Model	$R_{\text{e,sph}}$ (arcsec)	n_{sph}
1D maj.	S-bul + G-n	25.6	3.7
1D eq.	S-bul + G-n	24.8	4.1
2D	S-bul + m-n	25.2	3.7

Table 27

Best-fit Parameters for the Spheroidal Component of NGC 1399

Work	Model	$R_{\text{e,sph}}$ (arcsec)	n_{sph}
1D maj.	S-bul + m-c + e-id	405.2	10.0
1D eq.	S-bul + m-c + e-id	338.1	10.0
GD07 1D maj.	S-bul	...	16.8
R+13 1D eq.	core-Sérsic + (S+e)-halo	36.2	7.4
L+14 2D	S-bul + m-c	154.0	11.1

Note. R+13 used a combination of a Sérsic + exponential profile to model the galaxy’s halo and obtained the smallest estimate of the effective radius, one that is at odds with the fact that central cluster galaxies typically have large sizes.

Table 28

Best-fit Parameters for the Spheroidal Component of NGC 2273

Work	Model	$R_{\text{e,sph}}$ (arcsec)	n_{sph}
1D maj.	S-bul + e-d + F-bar	1.6	2.1
1D eq.	S-bul + e-d + F-bar	1.9	2.7
L+10 2D	S-bul + e-d + F-bar	2.6	1.8

Table 29

Best-fit Parameters for the Spheroidal Component of NGC 2549

Work	Model	$R_{\text{e,sph}}$ (arcsec)	n_{sph}
1D maj.	S-bul + e-d + F-bar + F-id	6.1	2.3
1D eq.	S-bul + e-d + F-bar + F-id	3.1	1.5
2D	S-bul + e-d + G-bar + G-id	5.6	2.1
S+11 2D	S-bul + e-d	11.6	7.0

Note. The model of S+11 does not account for the large-scale bar and therefore largely overestimates the bulge Sérsic index.

constitute our galaxies. However, given the level of accuracy and detail to which each galaxy decomposition has been performed in our analysis, it is hard to encompass all aspects of this matter in a few paragraphs. The modeling of each galaxy represented a particular and original problem, and we remand the reader to Section 5.1, where we provide individual descriptions of the galaxies that we analyzed.

Table 30

Best-fit Parameters for the Spheroidal Component of NGC 2778

Work	Model	$R_{\text{e,sph}}$ (arcsec)	n_{sph}
1D maj.	S-bul + e-d + F-bar + PSF-n	2.3	1.3
1D eq.	S-bul + e-d + F-bar + PSF-n	2.2	1.2
GD07 1D maj.	S-bul + e-d	2.3	1.6
S+11 2D	S-bul + e-d	2.5	2.5
V+12 2D	S-bul + e-d	1.5	2.7
L+14 2D	S-bul + e-d + S-bar	2.8	4.0

Table 31

Best-fit Parameters for the Spheroidal Component of NGC 2787

Work	Model	$R_{\text{e,sph}}$ (arcsec)	n_{sph}
1D maj.	S-bul + e-d + F-bar + F-id + PSF-nucleus	4.8	1.1
1D eq.	S-bul + e-d + F-bar + F-id + PSF-nucleus	3.3	1.3
GD07 1D maj.	S-bul + e-d	4.6	2.0
L+10 2D	S-bul + e-d + F-bar + F-l	4.0	1.3
S+11 2D	S-bul + e-d + G-bar + G-n	15.7	3.0
L+14 2D	S-bul + trunc. e-d + trunc. S-bar + S-id + PSF-n	14.3	2.8

Note. S+11 found larger estimates of the effective radius and Sérsic index because they did not account for the inner disk. L+14 also reported a larger effective radius and Sérsic index because they employed a truncated exponential disk and truncated Sérsic bar in their galaxy model.

Table 32
Best-fit Parameters for the Spheroidal Component of NGC 2974

Work	Model	$R_{\text{e,sph}}$ (arcsec)	n_{sph}
1D maj.	S-bul + e-d + F-bar + G-n + G-r	8.3	1.4
1D eq.	S-bul + e-d + F-bar + G-n + G-r	6.9	1.2
2D	S-bul + e-d + G-bar + m-n	10.6	1.3
S+11 2D	S-bul + G-n	27.2	3.0

Note. The model of S+11 does not account for the large-scale disk and thus overestimates the bulge effective radius and Sérsic index.

Table 33
Best-fit Parameters for the Spheroidal Component of NGC 2974

Work	Model	$R_{\text{e,sph}}$ (arcsec)	n_{sph}
1D maj.	S-bul + F-(bar+d) + G-n	6.8	1.3
1D eq.	S-bul + F-(bar+d) + G-n	4.3	1.1
S+11 2D	S-bul + e-d + G-bar + G-n	74.1	2.0

Note. It is not clear why S+11 obtained a dramatically larger bulge effective radius.

As stressed in Section 1, our investigation is primarily focused on the central spheroidal components of galaxies. The objects in our sample are either early-type galaxies (elliptical + lenticular) or “early-type spiral” galaxies (i.e., the morphological classification of our spiral galaxies is within Sa–Sc, with the only exception of NGC 4945, which is classified as Scd); therefore—by definition—they all have a bulge/spheroidal component, unlike “late-type spiral” galaxies that can be

Table 34

Best-fit Parameters for the Spheroidal Component of NGC 3091

Work	Model	$R_{\text{e,sph}}$ (arcsec)	n_{sph}
1D maj.	S-bul + m-c	100.5	7.6
1D eq.	S-bul + m-c	51.2	6.6
2D	S-bul + m-c	67.1	6.7
R+13 1D Equation	core-Sérsic	91.0	9.3

Table 35

Best-fit Parameters for the Spheroidal Component of NGC 3115

Work	Model	$R_{\text{e,sph}}$ (arcsec)	n_{sph}
1D maj.	S-bul + e-d + G-r	43.6	4.4
1D eq.	S-bul + e-d + G-r	34.4	5.1
S+11 2D	S-bul + e-d	27.1	3.0
L+14 2D	S-bul + e-d + S-halo	3.9	3.0

Note. L+14 used a model with a bulge encased in a larger disk and attributed the excess of light at large radii to a halo. In doing so, they obviously obtained a smaller bulge effective radius.

Table 36

Best-fit Parameters for the Spheroidal Component of NGC 3227

Work	Model	$R_{\text{e,sph}}$ (arcsec)	n_{sph}
1D maj.	S-bul + e-d + F-bar + G-n	8.1	1.7
1D eq.	S-bul + e-d + [F-bar] + G-n	4.6	1.1
L+10 2D	S-bul + e-d + F-bar	1.8	2.2
S+11 2D	S-bul + e-d	82.9	4.0
L+14 2D	S-bul + e-d + S-bar	0.7	4.1

Note. The models of L+10 and L+14 do not account for the bright nuclear component and thus underestimate the bulge effective radius and overestimate the bulge Sérsic index. The bulge effective radius obtained by S+11 is larger because they did not model the bar.

Table 37

Best-fit Parameters for the Spheroidal Component of NGC 3245

Work	Model	$R_{\text{e,sph}}$ (arcsec)	n_{sph}
1D maj.	S-bul + e-d + F-id	4.4	2.9
1D eq.	S-bul + e-d + F-id	2.4	1.7
2D	S-bul + e-d + G-id	1.9	1.8
GD07 1D maj.	S-bul + e-d	11.3	4.3
L+10 2D	S-bul + e-(d+l) + F-id	4.0	2.4
S+11 2D	S-bul + e-d	4.6	2.5
V+12 2D	S-bul + e-d	3.5	2.6
B+12 2D	S-bul + e-d	4.0	1.6
L+14 2D	S-bul + e-d + S-bar	2.0	1.6

bulgeless (e.g., NGC 300). We modeled spheroids/bulges with a Sérsic profile, without attempting to distinguish between classical and pseudobulges.

Disk were usually fit with the exponential model, although in the case of highly inclined or edge-on systems we preferred using an $n < 1$ Sérsic function. Pastrav et al. (2013a, 2013b) showed that, owing to projection effects, their simulated images of inclined galaxy disks are better fit by a Sérsic

Table 38

Best-fit Parameters for the Spheroidal Component of NGC 3377

Work	Model	$R_{\text{e,sph}}$ (arcsec)	n_{sph}
1D maj.	S-bul + 2 e-id	61.8	7.7
1D eq.	S-bul + 2 e-id	91.7	9.2
2D	S-bul + e-id + m-n	71.8	3.7
GD07 1D maj.	S-bul	44.1	3.0
S+11 2D	S-bul	55.2	6.0
B+12 2D	S-bul	43.5	3.5
L+14 2D	S-bul + e-id + e-d + S-halo	10.1	6.0

Note. L+14 obtained the smallest estimate of the effective radius because they oversubtracted a halo. In our 2D fit, we were not successful in modeling the nuclear disk and opted for masking the nuclear region of the galaxy. Such a 2D model resulted in a significantly lower Sérsic index, which we trust being underestimated.

Table 39

Best-fit Parameters for the Spheroidal Component of NGC 3384

Work	Model	$R_{\text{e,sph}}$ (arcsec)	n_{sph}
1D maj.	S-bul + e-d + F-bar + m-n	5.5	1.6
1D eq.	S-bul + e-d + F-bar + m-n	5.6	1.8
GD07 1D maj.	S-bul + e-d	2.5	1.7
L+10 2D	S-bul + e-d + 2 F-bar	4.0	1.5
S+11 2D	S-bul + e-d + G-bar	4.4	2.5
B+12 2D	S-bul + e-d	8.3	2.3
L+14 2D	S-bul + e-d + 2 S-id + S-bar	5.9	2.5

Table 40
Best-fit Parameters for the Spheroidal Component of NGC 3393

Work	Model	$R_{\text{e,sph}}$ (arcsec)	n_{sph}
1D maj.	S-bul + e-d + F-bar	1.4	3.4
1D eq.	S-bul + e-d + F-bar	1.4	2.6
2D	S-bul + e-d + G-bar	1.2	1.9

Table 41
Best-fit Parameters for the Spheroidal Component of NGC 3414

Work	Model	$R_{\text{e,sph}}$ (arcsec)	n_{sph}
1D maj.	S-bul + e-id + G-r	28.0	4.8
1D eq.	S-bul + e-id + G-r	25.5	4.5
L+10 2D	S-bul + e-d + F-bar	5.0	2.6

Note. L+10 used a model with a large-scale exponential disk; thus, they obtained a smaller bulge effective radius and Sérsic index.

Table 42
Best-fit Parameters for the Spheroidal Component of NGC 3489

Work	Model	$R_{\text{e,sph}}$ (arcsec)	n_{sph}
1D maj.	S-bul + e-d + F-bar	2.2	1.5
1D eq.	S-bul + e-d + F-bar	1.7	1.3
2D	S-bul + e-d + G-bar	1.7	2.1
L+10 2D	S-bul + e-d + F-bar	2.0	2.1
S+11 2D	S-bul + e-d	4.6	1.5

Table 43

Best-fit Parameters for the Spheroidal Component of NGC 3585

Work	Model	$R_{\text{e,sph}}$ (arcsec)	n_{sph}
1D maj.	S-bul + e-id	105.0	5.2
1D eq.	S-bul + e-id	86.3	6.3
S+11 2D	S-bul + e-d	15.5	2.5

Note. S+11 2D obtained smaller estimates of the effective radius and Sérsic index because they included a large-scale disk in their model.

Table 44

Best-fit Parameters for the Spheroidal Component of NGC 3607

Work	Model	$R_{\text{e,sph}}$ (arcsec)	n_{sph}
1D maj.	S-bul + e-id	69.3	5.5
1D eq.	S-bul + e-id	65.5	5.6
2D	S-bul + e-id	60.0	5.3
L+10 2D	S-bul + e-d	6.5	1.5
S+11 2D	S-bul + G-n	44.6	5.0
B+12 2D	S-bul	56.3	4.7

Note. L+10 obtained the smallest estimates of the effective radius and Sérsic index because they included a large-scale disk in their model.

Table 45

Best-fit Parameters for the Spheroidal Component of NGC 3608

Work	Model	$R_{\text{e,sph}}$ (arcsec)	n_{sph}
1D maj.	S-bul	47.5	5.2
1D eq.	S-bul	43.4	5.7
2D	S-bul	62.0	7.0
S+11 2D	S-bul	56.4	6.0
B+12 2D	S-bul	182.2	9.0
R+13 1D eq.	core-Sérsic	56.9	6.3
L+14 2D	S-bul	48.9	6.6

Note. B+12 obtained the largest estimates of the effective radius and Sérsic index, possibly owing to incorrect sky subtraction.

Table 46

Best-fit Parameters for the Spheroidal Component of NGC 3842

Work	Model	$R_{\text{e,sph}}$ (arcsec)	n_{sph}
1D maj.	S-bul + F-l + m-c	100.7	8.1
1D eq.	S-bul + F-l + m-c	73.6	8.2
R+13 1D eq.	core-Sérsic	58.8	6.3

function with $n < 1$ than by a pure exponential model. The inclined, embedded disks of some “elliptical” galaxies were described with Ferrer functions, rather than an $n < 1$ Sérsic function. This choice was partly motivated by the fact that a Sérsic + Ferrer model is less degenerate than a Sérsic + Sérsic model, since the Sérsic profile can assume any concave ($n > 1$) or convex ($n < 1$) curvature, whereas the Ferrer profile can only have a negative curvature as required for an inclined disk.

The presence of large-scale disks, such as those of lenticular and spiral galaxies, was known a priori from the galaxy

Table 47

Best-fit Parameters for the Spheroidal Component of NGC 3998

Work	Model	$R_{\text{e,sph}}$ (arcsec)	n_{sph}
1D maj.	S-bul + e-d + F-bar + F-l + G-n + G-r	5.8	1.2
1D eq.	S-bul + e-d + F-bar + F-l + G-n + G-r	4.8	1.3
L+10 2D	S-bul + e-d + F-bar + F-l	5.0	2.0
S+11 2D	S-bul + e-d + G-bar + G-n	4.7	1.5
B+12 2D	S-bul + e-d	5.7	2.3
L+14 2D	S-bul + trunc. e-d + PSF-n + S-bar + S-id	2.0	1.1

Table 48

Best-fit Parameters for the Spheroidal Component of NGC 4026

Work	Model	$R_{\text{e,sph}}$ (arcsec)	n_{sph}
1D maj.	S-bul + e-d + F-bar + S-id	3.4	2.4
1D eq.	S-bul + e-d + F-bar + S-id	6.3	2.1
S+11 2D	S-bul + e-d	11.4	3.5

Note. S+11 obtained larger estimates of the bulge effective radius and Sérsic index because they did not model the bar.

Table 49

Best-fit Parameters for the Spheroidal Component of NGC 4151

Work	Model	$R_{\text{e,sph}}$ (arcsec)	n_{sph}
1D maj.	S-bul + e-d + S-bar [+ m-n]	7.6	1.4
1D eq.	S-bul + e-d + S-bar [+ m-n]	6.8	1.9
S+11 2D	S-bul + e-d + G-n	5.4	3.5

Table 50

Best-fit Parameters for the Spheroidal Component of NGC 4261

Work	Model	$R_{\text{e,sph}}$ (arcsec)	n_{sph}
1D maj.	S-bul + m-c + F-id	52.6	4.7
1D eq.	S-bul + m-c + F-id	47.3	4.3
2D	S-bul + m-c + e-id	50.4	4.4
GD07 1D maj.	S-bul	88.6	7.3
S+11 2D	S-bul + e-d + G-n	22.6	4.0
V+12 2D	S-bul + m-c	24.2	3.5
B+12 2D	S-bul	48.8	4.3
R+13 1D eq.	core-Sérsic	77.1	6.3
L+14 2D	S-bul + m-c	68.4	6.5

Note. S+11 found the smallest estimate of the effective radius because they added a large-scale disk to their model. V+12 obtained a small estimate of the effective radius because of the limited radial extent of their data.

Table 51

Best-fit Parameters for the Spheroidal Component of NGC 4291

Work	Model	$R_{\text{e,sph}}$ (arcsec)	n_{sph}
1D maj.	S-bul + m-c	15.0	4.2
1D eq.	S-bul + m-c	15.4	5.9
2D	S-bul + m-c	20.8	7.7
GD07 1D maj.	S-bul	14.8	4.0
R+13 1D eq.	core-Sérsic	15.3	5.6
L+14 2D	S-bul + m-c	21.3	8.6

Table 52

Best-fit Parameters for the Spheroidal Component of NGC 4388

Work	Model	$R_{\text{e,sph}}$ (arcsec)	n_{sph}
1D maj.	S-bul + e-d + F-bar + G-n	4.6	0.6
1D eq.	S-bul + e-d + F-bar + G-n	4.2	1.3

Table 53

Best-fit Parameters for the Spheroidal Component of NGC 4459

Work	Model	$R_{\text{e,sph}}$ (arcsec)	n_{sph}
1D maj.	S-bul + e-d + G-n	18.4	3.1
1D eq.	S-bul + e-d + G-n	13.0	2.6
L+10 2D	S-bul + e-d + F-l	7.0	3.0
S+11 2D	S-bul + e-d	10.3	2.5
V+12 2D	S-bul + M-n	25.0	3.9
B+12 2D	S-bul	155.2	7.4

Note. B+12 did not model the large-scale disk and thus overestimated the bulge effective radius and Sérsic index.

Table 54

Best-fit Parameters for the Spheroidal Component of NGC 4473

Work	Model	$R_{\text{e,sph}}$ (arcsec)	n_{sph}
1D maj.	S-bul + e-id + G-n	45.9	2.3
1D eq.	S-bul + e-id + G-n	36.9	2.9
GD07 1D maj.	S-bul	39.6	2.7
S+11 2D	S-bul	49.3	7.0
V+12 2D	S-bul + m-c	21.3	4.3
B+12 2D	S-bul + e-d	10.6	2.2
L+14 2D	S-bul	27.9	5.1

Note. B+12 obtained the smallest estimates of the effective radius and Sérsic index because they included a large-scale disk in their model.

Table 55

Best-fit Parameters for the Spheroidal Component of NGC 4564

Work	Model	$R_{\text{e,sph}}$ (arcsec)	n_{sph}
1D maj.	S-bul + e-d + F-l	5.0	2.6
1D eq.	S-bul + e-d + F-l	6.0	3.0
GD07 1D maj.	S-bul + e-d	4.3	3.2
S+11 2D	S-bul + e-d	25.0	7.0
V+12 2D	S-bul + e-d	3.0	3.7

Note. The most discrepant results are obtained by S+11, although they used the same model as GD07 and V+12.

morphological classification (as listed on NED), although some of them were reclassified by us as having intermediate-scale embedded disks. These were identified in a number of different ways. If highly inclined, they can obviously be spotted from the galaxy image or the unsharp mask. Local maxima in the ellipticity and fourth harmonic profiles can provide footprints of less obvious embedded disks. In particular, the ellipticity profile helps distinguish embedded disks from large-scale disks. Galaxy disks typically have fixed ellipticity, reflecting their inclination to our line of sight. On the other hand, spheroids can have their ellipticities varying with radius, but

Table 56

Best-fit Parameters for the Spheroidal Component of NGC 4596

Work	Model	$R_{\text{e,sph}}$ (arcsec)	n_{sph}
1D maj.	S-bul + e-d + F-bar + G-r + S-id	6.6	2.7
1D eq.	S-bul + e-d + F-bar + G-r + S-id	9.0	3.0
L+10 2D	S-bul + e-d + F-bar + F-l	2.8	1.4
S+11 2D	S-bul + e-d + G-bar	28.0	3.0
V+12 2D	S-bul + e-d + S-bar	13.2	3.6
B+12 2D	S-bul + e-d	44.9	4.4

Note. B+12 fit neither the bar nor the inner disk and obtained the largest estimates of the bulge effective radius and Sérsic index. The models of S+11 and V+12 do not account for the inner disk and thus result in larger estimates of the bulge effective radius.

Table 57

Best-fit Parameters for the Spheroidal Component of NGC 4697

Work	Model	$R_{\text{e,sph}}$ (arcsec)	n_{sph}
1D maj.	S-bul + 2 S-id	239.3	7.2
1D eq.	S-bul + 2 S-id	226.4	6.7
2D	S-bul + e-id	121.4	5.0
GD07 1D maj.	S-bul	—	4.0
S+11 2D	S-bul	100.5	5.0
V+12 (1) 2D	S-bul	39.1	3.8
V+12 (2) 2D	S-bul + e-d	10.0	2.9
L+14 2D	S-bul + e-d + PSF-n + S-halo	6.3	2.1

Note. In both their models, V+12 underestimated the effective radius and the Sérsic index because of the small radial range of their data. In an effort to model the curved light profile, L+14 included a large-scale disk plus a halo and thus underestimated the spheroid effective radius and the Sérsic index.

Table 58

Best-fit Parameters for the Spheroidal Component of NGC 4889

Work	Model	$R_{\text{e,sph}}$ (arcsec)	n_{sph}
1D maj.	S-bul + m-c	119.7	8.1
1D eq.	S-bul + m-c	60.8	6.8
2D	S-bul + m-c	104.3	7.8
R+13 1D eq.	core-Sérsic	169.2	9.8

Table 59

Best-fit Parameters for the Spheroidal Component of NGC 4945

Work	Model	$R_{\text{e,sph}}$ (arcsec)	n_{sph}
1D maj.	S-bul + e-d	13.9	1.4
1D eq.	S-bul + e-d	9.5	1.7
2D	S-bul + e-d	16.2	0.8

they are usually rounder than inclined disks; thus, their average ellipticities are lower than those of inclined disks. If the ellipticity profile of a galaxy increases with radius, this can be ascribed to an inclined disk that becomes progressively more important over the spheroid, whereas a radial decrease of ellipticity signifies the opposite case. Therefore, in a situation where a disk is identified from the galaxy image, but its extent

Table 60

Best-fit Parameters for the Spheroidal Component of NGC 5077

Work	Model	$R_{\text{e,sph}}$ (arcsec)	n_{sph}
1D maj.	S-bul + m-c	23.5	4.2
1D eq.	S-bul + m-c	23.0	5.7
2D	S-bul + m-c	30.5	6.8
S+11 2D	S-bul + G-n	29.2	6.0

Table 61

Best-fit Parameters for the Spheroidal Component of NGC 5128

Work	Model	$R_{\text{e,sph}}$ (arcsec)	n_{sph}
1D maj.	S-bul + e-halo + G-n	61.3	1.2
1D eq.	S-bul + e-halo + G-n	60.8	2.2
S+11 2D	S-bul + e-d + G-n	103.6	3.5

Table 62

Best-fit Parameters for the Spheroidal Component of NGC 5576

Work	Model	$R_{\text{e,sph}}$ (arcsec)	n_{sph}
1D maj.	S-bul	61.5	3.3
1D eq.	S-bul	49.3	3.7
2D	S-bul	45.9	8.3
S+11 2D	S-bul	34.3	7.0
V+12 2D	S-bul	16.9	5.1
B+12 2D	S-bul	77.6	8.7

Note. The results obtained by S+11 and B+12 agree best with the results from our 2D model, in which we did not mask the inner region of the galaxy. The small radial extent of the data used by V+12 led them to underestimate the effective radius.

Table 63

Best-fit Parameters for the Spheroidal Component of NGC 5845

Work	Model	$R_{\text{e,sph}}$ (arcsec)	n_{sph}
1D maj.	S-bul + e-d	3.6	2.5
1D eq.	S-bul + e-d	3.1	2.3
2D	S-bul + e-d	2.8	2.4
GD07 1D maj.	S-bul	4.1	3.2
S+11 2D	S-bul	3.7	3.0
V+12 2D	S-bul	3.5	2.6
B+12 2D	S-bul	4.1	3.5
L+14 2D	S-bul	3.5	2.8

(large or intermediate scale) is ambiguous, the shape of the ellipticity profile can be decisive. Another way to establish the presence of an embedded disk is to look at the velocity map of a galaxy, following the approach of Arnold et al. (2014). A local angular momentum decrease with increasing radius is indicative of an intermediate-scale disk that fades toward larger radii. Savorgnan & Graham (2015a) extensively discuss the topic of galaxies with intermediate-scale disks and show that, when these disks are misclassified and modeled as large-scale disks, the luminosity of the spheroidal component is underestimated, which makes these galaxies falsely appear as

Table 64

Best-fit Parameters for the Spheroidal Component of NGC 5846

Work	Model	$R_{\text{e,sph}}$ (arcsec)	n_{sph}
1D maj.	S-bul + m-c	105.1	6.4
1D eq.	S-bul + m-c	83.4	5.7
2D	S-bul + m-c	85.1	5.2
S+11 2D	S-bul	36.4	3.0
V+12 2D	S-bul + m-c	46.3	3.7
R+13 1D eq.	core-Sérsic	113.2	5.3

Note. S+11 did not mask the core and thus underestimated the effective radius and Sérsic index.

Table 65

Best-fit Parameters for the Spheroidal Component of NGC 6251

Work	Model	$R_{\text{e,sph}}$ (arcsec)	n_{sph}
1D maj.	S-bul + m-c	41.7	6.8
1D eq.	S-bul + m-c	30.1	5.6
2D	S-bul + m-c	39.3	7.1
GD07 1D maj.	S-bul	173.9	11.8
S+11 2D	S-bul + G-n	42.4	7.0
L+14 2D	S-bul	20.6	5.0

Note. It is not clear why GD07 obtained the largest estimates of the effective radius and Sérsic index (possibly the AGN was bright in their R-band image and added to the central cusp).

Table 66

Best-fit Parameters for the Spheroidal Component of NGC 7052

Work	Model	$R_{\text{e,sph}}$ (arcsec)	n_{sph}
1D maj.	S-bul + m-c	59.4	4.2
1D eq.	S-bul + m-c	37.0	5.6
2D	S-bul + m-c	36.2	4.0
GD07 1D maj.	S-bul	70.4	4.6
S+11 2D	S-bul	39.3	5.0
V+12 2D	S-bul + e-d	4.3	1.8
L+14 2D	S-bul	26.6	4.2

Note. The model of V+12 2D includes an artificial large-scale disk and thus results in the lowest estimates of the effective radius and Sérsic index.

Table 67

Best-fit Parameters for the Spheroidal Component of NGC 7619

Work	Model	$R_{\text{e,sph}}$ (arcsec)	n_{sph}
1D maj.	S-bul + e-id	63.2	5.3
1D eq.	S-bul + e-id	58.0	5.2
R+13 1D eq.	core-Sérsic	100.1	9.3

extreme outliers in the black hole mass–spheroid stellar mass diagram.

Bars are usually recognizable from galaxy images and unsharp masks, although local maxima/minima or abrupt changes in the radial profiles of the isophotal parameters can provide additional evidence for less obvious bars. As noted, we were able to successfully fit bars with a Ferrer function (NGC

Table 68
Best-fit Parameters for the Spheroidal Component of NGC 7768

Work	Model	$R_{\text{e,sph}}$ (arcsec)	n_{sph}
1D maj.	S-bul + m-c	92.9	8.4
1D eq.	S-bul + m-c	42.1	6.7
R+13 1D eq.	core-Sérsic	46.1	6.2

Table 69
Best-fit Parameters for the Spheroidal Component of UGC 03789

Work	Model	$R_{\text{e,sph}}$ (arcsec)	n_{sph}
1D maj.	S-bul + e-d + F-bar + G-r	1.8	1.9
1D eq.	S-bul + e-d + F-bar + G-r	2.4	1.4

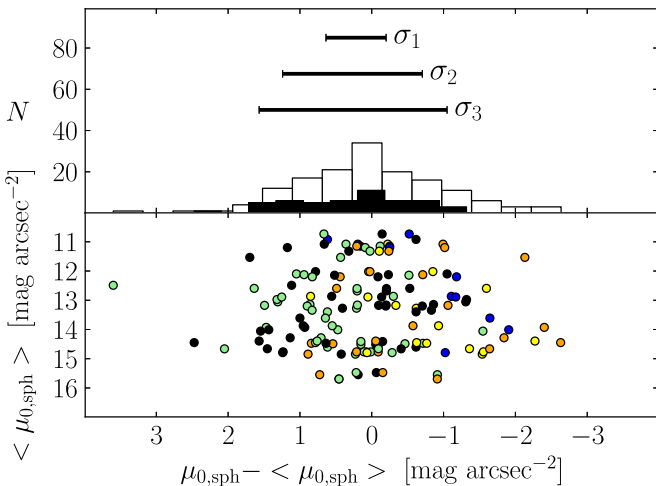


Figure 13. Bottom panel: 49 galaxies for which at least one measurement of the spheroid central surface brightness $\mu_{0,\text{sph}}$ —either in the K band or at $3.6 \mu\text{m}$ —is available from the literature (Table 3), in addition to that measured by us. The K -band magnitudes were converted into $3.6 \mu\text{m}$ magnitudes (see Section 4.2 for details). The average value $\langle \mu_{0,\text{sph}} \rangle$ is plotted against the difference between the individual measurements of a galaxy and the average value for that same galaxy. See Figure 9 for color description and explanation of the top panel.

4151 is the only case for which we described the bar with an $n \sim 0.2$ Sérsic model). Disk-like components embedded in the bulges of spiral galaxies were described with an $n \lesssim 1$ Sérsic model or, in a few cases, with a Ferrer function.¹⁵ This approach is similar to that of Laurikainen et al. (2010), who fit bars with a Ferrer function and inner disks with a Sérsic model. Given that our galaxy sample lacks “late-type spiral” galaxies, it is not surprising (Gadotti & de Souza 2006) that we did not find bars with exponential profiles (e.g., Elmegreen & Elmegreen 1985; Gadotti 2008; Kim et al. 2015). The bars in our sample were found to have rather flat inner profiles, as is commonly found for bars in “early-type spiral” galaxies (Gadotti & de Souza 2006).

The presence of a nuclear component—either resolved or unresolved—was generally expected in (but not restricted to) galaxies that host an optical AGN and circumnuclear dust.

¹⁵ One advantage of choosing a Ferrer function over a Sérsic profile to fit a disk-like component embedded in the bulge is to reduce degeneracies with the Sérsic profile that describes the bulge.

Nuclear stellar disks and nuclear star clusters fall into the category of nuclear components too, but their identification can be more subtle than for AGNs. Nuclear clusters have typical sizes of a few parsecs; therefore, for the majority of our galaxies they are unresolved in *Spitzer*/IRAC $3.6 \mu\text{m}$ observations. If an identification from high-resolution observations was available from the literature, we relied on that; otherwise, we concluded that a galaxy was nucleated from an excess of nuclear light in the residuals of the fit.¹⁶ Unresolved nuclear components were fit with our optimal Moffat PSF, whereas resolved nuclear components were modeled with (PSF-convolved) narrow Gaussian functions (for a discussion of the importance of fitting nuclear components, see Wadadekar et al. 1999; Ravindranath et al. 2001; Peng et al. 2002; Gadotti 2008). Rings were identified from galaxy images and unsharp masks and modeled with symmetric Gaussian ring profiles (e.g., Sheth et al. 2010; Kim et al. 2014).

As an illustration, we consider the galaxy NGC 2974, a spiral galaxy that has been misclassified as an elliptical galaxy in the RC3 catalog (de Vaucouleurs et al. 1991). This galaxy hosts a Seyfert AGN (Véron-Cetty & Véron 2006) and filamentary dust in its center (Tran et al. 2001). NGC 2974 is classified as a fast rotator by the ATLAS^{3D} survey, and indeed the velocity map obtained by the SLUGGS survey shows that the galaxy kinematics is rotation dominated well beyond three effective radii ($R > 150''$), as expected from a large-scale disk. From an inspection of the unsharp mask, we identified a ring at $R \sim 50''$, which might be a residual of two tightly wound spiral arms, and an elongated bar-like component within $R \lesssim 30''$, which is in addition to the more spherical bulge and produces a peak in the ellipticity and position angle profiles at $R \sim 20''$. Our 1D galaxy decomposition for NGC 2974 (Figure 4) consists of a Sérsic bulge, an exponential large-scale disk, a Ferrer bar, a Gaussian nuclear component (AGN), and a Gaussian ring. Although the ring is extremely faint, it is important to account for it in the galaxy decomposition. A model without the ring component results in a “steeper” exponential profile for the disk (i.e., the exponential model has a smaller scale length and a brighter central surface brightness) and produces bad residual structures within $R \lesssim 40''$. Our best-fit model returns a $3.6 \mu\text{m}$ bulge major-axis effective radius $R_{\text{e,sph}}^{\text{maj}} = 8.3$ arcsec, equivalent-axis Sérsic index $n_{\text{sph}}^{\text{eq}} = 1.2$, and apparent magnitude $m_{\text{sph}} = 8.65$ mag. Sani et al. (2011) modeled NGC 2974 with a Sérsic bulge and a Gaussian nuclear component (AGN), but did not account for the large-scale disk. From their best-fit 2D model, they obtained a three times larger $3.6 \mu\text{m}$ bulge major-axis effective radius ($R_{\text{e,sph}}^{\text{maj}} = 27.2$ arcsec), a 2.5 times larger Sérsic index ($n_{\text{sph}} = 3$), and a significantly brighter apparent magnitude ($m_{\text{sph}} = 7.28$ mag).

3.6. 2D Fits

2D decompositions were carried out using the software IMFIT (Erwin 2015). For each galaxy, we built a 2D model that was consistent with the corresponding 1D model in terms of

¹⁶ This conclusion was drawn after going through the following steps. First we identified all the subcomponents of a galaxy (assuming that the galaxy was not nucleated), built a model accordingly, and fit it to the data. If the residuals of the fit showed a nuclear light excess, we repeated the fit by excluding the data points within the nuclear region. Only after checking that the outcome of the last fit was consistent with a fit that included a small nuclear component did we infer the presence of a stellar nuclear component.

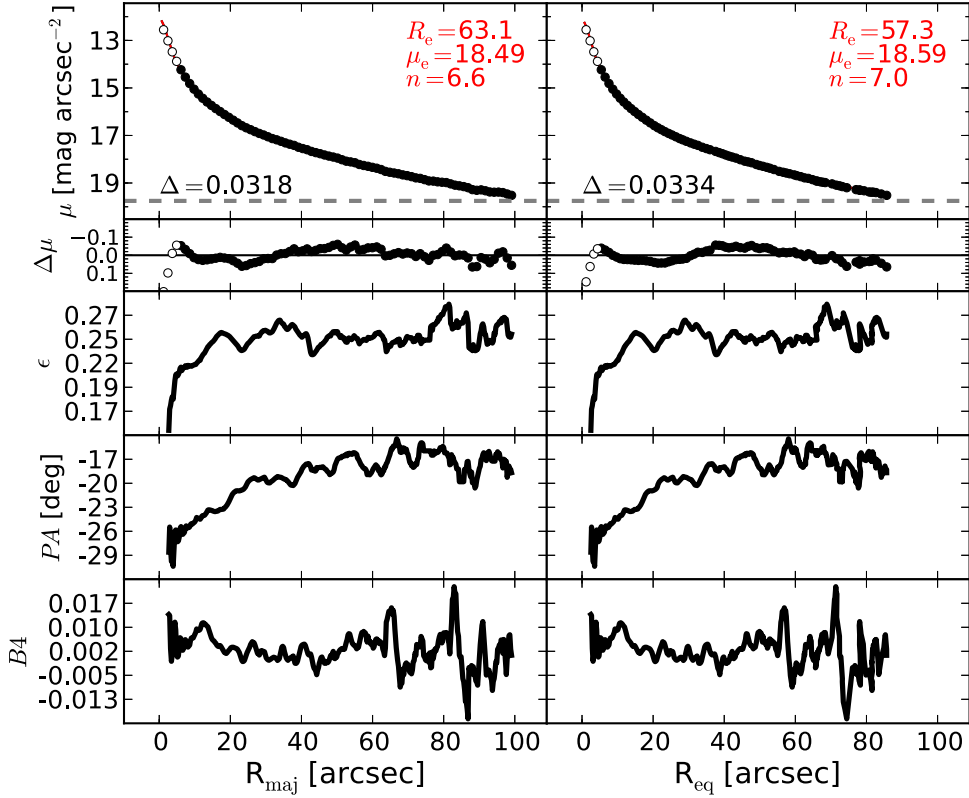


Figure 14. IC 1459: an elliptical galaxy with a fast counterrotating stellar component (Franx & Illingworth 1988; Cappellari et al. 2002), nuclear dust, and indications of a nuclear stellar disk (Forbes et al. 1994). The kinematically decoupled component cannot be identified as a separate structure in photometric observations. This galaxy also has an unresolved partially depleted core (Rusli et al. 2013a). Our isophotal analysis confirms a simple morphology for IC 1459, with no evident embedded components. After masking the innermost $6''$, we fit this galaxy with a Sérsic profile.

number and type of components. The only difference between our 1D and 2D models pertains to the description of bars: because the Ferrer profile is not made available in IMFIT, bars were fit with a 2D Gaussian function.

The 2D decomposition of NGC 2974 is presented in Figure 5. The galaxy was modeled with a Sérsic bulge, an exponential disk, and a Gaussian bar. The nuclear component was masked, and the ring was not modeled.¹⁷ Our best-fit 2D model returns a bulge major-axis effective radius $R_{\text{e,sph}}^{\text{maj}} = 10.5$ arcsec, a bulge Sérsic index $n_{\text{sph}} = 1.3$, and a $3.6 \mu\text{m}$ bulge apparent magnitude $m_{\text{sph}} = 8.39$ mag, in fairly good agreement with our 1D decomposition. Fits and descriptions for the other galaxies are available online.

4. RESULTS

For each galaxy, after we identified its various components and built a model accordingly, we simultaneously performed a set of four 1D fits. All four fits use a Moffat-convolved model. Two fits use the major-axis surface brightness profile, and the remaining two use the equivalent-axis surface brightness profile. For each of these pairs, we use a logarithmically sampled surface brightness profile and a linearly sampled surface brightness profile. Because our fitting routine intentionally does not employ an error-weighting scheme on the data

points that constitute the surface brightness profile, a fit to a logarithmically sampled profile puts more weight on the inner region of the galaxy and poorly constrains the outskirts. On the other hand, a fit to a linearly sampled surface brightness profile equally treats inner and outer regions, but is more susceptible to sky-background subtraction issues.

We found that the fits are, in general, more sensitive to the choice of the initial parameters when using logarithmically sampled profiles than linearly sampled profiles. In addition, a visual examination of the residuals revealed that the quality of the fit within one galaxy effective radius is superior when tighter constraints are put on the galaxy outskirts. In other words, the better quality of the residuals led us to prefer the fits that use linearly sampled surface brightness profiles, although the results were usually very similar, as might be expected.

Among the initial sample of 75 galaxies, we did not attempt to model three galaxies: M32, NGC 4486A, and the Circinus galaxy. The first two have been stripped by their massive companions and thus have uncertain morphology. The Circinus galaxy lies at only 4° from the Galactic plane; therefore, its image mosaic is contaminated by a large number of foreground stars. Of the remaining 72 galaxies, we obtained satisfactory 1D decompositions for 66, whereas the models of 6 galaxies were judged not reliable and were thus excluded. We also performed reliable 2D decompositions for 31 galaxies.

A galaxy-by-galaxy comparison between our best-fit models and those from the previous literature helped identify the optimal decompositions and past problems. We compared our best-fit models with those of Graham & Driver (2007a), Sani et al. (2011), Beifiori et al. (2012), Vika et al. (2012), and Läsker et al.

¹⁷ We built the 2D model first including and then omitting a Gaussian ring component, but both models converged to the same solution, i.e., the fit “ignored” the presence of the faint ring. This did not happen in the 1D decomposition because of the different weighting scheme used by the fitting routines.

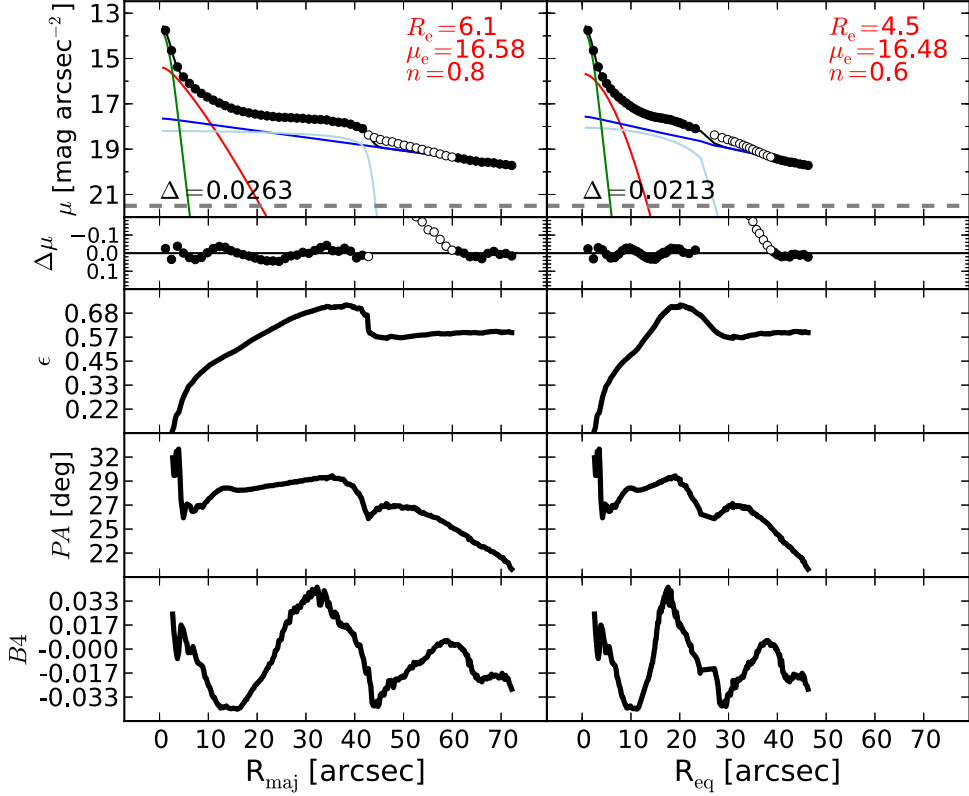


Figure 15. IC 2560: a barred spiral galaxy with a Seyfert AGN (Véron-Cetty & Véron 2006) and dust within the central $2''.5$ (Martini et al. 2003). A visual inspection of the image of IC 2560 reveals a boxy bulge and a large-scale bar that extends out to $R_{\text{maj}} \lesssim 43''$. The disk appears to be slightly lopsided along the direction of the bar, owing to two nonsymmetric ansae, but it becomes symmetric beyond $R_{\text{maj}} \gtrsim 60''$. This is why the surface brightness profile deviates from a perfect exponential in the radial range $42'' \lesssim R_{\text{maj}} \lesssim 60''$, which is excluded from the fit. Motivated by the presence of a strong optical AGN and dust in the nucleus (which adds rather than obscures at $3.6 \mu\text{m}$), we account for an excess of nonstellar light by adding a central Gaussian component to the model.

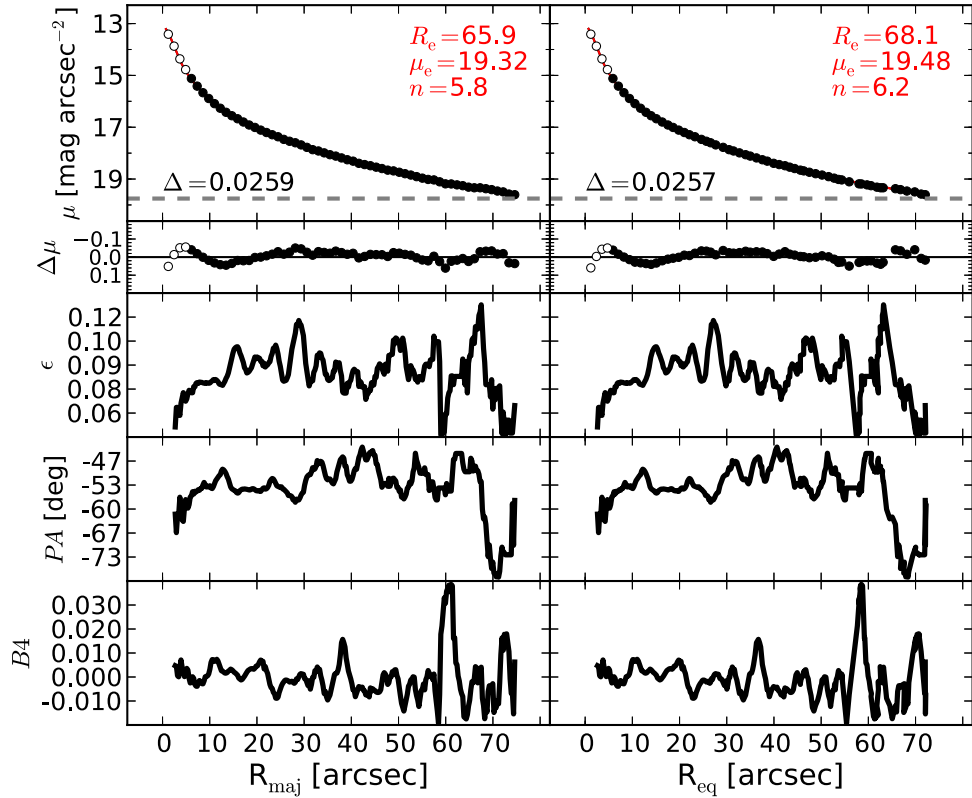


Figure 16. IC 4296: an elliptical galaxy. Owing to its high stellar velocity dispersion, this galaxy is expected to host a partially depleted core. After masking the innermost $6''.1$, we find that a single Sérsic profile provides a good description of this galaxy.

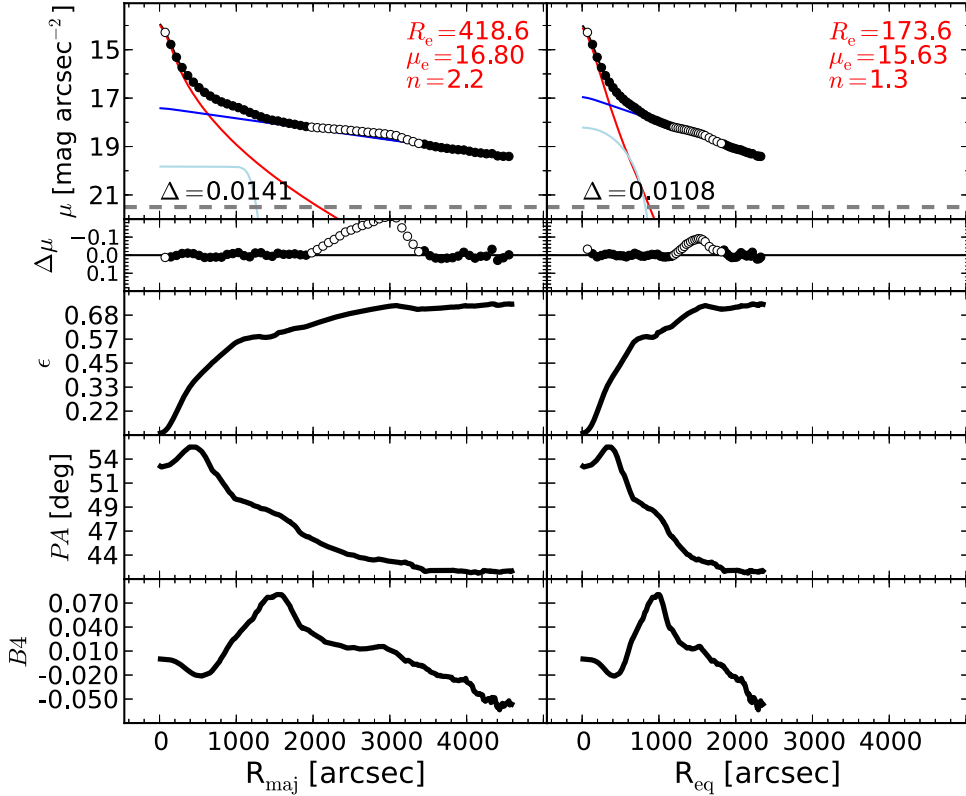


Figure 17. M31 (Andromeda galaxy): a spiral galaxy. Although for decades this galaxy had been classified as an unbarred spiral, recent works have revealed the presence of a bar (Athanioula & Beaton 2006; Beaton et al. 2007; Morrison et al. 2011), seen as the plateau at $800'' \lesssim R_{\text{maj}} \lesssim 1000''$. M31 also features a broad ring-like structure at $R_{\text{maj}} \sim 50'$ (Athanioula & Beaton 2006). We applied the *smoothing* technique described in Section 3.4 to the analysis of M31. The region $2000'' \lesssim R_{\text{maj}} \lesssim 3400''$, where the pseudoring is observed, is excluded from the fit. A Sérsic + exponential fit is not adequate to describe the light profile of M31, as the residuals of such a fit display a structure in correspondence of the bar ($R_{\text{maj}} \lesssim 1500''$). The addition of a Ferrer function to account for the bar notably improves the fit.

(2014a). We also considered the best-fit models of Laurikainen et al. (2010) and Rusli et al. (2013a) because, although they did not specifically deal with black hole—galaxy scaling relations, their galaxy samples significantly overlap with ours.

Table 2 lists the results from both the 1D and 2D fits.

4.1. 1D versus 2D Decompositions

Here we explore how 1D and 2D decompositions compare with each other. Readers not interested in our practical knowledge, having dealt with 1D and 2D techniques of galaxy modeling at the same time, can skip to Section 4.2. We summarize our experience in the following points.

1. A visual inspection of galaxy images and their unsharp masks is often not sufficient to accurately identify all of a galaxy’s components. Weak bars and some embedded disks can easily be missed. Other (inclined) embedded disks can be confused with large-scale disks. In this regard, the 1D isophotal analysis is extremely helpful. Local minima/maxima or abrupt changes in the ellipticity, position angle, and fourth harmonic profiles contain precious information about a galaxy’s constituents.
2. The ellipticity and position angle of triaxial spheroids can vary with radius. The analytic functions used by 2D decomposition codes to fit galaxy components have fixed ellipticity and position angle; thus, they cannot account for these radial gradients. This problem is overcome with 1D decomposition techniques because the ellipticity and

additionally the deviations from elliptical isophotes are efficiently included in the equivalent-axis fit (see the Appendix of Ciambur 2015).

3. The interpretation of the residual surface brightness profile is often crucial to identify the optimal decomposition for a galaxy. In our experience, we found that interpreting 1D residuals was easier and more productive than 2D residuals.

Although we attempted 2D modeling for the 72 galaxies in our sample, more than half of the 2D decompositions were not successful or did not converge to a meaningful solution. This should serve as a tip to users of 2D fitting codes. When physically meaningful spheroid parameters are required, the output may not be reliable and should be inspected. For the 31 galaxies that had successful 2D decompositions, we compare with their 1D parameters in Figures 6–8. The agreement between 1D and 2D effective radii and magnitudes is remarkable, whereas a larger amount of scatter in the Sérsic indices can be caused by the fact that 2D measurements do not exactly correspond to 1D equivalent-axis measurements. No systematic effects are observed in any of these three plots, which indicates that 1D and 2D techniques of galaxy modeling—when performed on the same galaxy—can give consistent results.

In conclusion, since we found that the best-fit parameters do not depend on the decomposition method (1D or 2D) used, and given that we obtained more successful 1D decompositions than 2D, we will base our analysis on the results from the 1D fits.

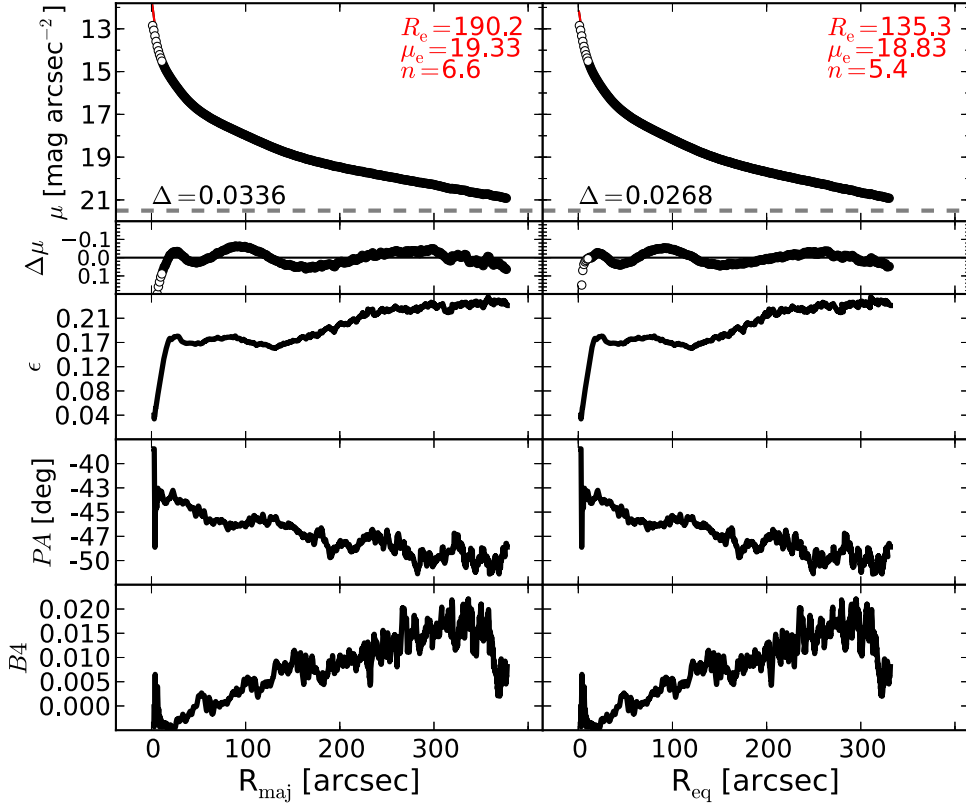


Figure 18. M49: the brightest member of the Virgo Cluster, a giant elliptical galaxy with a slightly resolved partially depleted core (Rusli et al. 2013a). The data within the innermost $12''$ are excluded from the fit. We fit M49 with a single Sérsic profile.

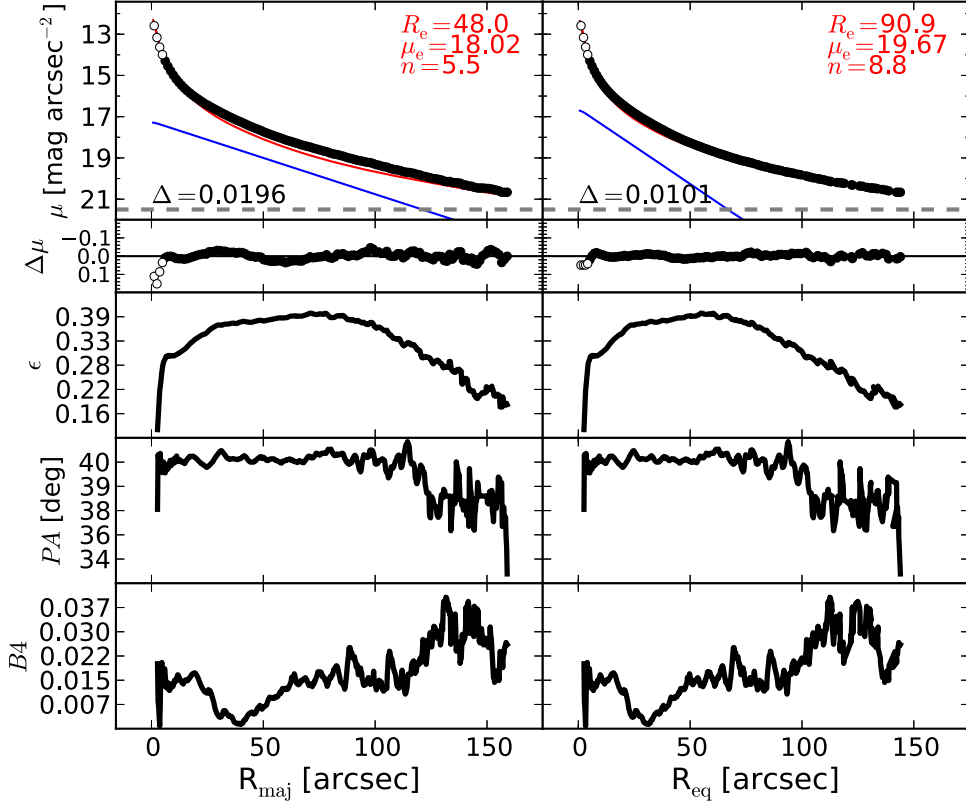


Figure 19. M59: an elliptical galaxy with an edge-on, intermediate-scale embedded disk (Scorza & Bender 1995) and a thin, faint nuclear stellar disk (Ferrarese et al. 2006; Ledo et al. 2010). The intermediate-scale embedded disk is clearly visible in our unsharp mask image (not shown), and the velocity map (ATLAS 3D) confirms the presence of this rapidly rotating component, which is modeled with an exponential function. We choose not to account for the nuclear stellar disk by excluding the innermost $6.''1$ from the fit.

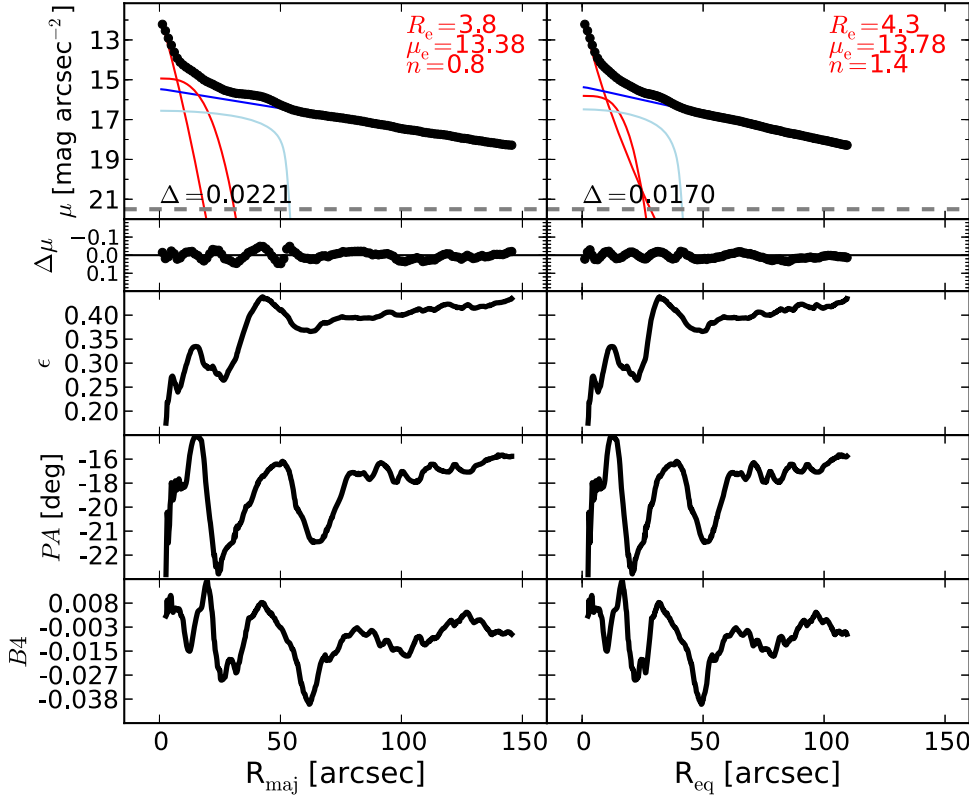


Figure 20. M64: a dusty spiral galaxy with a Seyfert AGN (Véron-Cetty & Véron 2006). A large-scale bar ($R_{\text{maj}} \lesssim 50''$) can be identified in the unsharp mask and produces corresponding peaks in the ellipticity, PA, and $B4$ profiles. This is modeled with a Ferrer function. Additional peaks in the ellipticity, PA, and $B4$ profiles at $R_{\text{maj}} \sim 15''$ signal the presence of an embedded disk component, which we describe with a low- n Sérsic function. Although the galaxy is dusty and hosts an AGN, we do not observe any nuclear excess of light in the fit residuals, and therefore we found it unnecessary to add a nuclear component to our model.

4.2. Parameter Uncertainty

Estimating the uncertainties associated with the best-fit parameters of our 1D galaxy decompositions is not straightforward. Monte Carlo simulations could be used for this purpose, but they would take into account only random errors and not unknown systematic errors. Systematic errors include incorrect sky subtraction, inaccurate masking of contaminating sources, imprecise description of the PSF, erroneous choice of model components (for example, when failing to identify a galaxy subcomponent and thus omitting it in the model, or when describing a galaxy subcomponent with an inadequate function), the radial extent of the surface brightness profile, and its sampling. These factors are not included in popular 2D fitting codes, which report only the random errors associated with their fitted parameters. Moreover, when performing multi-component decomposition of high-S/N images of nearby—and therefore well-resolved—galaxies, errors are dominated by systematics rather than Poisson noise. For this reason, we decided to estimate the uncertainties of the spheroid best-fit parameters with a method that took into account systematic errors.

4.2.1. Goodness of the Spheroid Modeling

For each of our fits, we calculated the associated rms scatter using

$$\Delta = \sqrt{\frac{\sum_{i=0}^N (\mu_i^{\text{obs}} - \mu_i^{\text{mod}})^2}{N_{\text{dof}}}}, \quad (2)$$

where N_{dof} is the number of degrees of freedom, μ_i^{obs} is the observed surface brightness, and μ_i^{mod} is the model surface brightness at each data point i . Although useful to evaluate the overall quality of a galaxy decomposition, the rms scatter alone cannot be used to assess the goodness of the fit for the spheroidal component only, unless the galaxy is a pure spheroid and has consequently been modeled with a single Sérsic profile. To illustrate this point with an example, one can imagine a situation in which a galaxy is thought to be made of a small bulge and a much more extended disk. This galaxy is decomposed with a Sérsic + exponential model. The exponential function provides an excellent description of the light profile of the disk, whereas the Sérsic function does not do the same for the bulge. The residuals of the fit will then be flat and close to zero at large radii, where the emission of the disk dominates over that of the bulge, while they will display significant departures at small radii, in correspondence with the poorly fit spheroidal component. In the case of linear sampling, because the part of the surface brightness profile pertaining to the disk may contain more data points than the part pertaining to the bulge, the global rms scatter will be relatively small, but it obviously will not reflect the accuracy of the fit to the spheroidal component only.

A simple but powerful way to get a feeling of how precisely the global model and its spheroidal component have fared is to look at the major- and equivalent-axis fits of each galaxy and visually inspect the structures of the residual surface brightness profile (i.e., the second row in Figure 4) within $\sim 1\text{--}2$ spheroid

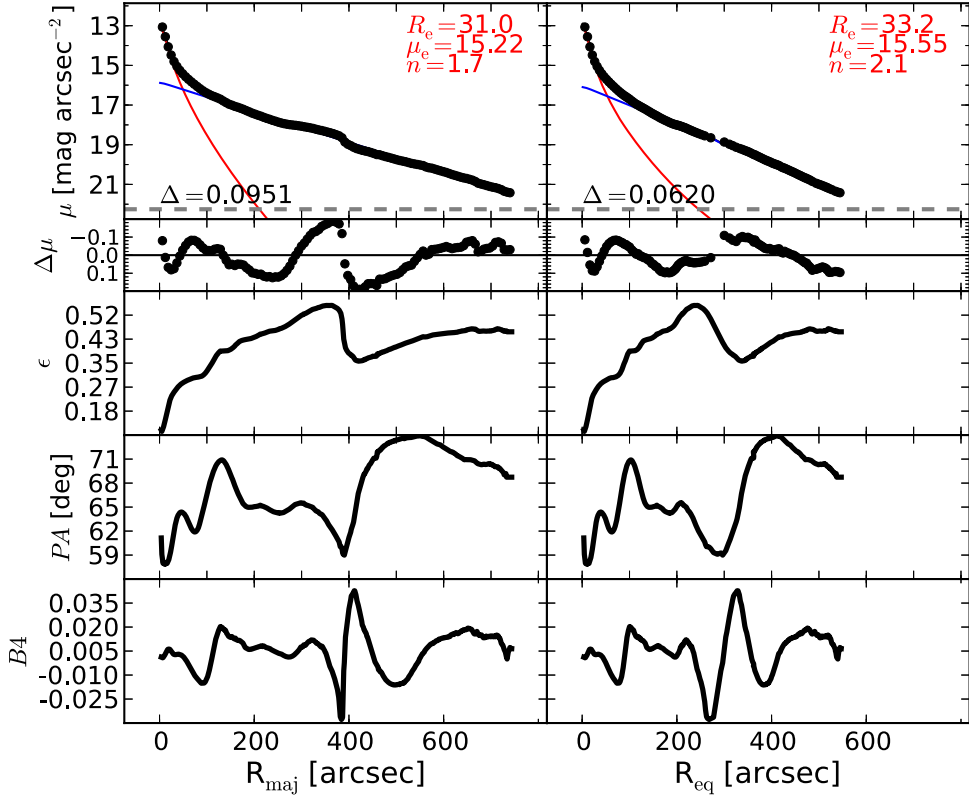


Figure 21. M81: an early-type spiral galaxy. This galaxy features a nuclear bar at $R_{\text{maj}} \lesssim 17''$ and a large-scale bar at $R_{\text{maj}} \lesssim 130''$ (Elmegreen et al. 1995; Gutiérrez et al. 2011; Erwin & Debattista 2013). We applied the smoothing technique described in Section 3.4 to the analysis of M81. The bars are not particularly evident in the galaxy image or in the unsharp mask. The bump at $R_{\text{maj}} \lesssim 400''$ is due to spiral arms. Attempts to account for the bars in the fit were unsuccessful. For this reason, we use a simple Sérsic + exponential model.

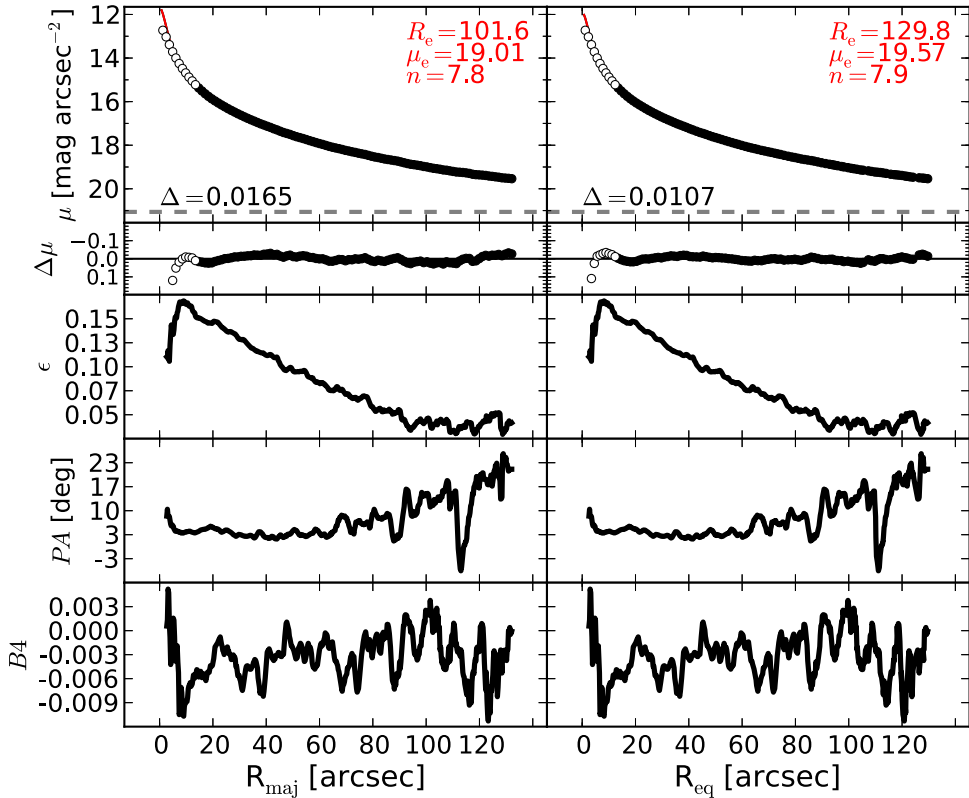


Figure 22. M84: an elliptical galaxy with a slightly resolved partially depleted core (Rusli et al. 2013a). The unsharp mask reveals a faint inner component ($R_{\text{maj}} \lesssim 12''$). We exclude the data within $R_{\text{maj}} < 13.8''$ and model the galaxy with a Sérsic profile.

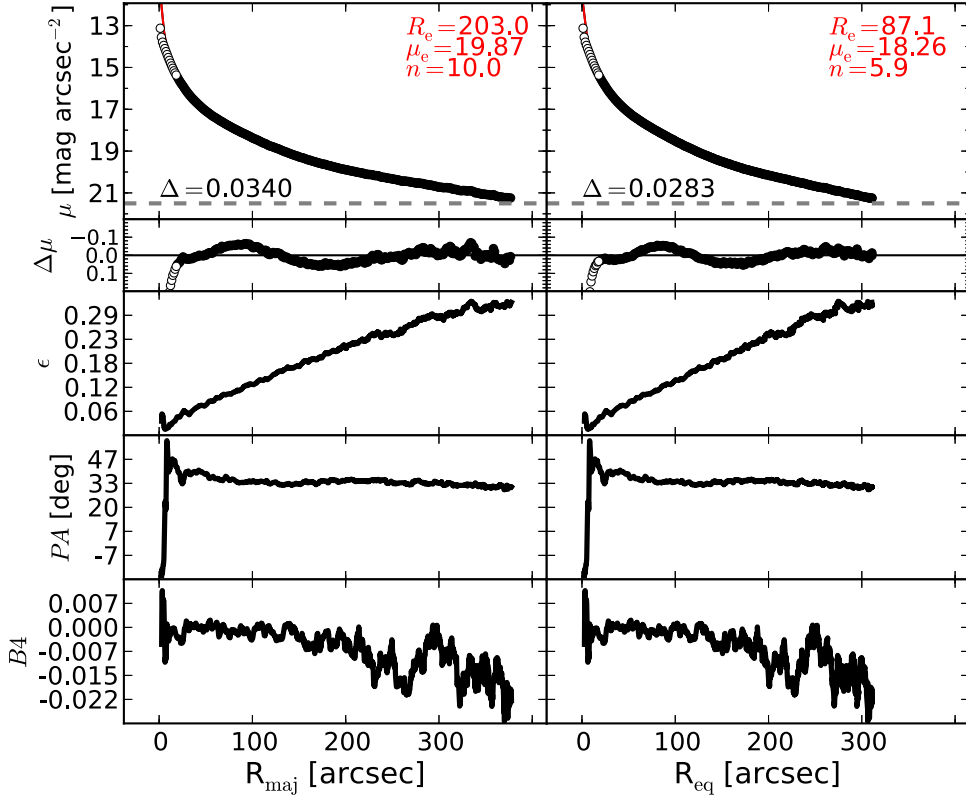


Figure 23. M87: a giant elliptical galaxy belonging to the Virgo Cluster. This galaxy has a large ($>7''$), partially depleted core (Ferrarese et al. 2006). The morphology of M87 is similar to that of M49. The innermost $18''$ are excluded, and a Sérsic model is used to fit M87. We note that the effective radius obtained from our 1D major-axis fit is more than a factor of two larger than that obtained from our 2D fit. This is due to the fact that the 2D model has fixed ellipticity and cannot account for the strong ellipticity gradient of the galaxy, which serves as a warning to some 2D fits in the literature.

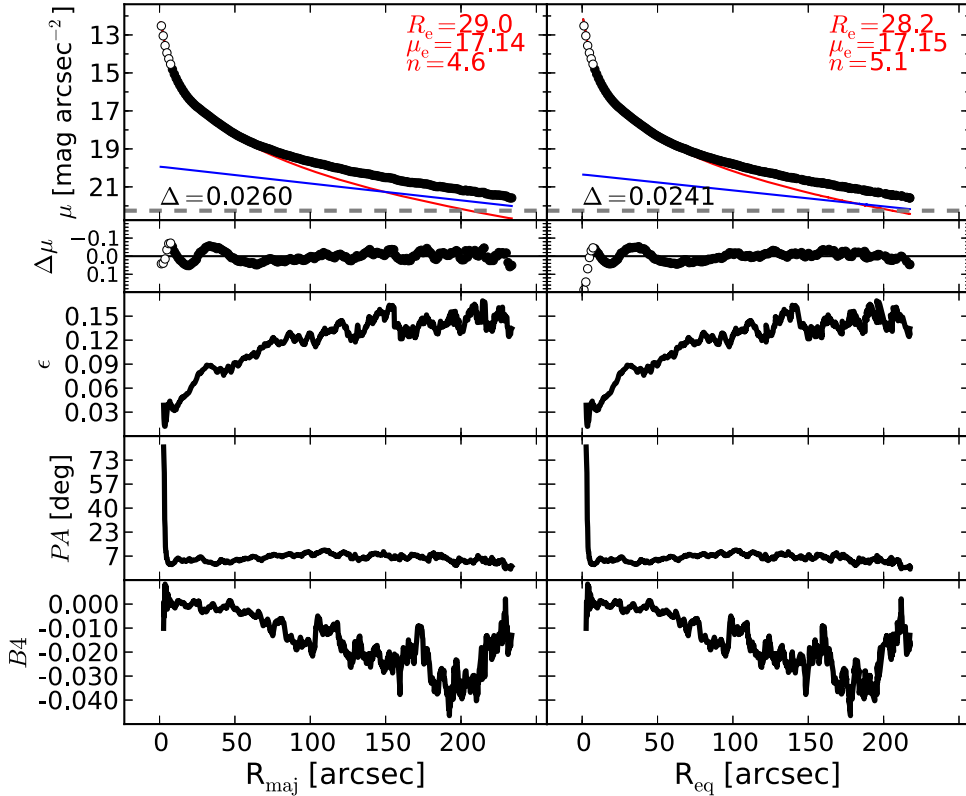


Figure 24. M89: an elliptical galaxy with an unresolved partially depleted core (Rusli et al. 2013a). The galaxy halo dominates the light at large radii, where the isophotes are significantly more elliptical than in the inner part of the galaxy. The halo is modeled with an exponential function.

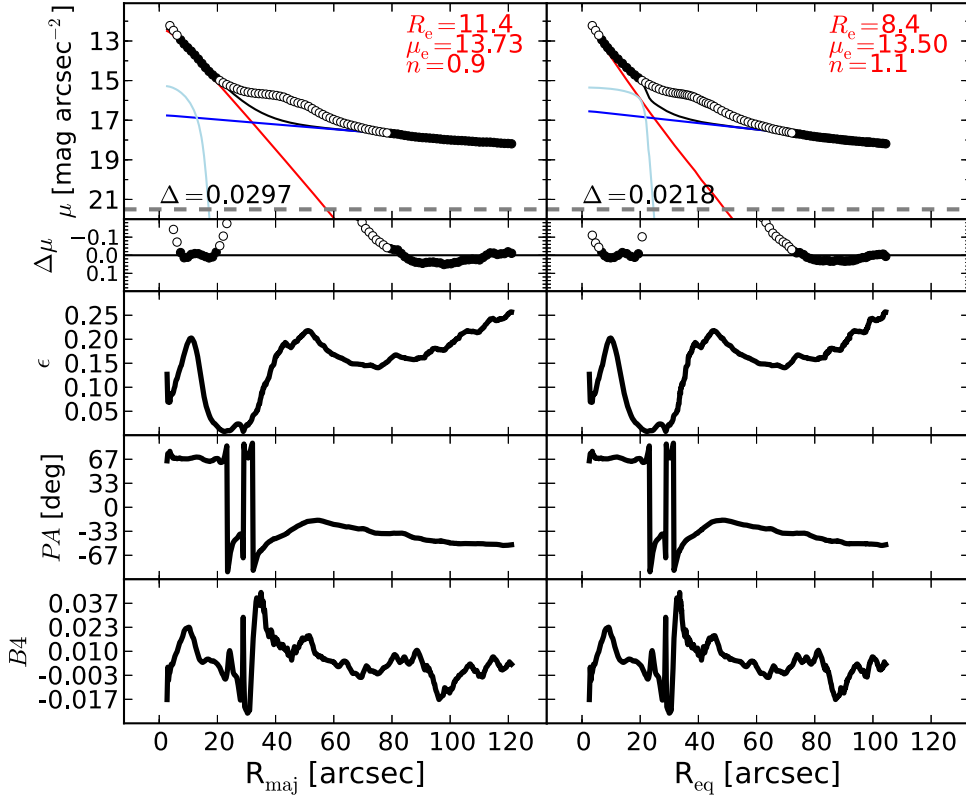


Figure 25. M94: a face-on spiral galaxy, with a Seyfert AGN (Véron-Cetty & Véron 2006) and circumnuclear dust (Elmegreen et al. 2002; Peebles & Martini 2006). This galaxy has a ring-like structure at $R_{\text{maj}} \sim 50''$ (Muñoz-Tunón et al. 1989). The ellipticity and $B4$ profiles display a local maximum at $R_{\text{maj}} \sim 10''$, indicating the presence of a disky component embedded in the bulge, as already noted by Fisher & Drory (2010). We model this component with a Ferrer function. We exclude the data within the innermost $6''/7$, owing to the AGN contribution. Attempts to model the ring were unsuccessful, resulting in a degenerate model; therefore, we exclude the data in the range $20'' \lesssim R_{\text{maj}} \lesssim 80''$.

effective radii. We did this using a grade from 1 to 3, assigned according to the following criteria.

1. A grade of 1 was given to the best fits, i.e., fits that do not exhibit any of the problems listed below.
2. A grade of 2 was issued in the following cases: the residuals in correspondence with the radial extent of the spheroidal component are not randomly distributed around zero, being symptomatic of a Sérsic model having a curvature (regulated by the Sérsic index n) that does not quite match the real “shape” of the spheroid; when we identified but were not able to model a galaxy subcomponent with the same accuracy dedicated to the other components; in the case of apparent inconsistencies between the model and the observed galaxy properties (e.g., an embedded disk modeled with an exponential function, whose scale length does not quite match the size of the disk as expected from the ellipticity profile or the velocity map); and when the Sérsic model used to describe the spheroidal component has a size—as measured by the effective radius—comparable to a few times the FWHM of the PSF. Galaxies in this category are reasonably well fit despite these issues.
3. A grade of 3 was assigned to the poorer and more anomalous fits, or those affected by an obvious degeneracy between the spheroid Sérsic profile and the remaining model components (e.g., when the spheroid Sérsic index varies by as much as 50% among the four different realizations of the fit, or when the output of

the fit strongly depends on the choice of the initial parameters).

As a result, we classified 27 galaxies (38% of the 72 galaxies for which we attempted a 1D decomposition) with grade 1, 29 galaxies (40%) with grade 2, and 10 galaxies (14%) with grade 3. Six galaxies could not be modeled. We report the assigned grades in Table 2 (column 10).

4.2.2. Uncertainties on n_{sph}

In Figure 9, for 58 galaxies, we compare the measurements of the spheroid Sérsic index obtained by different authors with those obtained by us. For each galaxy, we computed the average value $\langle \log(n_{\text{sph}}) \rangle$ of the available measurements, and we plot it against the scatter of the individual measurements around each spheroid’s $\langle \log(n_{\text{sph}}) \rangle$. The measurements are heterogeneous, in the sense that they were obtained from 1D or 2D decompositions of data in different wavelengths, and they refer either to the major axis, the equivalent axis, or some 2D average. In Figure 9, the black histogram shows the distribution of the scatter around $\langle \log(n_{\text{sph}}) \rangle$ for our measurements; 38% of this distribution lies within $-\sigma_1^- = -0.08$ dex and $+\sigma_1^+ = +0.06$ dex, 78% lies within $-\sigma_2^- = -0.21$ dex and $+\sigma_2^+ = +0.17$ dex, and 92% lies within $-\sigma_3^- = -0.25$ dex and $+\sigma_3^+ = +0.25$ dex. We elect to use $\pm\sigma_1^\pm$, $\pm\sigma_2^\pm$, and $\pm\sigma_3^\pm$ as 1σ uncertainties for our measurements of $\log(n_{\text{sph}})$ obtained from “grade 1,” “grade 2,” and “grade 3” fits, respectively. This means that if the fit to a galaxy was classified as “grade 1,” the (logarithmic) value of the spheroid Sérsic

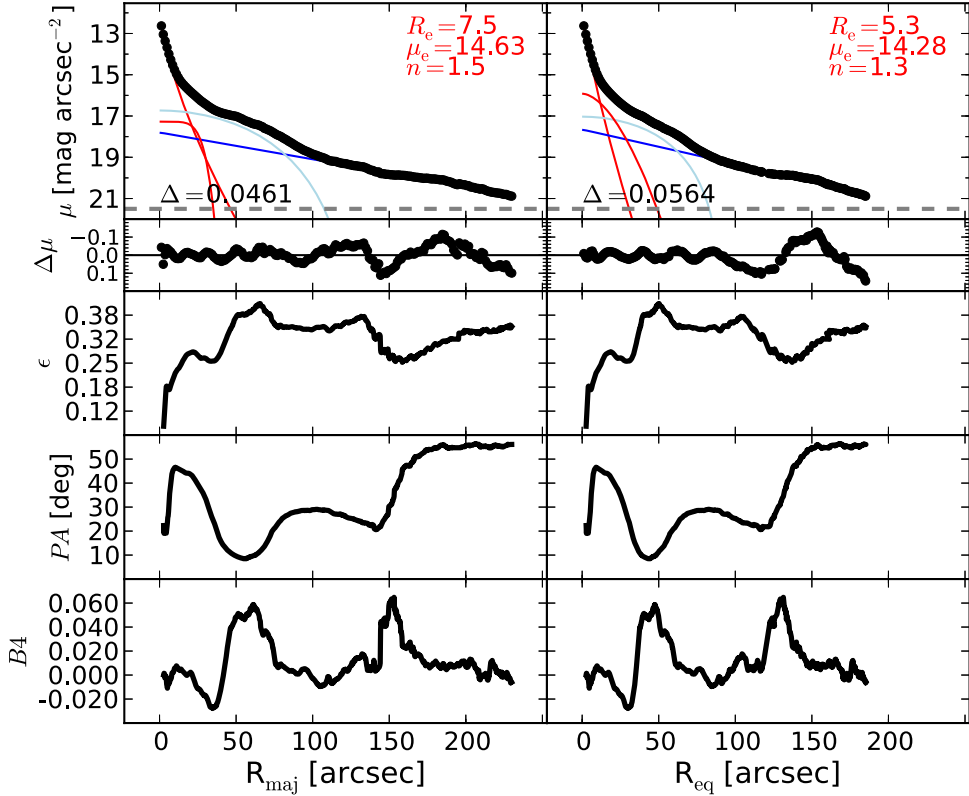


Figure 26. M96: a spiral galaxy with a large-scale bar and no AGN activity (Martini et al. 2003; Nowak et al. 2010). Erwin (2004) observed the presence of two bars in this galaxy. Nowak et al. (2010) reported the presence of a large pseudobulge and a tiny classical bulge ($R_{e,\text{sph}} = 1''.6$, $n_{\text{sph}} = 2.3$). However, they came to this conclusion by modeling only the innermost $8''/5$ of the light profile of M96 with a Sérsic-classical bulge and an exponential pseudobulge, but without subtracting the contribution of the large-scale disk and the large-scale bar. They also acknowledged the presence of a secondary inner bar, but did not include it in their fit. M96 has a complex morphology. The large-scale disk does not exhibit a perfect exponential profile, mainly because of wound spiral arms resembling a ring ($R_{\text{maj}} \sim 185''$), which however, are too faint and irregular to be described with a Gaussian ring model. The large-scale bar extends out to $R_{\text{maj}} \lesssim 80''$ and is modeled with a Ferrer function. A peak at $R_{\text{maj}} \sim 25''$ in the ellipticity profile reveals an inner disk component embedded in the bulge, which we model with a low- n Sérsic profile.

index \tilde{n}_{sph} and associated uncertainties would be $\log(\tilde{n}_{\text{sph}})^{+\sigma_1^+}_{-\sigma_1^-} = \log(\tilde{n}_{\text{sph}})^{+0.06}_{-0.08}$; if the fit to that galaxy was classified as “grade 2,” then one would have $\log(\tilde{n}_{\text{sph}})^{+\sigma_2^+}_{-\sigma_2^-} = \log(\tilde{n}_{\text{sph}})^{+0.17}_{-0.21}$; and so on.

4.2.3. Uncertainties on $R_{e,\text{sph}}$

The uncertainties on the spheroid effective radii were computed using the same methodology as employed for the Sérsic indices. However, in Figure 10 we include only major-axis measurements of $R_{e,\text{sph}}$. The associated 1σ uncertainties for our measurements of $\log(R_{e,\text{sph}})$ are $-\sigma_1^- = -0.11$ dex and $+\sigma_1^+ = +0.07$ dex, $-\sigma_2^- = -0.30$ dex and $+\sigma_2^+ = +0.32$ dex, and $-\sigma_3^- = -0.39$ dex and $+\sigma_3^+ = +0.42$ dex.

4.2.4. Uncertainties on m_{sph}

To estimate the uncertainties on the spheroid magnitudes, we compared (see Figure 11) only those literature measurements coming from K -band or $3.6\mu\text{m}$ observations. To do this, the $3.6\mu\text{m}$ magnitudes were converted into K -band magnitudes by applying an additive factor of 0.27 mag, which was estimated using the stellar population models of Worthey (1994), assuming a 13 Gyr old single-burst stellar population with solar metallicity. The associated 1σ uncertainties for our measurements of m_{sph} are $-\sigma_1^- = -0.11$ mag and $+\sigma_1^+ =$

+0.18 mag, $-\sigma_2^- = -0.58$ mag and $+\sigma_2^+ = +0.66$ mag, and $-\sigma_3^- = -0.66$ mag and $+\sigma_3^+ = +0.88$ mag.

4.2.5. Uncertainties on $\mu_{e,\text{sph}}$

As for the spheroid magnitudes, we estimated the uncertainties on the spheroid effective surface brightnesses $\mu_{e,\text{sph}}$ by comparing only K -band or $3.6\mu\text{m}$ measurements (see Figure 12) and accounting for the mean color difference of 0.27 mag. Not explicitly reported in the literature, effective surface brightnesses were calculated by us using

$$\begin{aligned} \mu_{e,\text{sph}} = m_{\text{sph}} + 5 \log & \left(R_{e,\text{sph}}^{\text{maj}} \sqrt{(b/a)_{\text{sph}}} \right) \\ & + 2.5 \log \left[2\pi n_{\text{sph}} e^{b_n} b_n^{-2n_{\text{sph}}} \Gamma(2n_{\text{sph}}) \right], \end{aligned} \quad (3)$$

where b_n and $\Gamma(2n_{\text{sph}})$ are defined in the Appendix and $(b/a)_{\text{sph}}$ is the spheroid axis ratio. While Laurikainen et al. (2010) and Sani et al. (2011) reported their estimates of $(b/a)_{\text{sph}}$, Vika et al. (2012) and Läsker et al. (2014a) did not. For the last two studies, we used the values of $(b/a)_{\text{sph}}$ reported by Sani et al. (2011). The associated 1σ uncertainties for our measurements of $\mu_{e,\text{sph}}$ are $-\sigma_1^- = -0.33$ mag and $+\sigma_1^+ = +0.57$ mag, $-\sigma_2^- = -0.84$ mag and $+\sigma_2^+ = +1.59$ mag, and $-\sigma_3^- = -1.06$ mag and $+\sigma_3^+ = +1.74$ mag.

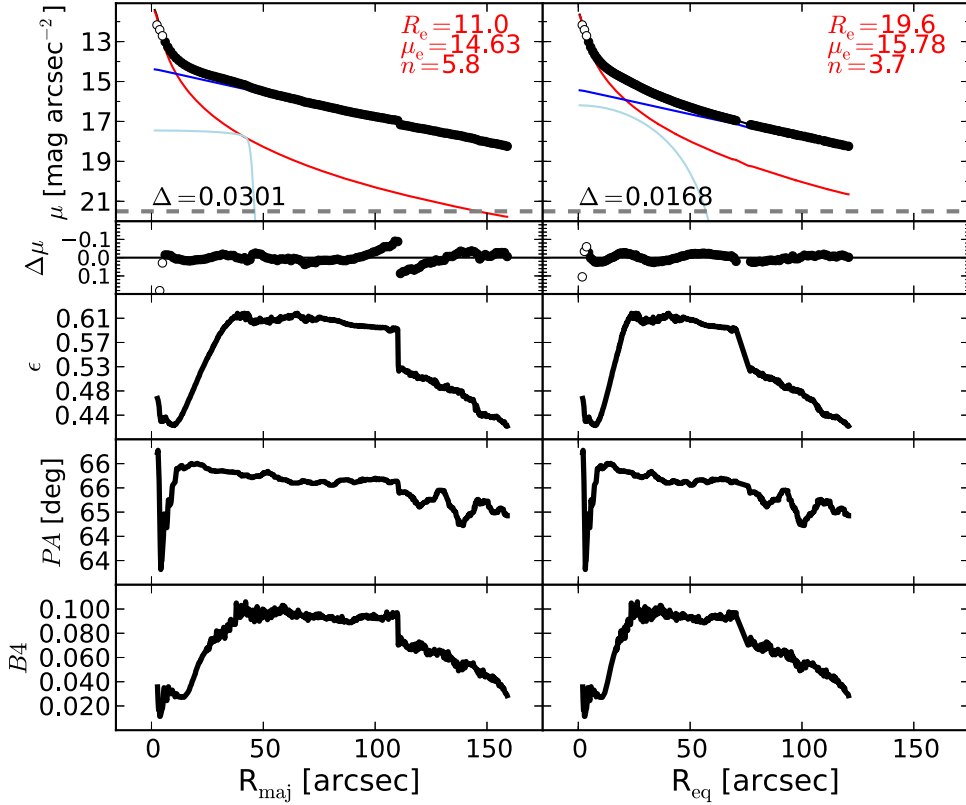


Figure 27. M104: a lenticular/spiral galaxy with a partially depleted core (Jardel et al. 2011). The data within the innermost $6''$ are excluded from the fit, and the most obvious elongated feature of this galaxy is modeled with a Ferrer function. The ellipticity profile indicates that the disk is of intermediate scale (for a thorough analysis of this galaxy, see Gadotti & Sánchez-Janssen 2012).

4.2.6. Uncertainties on $\mu_{0,\text{sph}}$

From the values of $\mu_{e,\text{sph}}$, we derived the central surface brightnesses $\mu_{0,\text{sph}}$ from the equation

$$\mu_{0,\text{sph}} = \mu_{e,\text{sph}} - \frac{2.5b_n}{\ln(10)}. \quad (4)$$

The associated 1σ uncertainties for our measurements of $\mu_{0,\text{sph}}$ are $-\sigma_1^- = -0.20$ mag and $+\sigma_1^+ = +0.64$ mag, $-\sigma_2^- = -0.70$ mag and $+\sigma_2^+ = +1.24$ mag, and $-\sigma_3^- = -1.05$ mag and $+\sigma_3^+ = +1.57$ mag.

5. CONCLUSIONS

The widespread presence of embedded components—in particular intermediate-scale disks—in massive early-type galaxies makes galaxy decomposition an essential tool to properly investigate the scaling relations between black hole masses and host spheroid properties.

Past studies often used different model components for the same galaxy and obtained significantly discrepant results, which led them to draw contrasting conclusions about the black hole–spheroid correlations. These inconsistencies motivated our effort to refine and secure the measure of spheroid properties in a sample of 66 galaxies with a dynamical estimate of the black hole mass. Using $3.6\mu\text{m}$ *Spitzer* satellite images, we performed state-of-the-art galaxy decompositions. The $3.6\mu\text{m}$ band is an excellent tracer of the stellar mass, superior to optical bands and the K band. Considerable care has been taken in the data reduction, image mosaicking, sky subtraction, and component model fitting to the galaxy light. We have

compared our best-fit models with those from the literature, to identify and explain discrepancies when present. Our analysis additionally benefited from recourse to kinematical information—not previously used—to aid in the identification of somewhat face-on disks, or the distinction between intermediate-scale disks and large-scale disks, missed in some past investigations and decompositions. Table 3 summarizes the main characteristics of the five past studies that, since 2007, attempted galaxy decompositions in order to derive black hole–spheroid scaling relations, and it highlights, in part, why our endeavor represents a substantial improvement over the past literature.

We reveal that 1D and 2D techniques of galaxy decomposition return the same results when applied to the same galaxy. However, in our practical experience, the failure rate of 2D decompositions is a factor of two higher than the failure rate of 1D decompositions, either because the fit does not converge or because the result is unphysical. A strong limitation of 2D codes is their inability to accommodate the radial gradients of ellipticity and position angle often observed in galaxy spheroids. The interpretation of 1D residual surface brightness profiles is easier than that of 2D residual images. A 1D isophotal analysis was extremely helpful and sometimes even necessary to accurately identify galaxy components. A correct interpretation of the residuals is fundamental to understand and determine the optimal model for a galaxy. Given the level of detail to which each galaxy decomposition was performed, we believe that our analysis cannot be reproduced by current automatic routines. The uncertainties associated with the literature best-fit parameters of the spheroid are dominated by

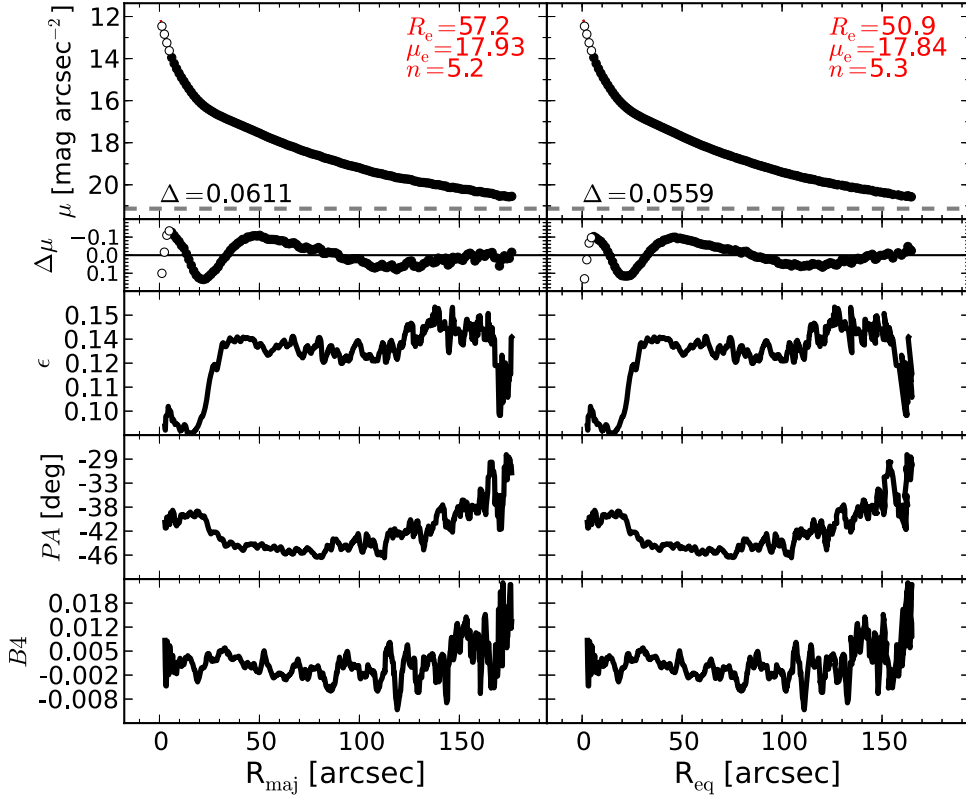


Figure 28. M105: an elliptical galaxy with an unresolved partially depleted core (Rusli et al. 2013a). M105 exhibits a mild isophotal twist and an abrupt change of ellipticity at $R_{\text{maj}} \sim 30''$. The velocity map (ATLAS^{3D}) shows rotation at least within $R_{\text{maj}} \lesssim 30''$, but no embedded disk can be recognized in the unsharp mask, and the ellipticity profile is quite unusual for a spheroidal system with an inner disk. The data within the innermost $6''/1$ are excluded from the fit. A single Sérsic model does not provide a good description of the galaxy light profile. However, the addition of a second function (of any analytic form) to the model does not improve the fit. We conclude that the galaxy may not yet be fully relaxed, and we fit it with a single Sérsic profile.

systematic errors (e.g., incorrect sky subtraction, inaccurate masking of contaminating sources, erroneous choice of model components) and only marginally affected by random errors. For this reason, we developed a method to estimate the uncertainties on the best-fit parameters that takes into account systematic errors (see Figures 9–13).

We will use the results from our 1D galaxy decompositions to obtain improved black hole mass scaling relations. These results will be presented in a series of forthcoming papers.

5.1. Individual Galaxy Decompositions

For each galaxy, we show a figure (Figures 14–79) and a table (Tables 4–69). The figure illustrates our 1D model and the galaxy isophotal parameters. The left panels refer to the major-axis R_{maj} , while the right panels refer to the equivalent-axis R_{eq} , i.e., the geometric mean of the major (a) and minor (b) axis ($R_{\text{eq}} = \sqrt{ab}$), equivalent to a circularized profile. The top panels display the galaxy surface brightness (μ) radial profiles obtained with a linear sampling. The black points are the observed data used in the fit, and the open points are the observed data excluded from the fit. The colored lines represent the individual (PSF-convolved) model components: red = Sérsic; dark blue = exponential; green = Gaussian; cyan = Ferrer; gray = Gaussian ring; pink = PSF. The parameters for the Sérsic spheroid model are inset. The total (PSF-convolved) model is shown with a black dashed line. The residual profile ($\text{data} - \text{model}$) is shown as $\Delta\mu$ in the second row. The horizontal gray dashed line corresponds to an intensity equal to

three times the rms of the sky background fluctuations ($3 \times \text{rms}_{\text{sky}}$). Δ denotes the rms scatter of the fit in units of mag arcsec^{-2} . The lower six panels show the ellipticity (ϵ), position angle (PA), and fourth harmonic ($B4$) radial profiles from the ellipse. The tables report a comparison between our results (from both our 1D and 2D decompositions) and those obtained by the following authors: GD07 = Graham & Driver (2007a, who performed 1D fits along the major-axis), L+10 = Laurikainen et al. (2010, who performed 2D fits), S+11 = Sani et al. (2011, who performed 2D fits), B+12 = Beifiori et al. (2012, who performed 2D fits), V+12 = Vika et al. (2012, who performed 2D fits), R+13 = Rusli et al. (2013a, who performed 1D fits along the equivalent axis), and L+14 = Läsker et al. (2014a, who performed 2D fits). Each galaxy model is the sum of its individual components, which are expressed with the following nomenclature: (analytic function)-(physical component). The analytic functions can be: S = Sérsic, e = exponential, G = Gaussian, F = Ferrer, M = Moffat, and PSF. The physical components can be: bul = bulge (or spheroid), d = disk, id = inner disk, bar, n = nucleus, l = lens or oval, r = ring, halo, and spiral arms. When a nuclear component or a partially depleted core has been masked, we signal it as “m-n” or “m-c,” respectively. For example, the model “S-bul + e-d + e-id + m-n + G-r” reads “Sérsic-bulge + exponential-disk + exponential-(inner disk) + mask-nucleus + Gaussian-ring.” The core-Sérsic model used by Rusli et al. (2013a) is always implicitly associated with the galaxy spheroidal component. Graham & Driver excluded the innermost data points when fitting their

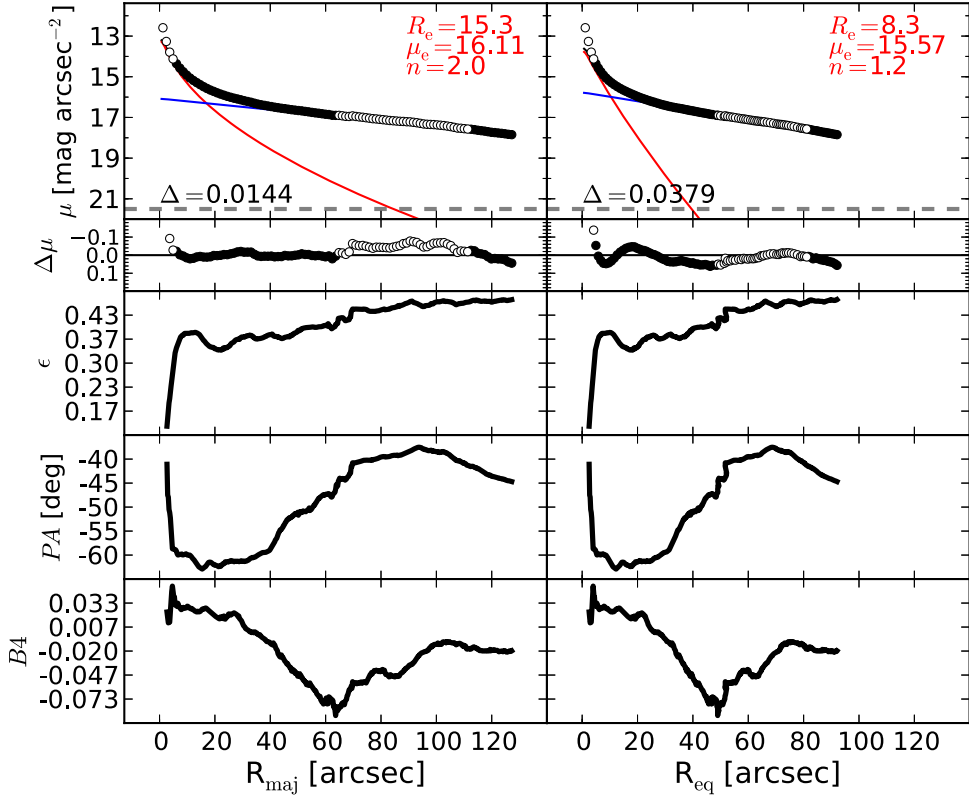


Figure 29. M106: a barred spiral galaxy, harboring a Seyfert AGN (Véron-Cetty & Véron 2006) with circumnuclear dust (Martini et al. 2003). We exclude from the fit the innermost $6''.1$ because it is affected by the AGN emission. The boxy bar, responsible for the minimum in the $B4$ profile at $R_{\text{maj}} \sim 65''$, is fainter than the large-scale disk, and in the light profile it is only detectable as a slight swelling within $65'' \lesssim R_{\text{maj}} \lesssim 110''$. This region is excluded from the fit. A peak in the ellipticity profile at $R_{\text{maj}} \sim 10''$ suggests the presence of a disky component embedded in the bulge, but a model that accounts for this component is degenerate with the other fitted components.

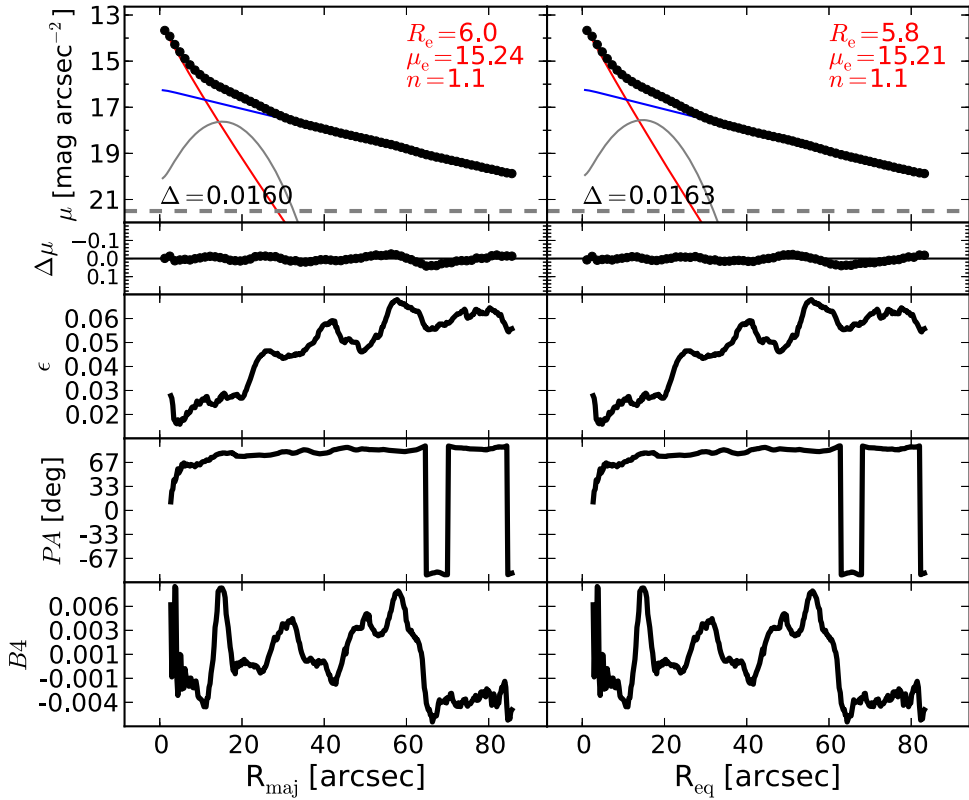


Figure 30. NGC 0524: an unbarred face-on lenticular galaxy. The unsharp mask of NGC 0524 reveals a faint multi-ring structure in the galaxy disk, with a substantial ring peaking at $R_{\text{maj}} \sim 20''$. We account for this brightest ring using a Gaussian ring profile.

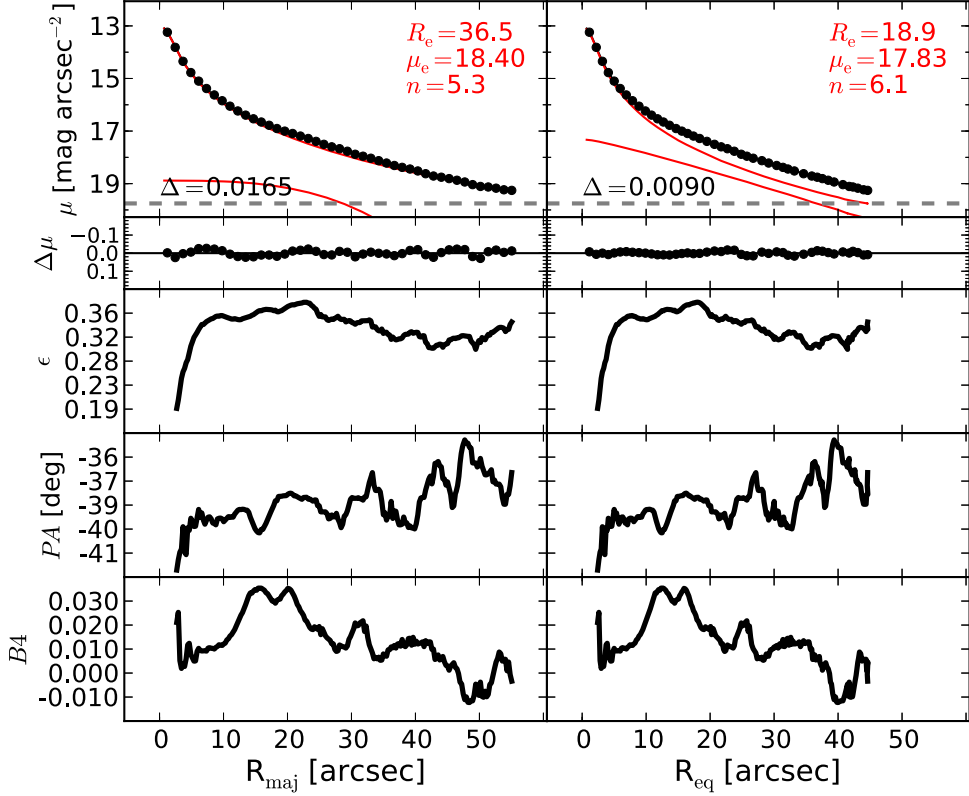


Figure 31. NGC 0821: an elliptical galaxy with an edge-on embedded disk. The ellipticity profile and the velocity map (ATLAS^{3D}, SLUGGS) show the presence of the faint intermediate-scale disk. Given its edge-on inclination, the disk is modeled with a low- n Sérsic function.

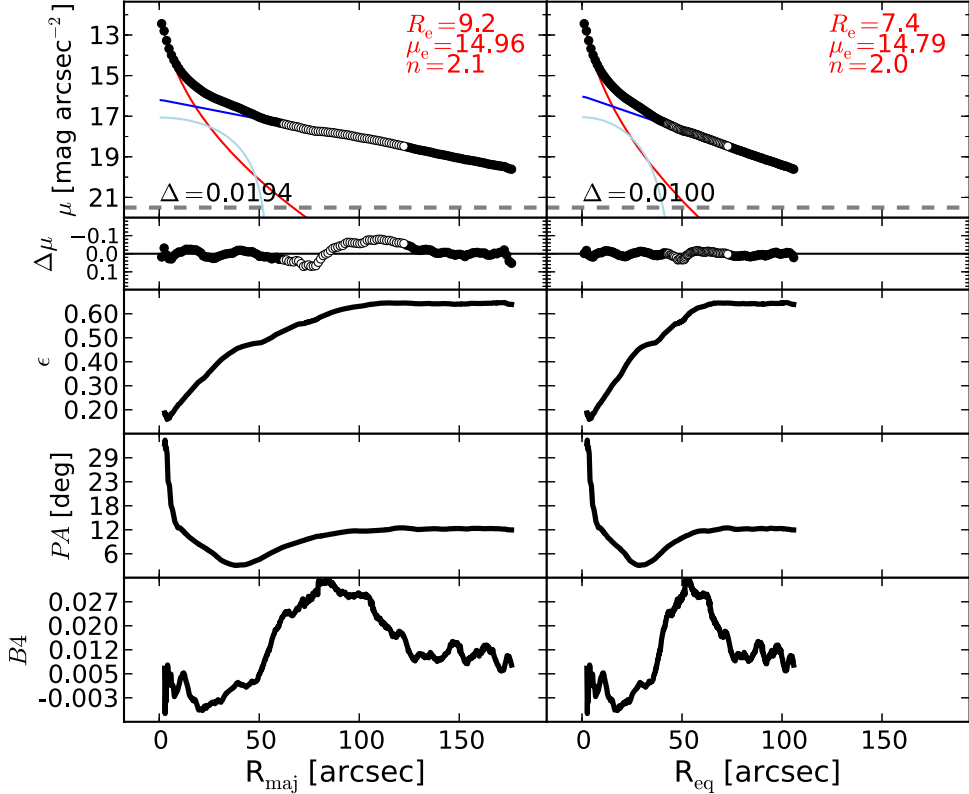


Figure 32. NGC 1023: a barred lenticular galaxy. The bar extends out to $R_{\text{maj}} \lesssim 40''$. Small deviations of the disk from a perfect exponential profile, within $60'' \lesssim R_{\text{maj}} \lesssim 125''$ (the data in this range are excluded from the fit), can be ascribed to faint residual spiral arms, also noticeable in the 2D residual image. The peak at $R_{\text{maj}} \sim 10''$ in the $B4$ profile signals the presence of an embedded (and faint) disk. The 1D residuals show a structure within $R_{\text{maj}} \lesssim 10''$ caused by this unsubtracted component, as also noted by Läsker et al. (2014a). Our attempts to account for the inner disk by adding a fourth function to the model did not significantly change the bulge best-fit parameters; thus, we elect not to model this embedded disk.

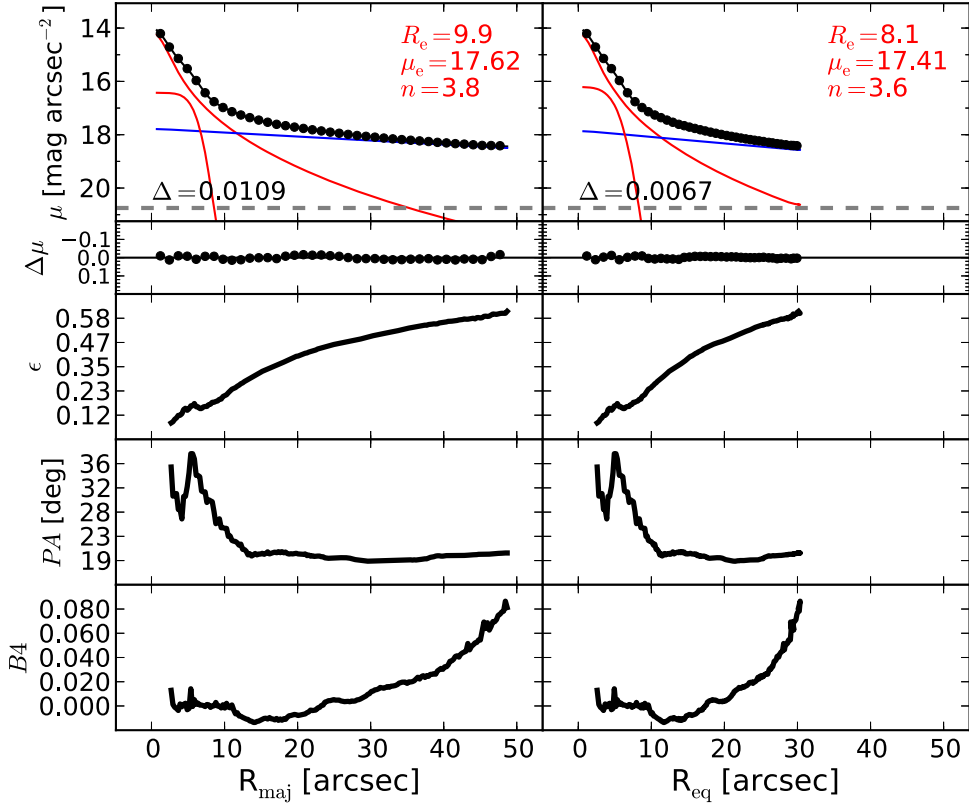


Figure 33. NGC 1300: a face-on, barred spiral galaxy. The morphology of NGC 1300 is quite complex. In addition to a large-scale disk and a bulge, the galaxy is composed of a large-scale bar that extends up to $R_{\text{maj}} \lesssim 90''$, two prominent spiral arms, and an inner disk-like component ($R_{\text{maj}} \lesssim 5''$), disclosed by the peaks in the ellipticity and PA profiles. We truncate the light profile at $R_{\text{maj}} \sim 50''$, and we fit the inner combination of the large-scale bar and the disk as a single component, using an exponential function. The embedded component is described with a low- n Sérsic profile.

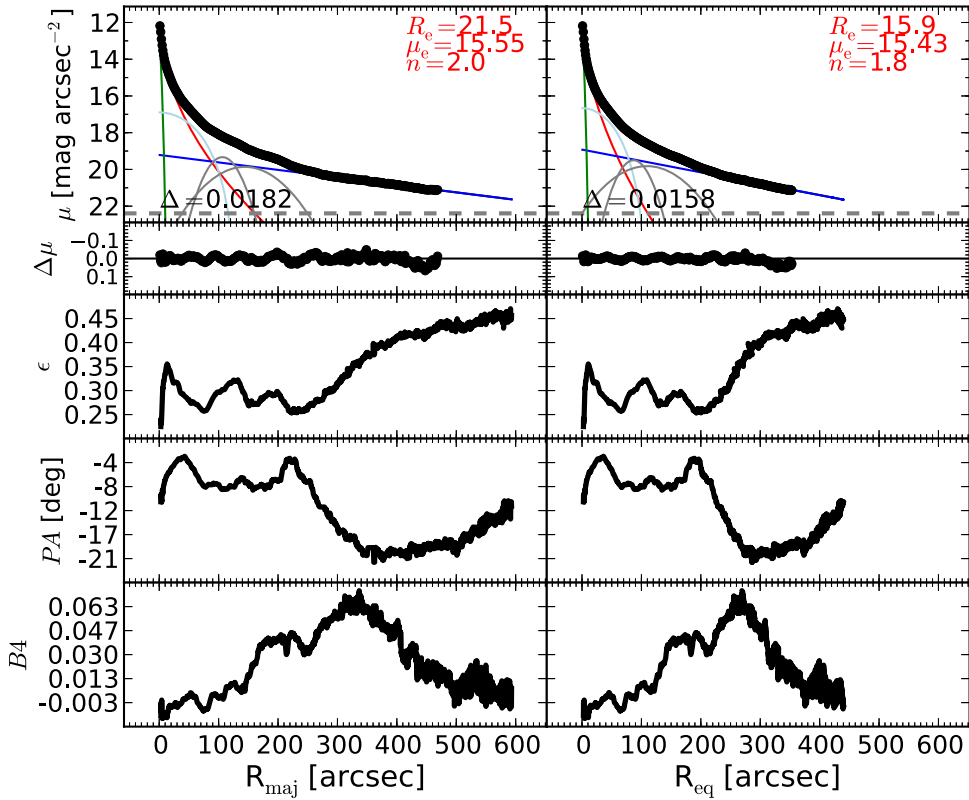


Figure 34. NGC 1316: a merger. The galaxy is composed of a bulge, an elongated structure that can be identified with a bar, two obvious rings, an outer exponential disk or halo, and a bright nuclear component.

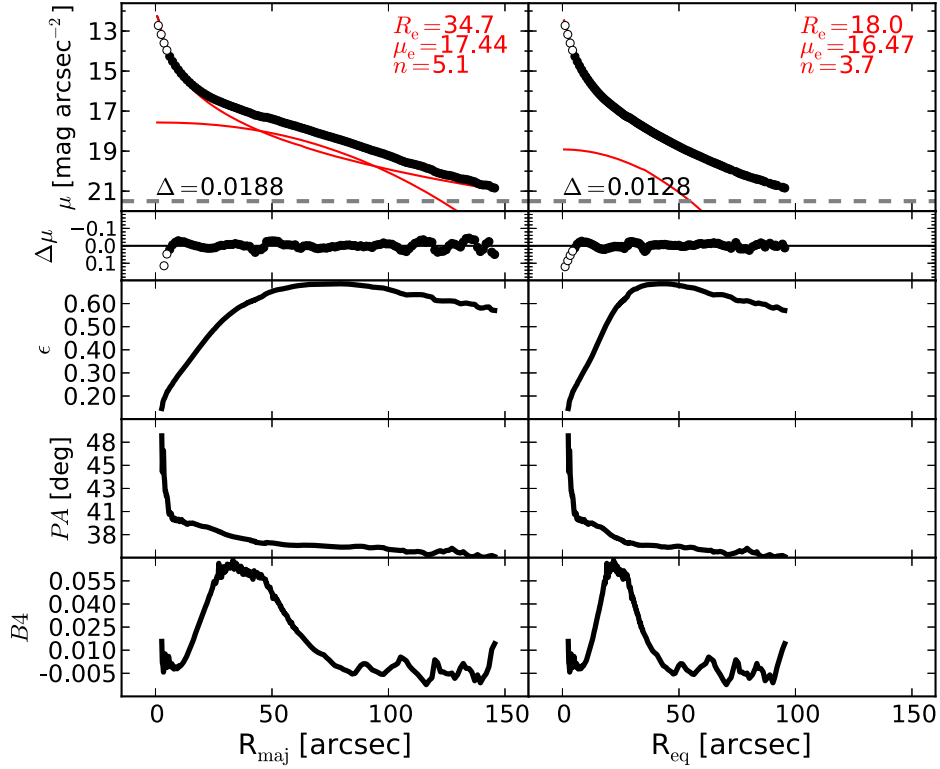


Figure 35. NGC 1332: an edge-on elliptical/lenticular galaxy. The identification of a disk is trivial owing to its edge-on orientation, although a visual inspection of the galaxy image is not enough to establish the radial extent of this disk. The ellipticity profile indicates that the disk is indeed intermediate-sized, i.e., it does not dominate at large radii. Given the edge-on inclination of this disk, we model it with a low- n Sérsic profile. The data within the innermost $6''$ are excluded from the fit. Our equivalent-axis decomposition returns a spheroidal component accounting for 95% of the total light, and an embedded disk accounting for the remaining 5%. In passing, we note that the bulge-disk decomposition performed by Rusli et al. (2011) on NGC 1332 is significantly different from our best-fit model. Rusli et al. (2011) did not identify the intermediate-scale embedded disk, but instead proposed a model featuring a Sérsic bulge ($n_{\text{sph}} \sim 2.3$, $R_{e,\text{sph}} \sim 8''$), accounting for 43% of the total light, and a large-scale exponential disk. This result led them to the conclusion that NGC 1332 is a disk-dominated lenticular galaxy and is displaced from the $M_{\text{BH}}-L_{K,\text{sph}}$ (black hole mass vs. K-band spheroid luminosity) relation of Marconi & Hunt (2003) by an order of magnitude along the M_{BH} direction. Instead, the galaxy spheroid is a factor of two more luminous than claimed by Rusli et al. (2011), and NGC 1332 is not an outlier in our $M_{\text{BH}}-L_{\text{sph}}$ diagram.

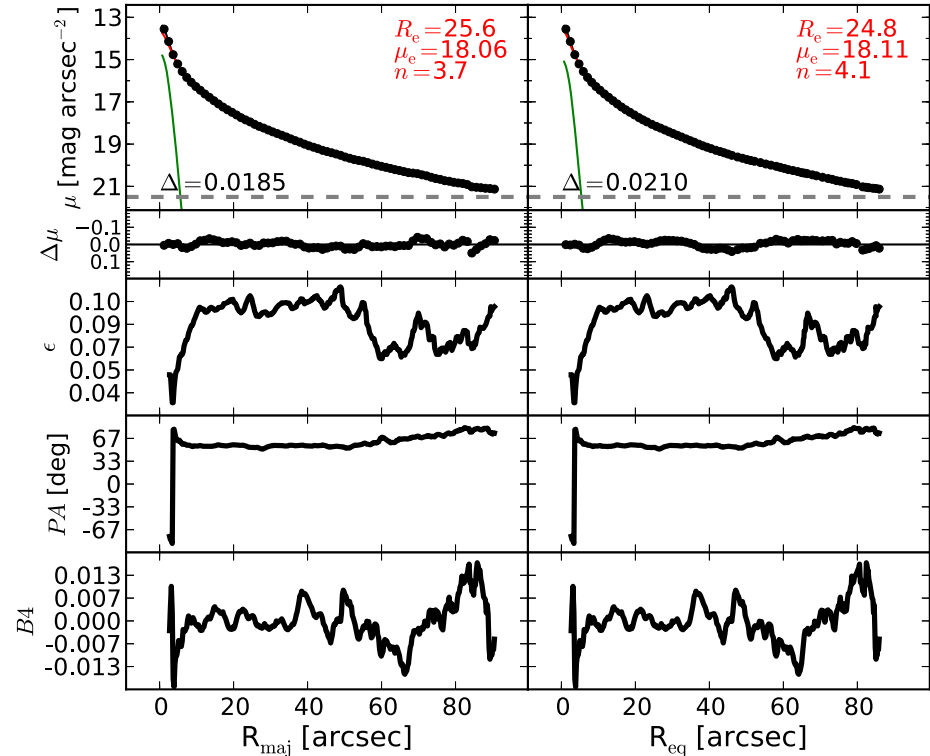


Figure 36. NGC 1374: an elliptical galaxy. A Gaussian function in our model accounts for the relatively faint additional nuclear component.

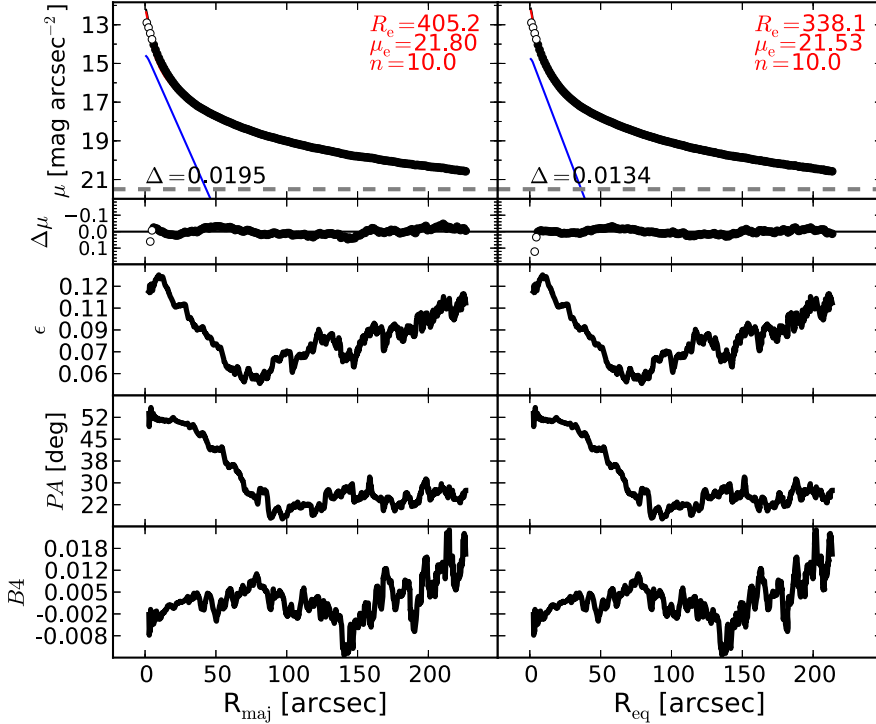


Figure 37. NGC 1399: the central galaxy of the Fornax Cluster, an elliptical galaxy with a slightly resolved partially depleted core (Rusli et al. 2013a; Dullo & Graham 2014). The nuclear activity of NGC 1399 is classified as Seyfert (Véron-Cetty & Véron 2006), but the galaxy lacks dust emission (Tran et al. 2001). The ellipticity and PA profiles display a steep decline with increasing radius within $R_{\text{maj}} \lesssim 60''$, suggesting the presence of an embedded disk. This inner component is also visible, although faint, in the unsharp mask. We note that, after excluding the innermost $6.''1$, a single Sérsic profile is not sufficient to describe the whole galaxy light profile. The addition of an inner exponential function to model the disk notably improves the fit.

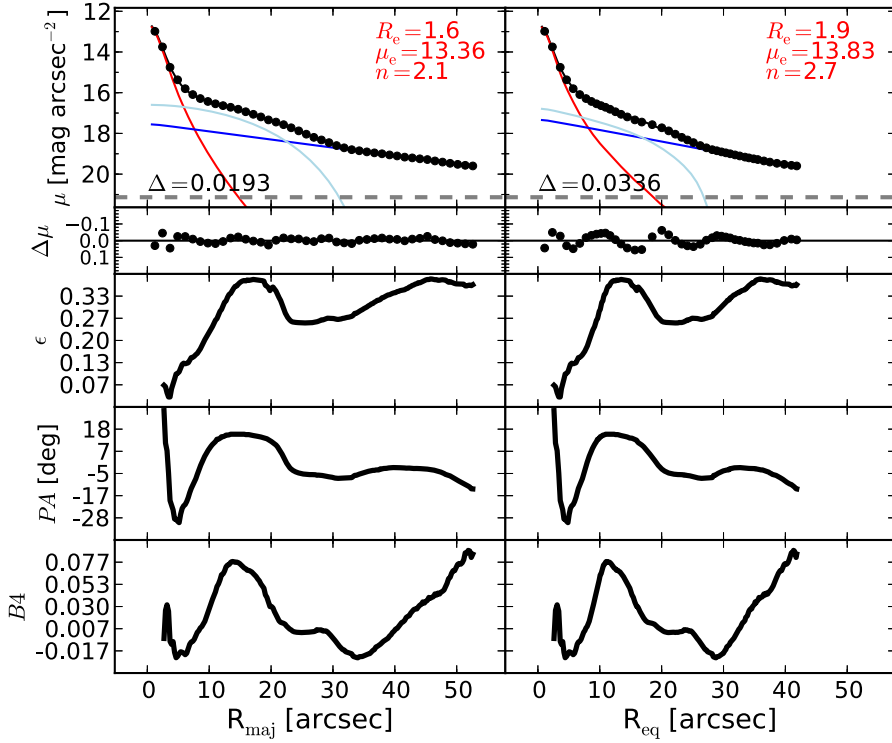


Figure 38. NGC 2273: a barred spiral galaxy with a Seyfert AGN (Contini et al. 1998) and circumnuclear dust (Simões Lopes et al. 2007). Its bar is surrounded by two tightly wound star-forming spiral arms that resemble a ring (Comerón et al. 2010). The bar of NGC 2273 extends out to $R_{\text{maj}} \lesssim 25''$. The pseudoring does not produce any evident swelling in the light profile; therefore, we do not account for it in the galaxy model. The isophotal parameters confirm the presence of a nuclear disk-like component within $R_{\text{maj}} \lesssim 5''$. However, as noted by Laurikainen et al. (2005), any attempt to account for the embedded disk resulted in a degenerate model. This is not surprising if one considers the poor spatial resolution of the galaxy image, with the effective radius of the bulge comparable to the FWHM of the instrumental PSF. Although NGC 2273 hosts an optical AGN and nuclear dust, no central excess of light is observed in the 1D residuals. The addition of a nuclear component to the model does not significantly improve the fit or change the bulge parameters.

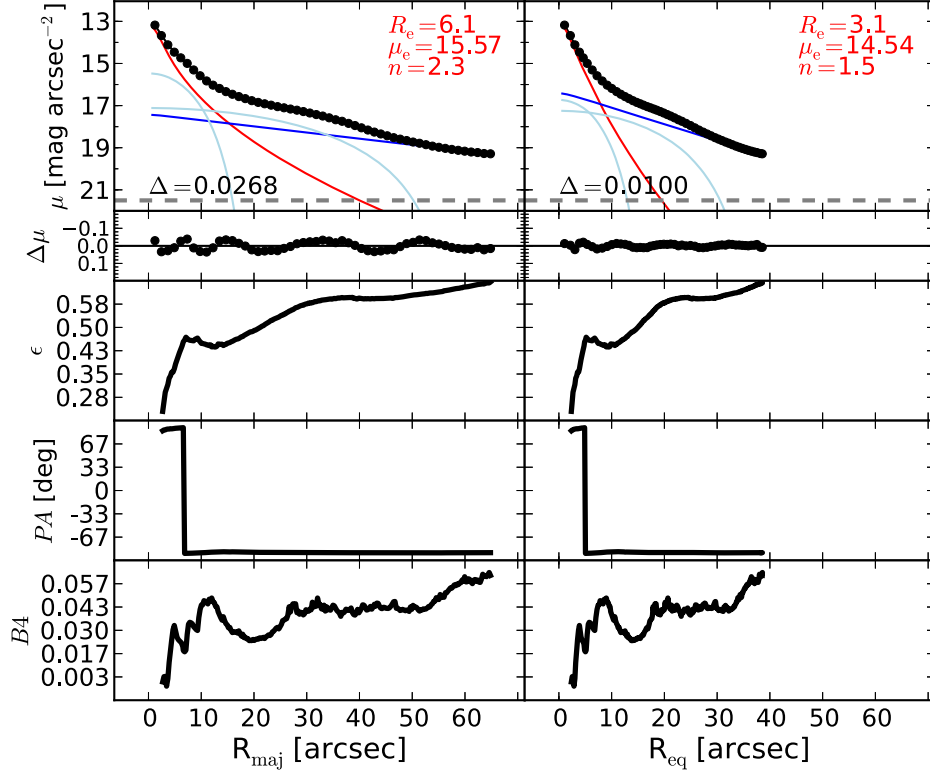


Figure 39. NGC 2549: an edge-on barred lenticular galaxy. Although the edge-on inclination of NGC 2549 complicates the identification of additional embedded components, a large-scale bar ($R_{\text{maj}} \lesssim 45''$) can be recognized in the galaxy image and—more easily—in the light profile. We model the large-scale bar with a Ferrer function. A peak in the ellipticity profile discloses the presence of a disk-like component embedded in the bulge ($R_{\text{maj}} \lesssim 10''$). This inner component can be spotted also by looking at the velocity map (ATLAS^{3D}), and we fit it with a Ferrer function.

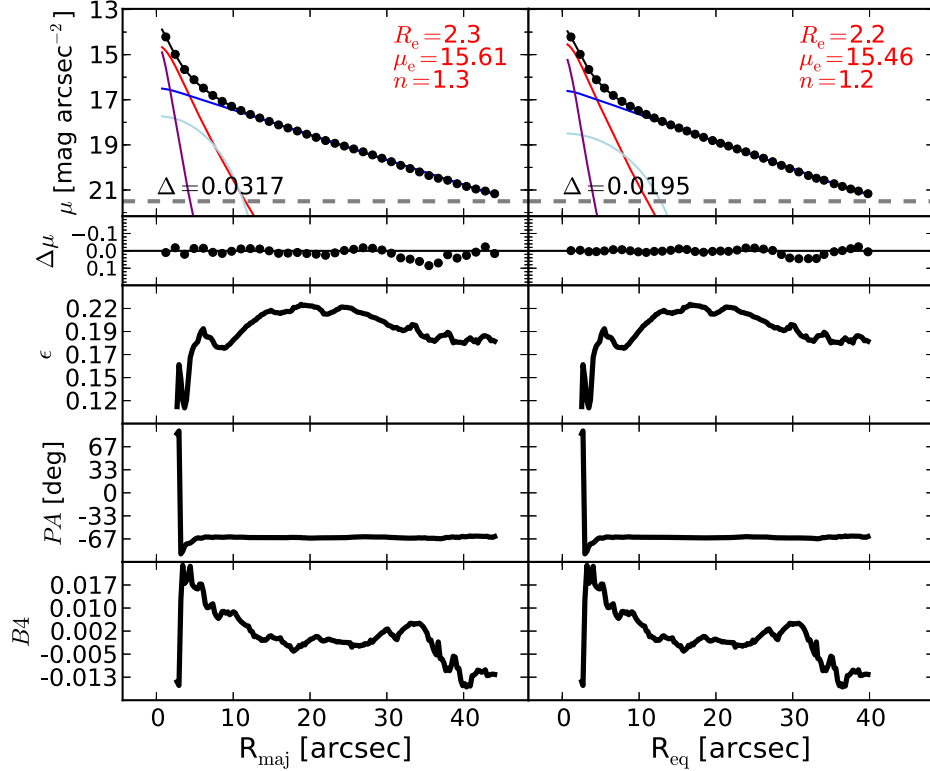


Figure 40. NGC 2778: a face-on lenticular galaxy. The peak in the ellipticity profile at $R_{\text{maj}} \sim 5''$ reveals the existence of a nuclear component embedded in the galaxy bulge. After an inspection of the unsharp mask, we identified this component with a small bar, which we model with a Ferrer function. We also account for some nuclear light excess by adding a PSF component to the model. We note that excluding the PSF component from our model does not significantly change the bulge effective radius, but it does increase the bulge Sérsic index to $n_{\text{sph}} \sim 2$.

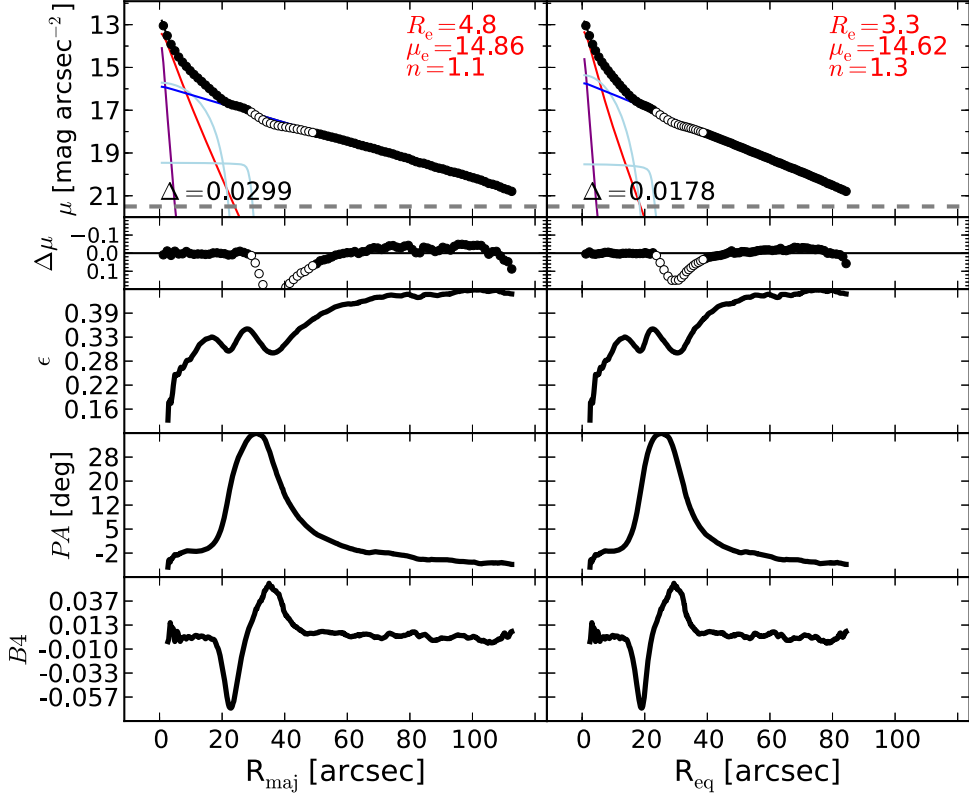


Figure 41. NGC 2787: a barred lenticular galaxy with LINER nuclear activity (Véron-Cetty & Véron 2006). An inner disk is embedded in the bulge of this galaxy (Erwin et al. 2003). NGC 2787 features a spectacular structure of dust rings at its center (Erwin & Sparke 2003) and a nuclear stellar disk (with size $\lesssim 1''.8$; Ledo et al. 2010). NGC 2787 has an undoubtedly complex morphology. This galaxy is composed of a bulge, a large-scale disk, a bar (see the peaks in the ellipticity, PA, and $B4$ profiles at $R_{\text{maj}} \sim 30''$) with two ansae, an inner disk (or bar?) embedded in the bulge (see the peak in the ellipticity profile at $R_{\text{maj}} \sim 17''$), and a bright nucleus. After masking the data affected by the ansae within $30'' \lesssim R_{\text{maj}} \lesssim 50''$, we use a Ferrer function for the bar, a second Ferrer function for the inner disk (or bar), and a PSF component for the nucleus.

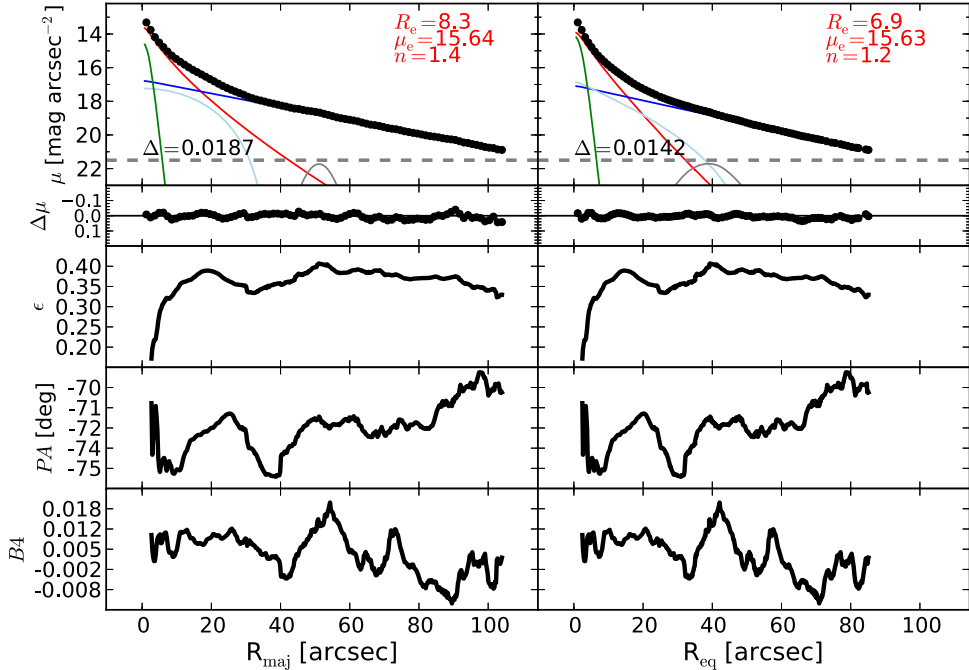


Figure 42. NGC 2974: a spiral galaxy that has been misclassified as an elliptical galaxy in the RC3 catalog. The galaxy hosts a Seyfert AGN (Véron-Cetty & Véron 2006) and filamentary dust in its center (Tran et al. 2001). From an inspection of the unsharp mask, we identified a ring structure at $R_{\text{maj}} \sim 50''$, probably a residual of two tightly wound spiral arms, and an elongated bar-like component within $R_{\text{maj}} \lesssim 30''$, which we fit with a Ferrer function. The pseudoring produces a peak in the $B4$ profile at $R_{\text{maj}} \sim 50''$, and the bar produces a peak in the ellipticity profile at $R_{\text{maj}} \sim 20''$. Although the ring is extremely faint, it is important to account for it in the galaxy decomposition. A model without the ring component results in a “steeper” exponential disk (i.e., the disk would have a smaller scale length and a brighter central surface brightness) and produces poor residuals within $R_{\text{maj}} \lesssim 40''$. The nuclear component is fit with a Gaussian profile.

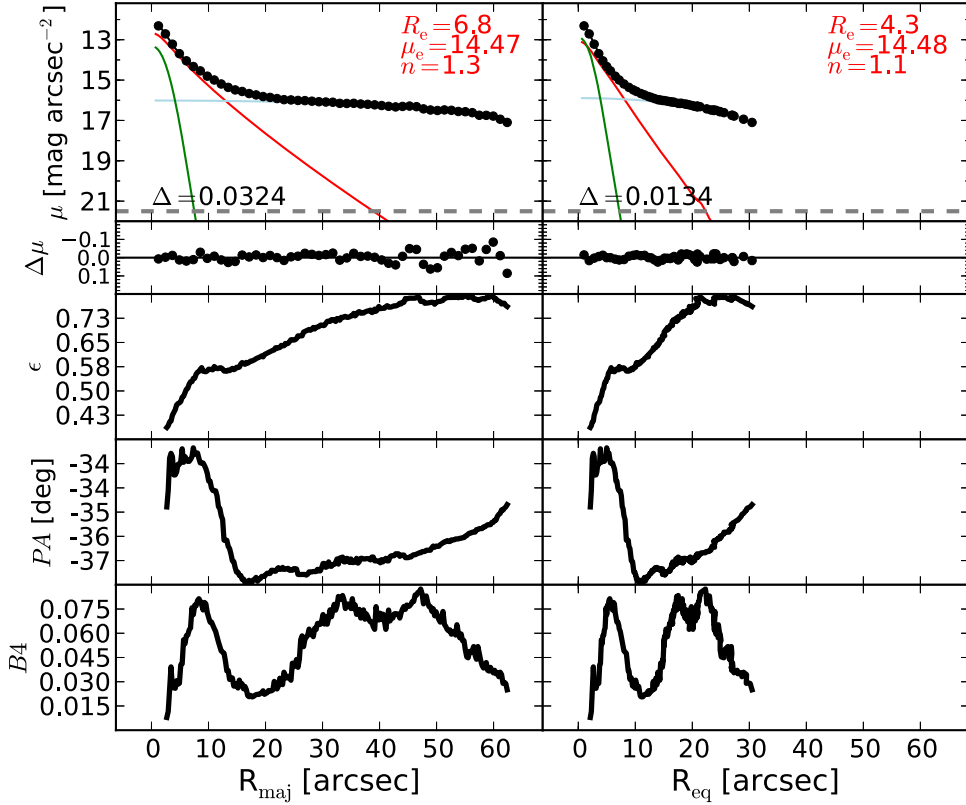


Figure 43. NGC 3079: an edge-on, late-type barred spiral galaxy with a Seyfert AGN (Véron-Cetty & Véron 2006) and circumnuclear dust (Martini et al. 2003). The bar extends out to $R_{\text{maj}} \lesssim 70''$. We truncate the light profile at $R_{\text{maj}} \sim 65''$, before the “edge” of the bar, and we successfully model the combination of the disk and the bar with a Ferrer function. A Gaussian function accounts for the AGN emission.

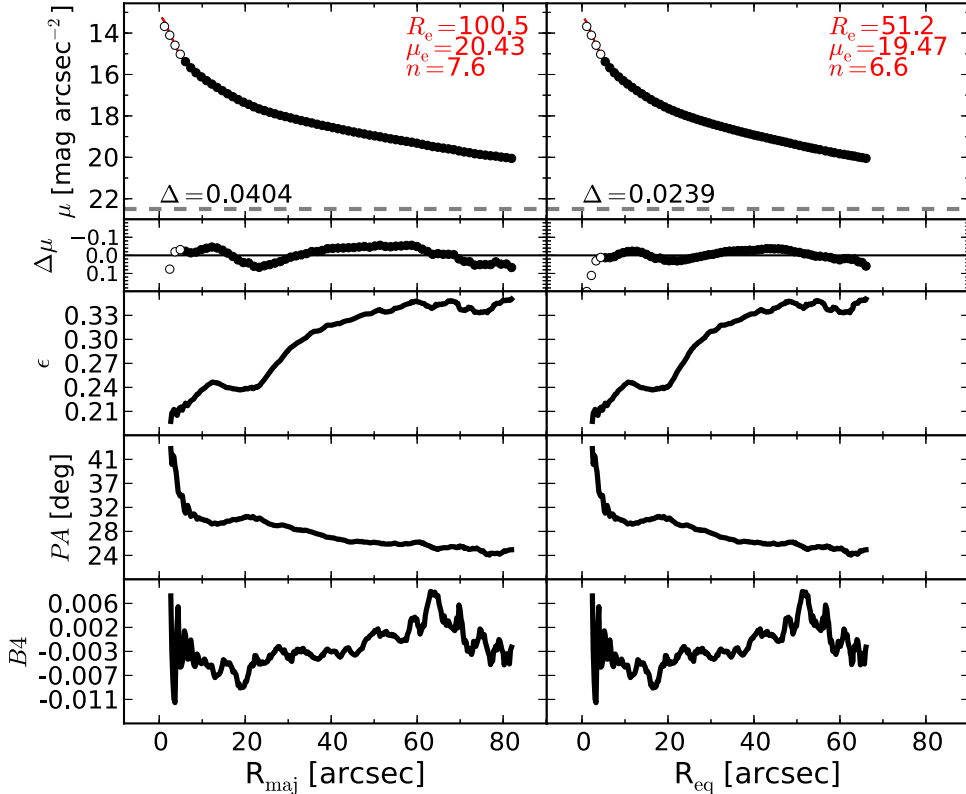


Figure 44. NGC 3091: an elliptical galaxy with an unresolved partially depleted core (Rusli et al. 2013a). The data within the innermost $6''$ are excluded from the fit. A faint embedded component ($R_{\text{maj}} \lesssim 10''$) can be recognized in the unsharp mask and has a corresponding peak in the ellipticity profile. This extra component is clearly visible in the residual image obtained by subtracting a 2D Sérsic model from the galaxy image. However, any attempt to account for the embedded component resulted in an unsatisfactory fit and did not significantly change the bulge parameters. We thus elect not to model the inner component.

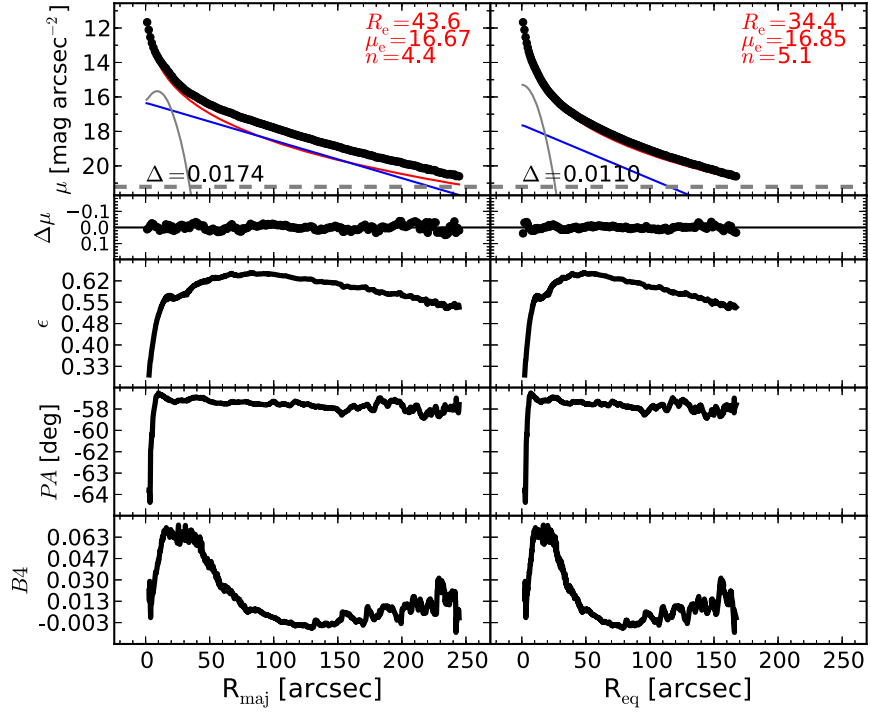


Figure 45. NGC 3115: an edge-on elliptical/lenticular galaxy. This galaxy features an intermediate-scale disk and a nuclear stellar disk (with size $\sim 1''$; Scorz & Bender 1995; Ledo et al. 2010). The presence of the intermediate-scale disk is immediately evident by looking at the ellipticity and B_4 profiles. From the galaxy center to the outskirts, the ellipticity increases until it reaches a maximum ($\epsilon \sim 0.65$) at $R_{\text{maj}} \sim 90''$. After this point, it starts declining, being as low as $\epsilon \sim 0.55$ at $R_{\text{maj}} \sim 240''$. The galaxy isophotes display a positive diskyness within $R_{\text{maj}} \sim 90''$, but become perfect ellipses ($B_4 \sim 0$) beyond that point. Because galaxy disks typically have fixed ellipticity, reflecting their inclination to our line of sight, the previous observations tell us that, going from the galaxy center to the outer regions, the disk of NGC 3115 becomes increasingly important relative to the spheroid light, reaching its maximum at $R \sim 90''$. Beyond $R_{\text{maj}} \gtrsim 90''$, the contribution from the disk light starts declining more rapidly than the spheroid light. This interpretation is supported by the results of Arnold et al. (2011), who found that, within $R_{\text{maj}} \sim 110''$, the bulge of NGC 3115 is flattened and rotates rapidly ($v/\sigma \gtrsim 1.5$), whereas at larger radii the rotation declines dramatically (to $v/\sigma \sim 0.7$), but remains well aligned with the inner regions. From an inspection of the unsharp mask, we identify a faint nuclear edge-on ring ($R_{\text{maj}} \sim 15''$), which produces a corresponding peak in the ellipticity profile. We do not observe any nuclear excess of light in the 1D residuals. The addition of a PSF component to the final model does not significantly change the outcome of the fit.

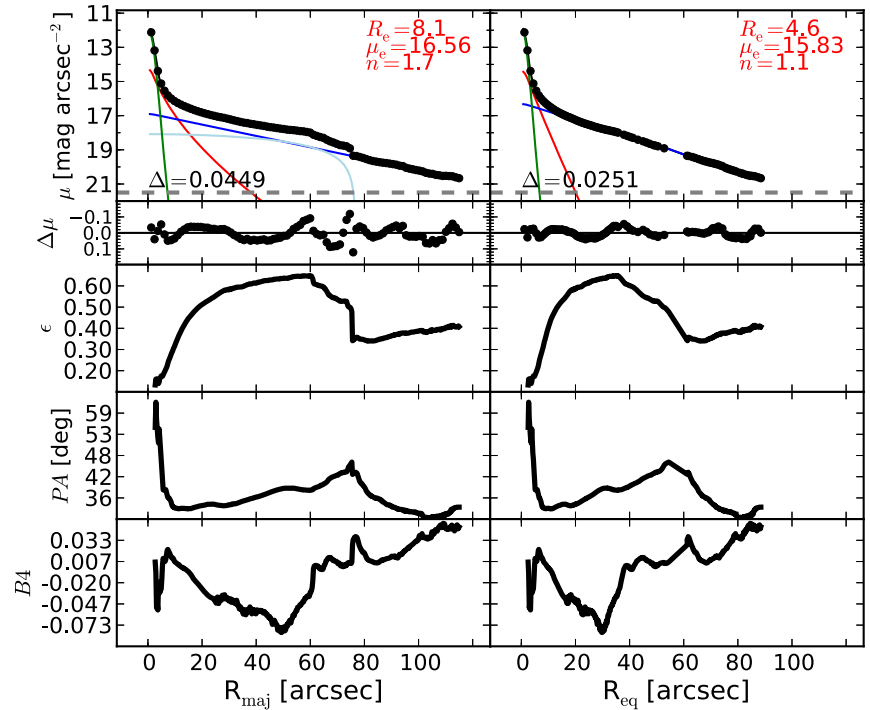


Figure 46. NGC 3227: a spiral galaxy with a large-scale bar. This galaxy hosts a Seyfert AGN (Khachikian & Weedman 1974) and circumnuclear dust (Martini et al. 2003). The large-scale bar produces an evident bump in the major-axis surface brightness profile, which is absent in the equivalent-axis profile. We model the bar with a Ferrer function and the nucleus with a Gaussian function. The Ferrer component is rejected by the equivalent-axis fit.

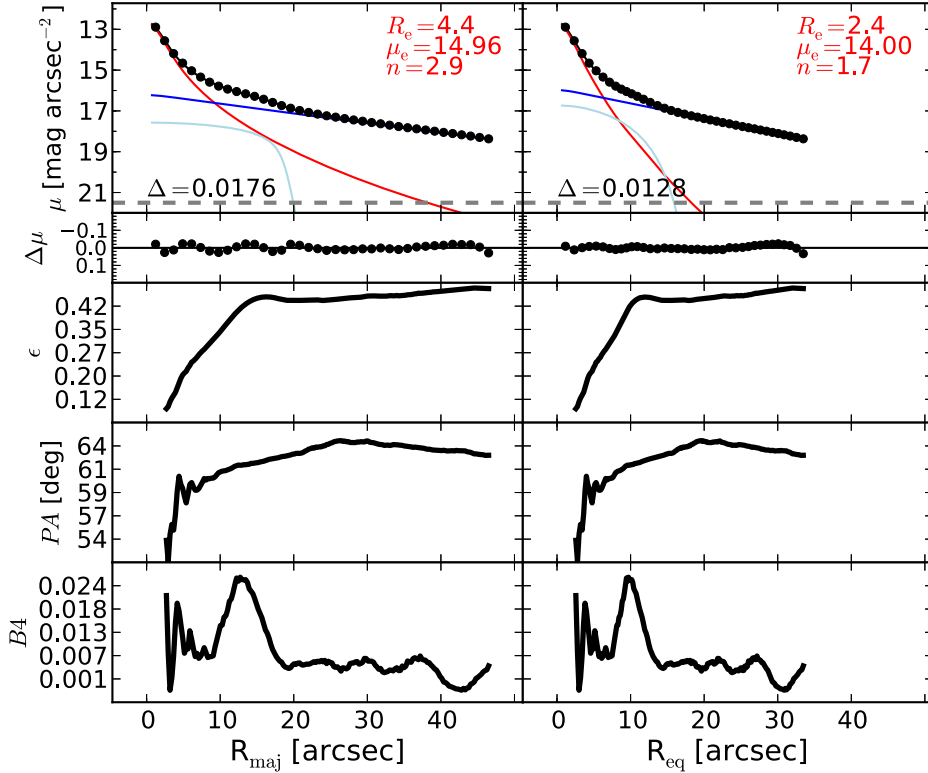


Figure 47. NGC 3245: a lenticular galaxy. The unsharp mask reveals the presence of an embedded disk ($R_{\text{maj}} \lesssim 15''$), confirmed by the corresponding peaks in the ellipticity and B_4 profiles. We model this inner component with a Ferrer function.

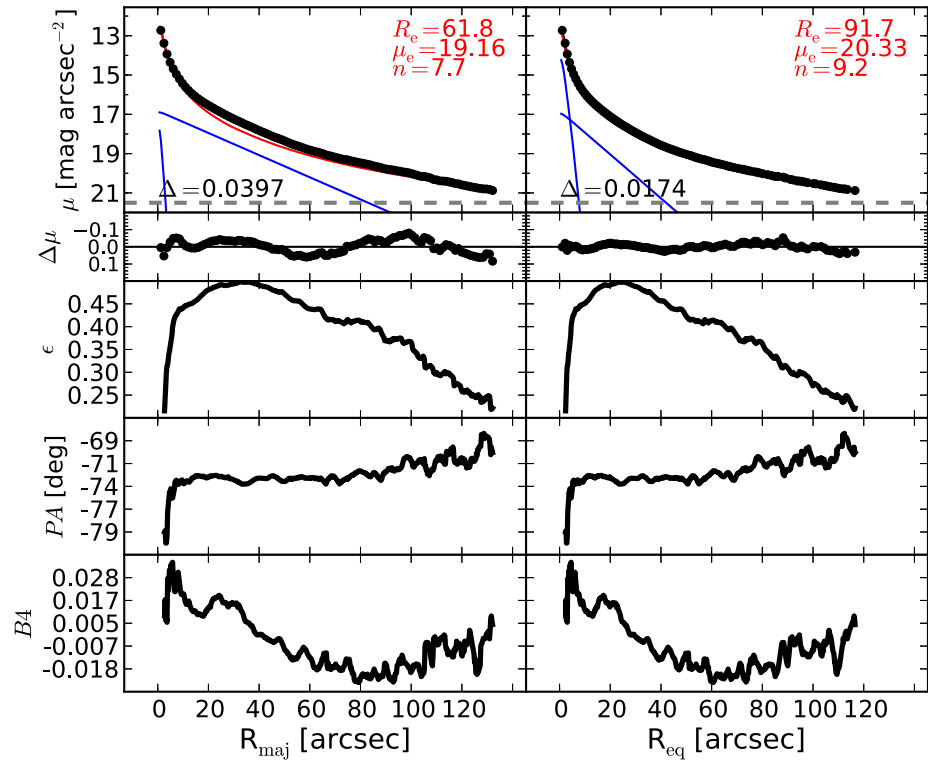


Figure 48. NGC 3377: an elliptical galaxy with an intermediate-scale disk and a nuclear stellar disk (Ledo et al. 2010). For this galaxy, Arnold et al. (2014) reported a strong decline in local specific angular momentum beyond $\sim 35''$, with a disk-to-bulge transition occurring at about $R_{\text{maj}} \sim 50''$. Arnold et al. (2014) attempted a three-component decomposition (accounting for a bulge, an embedded disk, and a central cusp), but unfortunately they fit the spheroidal component with a limited two-parameter $R^{1/4}$ function rather than a three-parameter $R^{1/n}$ Sérsic function. Here we use a surface brightness profile twice as extended as that used by Arnold et al. (2014), and we identify a nuclear disk and an intermediate-scale disk, both embedded in a larger spheroidal component. The presence of the intermediate-scale disk is also evident in the unsharp mask of the image mosaic and also from the ellipticity, which increases with increasing radius until $R_{\text{maj}} \sim 45''$ and then drops at larger radii. The nuclear stellar disk can be spotted from the peak at $R_{\text{maj}} \sim 5''$ in the B_4 profile. Each of the two disks is modeled with an exponential profile.

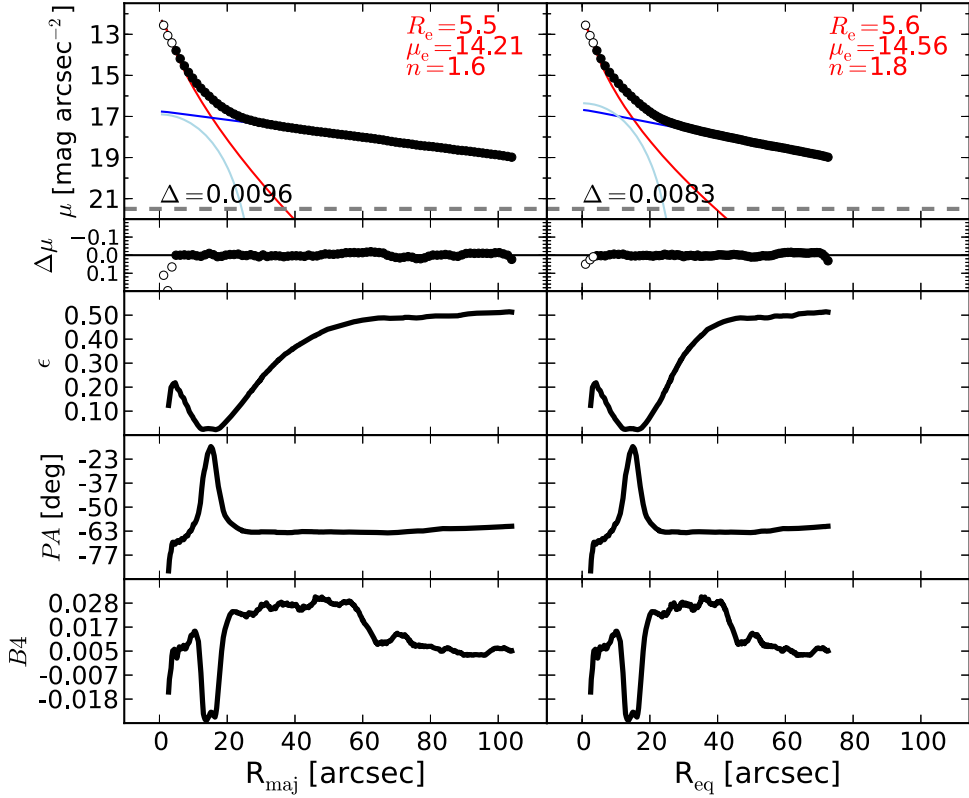


Figure 49. NGC 3384: a barred lenticular galaxy that hosts an embedded disk (with size $\lesssim 11''$; Erwin 2004) and a nuclear stellar disk (with size $\lesssim 0''.8$; Ledo et al. 2010). The isophotal parameters show clearly the presence of a boxy bar that extends out to $R_{\text{maj}} \lesssim 18''$. We model the bar with a Ferrer function. An embedded disk can be seen in the unsharp mask and produces the peak in the ellipticity profile at $R_{\text{maj}} \sim 4''$. However, any attempt to account for this component resulted in a degenerate model. We elect to fit neither the embedded disk nor the nuclear disk, by excluding from the fit the data within $R_{\text{maj}} < 3''7$.

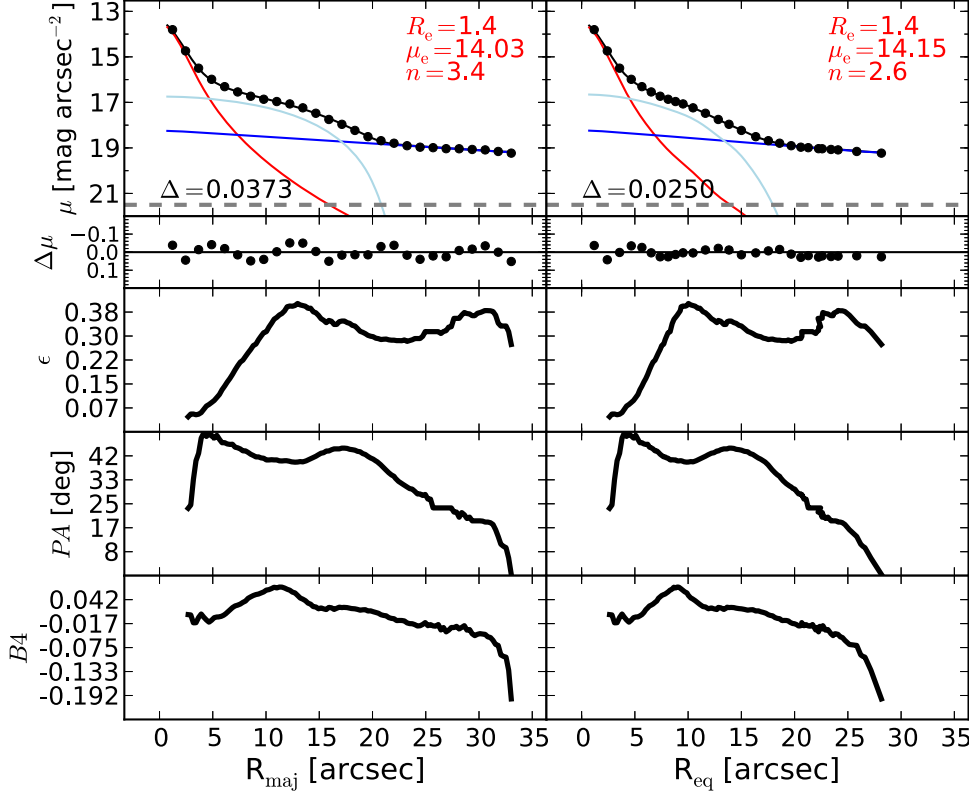


Figure 50. NGC 3393: an edge-on spiral galaxy hosting a Seyfert AGN (Diaz et al. 1988) and circumnuclear dust (Martini et al. 2003). The galaxy has a large-scale bar and a nuclear bar (with size $\lesssim 3''$, Erwin 2004). The large-scale bar ($R_{\text{maj}} \lesssim 20''$) is modeled with a Ferrer function. We do not model the nuclear bar and the AGN component because the poor spatial resolution of the data does not allow us to fit them.

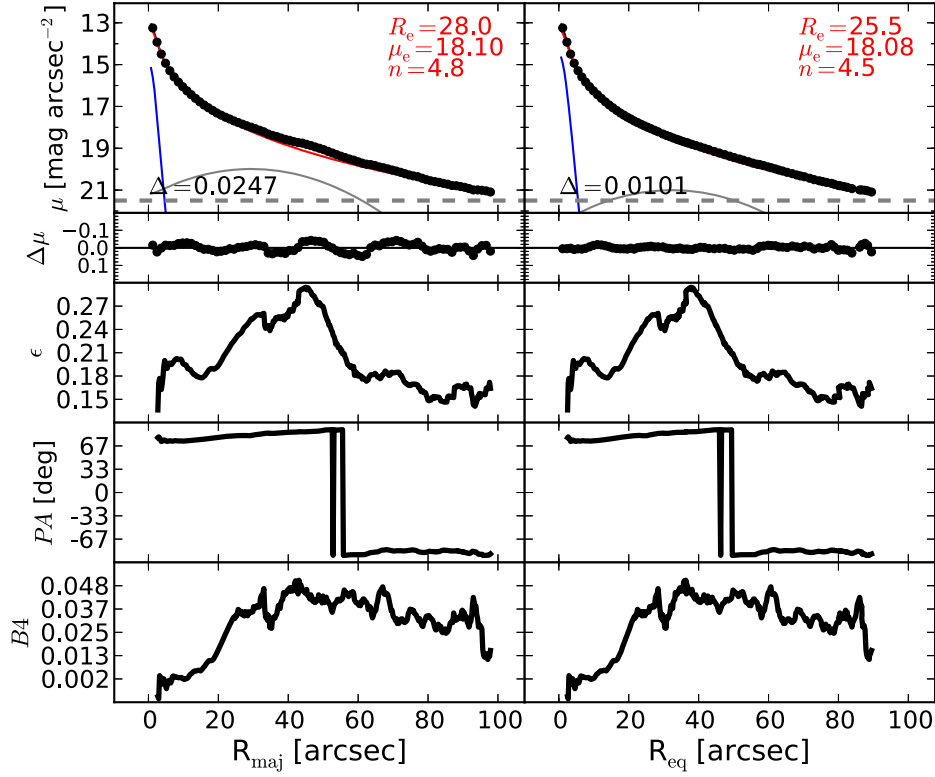


Figure 51. NGC 3414: a peculiar lenticular/elliptical galaxy. Different interpretations have been proposed about the morphology of this galaxy. Whitmore et al. (1990) suggested that NGC 3414 is a spheroidal galaxy with a large-scale edge-on polar ring, rather than a face-on barred lenticular galaxy. Laurikainen et al. (2010) decomposed NGC 3414 as a barred lenticular galaxy, but they cautioned against the uncertainty of their solution owing to the possible misinterpretation of the galaxy morphology. The unsharp mask clearly shows that an embedded component does not extend all the way through the center of the galaxy, but instead it is truncated at $R_{\text{maj}} \sim 20''$. However, an elongated structure in the galaxy center resembles a nuclear edge-on disk ($R_{\text{maj}} \lesssim 5''$). The velocity map (ATLAS^{3D}) shows rotation within $R_{\text{maj}} \lesssim 5''$, no rotation within $5'' \lesssim R_{\text{maj}} \lesssim 15''$, and counterrotation beyond $R_{\text{maj}} \gtrsim 15''$. The velocity pattern is consistent with the galaxy being a spheroidal system containing an edge-on polar ring and an edge-on nuclear disk.

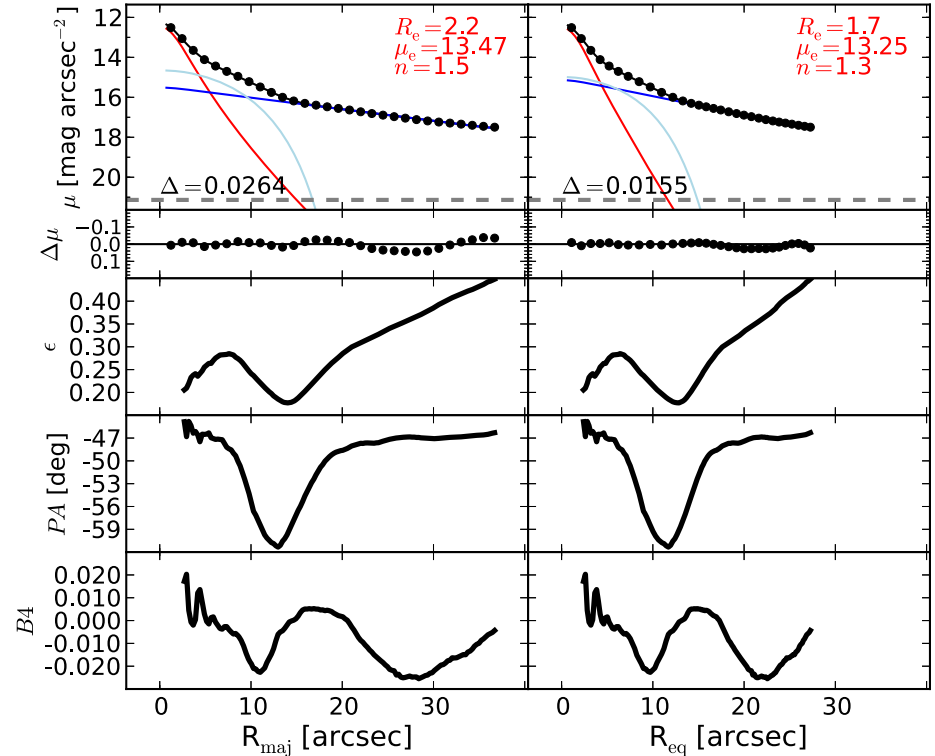


Figure 52. NGC 3489: a barred lenticular galaxy. Its disk has a smooth antitruncation at $R_{\text{maj}} \sim 85''$ (Erwin et al. 2008). The bar is fit with a Ferrer function.

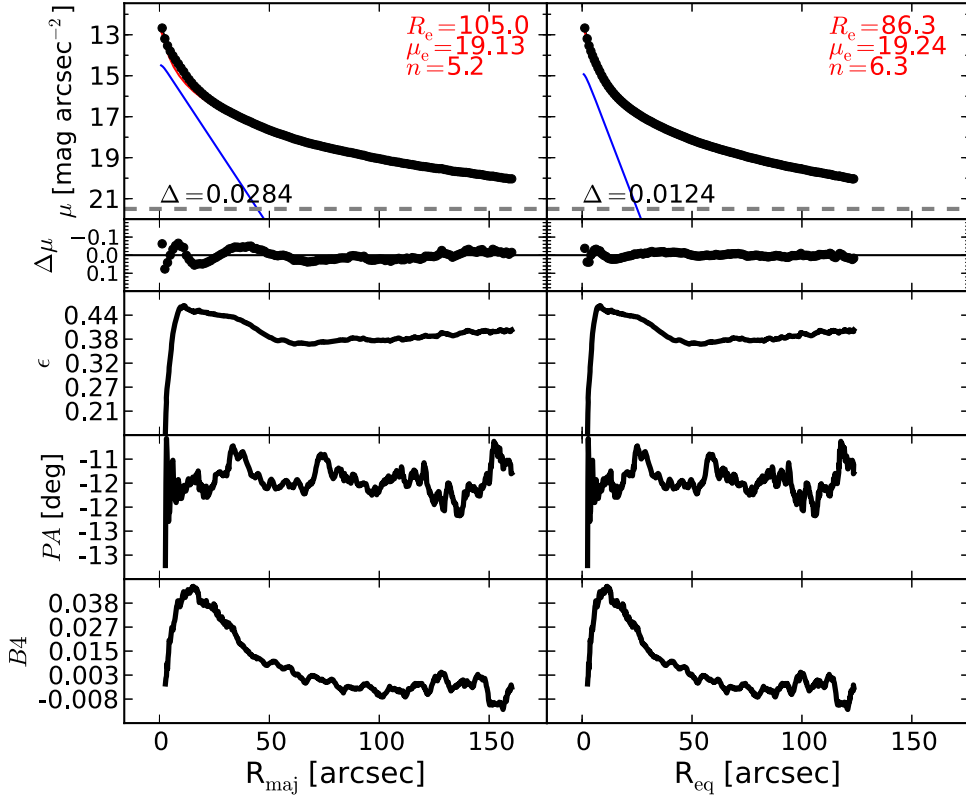


Figure 53. NGC 3585: an elliptical galaxy with an embedded disk (Scorza & Bender 1995). The embedded disk is visible in the unsharp mask and modeled with an exponential function.

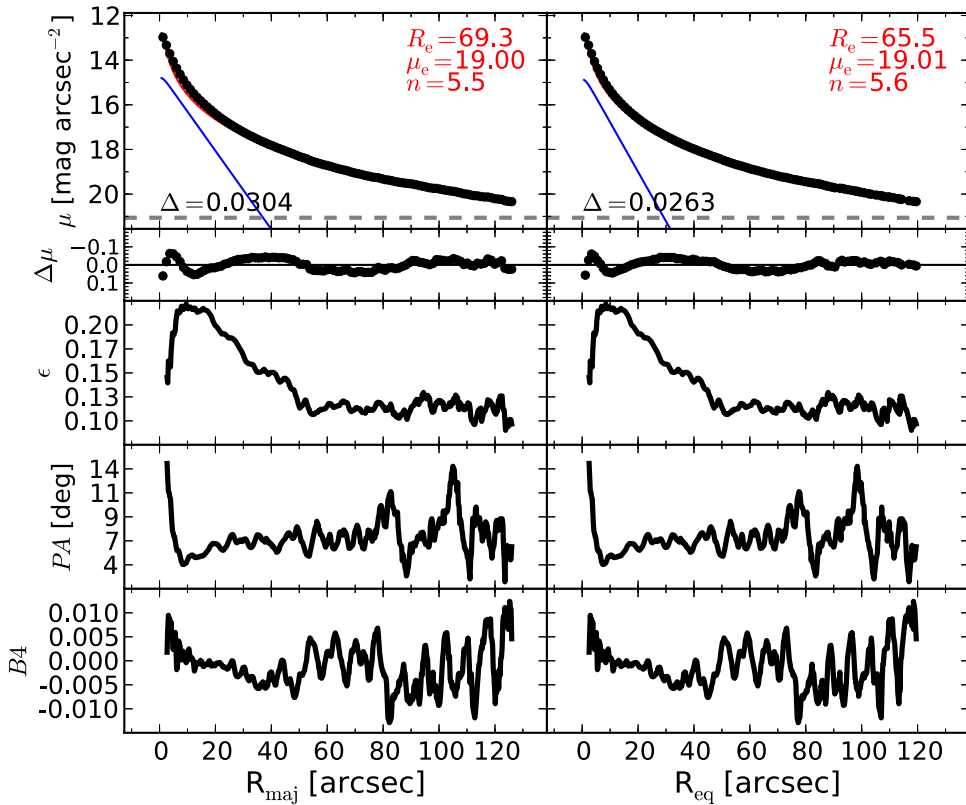


Figure 54. NGC 3607: an elliptical galaxy with an embedded disk. The velocity map (ATLAS^{3D}) shows rotation only within $R_{\text{maj}} \lesssim 20''$.

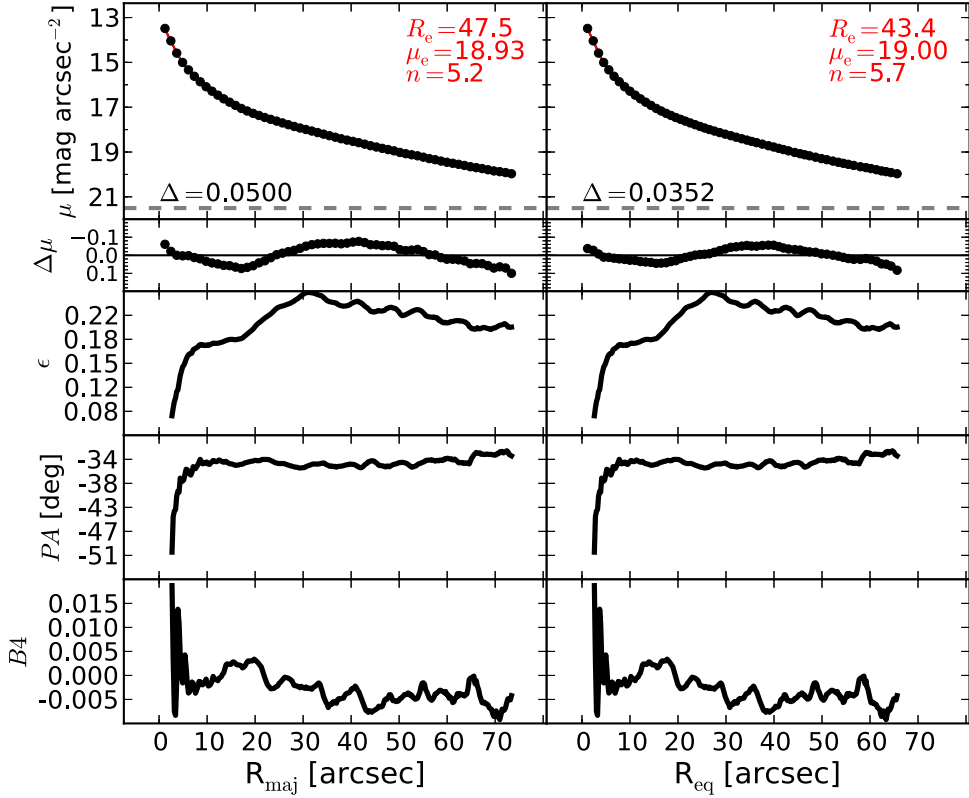


Figure 55. NGC 3608: an elliptical galaxy with an unresolved partially depleted core (Rusli et al. 2013a) and a kinematically decoupled core (ATLAS^{3D}, SLUGGS). We find that masking the nuclear region of this galaxy is unnecessary, and we fit the light profile with a single Sérsic model.

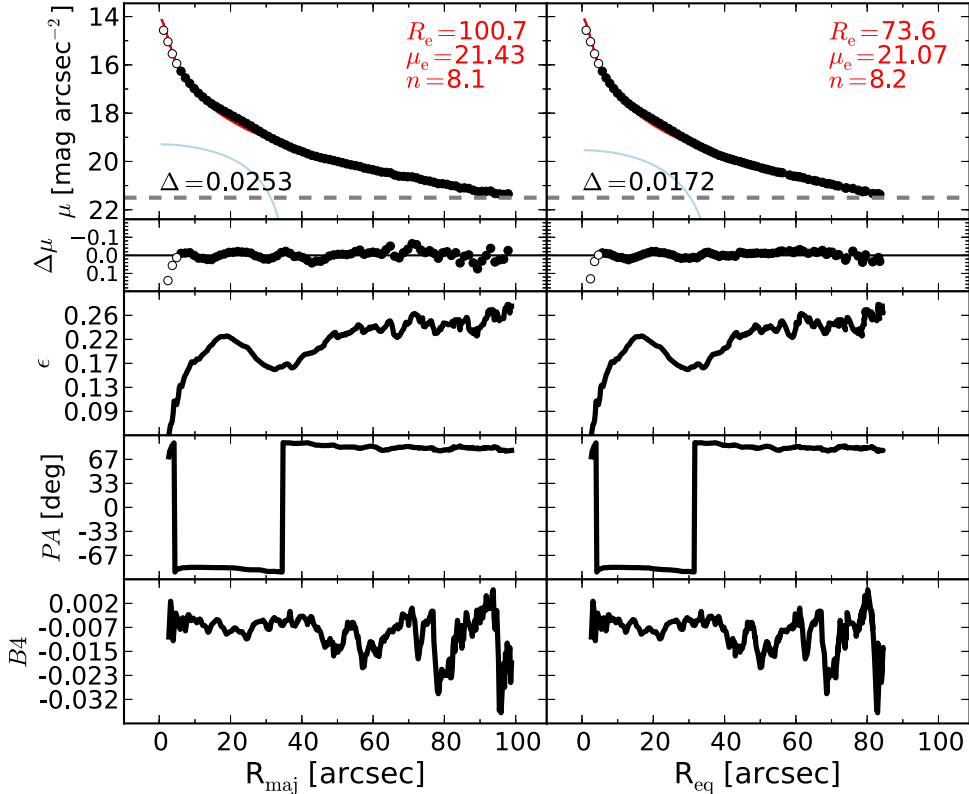


Figure 56. NGC 3842: the brightest member of the Leo Cluster (Abell 1367), an elliptical galaxy with an unresolved partially depleted core (Rusli et al. 2013a; Dullo & Graham 2014). The light profile presents a swelling at $R_{\text{maj}} \sim 20''$, and the ellipticity profile has a peak in the same position. One can also glimpse a faint elongated oval in the unsharp mask. The innermost $6.''1$ are excluded from the fit. A single Sérsic model is not sufficient to provide a good description of the galaxy light profile; therefore, we add a second component (Ferrer function) to account for the embedded lens.

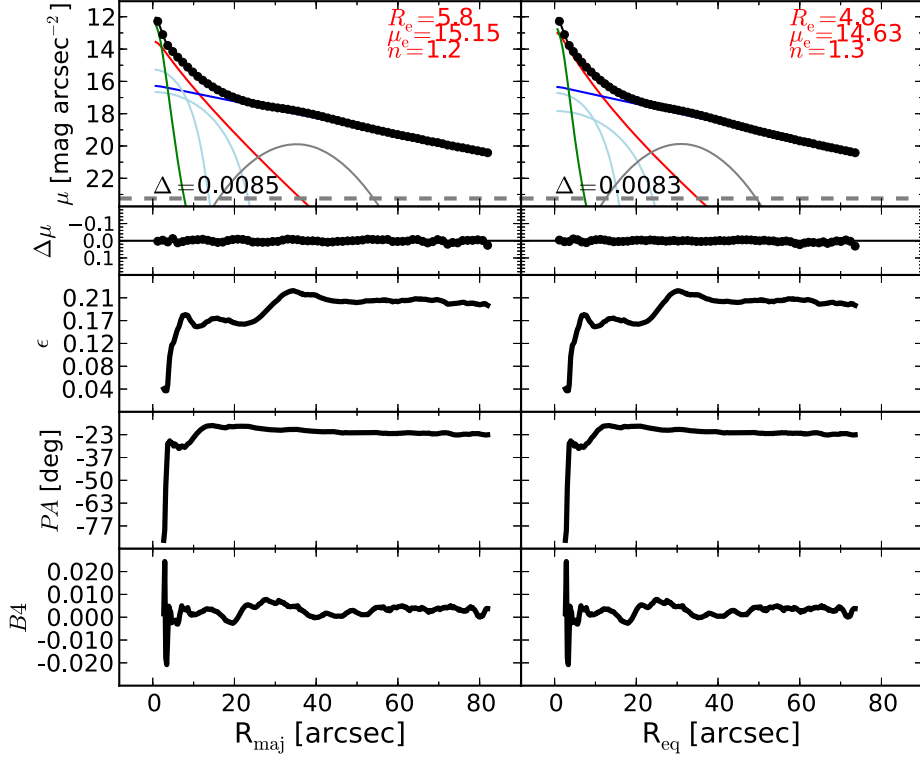


Figure 57. NGC 3998: a barred lenticular galaxy with a Seyfert AGN and nuclear dust (Knapp et al. 1996). Despite its large stellar velocity dispersion, this galaxy does not have a partially depleted core. Gutiérrez et al. (2011) identified a bar at $R_{\text{maj}} \lesssim 8''$, a ring between $30'' \lesssim R_{\text{maj}} \lesssim 50''$, and an antitruncation in the light profile of the disk at $R_{\text{maj}} \sim 122''$. Laurikainen et al. (2010) found that NGC 3998 features a weak bar at $R_{\text{maj}} < 8''$, a bright lens at $R_{\text{maj}} < 15''$, and a weak bump in the surface brightness profile at $R_{\text{maj}} \sim 40''$. We see three distinct peaks in the ellipticity profile. The first two peaks occur at $R_{\text{maj}} \sim 7''$ and $R_{\text{maj}} \sim 15''$, and they correspond to a weak bar and to a faint oval component, respectively. These components are fit with two Ferrer functions. The third peak at $R_{\text{maj}} \sim 35''$ coincides with a bump in the surface brightness profile and is produced by a ring. The AGN component is modeled with a Gaussian profile.

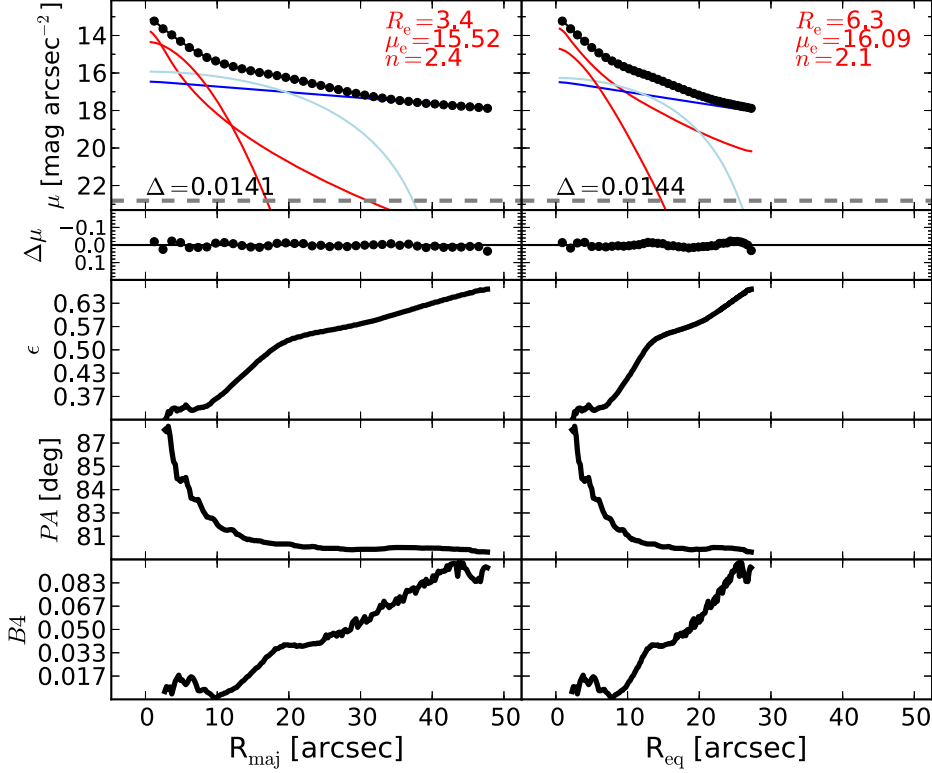


Figure 58. NGC 4026: an edge-on lenticular galaxy with a nuclear stellar disk (with size $\lesssim 0''.5$; Lledo et al. 2010). The unsharp mask reveals the presence of a bar ($R_{\text{maj}} \lesssim 30''$) and a disky component embedded in the bulge that is responsible for the peak at $R_{\text{maj}} \sim 5''$ in the B4 profile. The disky component can also be recognized in the velocity map (ATLAS^{3D}). The bar is fit with a Ferrer function and the inner disk with a low- n Sérsic profile. We do not model the nuclear component to avoid degeneracies.

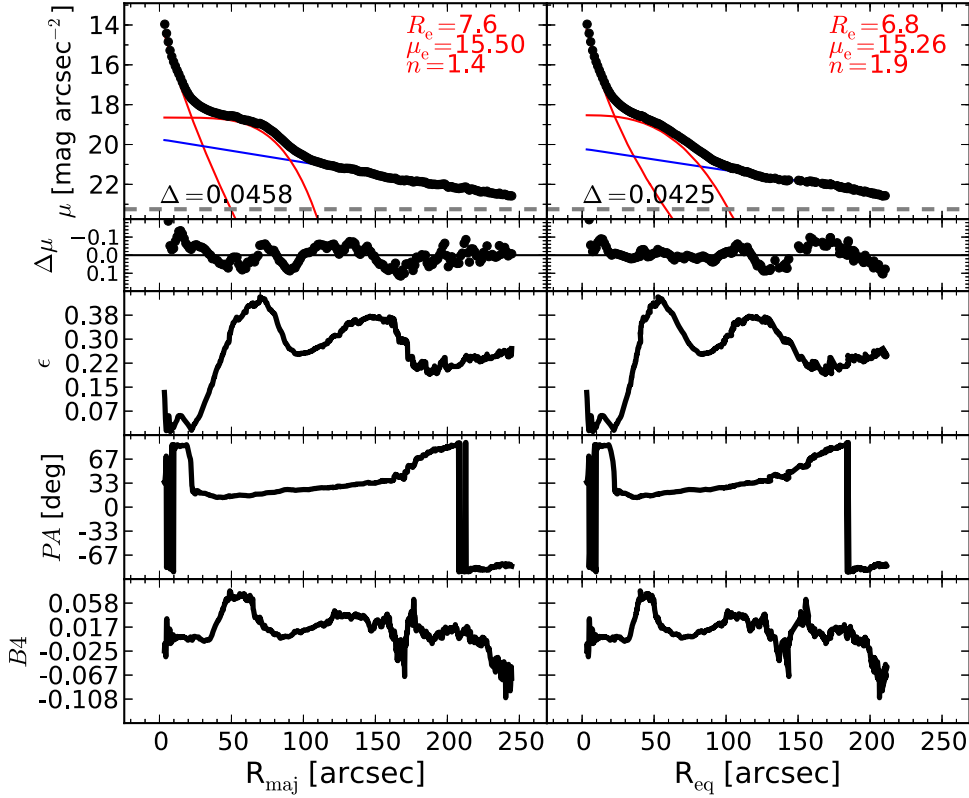


Figure 59. NGC 4151: a face-on barred spiral galaxy that hosts a Seyfert AGN (Véron-Cetty & Véron 2006) and circumnuclear dust (Pott et al. 2010). The nucleus of this galaxy is very bright, and the IRAF task `ellipse` fails at fitting the isophotes within $R_{\text{maj}} < 4''$; thus, our light profile starts at $R_{\text{maj}} \sim 4''$. The bar is fit with a low- n Sérsic profile.

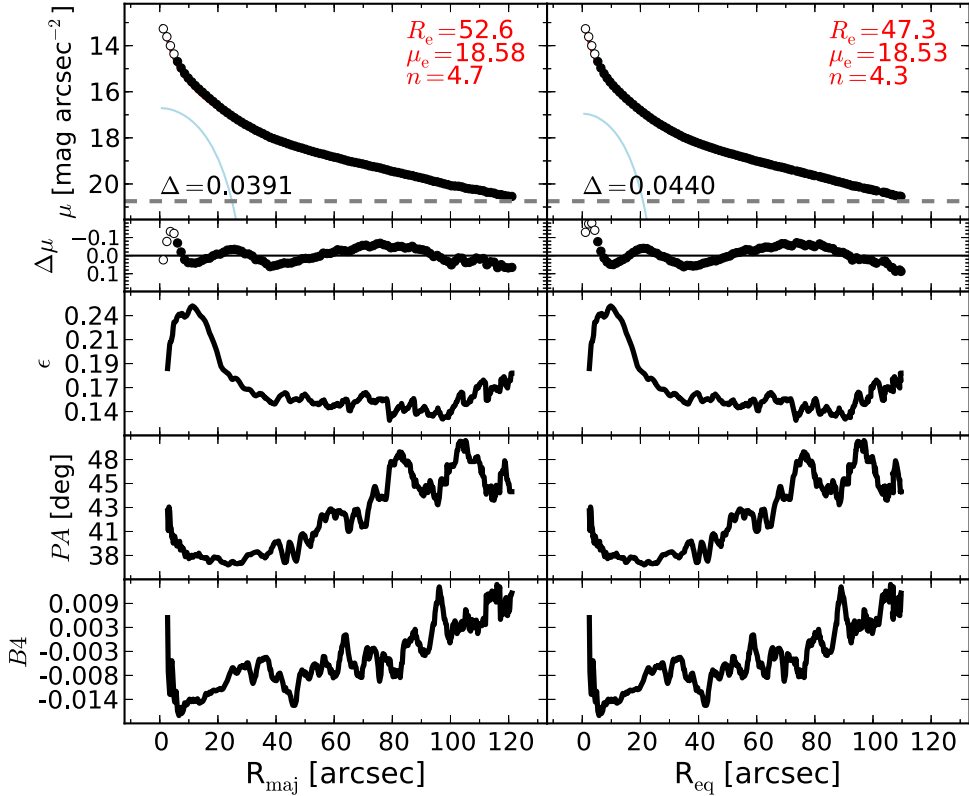


Figure 60. NGC 4261: an elliptical galaxy with a LINER nucleus (Véron-Cetty & Véron 2006) and a dusty nuclear disk (Tran et al. 2001). The galaxy features an unresolved partially depleted core (Rusli et al. 2013a). The ellipticity profile has a peak at $R_{\text{maj}} \sim 10''$, revealing the presence of an embedded component, which we model with a Ferrer function. The data within the innermost $6''$ are excluded from the fit.

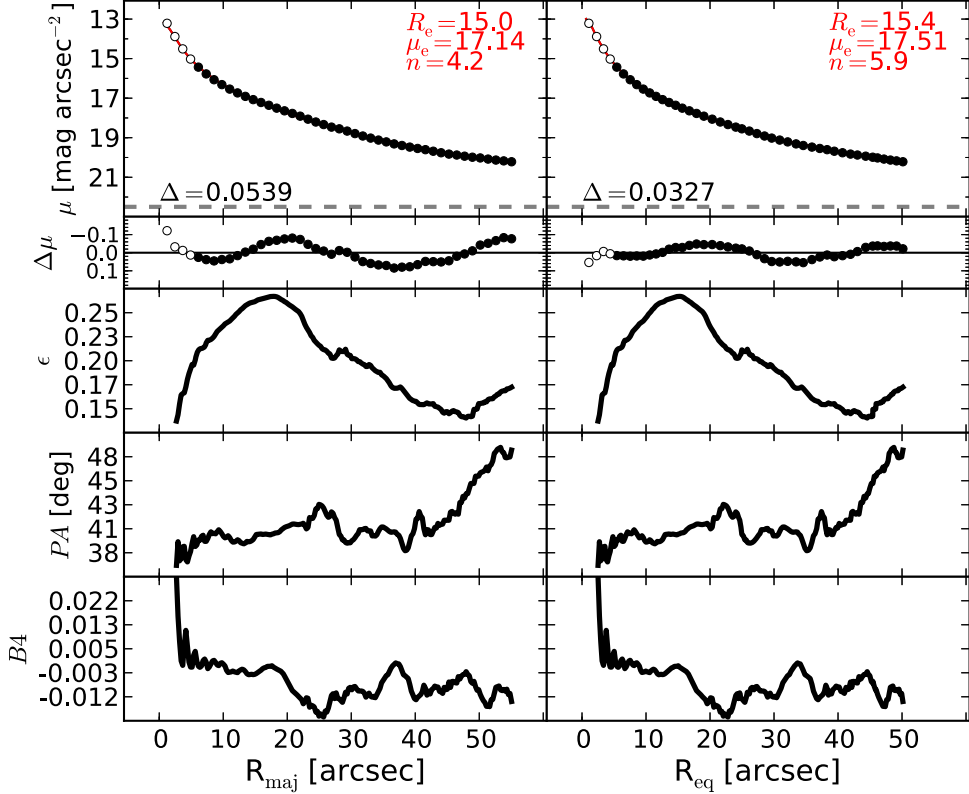


Figure 61. NGC 4291: an elliptical galaxy with an unresolved partially depleted core (Rusli et al. 2013a). After excluding the data within the innermost $6''$ from the fit, we observe that NGC 4291 can be reasonably well modeled with a Sérsic profile.

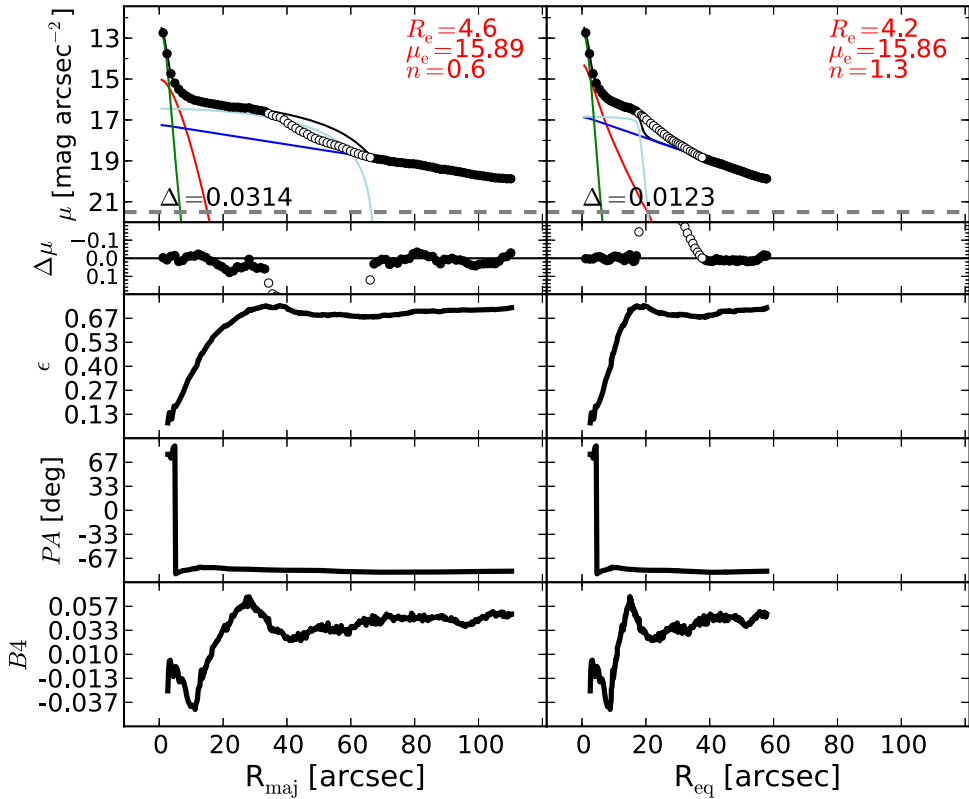


Figure 62. NGC 4388: an edge-on spiral galaxy with a Seyfert AGN (Véron-Cetty & Véron 2006) and copious nuclear dust (Martini et al. 2003). The peaks at $R_{\text{maj}} \sim 30''$ in the ellipticity and $B4$ profiles signal the presence of a bar. The data between $35'' \lesssim R_{\text{maj}} \lesssim 65''$ are excluded from the fit. The AGN component is fit with a Gaussian profile.

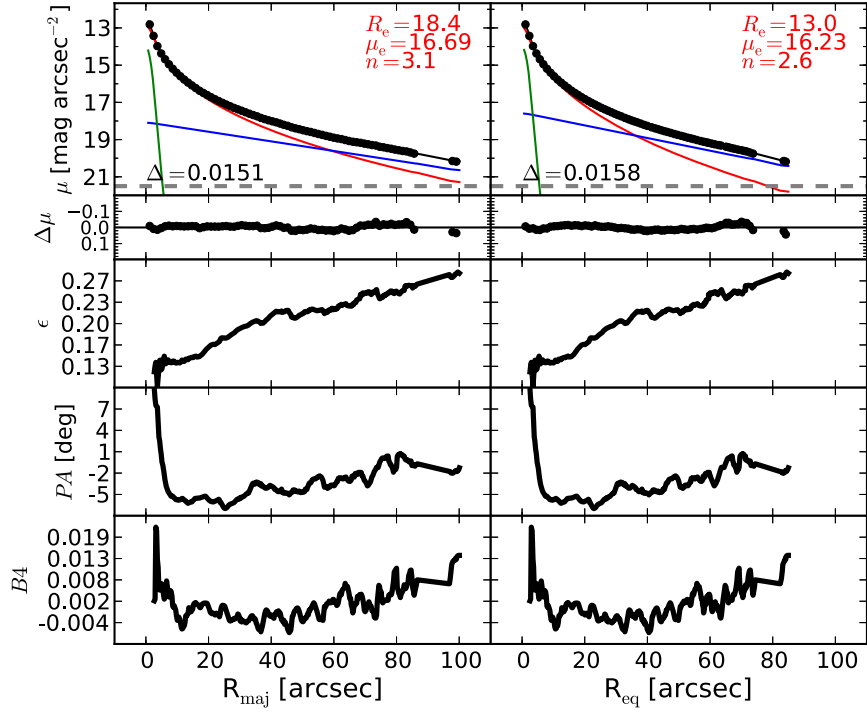


Figure 63. NGC 4459: a lenticular galaxy, whose disk profile has been reported to have an antitruncation at $R_{\text{maj}} \sim 119''$ (Gutiérrez et al. 2011). The ellipticity constantly increases across the entire observed radial range ($R_{\text{maj}} \lesssim 100''$). This is an indication that, going from the galaxy center to the outskirts, the disk component becomes increasingly more important over the spheroidal component. However, the lack of a plateau in the ellipticity profile at large radii implies that at $R_{\text{maj}} \sim 100''$ the contribution from the bulge is still significant compared to that of the disk. We note that the antitruncation reported by Gutiérrez et al. (2011) could be an artificial feature produced by the transition from the Sérsic bulge to the exponential disk. According to their analysis of the surface brightness profile of NGC 4459 (their Figure 14), the contribution from the disk completely overcomes that of the bulge beyond $R_{\text{maj}} \gtrsim 60''$. In the surface brightness profile, they identified two exponential declines with different scale lengths (the first between $60'' \lesssim R_{\text{maj}} \lesssim 110''$, and the second beyond $R_{\text{maj}} \gtrsim 120''$). However, we checked that in the radial range $60'' \lesssim R_{\text{maj}} \lesssim 110''$ the surface brightness profile is not a perfect exponential, but presents a curvature. This can be securely assessed only by fitting the data within the mentioned radial range with a single exponential function and plotting the residuals; if the residuals betray a curvature, the data cannot be accommodated by a single exponential function. According to our decomposition, the disk of NGC 4459 starts dominating beyond $R_{\text{maj}} \gtrsim 100''$. The exponential function of our model seems to nicely match the “second” exponential decline identified by Gutiérrez et al. (2011). We do not find evidence for any embedded components in our data. A nuclear light excess is modeled with a Gaussian profile.

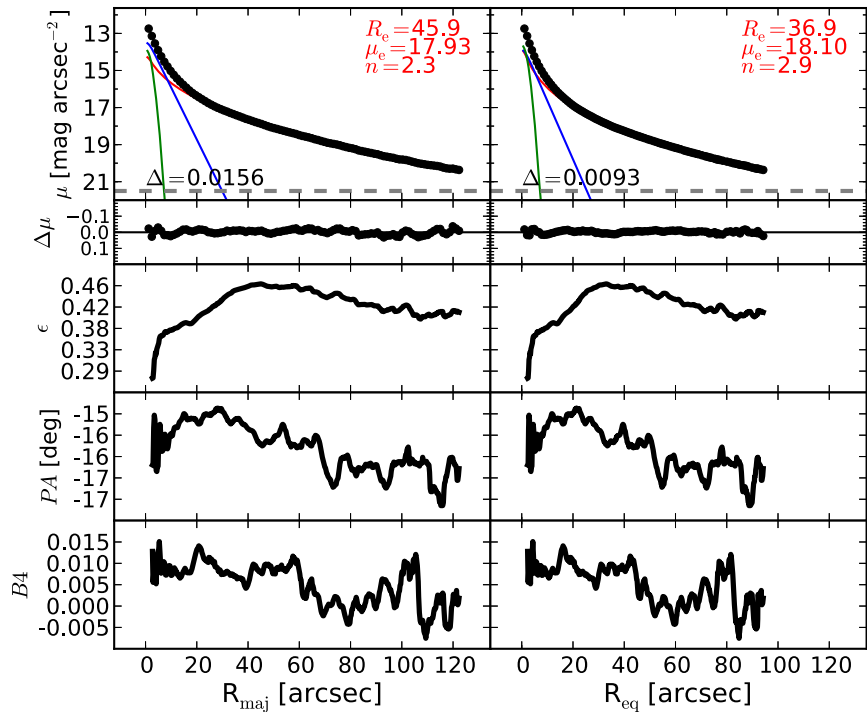


Figure 64. NGC 4473: an elliptical galaxy with an embedded disk (Ledo et al. 2010). The disk is clearly visible in the velocity map (ATLAS^{3D}, SLUGGS). We account for a nuclear excess of light by adding a narrow Gaussian function to the model.

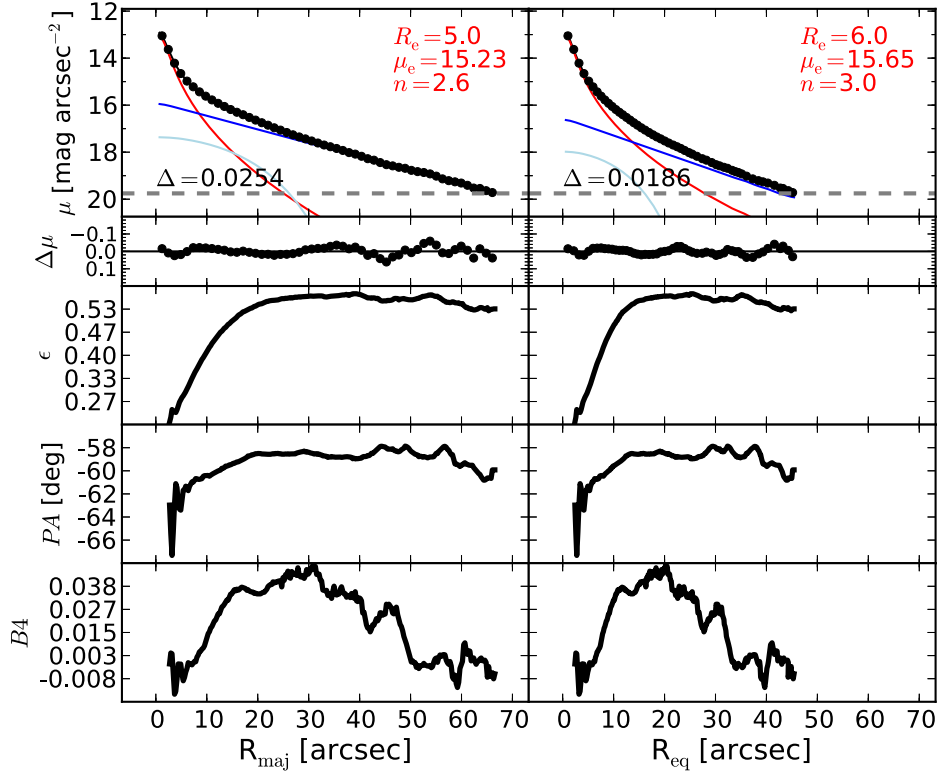


Figure 65. NGC 4564: an edge-on lenticular galaxy. In the unsharp mask, one can glimpse an oval structure extending out to $R_{\text{maj}} \lesssim 15''$ (see the peak in the $B4$ profile). Fitting NGC 4564 with a Sérsic + exponential model produces poor residuals. However, the addition of a Ferrer function to the model dramatically improves the fit and smoothes the residuals.

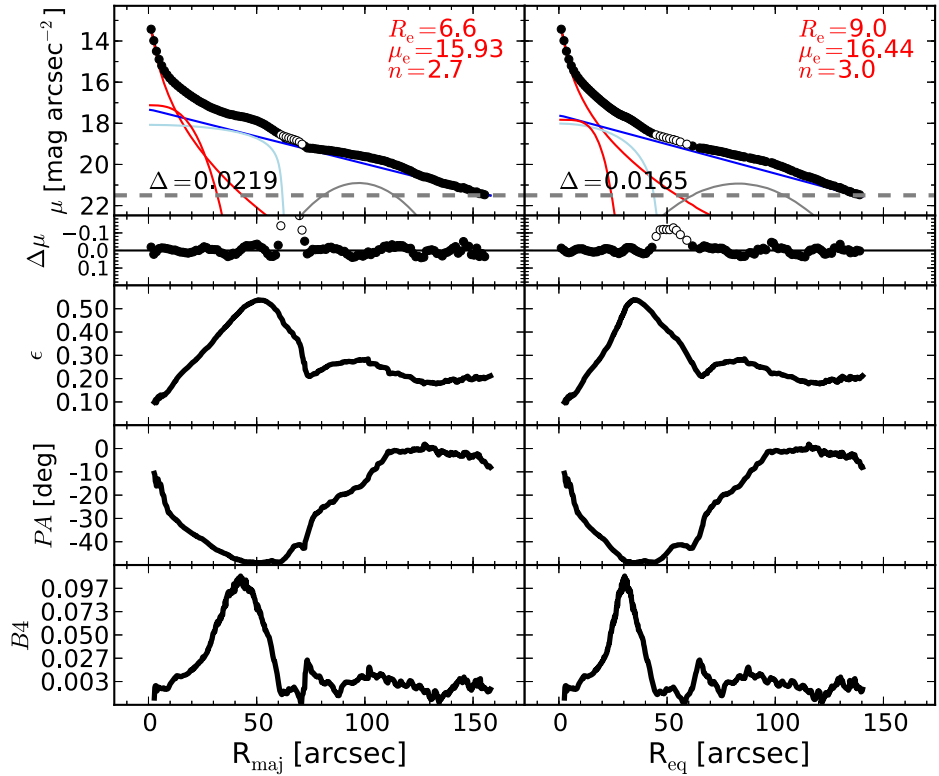


Figure 66. NGC 4596: an edge-on barred lenticular galaxy. The morphology of this galaxy is quite complex. The bar extends out to $R_{\text{maj}} \lesssim 50''$ and concludes in two evident ansae. The large-scale disk features a wide ring that is responsible for the curvature in the light profile observed within $60'' \lesssim R_{\text{maj}} \lesssim 130''$ (see also Comerón et al. 2014). An additional embedded disk component ($R_{\text{maj}} \lesssim 15''$) can be recognized in the $B4$ profile and in the velocity map. The bump in the light profile within $60'' \lesssim R_{\text{maj}} \lesssim 70''$ corresponds to the ansae of the bar, and this data range is therefore excluded from the fit. The large-scale bar is fit with a Ferrer function and the inner disk with a low- n Sérsic profile.

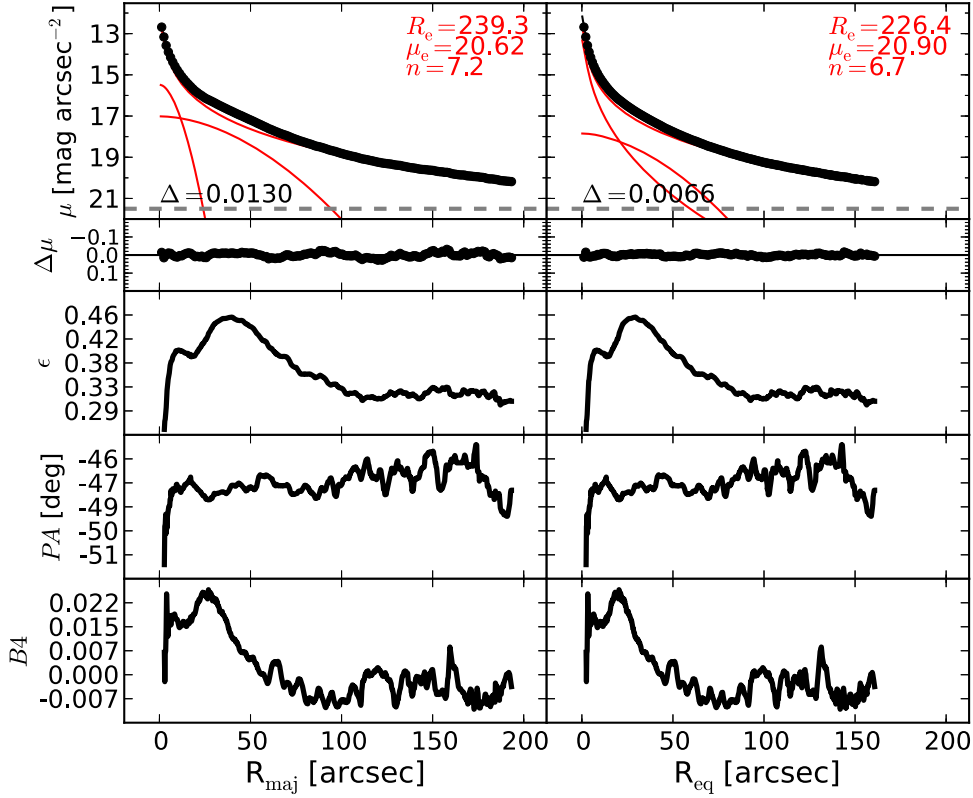


Figure 67. NGC 4697: an elliptical galaxy with an embedded disk (Scorza & Bender 1995). The velocity map (ATLAS^{3D}, SLUGGS) and the unsharp mask of NGC 4697 clearly show the presence of an intermediate-size disk embedded in the galaxy's spheroidal component. However, the ellipticity profile presents two peaks. The peak at $R_{\text{maj}} \sim 40''$ corresponds to the intermediate-size embedded disk just mentioned, while the peak at $R_{\text{maj}} \sim 10''$ pertains to a smaller inner disk. After testing different decomposition models, in which we fit the two embedded disks with different functions (exponential, Sérsic, Ferrer), while always describing the main spheroidal component with a Sérsic profile, we noticed that the spheroid parameters do not significantly vary among the various decompositions. Our preferred model for NGC 4697 consists of a Sérsic bulge + two Sérsic inner disks.

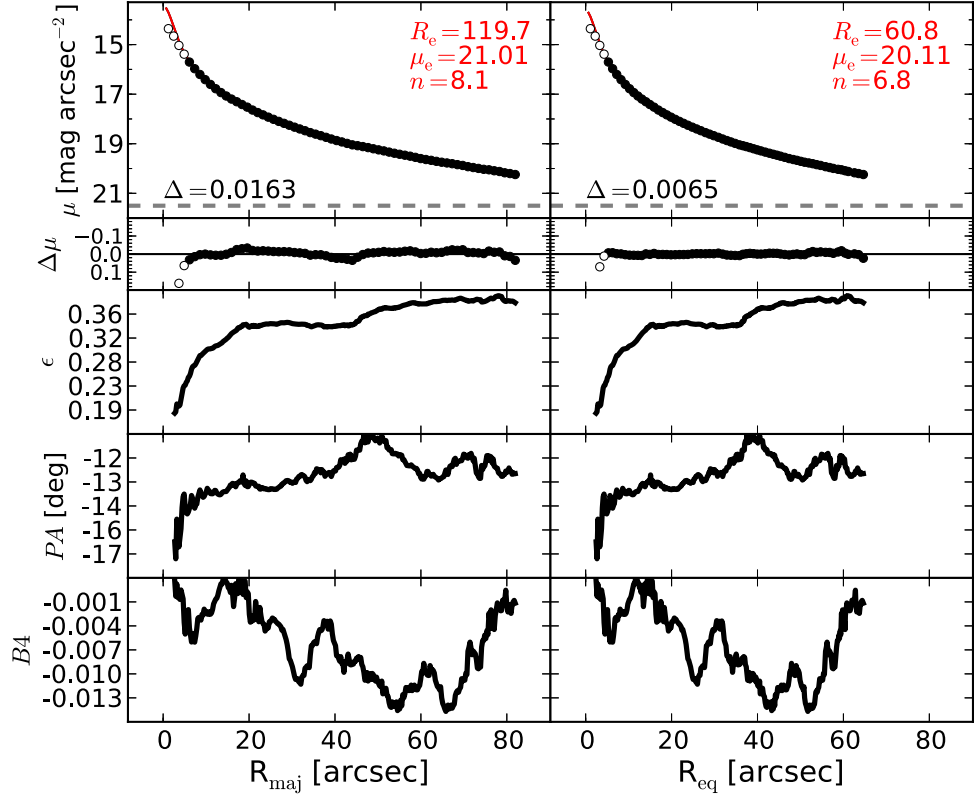


Figure 68. NGC 4889: the brightest member of the Coma Cluster, an elliptical galaxy with an unresolved partially depleted core (Rusli et al. 2013a). We exclude the innermost $6''$ from the fit and successfully model the galaxy with a single Sérsic profile.

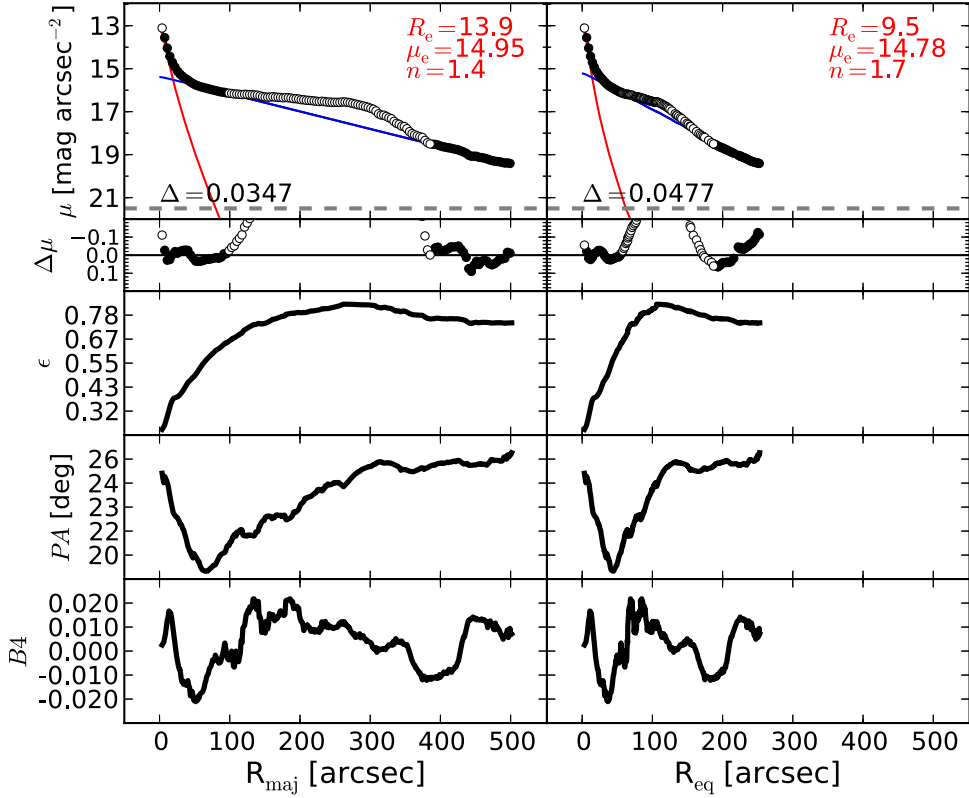


Figure 69. NGC 4945: an edge-on, dusty spiral galaxy that hosts a Seyfert AGN (Lin et al. 2011). The light profile has an obvious bump that can be ascribed to the bar. This bump cannot be easily modeled with a Ferrer function or with a Sérsic profile; thus, we exclude the data in the range $100'' \lesssim R_{\text{maj}} \sim 400''$ from the fit. We also exclude the data within the innermost $6.''4$ owing to the contribution from the AGN.

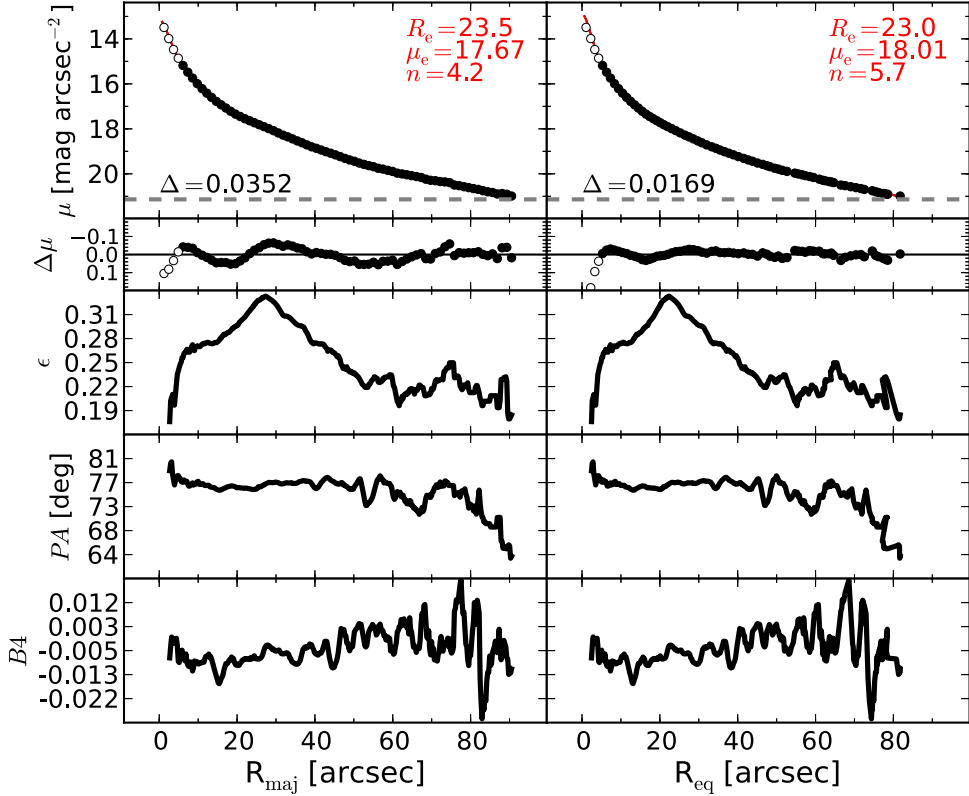


Figure 70. NGC 5077: an elliptical galaxy with an unresolved partially depleted core (Trujillo et al. 2004). We mask the data within the innermost $6.''1$ and fit the galaxy with a Sérsic profile.

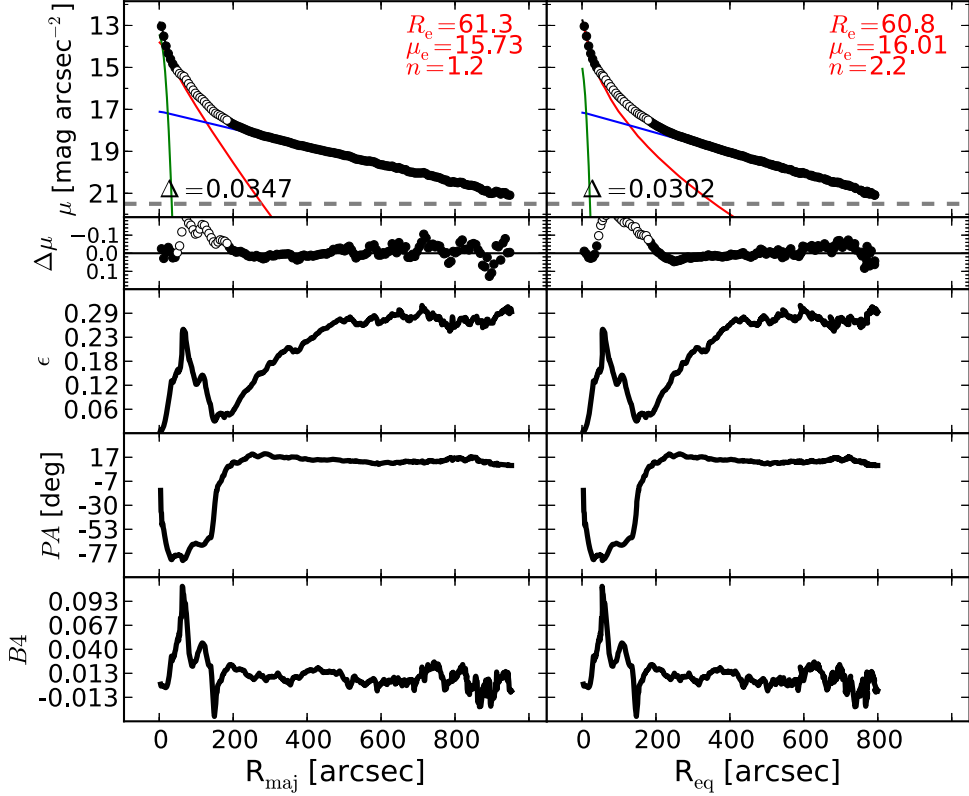


Figure 71. NGC 5128: a merging system. The data within $50'' \lesssim R_{\text{maj}} \lesssim 200''$ are excluded from the fit.

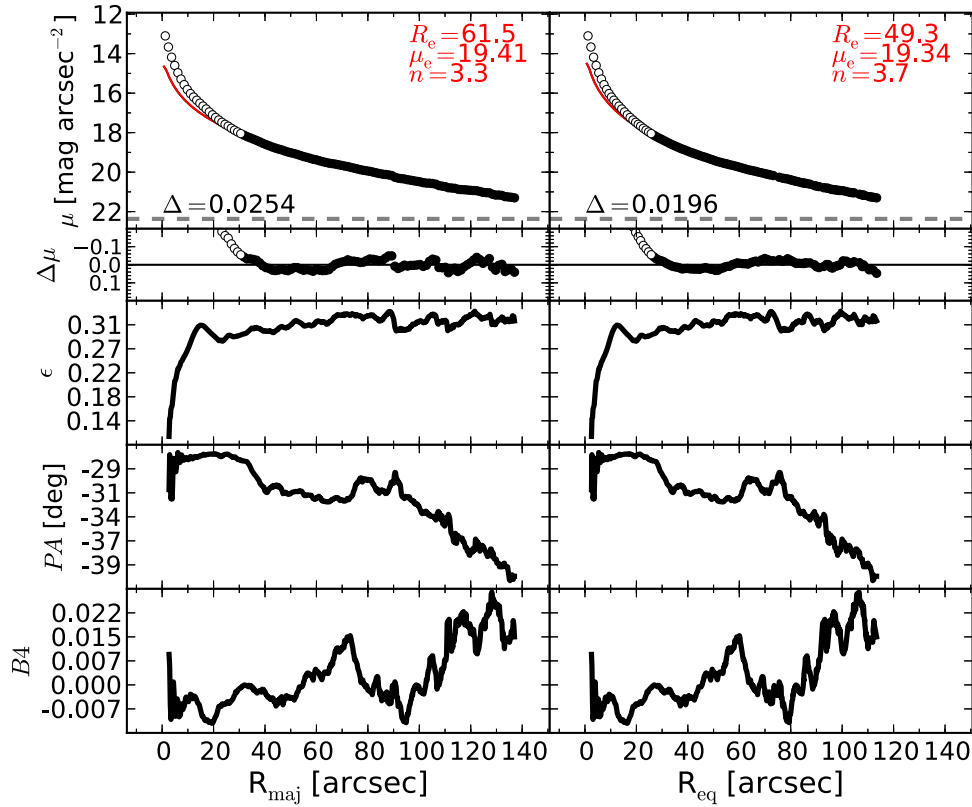


Figure 72. NGC 5576: an elliptical galaxy with a disturbed morphology. The isophotal parameters suggest the presence of an embedded disk ($R_{\text{maj}} \lesssim 20''$), but attempts to account for such a component were unsuccessful. The data within $R_{\text{maj}} \lesssim 36''$ are excluded from the fit, and the galaxy is modeled with a Sérsic profile.

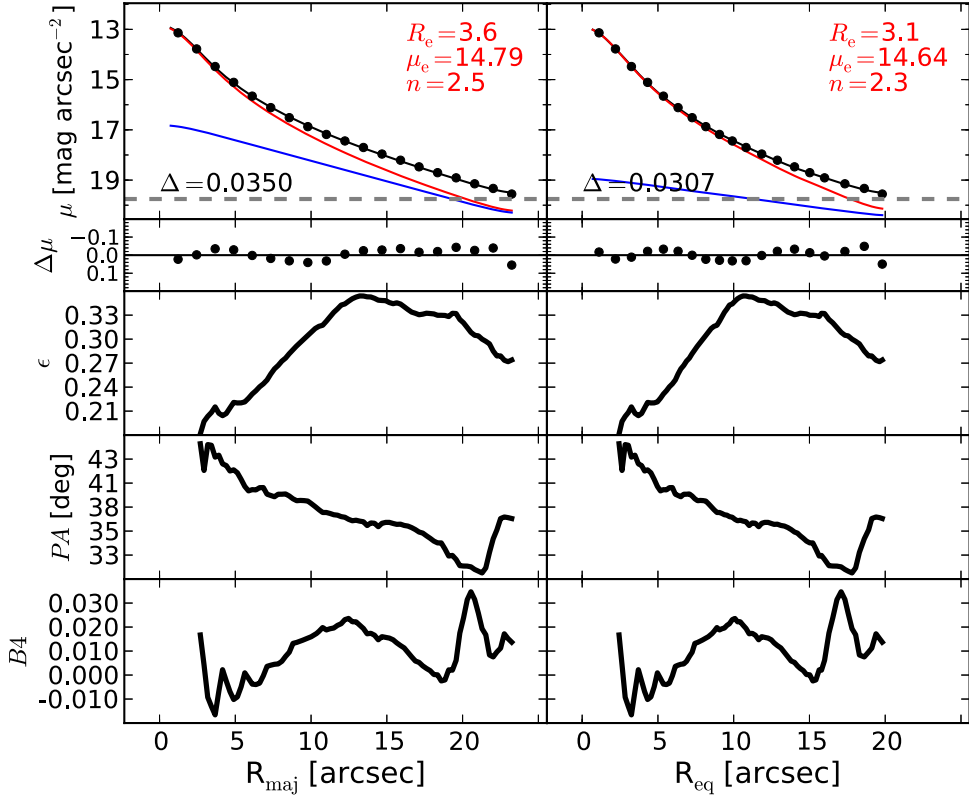


Figure 73. NGC 5845: a lenticular galaxy. From the unsharp mask and the velocity map (ATLAS^{3D}), we identify a disk, but it is not clear whether the disk is large scale or intermediate scale. The ellipticity profile has a peak at $R_{\text{maj}} \sim 13''$, which suggests that the disk is indeed intermediate scale, i.e., it does not dominate at large radii.

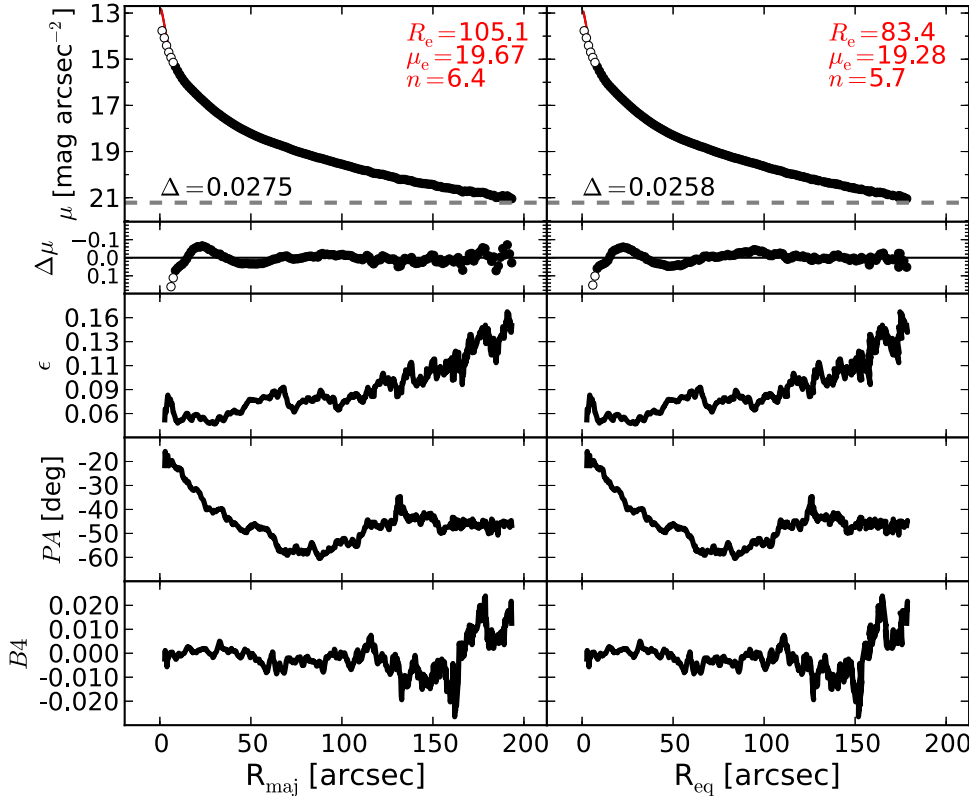


Figure 74. NGC 5846: an elliptical galaxy with an unresolved partially depleted core (Rusli et al. 2013a). This galaxy has a LINER nucleus (Carrillo et al. 1999) and filamentary nuclear dust (Tran et al. 2001). It also displays a strong isophotal twist between its center and $R_{\text{maj}} \sim 70''$. The light profile presents a slight bump at $R_{\text{maj}} \sim 20''$. However, the isophotal parameters, the unsharp mask, and the velocity map (ATLAS^{3D}) lack clear evidence for an embedded component. We thus model NGC 5846 with a single Sérsic profile, after masking the data within the innermost $6''$.

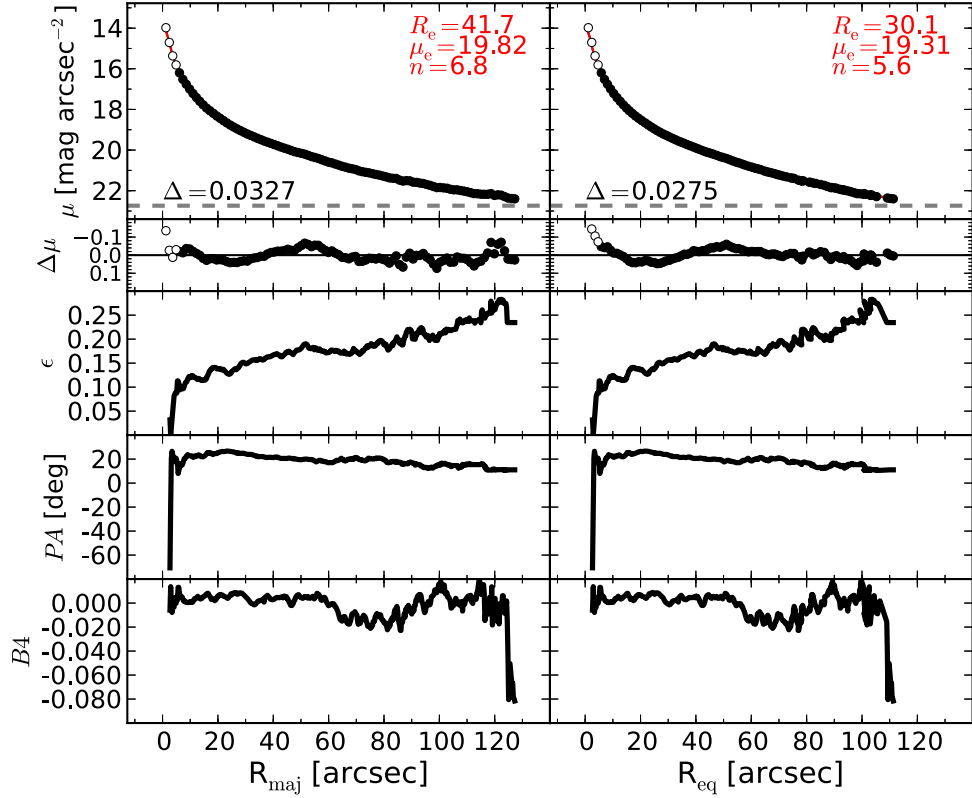


Figure 75. NGC 6251: an elliptical galaxy. Its large stellar velocity dispersion suggests the presence of a partially depleted core. The galaxy features a nuclear disk of dust (Ferrarese & Ford 1999) and a Seyfert AGN (Panessa & Bassani 2002). We mask the data within the innermost $6''.1$. A single Sérsic profile provides a good description of this galaxy.

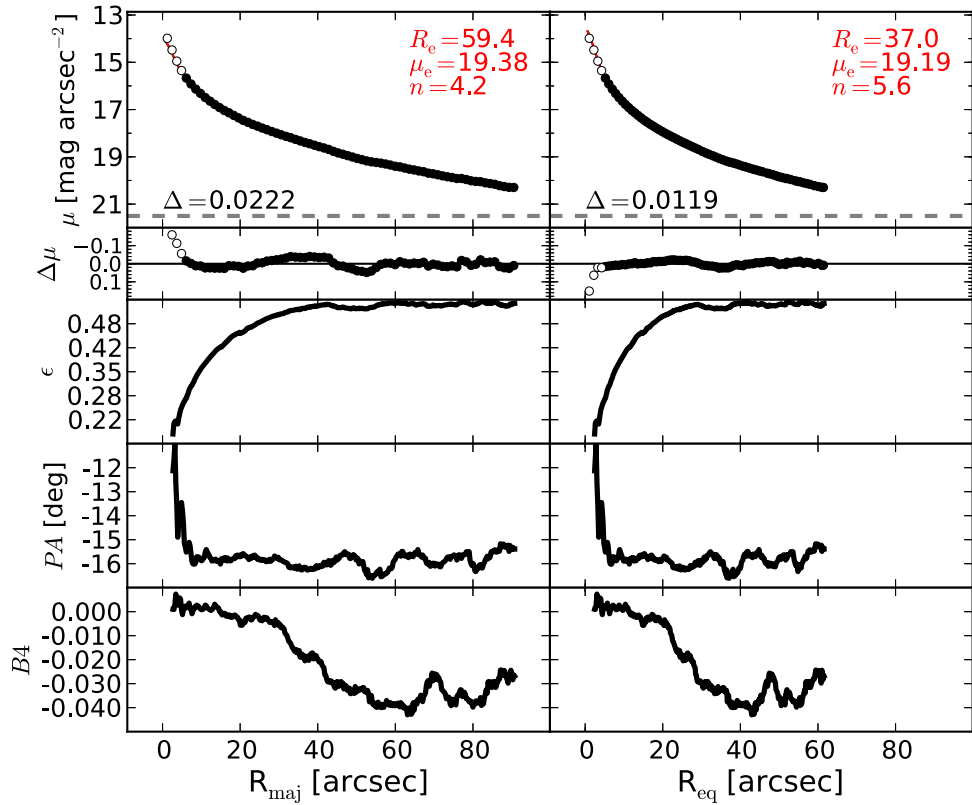


Figure 76. NGC 7052: an elliptical galaxy with an unresolved partially depleted core (Quillen et al. 2000). We mask the data within the innermost $6''.1$ and model the galaxy with a single Sérsic profile.

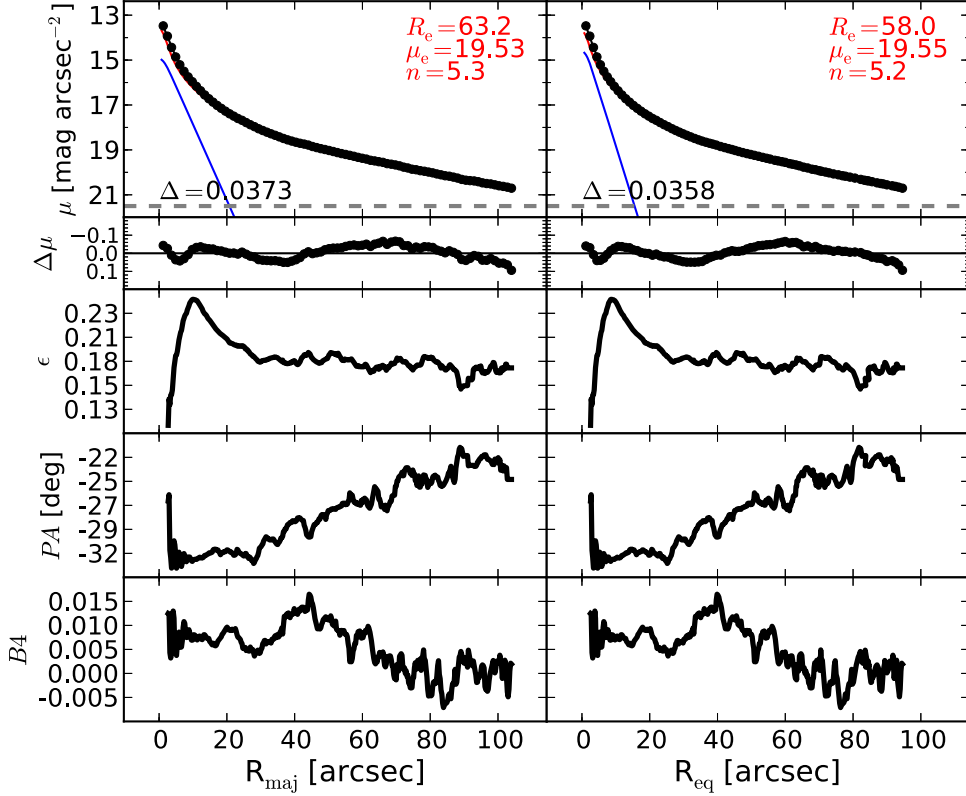


Figure 77. NGC 7619: an elliptical galaxy with an unresolved partially depleted core (Rusli et al. 2013a). We identified an embedded disk signaled by the peak at $R_{\text{maj}} \sim 10''$ in the ellipticity profile. The velocity map of this galaxy confirms the presence of a fast-rotating component (J. Falcon-Barroso 2015, private communication). We note that the residuals obtained from our bulge + inner-disk model do not suggest the presence of a partially depleted core.

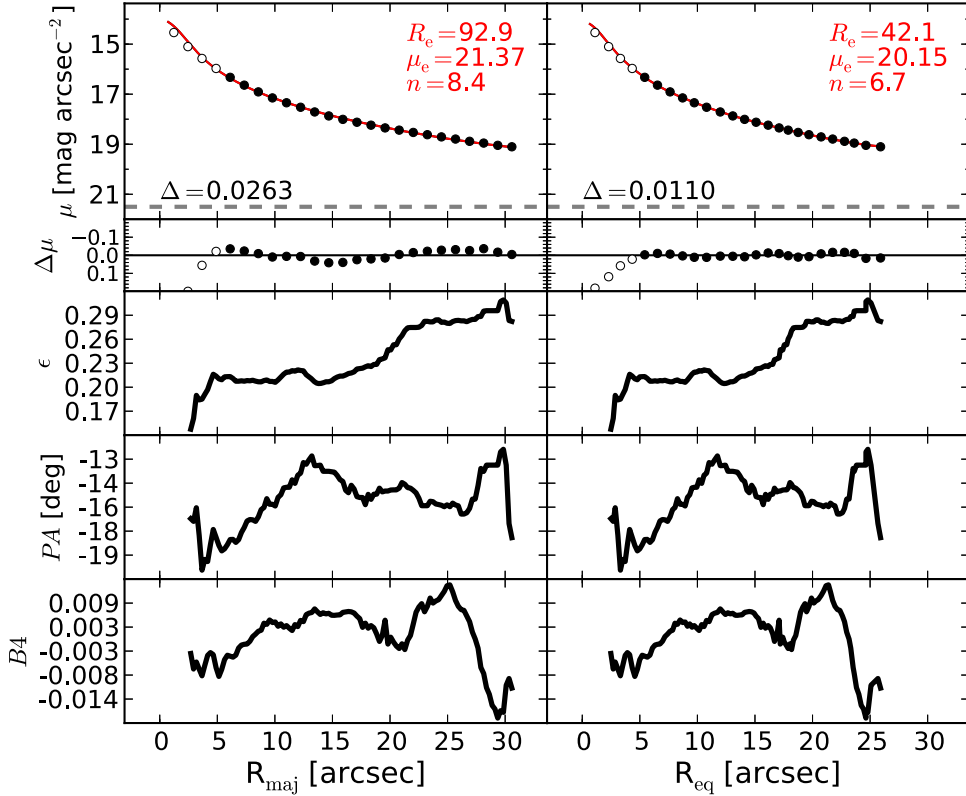


Figure 78. NGC 7768: an elliptical galaxy with an unresolved partially depleted core (Rusli et al. 2013a). The image of NGC 7768 is corrupted by a saturated star, which lies close to the galaxy. The sky background is not constant across the image. To be safe, we fit only the data within the innermost $R_{\text{maj}} \lesssim 30''$, where the contribution from the background is negligible. The data within $R_{\text{maj}} < 6.''1$ are excluded from the fit.

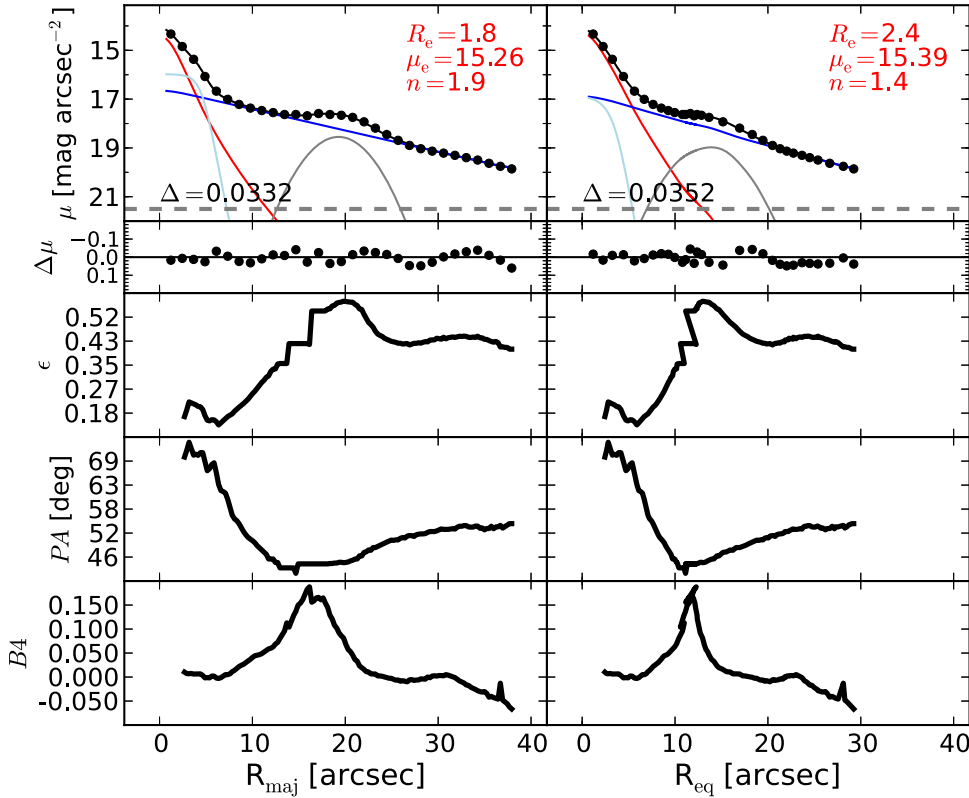


Figure 79. UGC 03789: a face-on spiral galaxy, featuring a ring ($R_{\text{maj}} \sim 20''$) and a nuclear bar ($R_{\text{maj}} \lesssim 4''$), which can be seen in the unsharp mask and produces corresponding peaks in the ellipticity and PA profiles. The bar is fit with a Ferrer function.

galaxy light profiles; therefore, their models implicitly include “m-n” or “m-c.” In the table caption, we comment on the most significant discrepancies between our results and those obtained by the other studies.

G.S. acknowledges the invaluable support received from Alessandro Marconi, Eleonora Sani, and Leslie Hunt in the early stages of this research. G.S. warmly thanks Chieng Peng, Peter Erwin, Luca Cortese, Giuseppe Gavazzi, Bililign Dullo, Paolo Bonfini, Elisabete Lima Da Cunha, and Gonzalo Diaz for useful discussion. We thank the anonymous referee for their thorough review and highly appreciate the comments and suggestions, which significantly contributed to improving the quality of the publication. This research was supported by Australian Research Council funding through grants DP110103509 and FT110100263. This work is based on observations made with the IRAC instrument (Fazio et al. 2004) on board the *Spitzer Space Telescope*, which is operated by the Jet Propulsion Laboratory, California Institute of Technology, under a contract with NASA. This research has made use of the GOLDMine database (Gavazzi et al. 2003) and the NASA/IPAC Extragalactic Database (NED), which is operated by the Jet Propulsion Laboratory, California Institute of Technology, under contract with the National Aeronautics and Space Administration.

APPENDIX 1D ANALYTICAL FUNCTIONS

Here we provide the mathematical expressions of the analytical functions used to model the observed surface brightness profiles, $\mu(R)$, of galaxies. The projected galactic

radius, R , corresponds to the distance of the isophotes from the galaxy center (along either the major or equivalent axis).

The Sérsic (1963, 1968) model is a three-parameter function of the following form:

$$\mu_{\text{Sérsic}}(\mu_e, R_e, n; R) = \mu_e + \frac{2.5 b_n}{\ln(10)} \left[\left(\frac{R}{R_e} \right)^{1/n} - 1 \right], \quad (5)$$

(Caon et al. 1993; Andredakis et al. 1995; Graham & Driver 2005), where μ_e is the surface brightness at the effective radius R_e that encloses half of the total light from the model. The Sérsic index n is the parameter that measures the curvature of the radial light profile, and b_n is a scalar value defined in terms of the Sérsic index n such that

$$\Gamma(2n) = 2\gamma(2n, b_n), \quad (6)$$

where Γ is the complete gamma function (Ciotti 1991) and γ is the incomplete gamma function defined by

$$\gamma(2n, x) = \int_0^x e^{-t} t^{2n-1} dt. \quad (7)$$

The exponential model is a special case ($n = 1$) of the Sérsic model. It can therefore be written as a two-parameter function such that

$$\mu_{\text{exponential}}(\mu_0, h; R) = \mu_0 + \frac{2.5}{\ln(10)} \left(\frac{R}{h} \right), \quad (8)$$

where μ_0 is the central surface brightness and h is the scale length equal to $R_e/1.678$.

The Gaussian model is another special case ($n = 0.5$) of the Sérsic model, and thus also a two-parameter function of the

following form:

$$\mu_{\text{Gaussian}}(\mu_0, \text{FWHM}; R) = \mu_0 + \frac{2.5}{\ln(10)} \left[\frac{R^2}{2(\text{FWHM}/2.355)^2} \right], \quad (9)$$

where μ_0 is the central surface brightness and FWHM is the full width at half-maximum of the Gaussian profile.

The Moffat (1969) model is a three-parameter function that can be expressed as

$$\mu_{\text{Moffat}}(\mu_0, \alpha, \beta; R) = \mu_0 - 2.5 \log \left[1 + \left(\frac{R}{\alpha} \right)^2 \right]^{-\beta}, \quad (10)$$

where μ_0 is the central surface brightness, α is related to the FWHM through

$$\text{FWHM} = 2\alpha\sqrt{2^{1/\beta} - 1}, \quad (11)$$

and β regulates the shape of the profile at large radii.

The Ferrer model is a four-parameter function defined as

$$\mu_{\text{Ferrer}}(\mu_0, R_{\text{out}}, \alpha, \beta; R) = \begin{cases} \mu_0 - 2.5 \log \left[1 - \left(\frac{R}{R_{\text{out}}} \right)^{2-\beta} \right]^{\alpha} & \text{for } R < R_{\text{out}}, \\ +\infty & \text{for } R \geq R_{\text{out}} \end{cases}, \quad (12)$$

where μ_0 is the central surface brightness, α controls the sharpness of the truncation, β is related to the central slope, and R_{out} is the outer radial limit within which the function is defined.

The symmetric Gaussian ring is a three-parameter function of the following form:

$$\mu_{\text{Gaussian}}(\mu_0, R_0, \text{FWHM}; R) = \mu_0 + \frac{2.5}{\ln(10)} \left[\frac{(R - R_0)^2}{2(\text{FWHM}/2.355)^2} \right], \quad (13)$$

where μ_0 and FWHM have the same meaning as in Equation (9), and R_0 is the radius at which the Gaussian profile is centered.

REFERENCES

- Andredakis, Y. C., Peletier, R. F., & Balcells, M. 1995, *MNRAS*, **275**, 874
 Arnold, J. A., Romanowsky, A. J., Brodie, J. P., et al. 2011, *ApJL*, **736**, L26
 Arnold, J. A., Romanowsky, A. J., Brodie, J. P., et al. 2014, *ApJ*, **791**, 80
 Athanassoula, E., & Beaton, R. L. 2006, *MNRAS*, **370**, 1499
 Beaton, R. L., Majewski, S. R., Guhathakurta, P., et al. 2007, *ApJL*, **658**, L91
 Beifiori, A., Courteau, S., Corsini, E. M., & Zhu, Y. 2012, *MNRAS*, **419**, 2497
 Bender, R. 1990, *A&A*, **229**, 441
 Caon, N., Capaccioli, M., & D'Onofrio, M. 1993, *MNRAS*, **265**, 1013
 Capaccioli, M. 1987, in IAU Symp. 127, Structure and Dynamics of Elliptical Galaxies, ed. P. T. de Zeeuw, **47**
 Cappellari, M., Emsellem, E., Krajnović, D., et al. 2011, *MNRAS*, **413**, 813
 Cappellari, M., Verolme, E. K., van der Marel, R. P., et al. 2002, *ApJ*, **578**, 787
 Carrillo, R., Masegosa, J., Dultzin-Hacyan, D., & Ordoñez, R. 1999, RMxAA, **35**, 187
 Carter, D. 1987, *ApJ*, **312**, 514
 Ciambri, B. C. 2015, arXiv:1507.02691
 Ciotti, L. 1991, *A&A*, **249**, 99
 Comastri, A., Gilli, R., Marconi, A., Risaliti, G., & Salvati, M. 2015, arXiv:1501.03620
 Comerón, S., Elmegreen, B. G., Salo, H., et al. 2012, *ApJ*, **759**, 98
 Comerón, S., Knapen, J. H., Beckman, J. E., et al. 2010, *MNRAS*, **402**, 2462
 Comerón, S., Salo, H., Laurikainen, E., et al. 2014, *A&A*, **562**, A121
 Contini, T., Consideré, S., & Davoust, E. 1998, *A&AS*, **130**, 285
 de Vaucouleurs, G., de Vaucouleurs, A., Corwin, H. G., Jr., et al. 1991, Third Reference Catalogue of Bright Galaxies. Vol. I: Explanations and References. Vol. II: Data for Galaxies Between 0^h and 12^h. Vol. III: Data for Galaxies Between 12^h and 24^h
 Diaz, A. I., Prieto, M. A., & Wamsteker, W. 1988, *A&A*, **195**, 53
 D'Onofrio, M., Zaggia, S. R., Longo, G., Caon, N., & Capaccioli, M. 1995, *A&A*, **296**, 319
 Dressler, A. 1989, in IAU Symp. 134, Active Galactic Nuclei, ed. D. E. Osterbrock, & J. S. Miller, **217**
 Dullo, B. T., & Graham, A. W. 2013, arXiv:1310.5867
 Dullo, B. T., & Graham, A. W. 2014, *MNRAS*, **444**, 2700
 Elmegreen, B. G., & Elmegreen, D. M. 1985, *ApJ*, **288**, 438
 Elmegreen, D. M., Chromey, F. R., & Johnson, C. O. 1995, *AJ*, **110**, 2102
 Elmegreen, D. M., Elmegreen, B. G., & Eberwein, K. S. 2002, *ApJ*, **564**, 234
 Emsellem, E., Cappellari, M., Krajnović, D., et al. 2011, *MNRAS*, **414**, 888
 Erwin, P. 2004, *A&A*, **415**, 941
 Erwin, P. 2015, *ApJ*, **799**, 226
 Erwin, P., Beckman, J. E., & Pohlen, M. 2005, *ApJL*, **626**, L81
 Erwin, P., Beltrán, J. C. V., Graham, A. W., & Beckman, J. E. 2003, *ApJ*, **597**, 929
 Erwin, P., & Debattista, V. P. 2013, *MNRAS*, **431**, 3060
 Erwin, P., & Gadotti, D. A. 2012, *AdAst*, **2012**, 4
 Erwin, P., Gutiérrez, L., & Beckman, J. E. 2012, *ApJL*, **744**, L11
 Erwin, P., Pohlen, M., & Beckman, J. E. 2008, *AJ*, **135**, 20
 Erwin, P., & Sparke, L. S. 2003, *ApJS*, **146**, 299
 Fazio, G. G., Hora, J. L., Allen, L. E., et al. 2004, *ApJS*, **154**, 10
 Ferrarese, L., Côté, P., Jordán, A., et al. 2006, *ApJS*, **164**, 334
 Ferrarese, L., & Ford, H. C. 1999, *ApJ*, **515**, 583
 Ferrarese, L., & Merritt, D. 2000, *ApJL*, **539**, L9
 Fisher, D. B., & Drory, N. 2010, *ApJ*, **716**, 942
 Fontanot, F., Monaco, P., & Shankar, F. 2015, *MNRAS*, **453**, 4112
 Forbes, D. A., Brodie, J. P., & Huchra, J. 1997, *AJ*, **113**, 887
 Forbes, D. A., Franx, M., & Illingworth, G. D. 1994, *ApJL*, **428**, L49
 Franx, M., & Illingworth, G. D. 1988, *ApJL*, **327**, L55
 Gadotti, D. A. 2008, *MNRAS*, **384**, 420
 Gadotti, D. A., & de Souza, R. E. 2006, *ApJS*, **163**, 270
 Gadotti, D. A., & Sánchez-Janssen, R. 2012, *MNRAS*, **423**, 877
 Gavazzi, G., Boselli, A., Donati, A., Franzetti, P., & Scodéglio, M. 2003, *A&A*, **400**, 451
 Gebhardt, K., Bender, R., Bower, G., et al. 2000, *ApJL*, **539**, L13
 Graham, A. W. 2015, arXiv:1501.02937
 Graham, A. W., Colless, M. M., Busarello, G., Zaggia, S., & Longo, G. 1998, *A&AS*, **133**, 325
 Graham, A. W., & Driver, S. P. 2005, *PASA*, **22**, 118
 Graham, A. W., & Driver, S. P. 2007a, *ApJ*, **655**, 77
 Graham, A. W., & Driver, S. P. 2007b, *MNRAS*, **380**, L15
 Graham, A. W., Driver, S. P., Allen, P. D., & Liske, J. 2007, *MNRAS*, **378**, 198
 Graham, A. W., Dullo, B. T., & Savorgnan, G. A. D. 2015, *ApJ*, **804**, 32
 Graham, A. W., Erwin, P., Caon, N., & Trujillo, I. 2001, *ApJL*, **563**, L11
 Graham, A. W., Erwin, P., Trujillo, I., & Asensio Ramos, A. 2003, *AJ*, **125**, 2951
 Graham, A. W., & Guzmán, R. 2003, *AJ*, **125**, 2936
 Graham, A. W., & Scott, N. 2013, *ApJ*, **764**, 151
 Graham, A. W., & Scott, N. 2015, *ApJ*, **798**, 54
 Greenhill, L. J., Booth, R. S., Ellingsen, S. P., et al. 2003, *ApJ*, **590**, 162
 Grillmair, C. J., Faber, S. M., Lauer, T. R., et al. 1994, *AJ*, **108**, 102
 Gutiérrez, L., Erwin, P., Aladro, R., & Beckman, J. E. 2011, *AJ*, **142**, 145
 Häring, N., & Rix, H.-W. 2004, *ApJL*, **604**, L89
 Haynes, M. P., Giovanelli, R., Salzer, J. J., et al. 1999, *AJ*, **117**, 1668
 Jardel, J. R., Gebhardt, K., Shen, J., et al. 2011, *ApJ*, **739**, 21
 Jedrzejewski, R. I. 1987, *MNRAS*, **226**, 747
 Jun, H. D., & Im, M. 2008, *ApJL*, **678**, L97
 Khachikian, E. Y., & Weedman, D. W. 1974, *ApJ*, **192**, 581
 Kim, T., Gadotti, D. A., Sheth, K., et al. 2014, *ApJ*, **782**, 64
 Kim, T., Sheth, K., Gadotti, D. A., et al. 2015, *ApJ*, **799**, 99
 King, I. R., & Minkowski, R. 1966, *ApJ*, **143**, 1002
 Knapp, G. R., Rupen, M. P., Fich, M., Harper, D. A., & Wynn-Williams, C. G. 1996, *A&A*, **315**, L75
 Kormendy, J., & Gebhardt, K. 2001, in AIP Conf. Ser. 586, 20th Texas Symp. on Relativistic Astrophysics, ed. J. C. Wheeler, & H. Martel (Melville, NY: AIP), **363**

- Kormendy, J., & Richstone, D. 1995, *ARA&A*, **33**, 581
- Krajnović, D., Alatalo, K., Blitz, L., et al. 2013, *MNRAS*, **432**, 1768
- Krajnović, D., Emsellem, E., Cappellari, M., et al. 2011, *MNRAS*, **414**, 2923
- Laor, A., Fiore, F., Elvis, M., Wilkes, B. J., & McDowell, J. C. 1997, *ApJ*, **477**, 93
- Läske, R., Ferrarese, L., & van de Ven, G. 2014a, *ApJ*, arXiv:1311.1530
- Läske, R., Ferrarese, L., van de Ven, G., & Shankar, F. 2014b, *ApJ*, arXiv:1311.1531
- Laurikainen, E., Salo, H., & Buta, R. 2005, *MNRAS*, **362**, 1319
- Laurikainen, E., Salo, H., Buta, R., Knapen, J. H., & Comerón, S. 2010, *MNRAS*, **405**, 1089
- ledo, H. R., Sarzi, M., Dotti, M., Khochfar, S., & Morelli, L. 2010, *MNRAS*, **407**, 969
- Lin, L.-H., Taam, R. E., Yen, D. C. C., Muller, S., & Lim, J. 2011, *ApJ*, **731**, 15
- Magorrian, J., Tremaine, S., Richstone, D., et al. 1998, *AJ*, **115**, 2285
- Makovoz, D., & Marleau, F. R. 2005, *PASP*, **117**, 1113
- Marconi, A., & Hunt, L. K. 2003, *ApJL*, **589**, L21
- Martini, P., Regan, M. W., Mulchaey, J. S., & Pogge, R. W. 2003, *ApJS*, **146**, 353
- Moffat, A. F. J. 1969, *A&A*, **3**, 455
- Morrison, H., Caldwell, N., Schiavon, R. P., et al. 2011, *ApJL*, **726**, L9
- Muñoz-Mateos, J. C., Sheth, K., Gil de Paz, A., et al. 2013, *ApJ*, **771**, 59
- Munoz-Tunon, C., Prieto, M., Beckman, J., & Cepa, J. 1989, *Ap&SS*, **156**, 301
- Nieto, J.-L., Bender, R., Arnaud, J., & Surma, P. 1991, *A&A*, **244**, L25
- Nowak, N., Thomas, J., Erwin, P., et al. 2010, *MNRAS*, **403**, 646
- Panessa, F., & Bassani, L. 2002, *A&A*, **394**, 435
- Pastrav, B. A., Popescu, C. C., Tuffs, R. J., & Sansom, A. E. 2013a, *A&A*, **553**, A80
- Pastrav, B. A., Popescu, C. C., Tuffs, R. J., & Sansom, A. E. 2013b, *A&A*, **557**, A137
- Peeples, M. S., & Martini, P. 2006, *ApJ*, **652**, 1097
- Peng, C. Y., Ho, L. C., Impey, C. D., & Rix, H.-W. 2002, *AJ*, **124**, 266
- Peng, C. Y., Ho, L. C., Impey, C. D., & Rix, H.-W. 2010, *AJ*, **139**, 2097
- Pott, J.-U., Malkan, M. A., Elitzur, M., et al. 2010, *ApJ*, **715**, 736
- Quillen, A. C., Bower, G. A., & Stritzinger, M. 2000, *ApJS*, **128**, 85
- Ravindranath, S., Ho, L. C., Peng, C. Y., Filippenko, A. V., & Sargent, W. L. W. 2001, *AJ*, **122**, 653
- Richings, A. J., Uttley, P., & Körding, E. 2011, *MNRAS*, **415**, 2158
- Richstone, D., Ajhar, E. A., Bender, R., et al. 1998, *Natur*, **395**, A14
- Rix, H.-W., & White, S. D. M. 1990, *ApJ*, **362**, 52
- Rix, H.-W., & White, S. D. M. 1992, *MNRAS*, **254**, 389
- Rusli, S. P., Erwin, P., Saglia, R. P., et al. 2013a, *AJ*, **146**, 160
- Rusli, S. P., Thomas, J., Erwin, P., et al. 2011, *MNRAS*, **410**, 1223
- Rusli, S. P., Thomas, J., Saglia, R. P., et al. 2013b, *AJ*, **146**, 45
- Salucci, P., Szuszkiewicz, E., Monaco, P., & Danese, L. 1999, *MNRAS*, **307**, 637
- Sani, E., Marconi, A., Hunt, L. K., & Risaliti, G. 2011, *MNRAS*, **413**, 1479
- Savorgnan, G., Graham, A. W., Marconi, A., et al. 2013, *MNRAS*, **434**, 387
- Savorgnan, G. A. D., & Graham, A. W. 2015a, *MNRAS*, submitted
- Savorgnan, G. A. D., & Graham, A. W. 2015b, *MNRAS*, **446**, 2330
- Schaye, J., Crain, R. A., Bower, R. G., et al. 2015, *MNRAS*, **446**, 521
- Scorza, C., & Bender, R. 1990, *A&A*, **235**, 49
- Scorza, C., & Bender, R. 1995, *A&A*, **293**, 20
- Scott, N., Davies, R. L., Houghton, R. C. W., et al. 2014, *MNRAS*, **441**, 274
- Sérsic, J. L. 1963, *BAAA*, **6**, 41
- Sérsic, J. L. 1968, *Atlas de Galaxias Australes*
- Shankar, F. 2009, *NewAR*, **53**, 57
- Shankar, F. 2013, *CQGra*, **30**, 244001
- Sheth, K., Regan, M., Hinz, J. L., et al. 2010, *PASP*, **122**, 1397
- Simões Lopes, R. D., Storchi-Bergmann, T., de Fátima Saraiva, M., & Martini, P. 2007, *ApJ*, **655**, 718
- Tran, H. D., Tsvetanov, Z., Ford, H. C., et al. 2001, *AJ*, **121**, 2928
- Trujillo, I., Erwin, P., Asensio Ramos, A., & Graham, A. W. 2004, *AJ*, **127**, 1917
- Trujillo, I., Graham, A. W., & Caon, N. 2001, *MNRAS*, **326**, 869
- Véron-Cetty, M.-P., & Véron, P. 2006, *A&A*, **455**, 773
- Vika, M., Driver, S. P., Cameron, E., Kelvin, L., & Robotham, A. 2012, *MNRAS*, **419**, 2264
- Wadadekar, Y., Robbason, B., & Kembhavi, A. 1999, *ApJ*, **117**, 1219
- Whitmore, B. C., Lucas, R. A., McElroy, D. B., et al. 1990, *AJ*, **100**, 1489
- Worley, G. 1994, *ApJS*, **95**, 107
- Yee, H. K. C. 1992, in ASP Conf. Ser. 31, Relationships between Active Galactic Nuclei and Starburst Galaxies, ed. A. V. Filippenko (San Francisco, CA: ASP), 417

$M_{\text{BH}} - L_{\text{gal}}$, $M_{\text{BH}} - L_{\text{sph}}$ and $M_{\text{BH}} - M_{*,\text{sph}}$

In Chapter 3, reliable and accurate multicomponent decompositions were presented for 66 galaxies out of the 75 belonging to the initial sample. These 66 galaxies constitute our final sample, which is currently the largest sample to date used to investigate correlations between directly measured black hole masses and host galaxy parameters.

This Chapter is dedicated to the analysis of three black hole mass correlations: the $M_{\text{BH}} - L_{\text{gal}}$, $M_{\text{BH}} - L_{\text{sph}}$ and $M_{\text{BH}} - M_{*,\text{sph}}$ relations. Four principal questions will be addressed.

1. Is the $M_{\text{BH}} - L_{\text{sph}}$ relation more fundamental than the $M_{\text{BH}} - L_{\text{gal}}$ relation (e.g. Kormendy & Ho 2013), or are they equally important (e.g. Läsker et al. 2014b)?
2. Graham & Scott (2013) identified two different sequences of spheroids in the $M_{\text{BH}} - L_{\text{sph}}$ diagram, namely Sérsic and core-Sérsic. However, their bulge luminosities were not derived from individual galaxy decompositions, but they were inferred from observed, total galaxy magnitudes through a mean statistical correction. Do we recover their result here, using the present dataset?
3. Does the quality of the present dataset allow us to identify any (additional) substructure in the three diagrams under study?
4. Some studies have distinguished pseudobulges and classical bulges according to their Sérsic index, and claimed that in the $M_{\text{BH}} - L_{\text{sph}}$ diagram pseudobulges are offset from the correlation defined by classical bulges. Here we test this result with our data.

A robust linear regression analysis is crucial for the study of black hole mass correlations. In particular, more emphasis is typically given to the slope rather than the intercept of scaling

relations, because the slope is the parameter that theoretical models (currently) predict. Several studies (e.g. Tremaine et al. 2002; Graham 2007; Tundo et al. 2007; Graham 2016b) have pointed out inconsistencies between the values of the slope measured by different groups for the same correlation. These discrepancies can arise from the use of different galaxy samples, selection biases, or the statistical techniques used to perform the linear regression analysis.

In the following analysis, we will make use of three linear regression routines: the BCES code from Akritas & Bershady (1996), the FITEXY routine (Press et al., 1992), as modified by Tremaine et al. (2002), and the Bayesian estimator linmix_err (Kelly, 2007). Albeit its remarkable computational speed, the BCES estimator is not reliable in case of poor number statistics of the galaxy sample analysed, or when at least one low-precision measurement is included in the dataset, or if the mean square of the uncertainties associated with the independent variable is comparable to the variance of the distribution of the independent variable (Tremaine et al., 2002). When any of these circumstances occur, the modified FITEXY routine and the Bayesian estimator linmix_err perform better than the BCES routine (Tremaine et al., 2002; Novak et al., 2006; Park et al., 2012). All of these three estimators take into account the intrinsic scatter of a correlation, but only the FITEXY and the linmix_err codes allow one to measure it. The interest in measuring the intrinsic scatter of black hole mass scaling relations relies on the assumption that the galaxy parameter associated with the smallest intrinsic residual variance has the best chance of being causally correlated to the black hole mass.

The remainder of this chapter comprises the published version of the paper “Supermassive Black Holes and Their Host Spheroids. II. The Red and Blue Sequence in the $M_{\text{BH}} - M_{*,\text{sph}}$ Diagram” by G. A. D. Savorgnan et al., as it appears in Volume 817 of the *The Astrophysical Journal*.



SUPERMASSIVE BLACK HOLES AND THEIR HOST SPHEROIDS. II. THE RED AND BLUE SEQUENCE IN THE $M_{\text{BH}}-M_{*,\text{sph}}$ DIAGRAM

GIULIA A. D. SAVORGNAN¹, ALISTER W. GRAHAM¹, ALESSANDRO MARCONI², AND ELEONORA SANI³

¹ Centre for Astrophysics and Supercomputing, Swinburne University of Technology, Hawthorn, Victoria 3122, Australia; gsavorgn@astro.swin.edu.au

² Dipartimento di Fisica e Astronomia, Università di Firenze, via G. Sansone 1, I-50019 Sesto Fiorentino, Firenze, Italy

³ European Southern Observatory, Alonso de Cordova, Vitacura 3107, Santiago, Chile

Received 2015 July 17; accepted 2015 November 23; published 2016 January 19

ABSTRACT

In our first paper, we performed a detailed (i.e., bulge, disks, bars, spiral arms, rings, halo, nucleus, etc.) decomposition of 66 galaxies, with directly measured black hole masses, M_{BH} , imaged at 3.6 μm with *Spitzer*. Our sample is the largest to date and, for the first time, the decompositions were checked for consistency with the galaxy kinematics. We present correlations between M_{BH} and the host spheroid (and galaxy) luminosity, L_{sph} (and L_{gal}), and also stellar mass, $M_{*,\text{sph}}$. While most previous studies have used galaxy samples that were overwhelmingly dominated by high-mass, early-type galaxies, our sample includes 17 spiral galaxies, half of which have $M_{\text{BH}} < 10^7 M_{\odot}$, and allows us to better investigate the poorly studied low-mass end of the $M_{\text{BH}}-M_{*,\text{sph}}$ correlation. The bulges of early-type galaxies follow $M_{\text{BH}} \propto M_{*,\text{sph}}^{1.04 \pm 0.10}$ and define a tight *red sequence* with intrinsic scatter $\epsilon_{(M_{\text{BH}}|M_{*,\text{sph}})} = 0.43 \pm 0.06$ dex and a median $M_{\text{BH}}/M_{*,\text{sph}}$ ratio of $0.68 \pm 0.04\%$, i.e., a $\pm 2\sigma$ range of 0.1%–5%. At the low-mass end, the bulges of late-type galaxies define a much steeper *blue sequence*, with $M_{\text{BH}} \propto M_{*,\text{sph}}^{2-3}$ and $M_{\text{BH}}/M_{*,\text{sph}}$ equal to 0.02% at $M_{\text{BH}} \approx 10^6 M_{\odot}$. We additionally report that (1) our Sérsic galaxy sample follows $M_{\text{BH}} \propto M_{*,\text{sph}}^{1.48 \pm 0.20}$, a less steep sequence than previously reported; (2) bulges with Sérsic index $n_{\text{sph}} < 2$, argued by some to be pseudo-bulges, are not offset to lower M_{BH} from the correlation defined by the current bulge sample with $n_{\text{sph}} > 2$; and (3) L_{sph} and L_{gal} correlate equally well with M_{BH} , in terms of intrinsic scatter, only for early-type galaxies—once reasonable numbers of spiral galaxies are included, the correlation with L_{sph} is better than that with L_{gal} .

Key words: black hole physics – galaxies: bulges – galaxies: elliptical and lenticular, cD – galaxies: evolution – galaxies: structure

1. INTRODUCTION

A quarter of a century ago, Dressler (1989) foresaw a “rough scaling of black hole mass with the mass of the spheroidal component” of galaxies, as suggested by the sequence of five galaxies (M87, M104, M31, M32, and the Milky Way). Yee (1992) then announced a linear relation between what was effectively black hole mass and galaxy mass for high-luminosity, bulge-dominated, early-type galaxies radiating near the Eddington limit. This “rough scaling” was a premature version of the early correlations between black hole mass, M_{BH} , and host spheroid luminosity, L_{sph} , and also host spheroid mass, M_{sph} (Kormendy & Richstone 1995; Magorrian et al. 1998; Marconi & Hunt 2003; Häring & Rix 2004). These initial studies were dominated by high-mass, early-type galaxies, for which they too reported a quasi-linear $M_{\text{BH}}-M_{\text{sph}}$ relation. Subsequent studies of the $M_{\text{BH}}-L_{\text{sph}}$ and $M_{\text{BH}}-M_{\text{sph}}$ diagrams (Ferrarese & Ford 2005; Graham 2007; Lauer et al. 2007a; Gültekin et al. 2009; Sani et al. 2011; Beifiori et al. 2012; Erwin & Gadotti 2012; van den Bosch et al. 2012; Vika et al. 2012; Kormendy & Ho 2013; McConnell & Ma 2013) continued to use galaxy samples dominated by high-mass, early-type systems with $M_{\text{BH}} \gtrsim 0.5 \times 10^8 M_{\odot}$, and they too recovered a near-linear relation. However, the consensus about a linear $M_{\text{BH}}-M_{\text{sph}}$ correlation was not unanimous. Some studies had reported a slope steeper than one, or noticed that the low-mass spheroids were offset to the right of (or below) the relation traced by the high-mass spheroids (Laor 1998, 2001; Wandel 1999; Ryan et al. 2007). Graham (2012), Graham & Scott (2013), and Scott et al. (2013) found two distinct trends in

the $M_{\text{BH}}-L_{\text{sph}}$ and $M_{\text{BH}}-M_{\text{sph}}$ diagrams: a linear and a super-quadratic correlation at the high- and low-mass ends, respectively.⁴ Recently, Läsker et al. (2014a; 2014b) derived 2.2 μm bulge luminosities for 35 galaxies (among which only four were classified as spiral galaxies), and reported a slope below unity for their $M_{\text{BH}}-L_{\text{sph}}$ relation. They also claimed that the black hole mass correlates equally well with the total galaxy luminosity as it does with the bulge luminosity.

The $M_{\text{BH}}-L_{\text{sph}}$ relation for early-type (elliptical + lenticular) galaxies can be predicted by combining two other correlations that involve the bulge stellar velocity dispersion, σ . One of these is the $M_{\text{BH}}-\sigma$ relation (Ferrarese & Merritt 2000; Gebhardt et al. 2000), which can be described with a single power law ($M_{\text{BH}} \propto \sigma^{5-6}$) over a wide range in velocity dispersion (70–350 km s^{-1} , e.g., Graham et al. 2011; McConnell et al. 2011; Graham & Scott 2013). The other is the $L_{\text{sph}}-\sigma$ relation, which has long been known to be a “double power law,” with $L_{\text{sph}} \propto \sigma^{5-6}$ at the luminous end⁵ (Schechter 1980; Malumuth & Kirshner 1981; Lauer et al. 2007b; von der Linden et al. 2007; Liu et al. 2008) and $L_{\text{sph}} \propto \sigma^2$ at intermediate and faint luminosities (Davies et al. 1983; Held et al. 1992; de Rijcke et al. 2005; Matković & Guzmán 2005; Balcells et al. 2007; Chilingarian et al. 2008; Forbes et al. 2008; Cody et al. 2009; Tortora et al. 2009; Kourkchi

⁴ Readers interested in an extensive review about the early discovery and successive improvements of these correlations should consult Graham (2016).

⁵ Recent work has the $M_{\text{BH}}-\sigma$ correlation as steep as $M_{\text{BH}} \propto \sigma^{6.5}$ (Savorgnan & Graham 2015) and the high-luminosity end of the $L_{\text{sph}}-\sigma$ correlation as steep as $L_{\text{sph}} \propto \sigma^8$ (Montero-Dorta et al. 2015).

et al. 2012). The change in slope of the $L_{\text{sph}}-\sigma$ relation occurs at $M_B \approx -20.5$ mag, corresponding to $\sigma \approx 200 \text{ km s}^{-1}$. The $M_{\text{BH}}-L_{\text{sph}}$ relation should, therefore, be better described by a “broken,” rather than a single, power law: with $M_{\text{BH}} \propto L_{\text{sph}}^{2.5}$ at the low-luminosity end, and $M_{\text{BH}} \propto L_{\text{sph}}^1$ at the high-luminosity end. Due to the scatter in the $M_{\text{BH}}-L_{\text{sph}}$ (or $M_{\text{BH}}-M_{\text{sph}}$) diagram, studies that have not sufficiently probed below $M_{\text{BH}} \approx 10^7 M_\odot$ can easily miss the change in slope occurring at $M_{\text{BH}} \approx 10^{(8\pm1)} M_\odot$, and erroneously recover a single log-linear relation.

When Graham (2012) pointed out this overlooked inconsistency between these linear and bent relations, he identified two different populations of galaxies, namely the core-Sérsic spheroids (Graham et al. 2003; Trujillo et al. 2004) and the Sérsic spheroids⁶, and attributed the change in slope (from super-quadratic to linear) to their different formation mechanisms. In this scenario, core-Sérsic spheroids are built in dry merger events where the black hole and the bulge grow at the same pace, increasing their mass in lock steps ($M_{\text{BH}} \propto L_{\text{sph}}^1$), whereas Sérsic spheroids originate from gas-rich processes in which the mass of the black hole increases more rapidly than the mass of its host spheroid ($M_{\text{BH}} \propto L_{\text{sph}}^{2.5}$).

Graham & Scott (2013, hereafter GS13) and Scott et al. (2013) presented separate power-law linear regressions for the Sérsic and core-Sérsic spheroids in the $M_{\text{BH}}-L_{\text{sph}}$ and $M_{\text{BH}}-M_{*,\text{sph}}$ (spheroid stellar mass) diagrams, probing down to $M_{\text{BH}} \approx 10^6 M_\odot$. To obtain their dust-corrected *bulge* magnitudes, they did not perform bulge/disk decompositions, but converted the *B*-band and *K_S*-band observed, total galaxy magnitudes into bulge magnitudes using a mean statistical bulge-to-total ratio based on each object’s morphological type and disk inclination.⁷ These mean statistical bulge-to-total ratios were obtained from the results of two-component (Sérsic-bulge/exponential-disk) decompositions in the literature. Here we investigate in more detail the $M_{\text{BH}}-L_{\text{sph}}$ and $M_{\text{BH}}-M_{*,\text{sph}}$ diagrams using state-of-the-art galaxy decompositions (Savorgnan & Graham 2015, hereafter Paper I) for galaxies with directly measured black hole masses. Our galaxies are large and nearby, which allows us to perform accurate multicomponent decompositions (instead of simple bulge/disk decompositions). Our decompositions were performed on 3.6 μm *Spitzer* satellite imagery, which is an excellent proxy for the stellar mass, superior to the *K*-band (Sheth et al. 2010, and references therein). Nine of our galaxies have $M_{\text{BH}} \lesssim 10^7 M_\odot$, which allows us to better constrain the slope of the correlation at the low-mass end. Furthermore, our galaxy sample includes 17 spiral galaxies, representing a notable improvement over past studies dominated by early-type galaxies. In a forthcoming paper, we will explore the relation between the black hole mass and the bulge dynamical mass, $M_{\text{dyn},\text{sph}} \propto R_e \sigma^2$, and address the issue of a black hole fundamental plane.

2. DATA

Our galaxy sample (see Table 1) consists of 66 objects for which a dynamical measurement of the black hole mass had been tabulated in the literature (by GS13 or Rusli et al. 2013) at

⁶ Core-Sérsic spheroids have partially depleted cores relative to their outer Sérsic light profile, whereas Sérsic spheroids have no central deficit of stars.

⁷ While this resulted in individual bulge magnitudes not being exactly correct, their large sample size allowed them to obtain a reasonable $M_{\text{BH}}-L_{\text{sph}}$ relation for the ensemble.

the time that we started this project, and for which we were able to obtain useful spheroid parameters from 3.6 μm *Spitzer* satellite imagery.

Spheroid magnitudes were derived from our state-of-the-art galaxy decompositions, which take into account bulge, disks, spiral arms, bars, rings, halo, extended or unresolved nuclear source, and partially depleted core. Kinematical information (Emsellem et al. 2011; Arnold et al. 2014; Scott et al. 2014) was used to confirm the presence of rotationally supported disk components in most early-type (elliptical + lenticular) galaxies, and to identify their extent (intermediate-scale disks that are fully embedded in the bulge, or large-scale disks that encase the bulge and dominate the light at large radii). It is worth stressing that, contrary to common knowledge, the majority of “elliptical” galaxies contain disks, i.e., they are not single-component spheroidal systems. Paper I presents the data set used here, including details about the data reduction process and the galaxy modeling technique that we developed. It also discusses how we estimated the uncertainties⁸ on the bulge magnitudes and presents the individual 66 galaxy decompositions, along with a comparison and discussion of past decompositions.

Bulge luminosities⁹ (Table 1) from Paper I were converted into stellar masses using a constant 3.6 μm mass-to-light ratio, $\Gamma_{3.6} = 0.6$ (Meidt et al. 2014). We additionally explored a more sophisticated way to compute mass-to-light ratios, using the color- $\Gamma_{3.6}$ relation published by Meidt et al. (2014), their Equation (4), which allows one to estimate $\Gamma_{3.6}$ of a galaxy from its [3.6]–[4.5] color. Individual [3.6]–[4.5] colors¹⁰ were taken from Peletier et al. (2012, column 8 of their Table 1) when available for our galaxies, or were estimated from the bulge stellar velocity dispersion, σ , using the color- σ relation presented by Peletier et al. (2012, their Figure 6). We found that the range in [3.6]–[4.5] color is small (0.06 mag), and thus the range in $\Gamma_{3.6}$ is also small (0.04). After checking that using a single $\Gamma_{3.6} = 0.6$, independent of [3.6]–[4.5] color, does not significantly affect the results of our analysis, we decided to use individual, color-dependent mass-to-light ratios.

For each galaxy, the total luminosity (or galaxy luminosity, L_{gal}) is the sum of the luminosities of all its sub-components. Due to the complexity of their modeling, four galaxies (see Table 1, column 7) had their galaxy luminosities

⁸ By comparing, for each of our galaxies, the measurements of the bulge magnitude obtained by different authors with that obtained by us, we estimated the uncertainties on the bulge magnitudes, in effect taking into account systematic errors. Systematic errors include incorrect sky subtraction, inaccurate masking of contaminating sources, imprecise description of the PSF, erroneous choice of model components (for example, when failing to identify a galaxy subcomponent and thus omitting it in the model, or when describing a galaxy sub-component with an inadequate function), the radial extent of the surface brightness profile and one’s sampling of this. Most of these factors are not included in popular two-dimensional (2D) fitting codes which report only the statistical errors associated with their fitted parameters. In fact, when performing multicomponent decomposition of high signal-to-noise images of nearby—therefore, well spatially resolved—galaxies, errors are dominated by systematics rather than Poisson noise. Unlike many papers, we believe that we have not underestimated the uncertainties associated to the bulge best-fit parameters.

⁹ Following Sani et al. (2011), absolute luminosities were calculated assuming a 3.6 μm solar absolute magnitude of 3.25 mag. Absolute luminosities were not corrected for cosmological redshift dimming (this correction would be as small as -0.02 mag for galaxies at a distance of 40 Mpc or -0.05 mag for galaxies at a distance of 100 Mpc).

¹⁰ These are integrated [3.6]–[4.5] colors, measured in a circular aperture within each galaxy’s effective radius.

Table 1
Galaxy Sample

Galaxy	Type	Core	Distance (Mpc)	M_{BH} ($10^8 M_{\odot}$)	MAG_{sph} (mag)	MAG_{gal} (mag)	[3.6]–[4.5] (mag)	$M_{*,\text{sph}}$ ($10^{10} M_{\odot}$)
(1)	(2)	(3)	(4)	(5)	(6)	(7)	(8)	(9)
IC 1459	E	yes	28.4	24^{+10}_{-10}	$-26.15^{+0.18}_{-0.11}$	-26.15 ± 0.25	-0.12	27^{+3}_{-4}
IC 2560	Sp (bar)	no?	40.7	$0.044^{+0.044}_{-0.022}$	$-22.27^{+0.66}_{-0.58}$	-24.76 ± 0.25	-0.08	$1.0^{+0.7}_{-0.5}$
IC 4296	E	yes?	40.7	11^{+2}_{-2}	$-26.35^{+0.18}_{-0.11}$	-26.35 ± 0.25	-0.12	31^{+3}_{-5}
M31	Sp (bar)	no	0.7	$1.4^{+0.9}_{-0.3}$	$-22.74^{+0.18}_{-0.11}$	-24.67 ± 0.25	-0.09	$1.5^{+0.2}_{-0.2}$
M49	E	yes	17.1	25^{+3}_{-3}	$-26.54^{+0.18}_{-0.11}$	-26.54 ± 0.25	-0.12	39^{+4}_{-6}
M59	E	no	17.8	$3.9^{+0.4}_{-0.4}$	$-25.18^{+0.18}_{-0.11}$	-25.27 ± 0.25	-0.09	14^{+2}_{-2}
M64	Sp	no?	7.3	$0.016^{+0.004}_{-0.004}$	$-21.54^{+0.18}_{-0.11}$	-24.24 ± 0.25	-0.06	$0.64^{+0.07}_{-0.10}$
M81	Sp (bar)	no	3.8	$0.74^{+0.21}_{-0.11}$	$-23.01^{+0.88}_{-0.66}$	-24.43 ± 0.25	-0.09	$1.9^{+1.6}_{-1.1}$
M84	E	yes	17.9	$9.0^{+0.9}_{-0.8}$	$-26.01^{+0.66}_{-0.58}$	-26.01 ± 0.25	-0.10	28^{+20}_{-13}
M87	E	yes	15.6	$58.0^{+3.5}_{-3.5}$	$-26.00^{+0.66}_{-0.58}$	-26.00 ± 0.25	-0.11	26^{+18}_{-12}
M89	E	yes	14.9	$4.7^{+0.5}_{-0.5}$	$-24.48^{+0.66}_{-0.58}$	-24.74 ± 0.25	-0.11	$6.3^{+4.4}_{-2.9}$
M94	Sp (bar)	no?	4.4	$0.060^{+0.014}_{-0.014}$	$-22.08^{+0.18}_{-0.11}$	≤ -23.36	-0.07	$1.00^{+0.11}_{-0.15}$
M96	Sp (bar)	no	10.1	$0.073^{+0.015}_{-0.015}$	$-22.15^{+0.18}_{-0.11}$	-24.20 ± 0.25	-0.08	$0.97^{+0.11}_{-0.15}$
M104	S0/Sp	yes	9.5	$6.4^{+0.4}_{-0.4}$	$-23.91^{+0.66}_{-0.58}$	-25.21 ± 0.25	-0.12	$3.4^{+2.4}_{-1.6}$
M105	E	yes	10.3	4^{+1}_{-1}	$-24.29^{+0.66}_{-0.58}$	-24.29 ± 0.25	-0.10	$5.6^{+3.9}_{-2.5}$
M106	Sp (bar)	no	7.2	$0.39^{+0.01}_{-0.01}$	$-21.11^{+0.18}_{-0.11}$	-24.04 ± 0.25	-0.08	$0.37^{+0.04}_{-0.06}$
NGC 0524	S0	yes	23.3	$8.3^{+2.7}_{-1.3}$	$-23.19^{+0.18}_{-0.11}$	-24.92 ± 0.25	-0.09	$2.2^{+0.2}_{-0.3}$
NGC 0821	E	no	23.4	$0.39^{+0.26}_{-0.09}$	$-24.00^{+0.88}_{-0.66}$	-24.26 ± 0.25	-0.09	$4.7^{+4.0}_{-2.6}$
NGC 1023	S0 (bar)	no	11.1	$0.42^{+0.04}_{-0.04}$	$-22.82^{+0.18}_{-0.11}$	-24.20 ± 0.25	-0.10	$1.5^{+0.2}_{-0.2}$
NGC 1300	Sp (bar)	no	20.7	$0.73^{+0.69}_{-0.35}$	$-22.06^{+0.66}_{-0.58}$	-24.16 ± 0.25	-0.10	$0.70^{+0.49}_{-0.32}$
NGC 1316	merger	no	18.6	$1.50^{+0.75}_{-0.80}$	$-24.89^{+0.66}_{-0.58}$	-26.48 ± 0.25	-0.10	$9.5^{+6.7}_{-4.3}$
NGC 1332	E/S0	no	22.3	14^{+2}_{-2}	$-24.89^{+0.88}_{-0.66}$	-24.95 ± 0.25	-0.12	$8.2^{+6.8}_{-4.5}$
NGC 1374	E	no?	19.2	$5.8^{+0.5}_{-0.5}$	$-23.68^{+0.18}_{-0.11}$	-23.70 ± 0.25	-0.09	$3.6^{+0.4}_{-0.5}$
NGC 1399	E	yes	19.4	$4.7^{+0.6}_{-0.6}$	$-26.43^{+0.18}_{-0.11}$	-26.46 ± 0.25	-0.12	33^{+4}_{-5}
NGC 2273	Sp (bar)	no	28.5	$0.083^{+0.004}_{-0.004}$	$-23.00^{+0.66}_{-0.58}$	-24.21 ± 0.25	-0.08	$2.0^{+1.4}_{-0.9}$
NGC 2549	S0 (bar)	no	12.3	$0.14^{+0.02}_{-0.13}$	$-21.25^{+0.18}_{-0.11}$	-22.60 ± 0.25	-0.10	$0.35^{+0.04}_{-0.05}$
NGC 2778	S0 (bar)	no	22.3	$0.15^{+0.09}_{-0.10}$	$-20.80^{+0.66}_{-0.58}$	-22.44 ± 0.25	-0.09	$0.25^{+0.18}_{-0.12}$
NGC 2787	S0 (bar)	no	7.3	$0.40^{+0.04}_{-0.05}$	$-20.11^{+0.66}_{-0.58}$	-22.28 ± 0.25	-0.10	$0.12^{+0.08}_{-0.05}$
NGC 2974	Sp (bar)	no	20.9	$1.7^{+0.2}_{-0.2}$	$-22.95^{+0.66}_{-0.58}$	-24.16 ± 0.25	-0.09	$1.8^{+1.3}_{-0.8}$
NGC 3079	Sp (bar)	no?	20.7	$0.024^{+0.024}_{-0.012}$	$-23.01^{+0.66}_{-0.58}$	≤ -24.45	-0.07	$2.4^{+1.7}_{-1.1}$
NGC 3091	E	yes	51.2	36^{+1}_{-2}	$-26.28^{+0.18}_{-0.11}$	-26.28 ± 0.25	-0.12	30^{+3}_{-5}
NGC 3115	E/S0	no	9.4	$8.8^{+10.0}_{-2.7}$	$-24.22^{+0.18}_{-0.11}$	-24.40 ± 0.25	-0.11	$4.9^{+0.5}_{-0.7}$
NGC 3227	Sp (bar)	no	20.3	$0.14^{+0.10}_{-0.06}$	$-21.76^{+0.66}_{-0.58}$	-24.26 ± 0.25	-0.08	$0.67^{+0.47}_{-0.31}$
NGC 3245	S0 (bar)	no	20.3	$2.0^{+0.5}_{-0.5}$	$-22.43^{+0.18}_{-0.11}$	-23.88 ± 0.25	-0.10	$1.0^{+0.1}_{-0.2}$
NGC 3377	E	no	10.9	$0.77^{+0.04}_{-0.06}$	$-23.49^{+0.66}_{-0.58}$	-23.57 ± 0.25	-0.06	$4.0^{+2.8}_{-1.8}$
NGC 3384	S0 (bar)	no	11.3	$0.17^{+0.01}_{-0.02}$	$-22.43^{+0.18}_{-0.11}$	-23.74 ± 0.25	-0.08	$1.2^{+0.1}_{-0.2}$
NGC 3393	Sp (bar)	no	55.2	$0.34^{+0.02}_{-0.02}$	$-23.48^{+0.66}_{-0.58}$	-25.29 ± 0.25	-0.10	$2.8^{+1.9}_{-1.3}$
NGC 3414	E	no	24.5	$2.4^{+0.3}_{-0.3}$	$-24.35^{+0.18}_{-0.11}$	-24.42 ± 0.25	-0.09	$6.5^{+0.7}_{-1.0}$
NGC 3489	S0/Sp (bar)	no	11.7	$0.058^{+0.008}_{-0.008}$	$-21.13^{+0.66}_{-0.58}$	-23.07 ± 0.25	-0.06	$0.42^{+0.30}_{-0.19}$
NGC 3585	E	no	19.5	$3.1^{+1.4}_{-0.6}$	$-25.52^{+0.66}_{-0.58}$	-25.55 ± 0.25	-0.10	18^{+12}_{-8}
NGC 3607	E	no	22.2	$1.3^{+0.5}_{-0.5}$	$-25.36^{+0.66}_{-0.58}$	-25.45 ± 0.25	-0.10	15^{+10}_{-7}
NGC 3608	E	yes	22.3	$2.0^{+1.1}_{-0.6}$	$-24.50^{+0.66}_{-0.58}$	-24.50 ± 0.25	-0.08	$7.8^{+5.5}_{-3.6}$
NGC 3842	E	yes	98.4	97^{+30}_{-26}	$-27.00^{+0.18}_{-0.11}$	-27.04 ± 0.25	-0.11	61^{+7}_{-9}
NGC 3998	S0 (bar)	no	13.7	$8.1^{+2.0}_{-1.9}$	$-22.32^{+0.88}_{-0.66}$	-23.53 ± 0.25	-0.12	$0.78^{+0.65}_{-0.43}$
NGC 4026	S0 (bar)	no	13.2	$1.8^{+0.6}_{-0.3}$	$-21.58^{+0.88}_{-0.66}$	-23.16 ± 0.25	-0.09	$0.50^{+0.42}_{-0.28}$
NGC 4151	Sp (bar)	no	20.0	$0.65^{+0.07}_{-0.07}$	$-23.40^{+0.66}_{-0.58}$	-24.44 ± 0.25	-0.09	$2.8^{+2.0}_{-1.3}$
NGC 4261	E	yes	30.8	5^{+1}_{-1}	$-25.72^{+0.66}_{-0.58}$	-25.76 ± 0.25	-0.12	18^{+13}_{-8}
NGC 4291	E	yes	25.5	$3.3^{+0.9}_{-2.5}$	$-24.05^{+0.66}_{-0.58}$	-24.05 ± 0.25	-0.11	$3.9^{+2.8}_{-1.8}$
NGC 4388	Sp (bar)	no?	17.0	$0.075^{+0.002}_{-0.002}$	$-21.26^{+0.88}_{-0.66}$	≤ -23.50	-0.07	$0.46^{+0.39}_{-0.26}$
NGC 4459	S0	no	15.7	$0.68^{+0.13}_{-0.13}$	$-23.48^{+0.66}_{-0.58}$	-24.01 ± 0.25	-0.09	$2.9^{+2.1}_{-1.3}$
NGC 4473	E	no	15.3	$1.2^{+0.4}_{-0.9}$	$-23.88^{+0.66}_{-0.58}$	-24.11 ± 0.25	-0.10	$3.9^{+2.7}_{-1.8}$
NGC 4564	S0	no	14.6	$0.60^{+0.03}_{-0.09}$	$-22.30^{+0.18}_{-0.11}$	-22.99 ± 0.25	-0.11	$0.82^{+0.09}_{-0.12}$
NGC 4596	S0 (bar)	no	17.0	$0.79^{+0.38}_{-0.33}$	$-22.73^{+0.18}_{-0.11}$	-24.18 ± 0.25	-0.08	$1.6^{+0.2}_{-0.2}$
NGC 4697	E	no	11.4	$1.8^{+0.2}_{-0.1}$	$-24.82^{+0.88}_{-0.66}$	-24.94 ± 0.25	-0.09	10^{+8}_{-6}
NGC 4889	E	yes	103.2	210^{+160}_{-160}	$-27.54^{+0.18}_{-0.11}$	-27.54 ± 0.25	-0.12	91^{+10}_{-14}
NGC 4945	Sp (bar)	no?	3.8	$0.014^{+0.014}_{-0.007}$	$-20.96^{+0.66}_{-0.58}$	≤ -23.79	-0.06	$0.36^{+0.26}_{-0.17}$

Table 1
(Continued)

Galaxy	Type	Core	Distance (Mpc)	M_{BH} ($10^8 M_{\odot}$)	MAG_{sph} (mag)	MAG_{gal} (mag)	[3.6]–[4.5] (mag)	$M_{*,\text{sph}}$ ($10^{10} M_{\odot}$)
(1)	(2)	(3)	(4)	(5)	(6)	(7)	(8)	(9)
NGC 5077	E	yes	41.2	$7.4^{+4.7}_{-3.0}$	$-25.45^{+0.18}_{-0.11}$	-25.45 ± 0.25	-0.11	15^{+2}_{-2}
NGC 5128	merger	no?	3.8	$0.45^{+0.17}_{-0.10}$	$-23.89^{+0.88}_{-0.66}$	-24.97 ± 0.25	-0.07	$5.0^{+4.2}_{-2.8}$
NGC 5576	E	no	24.8	$1.6^{+0.3}_{-0.4}$	$-24.44^{+0.18}_{-0.11}$	-24.44 ± 0.25	-0.09	$7.1^{+0.8}_{-1.1}$
NGC 5845	S0	no	25.2	$2.6^{+0.4}_{-1.5}$	$-22.96^{+0.88}_{-0.66}$	-23.10 ± 0.25	-0.12	$1.4^{+1.2}_{-0.8}$
NGC 5846	E	yes	24.2	11^{+1}_{-1}	$-25.81^{+0.66}_{-0.58}$	-25.81 ± 0.25	-0.10	22^{+16}_{-10}
NGC 6251	E	yes?	104.6	5^{+2}_{-2}	$-26.75^{+0.18}_{-0.11}$	-26.75 ± 0.25	-0.12	46^{+5}_{-7}
NGC 7052	E	yes	66.4	$3.7^{+2.6}_{-1.5}$	$-26.32^{+0.18}_{-0.11}$	-26.32 ± 0.25	-0.11	33^{+4}_{-5}
NGC 7619	E	yes	51.5	25^{+8}_{-3}	$-26.35^{+0.66}_{-0.58}$	-26.41 ± 0.25	-0.11	33^{+23}_{-15}
NGC 7768	E	yes	112.8	13^{+5}_{-4}	$-26.90^{+0.66}_{-0.58}$	-26.90 ± 0.25	-0.11	57^{+40}_{-26}
UGC 03789	Sp (bar)	no?	48.4	$0.108^{+0.005}_{-0.005}$	$-22.77^{+0.88}_{-0.66}$	-24.20 ± 0.25	-0.07	$1.9^{+1.6}_{-1.0}$

Note. Column (1): Galaxy name. Column (2): morphological type (E = elliptical, S0 = lenticular, Sp = spiral, merger). The morphological classification of four galaxies is uncertain (E/S0 or S0/Sp). The presence of a bar is indicated. Column (3): presence of a partially depleted core. The question mark is used when the classification has come from the velocity dispersion criteria mentioned in Section 2. Column (4): distance. Column (5): black hole mass. Column (6): absolute 3.6 μm bulge magnitude. Bulge magnitudes come from our state-of-the-art multicomponent galaxy decompositions (Paper I), which include bulges, disks, bars, spiral arms, rings, halos, extended or unresolved nuclear sources, and partially depleted cores, and that—for the first time—were checked to be consistent with the galaxy kinematics. The uncertainties were estimated with a method that takes into account systematic errors, which are typically not considered by popular 2D fitting codes. Column (7): absolute 3.6 μm galaxy magnitude. Four galaxies had their magnitudes overestimated, which are given here as upper limits. Column (8): [3.6]–[4.5] color. Column (9): bulge stellar mass.

underestimated¹¹, which are given here as lower limits. Following GS13, we assumed a fixed uncertainty (0.25 mag) for the absolute galaxy magnitude MAG_{gal} .

The morphological classification (E = elliptical; E/S0 = elliptical/lenticular; S0 = lenticular; S0/Sp = lenticular/spiral; Sp = spiral; and “merger”) follows from the galaxy models presented in Paper I. Throughout this paper, we will refer to early-type galaxies (E+S0) and late-type galaxies (Sp). Two galaxies classified as E/S0 are obviously included in the early-type bin, whereas two galaxies classified as S0/Sp and another two classified as mergers are included in neither the early- nor the late-type bins.

The Sérsic/core-Sérsic classification presented in this work comes from the compilation of Savorgnan & Graham (2015), who identified partially depleted cores according to the same criteria used by GS13. When no high-resolution image analysis was available from the literature, they inferred the presence of a partially depleted core based on the stellar velocity dispersion: a spheroid is classified as core-Sérsic if $\sigma > 270 \text{ km s}^{-1}$, or as Sérsic if $\sigma < 166 \text{ km s}^{-1}$. All of the galaxies with velocity dispersions between these two limits had high-resolution images available.

3. ANALYSIS

We performed a linear regression analysis of the $M_{\text{BH}}-L_{\text{gal}}$ (see Table 2), $M_{\text{BH}}-L_{\text{sph}}$ (see Table 3), and $M_{\text{BH}}-M_{*,\text{sph}}$ (see Table 4) data, using the BCES code from Akritas & Bershady (1996). We also repeated the analysis using both the FITEXY routine (Press et al. 1992), as modified by Tremaine et al. (2002), and the Bayesian estimator `linmix_err` (Kelly 2007). All of these three linear regression routines account for the intrinsic scatter, but only the last two allow one to quantify it. We report linear regressions, both symmetrical and non-symmetrical, for Sérsic/core-Sérsic and for early-/late-type galaxies. Symmetrical regressions are meant to be compared

¹¹ These four cases are discussed in Paper I.

with theoretical expectations, whereas non-symmetrical forward ($M_{\text{BH}}|X$) regressions—which minimize the scatter in the $\log(M_{\text{BH}})$ direction—are best used to predict black hole masses.

4. RESULTS AND DISCUSSION

4.1. Black Hole Mass–Galaxy Luminosity

The $M_{\text{BH}}-L_{\text{gal}}$ diagram is shown in Figure 1. Four spiral galaxies had their total luminosities underestimated (see Table 1) and thus are not included in the linear regression analysis (see Table 2).

Läsker et al. (2014b) analyzed a sample of 35 galaxies, among which only four were classified as spiral galaxies, and claimed that the $M_{\text{BH}}-L_{\text{sph}}$ and $M_{\text{BH}}-L_{\text{gal}}$ relations, which they fit with a single power law, have consistent intrinsic scatter. Here, instead, thanks to our galaxy sample that includes 17 spiral galaxies, we show that the claim made by Läsker et al. (2014b) is valid only for early-type galaxies. That is, when considering only early-type galaxies, we find that the $M_{\text{BH}}-L_{\text{sph}}$ and $M_{\text{BH}}-L_{\text{gal}}$ relations have the same level of intrinsic scatter. However, our $M_{\text{BH}}-L_{\text{sph}}$ relation for all 66 galaxies, irrespective of their morphological type, has an intrinsic scatter $\epsilon_{(Y|X)} = 0.51 \pm 0.06 \text{ dex}$ (forward linear regression) and $\epsilon_{(X|Y)} = 0.60 \pm 0.09 \text{ dex}$ (inverse linear regression), whereas our $M_{\text{BH}}-L_{\text{gal}}$ relation for 62 (=66–4) galaxies has $\epsilon_{(Y|X)} = 0.63 \pm 0.07 \text{ dex}$ and $\epsilon_{(X|Y)} = 0.91 \pm 0.17 \text{ dex}$. Because the value of the intrinsic scatter depends on the size of the uncertainties associated with the absolute magnitudes,¹² we tested the robustness of our conclusion by increasing the uncertainties associated with the galaxy absolute magnitudes¹³

¹² The smaller (larger) the uncertainties, the larger (smaller) the intrinsic scatter.

¹³ The value of the intrinsic scatter obviously depends also on the size of the uncertainties associated with the black hole masses. However, black hole masses and their uncertainties have been estimated by various authors using different methods, thus we have limited to no control on their values.

Table 2
Linear Regression Analysis of the $M_{\text{BH}}-L_{\text{gal}}$ Diagram

Subsample (size)	Regression	α	β	$\langle \text{MAG}_{\text{gal}} \rangle$	ϵ	Δ
$\log[M_{\text{BH}}/M_{\odot}] = \alpha + \beta [(\text{MAG}_{\text{gal}} - \langle \text{MAG}_{\text{gal}} \rangle)/\text{mag}]$						
All (62)	BCES ($Y X$)	8.26 ± 0.08	-0.49 ± 0.06	-24.78	...	0.64
	mFITEXY ($Y X$)	$8.26^{+0.08}_{-0.08}$	$-0.49^{+0.06}_{-0.07}$	-24.78	$0.61^{+0.07}_{-0.06}$	0.64
	linmix_err ($Y X$)	8.26 ± 0.09	-0.49 ± 0.07	-24.78	0.63 ± 0.07	0.64
	BCES ($X Y$)	8.26 ± 0.12	-1.01 ± 0.15	-24.78	...	0.92
	mFITEXY ($X Y$)	$8.26^{+0.11}_{-0.12}$	$-1.03^{+0.13}_{-0.16}$	-24.78	$0.88^{+0.10}_{-0.08}$	0.93
	linmix_err ($X Y$)	8.26 ± 0.12	-1.02 ± 0.15	-24.78	0.91 ± 0.17	0.93
	BCES Bisector	8.26 ± 0.09	-0.72 ± 0.07	-24.78	...	0.71
	mFITEXY Bisector	$8.26^{+0.10}_{-0.10}$	$-0.73^{+0.09}_{-0.10}$	-24.78	...	0.71
	linmix_err Bisector	8.26 ± 0.10	-0.72 ± 0.07	-24.78	...	0.71
Early-type (E+S0) (45)	BCES ($Y X$)	8.56 ± 0.07	-0.44 ± 0.05	-24.88	...	0.45
	mFITEXY ($Y X$)	$8.56^{+0.06}_{-0.06}$	$-0.42^{+0.05}_{-0.05}$	-24.88	$0.41^{+0.06}_{-0.05}$	0.45
	linmix_err ($Y X$)	8.56 ± 0.07	-0.42 ± 0.06	-24.88	0.43 ± 0.06	0.45
	BCES ($X Y$)	8.56 ± 0.08	-0.64 ± 0.05	-24.88	...	0.53
	mFITEXY ($X Y$)	$8.56^{+0.08}_{-0.08}$	$-0.66^{+0.07}_{-0.08}$	-24.88	$0.51^{+0.07}_{-0.06}$	0.55
	linmix_err ($X Y$)	8.56 ± 0.09	-0.65 ± 0.08	-24.88	0.53 ± 0.10	0.54
	BCES Bisector	8.56 ± 0.07	-0.53 ± 0.04	-24.88	...	0.47
	mFITEXY Bisector	$8.56^{+0.07}_{-0.07}$	$-0.54^{+0.06}_{-0.06}$	-24.88	...	0.47
	linmix_err Bisector	8.56 ± 0.08	-0.53 ± 0.05	-24.88	...	0.47

Note. For each subsample, we indicate $\langle \text{MAG}_{\text{gal}} \rangle$, its average value of galaxy magnitudes. In the last two columns, we report ϵ , the intrinsic scatter, and Δ , the total rms scatter in the $\log(M_{\text{BH}})$ direction. Four spiral galaxies had their luminosities underestimated and thus are not included in the linear regression analysis (the sample of all galaxies contains $66-4 = 62$ objects). When considering all galaxies, irrespective of their morphological type, the $M_{\text{BH}}-L_{\text{gal}}$ correlation is weaker than the $M_{\text{BH}}-L_{\text{sph}}$ correlation, in terms of intrinsic scatter. However, when considering only early-type galaxies, the $M_{\text{BH}}-L_{\text{gal}}$ and $M_{\text{BH}}-L_{\text{sph}}$ correlations have consistent intrinsic scatter.

(we originally assumed 0.25 mag). The intrinsic scatter of the $M_{\text{BH}}-L_{\text{gal}}$ relation only becomes smaller than that of the $M_{\text{BH}}-L_{\text{sph}}$ relation when assuming an uncertainty larger than 0.7 mag for L_{gal} , which would be significantly larger than the typical value commonly recognized in the literature, and would also oddly exceed the typical uncertainty that we estimated for L_{sph} . Hence, we conclude that our determination of the relative intrinsic scatter is reliable and that M_{BH} correlates equally well with L_{sph} and L_{gal} only for early-type galaxies¹⁴, but not for all (early+late-type) galaxies.

4.2. Black Hole Mass–Spheroid Luminosity

The $M_{\text{BH}}-L_{\text{sph}}$ diagram is shown in Figure 2, and the linear regression analysis is presented in Table 3. Sérsic and core-Sérsic spheroids have slopes consistent with each other (within their 1σ uncertainties), in disagreement with the findings of GS13. The slope that we obtained for core-Sérsic spheroids ($M_{\text{BH}} \propto L_{\text{sph}}^{1.18 \pm 0.20}$) is consistent with the slope reported by GS13 in the K_s -band for the same population ($M_{\text{BH}} \propto L_{\text{sph}}^{1.10 \pm 0.20}$). However, the slope that we determined for Sérsic spheroids ($M_{\text{BH}} \propto L_{\text{sph}}^{1.53 \pm 0.20}$) is notably shallower than that found by GS13 ($M_{\text{BH}} \propto L_{\text{sph}}^{2.73 \pm 0.55}$).

Although the Sérsic/core-Sérsic classification used by GS13 slightly differs¹⁵ from the classification used here, the main cause of the inconsistency is that the bulge-to-total ratios obtained from our galaxy decompositions are different from

those assumed by GS13 to convert galaxy luminosities into bulge luminosities. Our bulge-to-total ratios for low-luminosity Sérsic spheroids ($3.6 \mu\text{m MAG}_{\text{sph}} \gtrsim -22$ mag) are smaller than those used by GS13. The host galaxies of such bulges are late-type, spiral galaxies, which typically present a complex morphology (bars, double bars, embedded disks, nuclear components, etc.). Our galaxy models account for the extra components, while the average bulge-to-total ratios of GS13 were based on less sophisticated Sérsic-bulge/exponential-disk decompositions which overestimated the bulge luminosity. This results in our bulge magnitudes being on average ~ 0.7 mag fainter than in GS13, after accounting for the different wavelength of the data. At the same time, our bulge-to-total ratios for the high-luminosity Sérsic spheroids ($3.6 \mu\text{m MAG}_{\text{sph}} \lesssim -24$ mag) are on average larger than those adopted by GS13. In this regime, the host systems are early-type galaxies that feature intermediate-scale disks.¹⁶ Past bulge/disk decompositions failed to correctly identify the extent of such disks and treated them as large-scale disks, thus underestimating the bulge luminosity. The magnitudes that we obtained for such spheroids are on average ~ 0.5 mag brighter than in GS13. These two effects explain the shallower slope that we obtained for the Sérsic spheroids.

The slope that we obtained for Sérsic spheroids (1.53 ± 0.20) is not consistent with the value of 2.5 expected from $M_{\text{BH}} \propto \sigma^5$ and $L_{\text{sph}} \propto \sigma^2$. In addition, the Sérsic and core-Sérsic spheroids do not appear to define two distinct $M_{\text{BH}}-L_{\text{sph}}$ sequences. This leads us to investigate substructure

¹⁴ The majority of our early-type galaxies are elliptical galaxies, some of which have a bulge-to-total ratio close to 1 ($L_{\text{gal}} \simeq L_{\text{sph}}$). One might wonder whether this constitutes a bias in our analysis. However, we checked that M_{BH} correlates equally well with L_{sph} and L_{gal} not only for early-type (elliptical+lenticular) galaxies, but also for lenticular galaxies only.

¹⁵ The classification has changed for the galaxies NGC 1316, NGC 1332, and NGC 3998.

¹⁶ Intermediate-scale disks are disks of stars fully embedded in the spheroidal component of their galaxy. They are typical of “disky” elliptical galaxies (e.g., NGC 3377), but they can also be found in other types of host galaxies. They can be considered an intermediate class between nuclear disks, with sizes of $\sim 10-100$ pc, and large-scale disks, that encase the bulge and dominate the light at large radii.

Table 3
Linear Regression Analysis of the $M_{\text{BH}}-L_{\text{sph}}$ Diagram

Subsample (size)	Regression	α	β	$\langle \text{MAG}_{\text{sph}} \rangle$	ϵ	Δ
$\log[M_{\text{BH}}/M_{\odot}] = \alpha + \beta[(\text{MAG}_{\text{sph}} - \langle \text{MAG}_{\text{sph}} \rangle)/\text{mag}]$						
All (66)	BCES ($Y X$)	8.16 ± 0.07	-0.44 ± 0.04	-23.86	...	0.56
	mFITEXY ($Y X$)	$8.17^{+0.06}_{-0.07}$	$-0.43^{+0.03}_{-0.04}$	-23.86	$0.49^{+0.06}_{-0.05}$	0.56
	linmix_err ($Y X$)	8.16 ± 0.07	-0.42 ± 0.04	-23.86	0.51 ± 0.06	0.56
	BCES ($X Y$)	8.16 ± 0.08	-0.61 ± 0.05	-23.86	...	0.68
	mFITEXY ($X Y$)	$8.15^{+0.07}_{-0.08}$	$-0.61^{+0.05}_{-0.05}$	-23.86	$0.58^{+0.07}_{-0.06}$	0.68
	linmix_err ($X Y$)	8.16 ± 0.09	-0.60 ± 0.06	-23.86	0.60 ± 0.09	0.67
	BCES Bisector	8.16 ± 0.07	-0.52 ± 0.04	-23.86	...	0.60
	mFITEXY Bisector	$8.16^{+0.07}_{-0.07}$	$-0.51^{+0.04}_{-0.04}$	-23.86	...	0.60
	linmix_err Bisector	8.16 ± 0.08	-0.51 ± 0.03	-23.86	...	0.59
$n > 2$ (43)	BCES ($Y X$)	8.58 ± 0.07	-0.42 ± 0.06	-24.77	...	0.46
	mFITEXY ($Y X$)	$8.57^{+0.07}_{-0.06}$	$-0.41^{+0.04}_{-0.04}$	-24.77	$0.38^{+0.06}_{-0.06}$	0.46
	linmix_err ($Y X$)	8.56 ± 0.07	-0.39 ± 0.05	-24.77	0.40 ± 0.06	0.46
	BCES ($X Y$)	8.58 ± 0.08	-0.58 ± 0.06	-24.77	...	0.56
	mFITEXY ($X Y$)	$8.56^{+0.08}_{-0.08}$	$-0.57^{+0.06}_{-0.07}$	-24.77	$0.44^{+0.08}_{-0.11}$	0.55
	linmix_err ($X Y$)	8.55 ± 0.09	-0.57 ± 0.08	-24.77	0.49 ± 0.10	0.55
	BCES Bisector	8.58 ± 0.07	-0.50 ± 0.05	-24.77	...	0.49
	mFITEXY Bisector	$8.57^{+0.07}_{-0.07}$	$-0.49^{+0.05}_{-0.05}$	-24.77	...	0.49
	linmix_err Bisector	8.56 ± 0.08	-0.48 ± 0.05	-24.77	...	0.49
Core- Sérsic (22)	BCES ($Y X$)	9.06 ± 0.09	-0.32 ± 0.11	-25.73	...	0.42
	mFITEXY ($Y X$)	$9.06^{+0.08}_{-0.09}$	$-0.26^{+0.08}_{-0.07}$	-25.73	$0.36^{+0.09}_{-0.06}$	0.42
	linmix_err ($Y X$)	9.04 ± 0.10	-0.24 ± 0.09	-25.73	0.40 ± 0.08	0.42
	BCES ($X Y$)	9.06 ± 0.12	-0.65 ± 0.12	-25.73	...	0.61
	mFITEXY ($X Y$)	$9.03^{+0.15}_{-0.16}$	$-0.72^{+0.17}_{-0.31}$	-25.73	$0.61^{+0.14}_{-0.09}$	0.68
	linmix_err ($X Y$)	9.03 ± 0.17	-0.69 ± 0.27	-25.73	0.68 ± 0.30	0.64
	BCES Bisector	9.06 ± 0.10	-0.47 ± 0.08	-25.73	...	0.48
	mFITEXY Bisector	$9.05^{+0.12}_{-0.13}$	$-0.47^{+0.12}_{-0.17}$	-25.73	...	0.48
	linmix_err Bisector	9.04 ± 0.14	-0.44 ± 0.12	-25.73	...	0.46
Sérsic (44)	BCES ($Y X$)	7.71 ± 0.09	-0.41 ± 0.08	-22.92	...	0.61
	mFITEXY ($Y X$)	$7.72^{+0.08}_{-0.09}$	$-0.41^{+0.07}_{-0.08}$	-22.92	$0.54^{+0.08}_{-0.07}$	0.61
	linmix_err ($Y X$)	7.73 ± 0.09	-0.41 ± 0.08	-22.92	0.55 ± 0.08	0.61
	BCES ($X Y$)	7.71 ± 0.14	-0.86 ± 0.16	-22.92	...	0.93
	mFITEXY ($X Y$)	$7.72^{+0.14}_{-0.13}$	$-0.86^{+0.13}_{-0.19}$	-22.92	$0.77^{+0.13}_{-0.10}$	0.93
	linmix_err ($X Y$)	7.73 ± 0.14	-0.86 ± 0.17	-22.92	0.79 ± 0.20	0.93
	BCES Bisector	7.71 ± 0.10	-0.61 ± 0.08	-22.92	...	0.71
	mFITEXY Bisector	$7.72^{+0.11}_{-0.11}$	$-0.61^{+0.10}_{-0.12}$	-22.92	...	0.71
	linmix_err Bisector	7.73 ± 0.12	-0.62 ± 0.09	-22.92	...	0.71
Early-type (E+S0) (45)	BCES ($Y X$)	8.56 ± 0.07	-0.33 ± 0.04	-24.47	...	0.46
	mFITEXY ($Y X$)	$8.56^{+0.06}_{-0.06}$	$-0.32^{+0.03}_{-0.04}$	-24.47	$0.40^{+0.06}_{-0.05}$	0.46
	linmix_err ($Y X$)	8.55 ± 0.07	-0.32 ± 0.04	-24.47	0.41 ± 0.06	0.46
	BCES ($X Y$)	8.56 ± 0.08	-0.48 ± 0.05	-24.47	...	0.55
	mFITEXY ($X Y$)	$8.54^{+0.08}_{-0.08}$	$-0.49^{+0.05}_{-0.06}$	-24.47	$0.49^{+0.08}_{-0.06}$	0.57
	linmix_err ($X Y$)	8.55 ± 0.09	-0.48 ± 0.06	-24.47	0.51 ± 0.10	0.56
	BCES Bisector	8.56 ± 0.07	-0.40 ± 0.04	-24.47	...	0.49
	mFITEXY Bisector	$8.55^{+0.07}_{-0.07}$	$-0.41^{+0.04}_{-0.05}$	-24.47	...	0.49
	linmix_err Bisector	8.55 ± 0.08	-0.40 ± 0.04	-24.47	...	0.49
Late-type (Sp) (17)	BCES ($Y X$)	7.18 ± 0.16	-0.79 ± 0.43	-22.33	—	0.70
	mFITEXY ($Y X$)	$7.20^{+0.15}_{-0.15}$	$-0.53^{+0.22}_{-0.24}$	-22.33	$0.55^{+0.15}_{-0.10}$	0.63
	linmix_err ($Y X$)	7.24 ± 0.19	-0.46 ± 0.32	-22.33	0.63 ± 0.16	0.62
	BCES ($X Y$)	7.18 ± 0.29	-1.71 ± 0.71	-22.33	...	1.26
	mFITEXY ($X Y$)	$7.38^{+0.54}_{-0.36}$	$-2.02^{+0.71}_{-2.13}$	-22.33	$1.09^{+0.41}_{-0.24}$	1.50
	linmix_err ($X Y$)	7.34 ± 0.43	-1.93 ± 1.30	-22.33	1.31 ± 0.97	1.43
	BCES Bisector	7.18 ± 0.20	-1.15 ± 0.27	-22.33	...	0.88
	mFITEXY Bisector	$7.26^{+0.40}_{-0.28}$	$-1.03^{+0.33}_{-0.52}$	-22.33	...	0.82
	linmix_err Bisector	7.27 ± 0.33	-0.96 ± 0.37	-22.33	...	0.78

Note. For each subsample, we indicate $\langle \text{MAG}_{\text{sph}} \rangle$, its average value of spheroid magnitudes. In the last two columns, we report ϵ , the intrinsic scatter, and Δ , the total rms scatter in the $\log(M_{\text{BH}})$ direction. Both the early- and late-type subsamples do not contain the two galaxies classified as S0/Sp and the two galaxies classified as mergers (45+17 = 66-2-2). The bold values are the linear regression parameters quoted in the text.

Table 4
Linear Regression Analysis of the $M_{\text{BH}}-M_{*,\text{sph}}$ Diagram

Subsample (size)	Regression	α	β	$\langle \text{MAG}_{\text{sph}} \rangle$	ϵ	Δ
$\log[M_{\text{BH}}/M_{\odot}] = \alpha + \beta \log[(M_{*,\text{sph}}/\langle M_{*,\text{sph}} \rangle)]$						
Core-Sérsic (22)	BCES ($Y X$)	9.06 ± 0.09	0.86 ± 0.28	$10^{11.28}$...	0.42
	mFITEXY ($Y X$)	$9.06^{+0.08}_{-0.08}$	$0.68^{+0.21}_{-0.20}$	$10^{11.28}$	$0.36^{+0.09}_{-0.06}$	0.42
	linmix_err ($Y X$)	9.04 ± 0.10	0.64 ± 0.25	$10^{11.28}$	0.40 ± 0.09	0.42
	BCES ($X Y$)	9.06 ± 0.12	1.70 ± 0.32	$10^{11.28}$...	0.61
	mFITEXY ($X Y$)	$9.03^{+0.15}_{-0.16}$	$1.90^{+0.85}_{-0.46}$	$10^{11.28}$	$0.62^{+0.13}_{-0.10}$	0.68
	linmix_err ($X Y$)	9.03 ± 0.17	1.80 ± 0.70	$10^{11.28}$	0.67 ± 0.30	0.65
	BCES Bisector	9.06 ± 0.10	1.19 ± 0.23	$10^{11.28}$...	0.47
	mFITEXY Bisector	$9.05^{+0.12}_{-0.13}$	$1.12^{+0.35}_{-0.27}$	$10^{11.28}$...	0.46
	linmix_err Bisector	9.04 ± 0.14	1.06 ± 0.26	$10^{11.28}$...	0.45
Sérsic (44)	BCES ($Y X$)	7.71 ± 0.09	0.95 ± 0.21	$10^{10.25}$...	0.64
	mFITEXY ($Y X$)	$7.72^{+0.10}_{-0.09}$	$0.96^{+0.21}_{-0.21}$	$10^{10.25}$	$0.58^{+0.09}_{-0.07}$	0.64
	linmix_err ($Y X$)	7.73 ± 0.10	0.98 ± 0.24	$10^{10.25}$	0.59 ± 0.08	0.65
	BCES ($X Y$)	7.71 ± 0.16	2.52 ± 0.54	$10^{10.25}$...	1.11
	mFITEXY ($X Y$)	$7.72^{+0.16}_{-0.16}$	$2.49^{+0.69}_{-0.45}$	$10^{10.25}$	$0.93^{+0.15}_{-0.13}$	1.10
	linmix_err ($X Y$)	7.73 ± 0.17	2.48 ± 0.59	$10^{10.25}$	0.95 ± 0.27	1.10
	BCES Bisector	7.71 ± 0.11	1.48 ± 0.20	$10^{10.25}$...	0.74
	mFITEXY Bisector	$7.72^{+0.13}_{-0.13}$	$1.49^{+0.33}_{-0.28}$	$10^{10.25}$...	0.74
	linmix_err Bisector	7.73 ± 0.14	1.49 ± 0.24	$10^{10.25}$...	0.74
Early-type (E+S0) (45)	BCES ($Y X$)	8.56 ± 0.07	0.85 ± 0.12	$10^{10.81}$...	0.48
	mFITEXY ($Y X$)	$8.56^{+0.06}_{-0.07}$	$0.83^{+0.11}_{-0.11}$	$10^{10.81}$	$0.42^{+0.07}_{-0.05}$	0.48
	linmix_err ($Y X$)	8.55 ± 0.07	0.82 ± 0.12	$10^{10.81}$	0.43 ± 0.06	0.48
	BCES ($X Y$)	8.56 ± 0.09	1.27 ± 0.13	$10^{10.81}$...	0.59
	mFITEXY ($X Y$)	$8.54^{+0.08}_{-0.09}$	$1.32^{+0.18}_{-0.15}$	$10^{10.81}$	$0.53^{+0.08}_{-0.07}$	0.61
	linmix_err ($X Y$)	8.55 ± 0.09	1.29 ± 0.17	$10^{10.81}$	0.54 ± 0.11	0.59
	BCES Bisector	8.56 ± 0.07	1.04 ± 0.10	$10^{10.81}$...	0.51
	mFITEXY Bisector	$8.55^{+0.07}_{-0.08}$	$1.05^{+0.14}_{-0.12}$	$10^{10.81}$...	0.51
	linmix_err Bisector	8.55 ± 0.08	1.03 ± 0.10	$10^{10.81}$...	0.51
Late-type (Sp) (17)	BCES ($Y X$)	7.18 ± 0.17	1.95 ± 1.52	$10^{10.05}$...	0.74
	mFITEXY ($Y X$)	$7.20^{+0.15}_{-0.16}$	$1.22^{+0.70}_{-0.62}$	$10^{10.05}$	$0.59^{+0.16}_{-0.11}$	0.66
	linmix_err ($Y X$)	7.23 ± 0.19	0.96 ± 0.96	$10^{10.05}$	0.67 ± 0.16	0.65
	BCES ($X Y$)	7.18 ± 0.39	5.89 ± 3.40	$10^{10.05}$...	1.70
	mFITEXY ($X Y$)	$7.44^{+1.45}_{-0.52}$	$7.14^{+26.31}_{-3.01}$	$10^{10.05}$	$1.49^{+0.56}_{-0.36}$	2.08
	linmix_err ($X Y$)	7.42 ± 0.64	6.96 ± 6.73	$10^{10.05}$	1.83 ± 1.86	2.03
	BCES Bisector	7.18 ± 0.21	3.00 ± 1.30	$10^{10.05}$...	0.94
	mFITEXY Bisector	$7.24^{+1.04}_{-0.39}$	$2.28^{+1.67}_{-1.01}$	$10^{10.05}$...	0.79
	linmix_err Bisector	7.26 ± 0.47	1.94 ± 1.24	$10^{10.05}$...	0.74

Note. For each subsample, we indicate $\langle M_{*,\text{sph}} \rangle$, its average value of spheroid stellar masses. In the last two columns, we report ϵ , the intrinsic scatter, and Δ , the total rms scatter in the $\log(M_{\text{BH}})$ direction. The bold values are the linear regression parameters quoted in the text.

in the $M_{\text{BH}}-L_{\text{sph}}$ diagram for early- and late-type galaxies. First, we checked that the elliptical and lenticular galaxies, taken separately, have slopes consistent with each other, and thus, taken together, they define a single *early-type sequence* in the $M_{\text{BH}}-L_{\text{sph}}$ diagram. We then fit the early-type galaxies with a single log-linear regression, and obtained $M_{\text{BH}} \propto L_{\text{sph}}^{1.00 \pm 0.10}$. We did not find any convincing evidence for the change in slope required for consistency with the $M_{\text{BH}}-\sigma$ and bent $L_{\text{sph}}-\sigma$ correlations. Because the change in slope should occur at $M_{\text{BH}} > 10^{8 \pm 1} M_{\odot}$, but all of the early-type galaxies in our sample have $M_{\text{BH}} \gtrsim 10^7 M_{\odot}$, one possible explanation is that we are still not probing enough low black hole masses for this subsample. An additional possibility is that there is no sharp transition going from $L_{\text{sph}} \propto \sigma^2$ at low luminosities to $L_{\text{sph}} \propto \sigma^5$ at high luminosities. Although the knowledge that many “elliptical” galaxies actually contain embedded stellar disks dates back at least three decades (Capaccioli 1987; Carter 1987; Bender 1990; Rix & White 1990, 1992; Scorza &

Bender 1990, 1995; Nieto et al. 1991), it is mainly thanks to large integral-field-spectrograph surveys of early-type galaxies, such as the ATLAS^{3D} Project (Cappellari et al. 2011), that our view has been further advanced and it is now commonly accepted that most “elliptical” galaxies contain disks. Past studies that investigated the $L_{\text{sph}}-\sigma$ diagram might have failed to identify and consequently model the disks in intermediate-luminosity, early-type galaxies, thus overestimating L_{sph} and mistakenly producing a sharp bend in the $L_{\text{sph}}-\sigma$ correlation, rather than a continuously curved relation (with $L_{\text{sph}} \propto \sigma^{3-4}$ at intermediate luminosities).

For the bulges of late-type galaxies, we obtained $M_{\text{BH}} \propto L_{\text{sph}}^{2.88 \pm 0.68}$. From a cursory inspection of Figure 2, one might be tempted to doubt the statistical significance of this “tentative” *late-type sequence*. However, a visual inspection of the plotted data requires one to take into account the error bars when judging-by-eye the strength of a correlation. Similarly, the Pearson’s and Spearman’s correlation coefficients are not applicable because they do not take into account the error bars

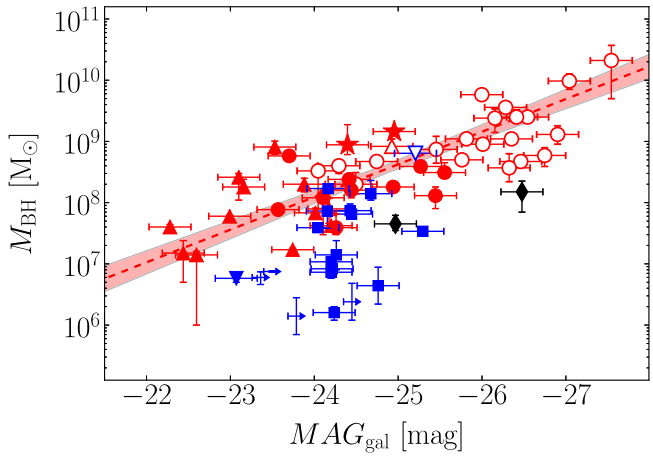


Figure 1. Black hole mass plotted against $3.6 \mu\text{m}$ galaxy absolute magnitude. Symbols are coded according to the galaxy morphological type: red circle = E, red star = E/S0, red upward triangle = S0, blue downward triangle = S0/Sp, blue square = Sp, black diamond = merger. Empty symbols represent core-Sérsic spheroids, whereas filled symbols are used for Sérsic spheroids. Four spiral galaxies had their magnitudes overestimated (luminosities underestimated) and are shown as upper limits. The red dashed line indicates the BCES bisector linear regression for the 45 early-type galaxies (E+S0), with the red shaded area denoting its 1σ uncertainty. M_{BH} correlates equally well with L_{gal} and L_{sph} only for early-type galaxies, but not for all (early+late-type) galaxies.

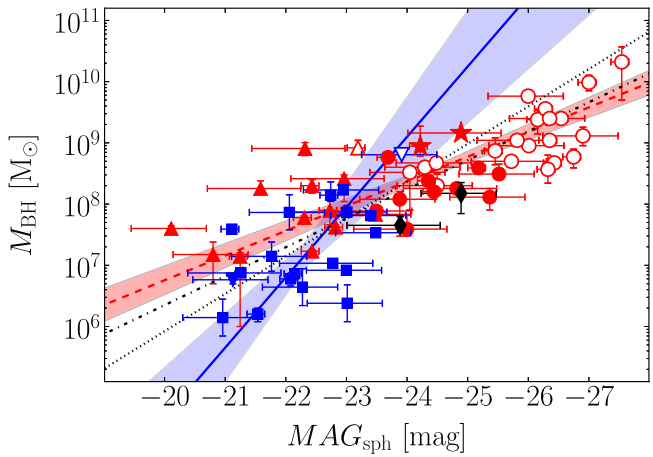


Figure 2. Black hole mass plotted against $3.6 \mu\text{m}$ spheroid absolute magnitude. Symbols have the same meaning as in Figure 1. The red dashed line indicates the BCES bisector linear regression for the spheroidal component of the 45 early-type (E+S0) galaxies, with the red shaded area denoting its 1σ uncertainty. The blue solid line shows the BCES bisector linear regression for the bulges of the 17 late-type (Sp) galaxies, with the blue shaded area denoting its 1σ uncertainty. The black dashed-dotted and dotted lines represent the BCES bisector linear regressions for the core-Sérsic and Sérsic spheroids, respectively.

on our data. We have, therefore, relied on the quantitative regression analysis.

4.2.1. Pseudo- versus Classical Bulges

Current views distinguish between classical bulges (which are considered to be spheroidal, pressure-supported systems, formed through violent processes, such as hierarchical clustering via minor mergers) and pseudo-bulges (thought to be disk-like, rotation-supported systems, built from secular evolution processes, such as instabilities of their surrounding disk or bar). Pseudo-bulges are notoriously hard to identify

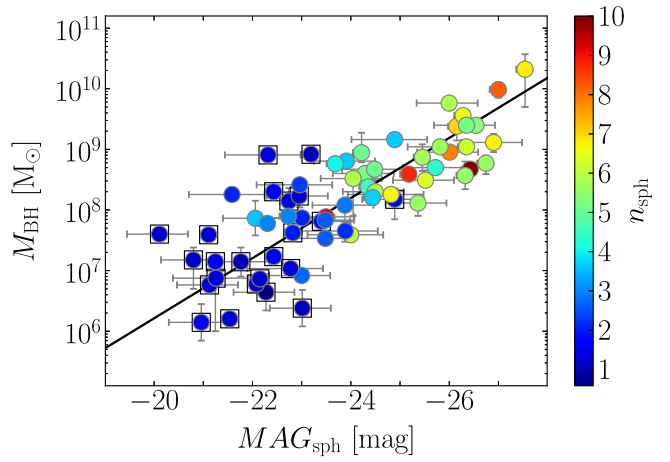


Figure 3. Black hole mass plotted against $3.6 \mu\text{m}$ spheroid absolute magnitude (as in Figure 2). Symbols are color coded according to the spheroid Sérsic index n_{sph} . Bulges with $n_{\text{sph}} < 2$, claimed by some to be pseudo-bulges, are enclosed with a square. The black solid line shows the BCES bisector linear regression for the spheroids that have $n_{\text{sph}} \geq 2$, such that $M_{\text{BH}} \propto L_{\text{sph}}^{1.25 \pm 0.13}$.

(Graham 2013, 2014, 2015, 2016). For example, mergers can create bulges that rotate (e.g., Bekki 2010; Keselman & Nusser 2012), and bars can spin-up classical bulges (e.g., Saha et al. 2012; Saha 2015), thus rotation is not a definitive signature of a pseudo-bulge. Furthermore, many galaxies host both a classical and a pseudo-bulge (e.g., Erwin et al. 2003, 2015; Athanassoula 2005; Gadotti 2009; MacArthur et al. 2009; Erwin 2010; dos Anjos & da Silva 2013; Seidel et al. 2015). In the recent literature, pseudo- and classical bulges have frequently been divided at the Sérsic index $n_{\text{sph}} = 2$ (e.g., Sani et al. 2011; Beifiori et al. 2012), although, from a selection of hundreds of disk galaxies imaged in the K -band, Graham & Worley (2008) observed no bimodality in the bulge Sérsic indices about $n_{\text{sph}} = 2$ or any other value. While pseudo-bulges are expected to have exponential-like surface brightness profiles ($n_{\text{sph}} \simeq 1$), being disk-like components that formed from their surrounding exponential disks (e.g., Bardeen 1975; Hohl 1975; Combes & Sanders 1981; Combes et al. 1990; Pfenniger & Friedli 1991), it has been shown that mergers can create bulges with $n_{\text{sph}} < 2$ (e.g., Eliche-Moral et al. 2011; Scannapieco et al. 2011; Querejeta et al. 2015), just as low-luminosity elliptical galaxies (not built from the secular evolution of a disk) are also well known to have $n_{\text{sph}} < 2$ and even $n_{\text{sph}} < 1$ (e.g., Davies et al. 1988; Young & Currie 1994; Jerjen et al. 2000). The use of the Sérsic index (in addition to rotation) to identify pseudo-bulges is thus a dangerous practice. We therefore do not assume that all bulges with $n_{\text{sph}} < 2$ are built from internal processes in the disk (i.e., are what some authors call pseudo-bulges). Sani et al. (2011) reported that pseudo-bulges—which they labelled as such according to the $n_{\text{sph}} < 2$ criterion—with low black hole masses ($M_{\text{BH}} < 10^7 M_{\odot}$) are significantly displaced from the correlation traced by their (classical) bulges with $n_{\text{sph}} > 2$. In Figure 3, we show the distribution of spheroid Sérsic indices¹⁷ in the $M_{\text{BH}}-L_{\text{sph}}$ diagram. Our aim is to check whether bulges with $n_{\text{sph}} < 2$ are offset to lower black hole masses from the correlation defined by bulges with $n_{\text{sph}} > 2$. To do this, we fit a symmetrical linear regression to the bulges that have $n_{\text{sph}} > 2$

¹⁷ The spheroid Sérsic indices are taken from our galaxy decompositions (Paper I).

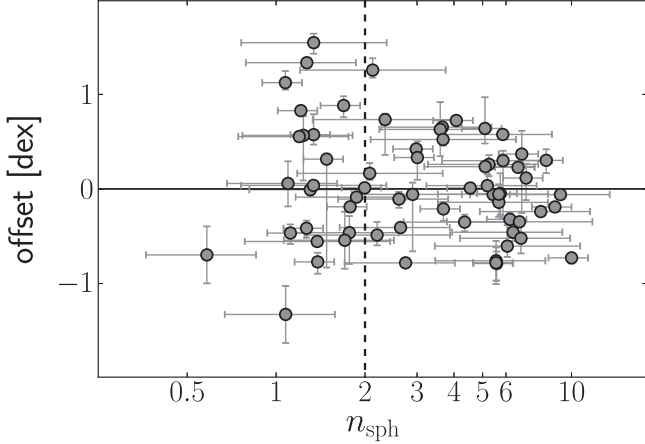


Figure 4. Vertical offset from the $M_{\text{BH}}-L_{\text{sph}}$ correlation defined by spheroids with $n_{\text{sph}} \geq 2$ (see Figure 3), plotted against n_{sph} . The vertical dashed line corresponds to $n_{\text{sph}} = 2$. The horizontal solid line is equivalent to a zero vertical offset. Among the bulges with $n_{\text{sph}} < 2$, 12 have a positive vertical offset and 11 have a negative vertical offset. Hence, bulges with $n_{\text{sph}} < 2$ are not randomly offset to lower black hole masses from the correlation traced by bulges with $n_{\text{sph}} \geq 2$.

and we then compute the vertical offset of all bulges from this regression. In Figure 4, we plot the vertical offset against n_{sph} . Among the 23 bulges with $n_{\text{sph}} < 2$, 12 have a positive vertical offset and 11 have a negative vertical offset. Kormendy (2015) provides a list of many pseudo-bulge classification criteria, including the divide at $n_{\text{sph}} = 2$, and cautions that each individual criterion has a failure rate of 0%–25%. If this is true, we should find that no less than 75% of bulges with $n_{\text{sph}} < 2$ display a negative vertical offset.¹⁸ What we observe, instead, is that there are the same number of bulges with $n_{\text{sph}} < 2$ lying above and below the correlation defined by bulges with $n_{\text{sph}} > 2$, and that the amplitude of their offset is the same ($\lesssim 1.5$ dex). That is, within the current data set, bulges with $n_{\text{sph}} < 2$ do not appear to be offset from the correlation traced by bulges with $n_{\text{sph}} > 2$.

4.3. Black Hole Mass–Spheroid Stellar Mass

Finally, we present the $M_{\text{BH}}-M_{*,\text{sph}}$ diagram in Figure 5, and its linear regression analysis in Table 4. The bulges of the early-type galaxies follow $M_{\text{BH}} \propto M_{*,\text{sph}}^{1.04 \pm 0.10}$, consistent with a dry-merging formation scenario¹⁹, and define a tight *early-type sequence* with intrinsic scatter $\epsilon_{(Y|X)} = 0.43 \pm 0.06$ dex. Graham (2012) reported that the $M_{\text{BH}}/M_{\text{dyn},\text{sph}}$ ratio for core-Sérsic galaxies was 0.36% ($M_{\text{dyn},\text{sph}}$ is the spheroid dynamical mass) and discussed the many implications of this. Using a larger data sample, Graham & Scott (2013) reported that the $M_{\text{BH}}/M_{*,\text{sph}}$ ratio was 0.49% for core-Sérsic galaxies. Here we find a median $M_{\text{BH}}/M_{*,\text{sph}}$ ratio of $0.50 \pm 0.04\%$ for the 22 core-Sérsic galaxies and $0.68 \pm 0.04\%$ for the 45 early-type galaxies. Among other things, this higher value (previously reported to be 0.1%–0.2% for all galaxy types, e.g., Marconi &

¹⁸ One reaches the same conclusion when using the vertical offset from the correlation defined by bulges with $n_{\text{sph}} > 3$ or even $n_{\text{sph}} > 4$. There are 13 and 10 bulges with $n_{\text{sph}} < 2$ that lie above and below, respectively, the correlation traced by bulges with $n_{\text{sph}} > 3$. Similarly, there are 15 and 8 bulges with $n_{\text{sph}} < 2$ that lie above and below, respectively, the correlation traced by bulges with $n_{\text{sph}} > 4$.

¹⁹ In dry mergers, the black hole and the bulge grow at the same pace, increasing their mass in lock step.

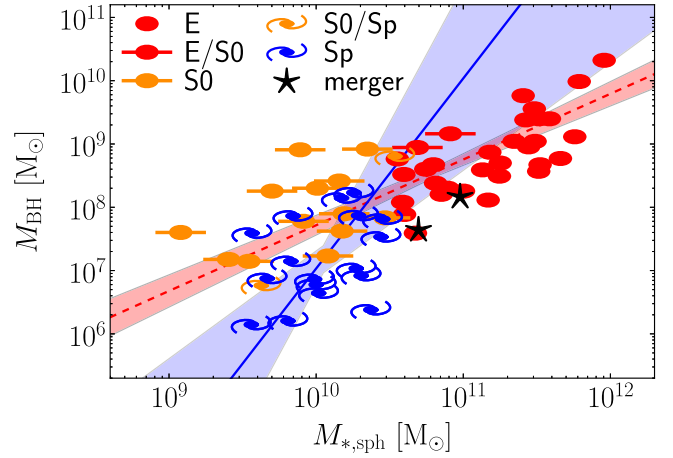


Figure 5. Black hole mass plotted against spheroid stellar mass. Symbols are coded according to the galaxy morphological type (see the legend). The red dashed line indicates the BCES bisector linear regression for the bulges of the 45 early-type galaxies (E+S0), with the red shaded area denoting its 1σ uncertainty. The bulges of early-type galaxies follow $M_{\text{BH}} \propto M_{*,\text{sph}}^{1.04 \pm 0.10}$, a near-linear relation consistent with a dry-merging formation scenario. The steeper blue solid line shows the BCES bisector linear regression for the bulges of the 17 late-type (Sp) galaxies, with the blue shaded area denoting its 1σ uncertainty. The bulges of late-type galaxies follow $M_{\text{BH}} \propto M_{*,\text{sph}}^{2-3}$, indicating that gas-rich processes feed the black hole more efficiently (“quadratically” or “cubically”) than the host bulge grows in stellar mass. We note that AGNs with $10^5 \lesssim M_{\text{BH}}/M_{\odot} \lesssim 2 \times 10^6$ (Jiang et al. 2011) appear to follow the blue line (see A. W. Graham et al. 2015, in preparation).

Hunt 2003), boosts estimates of the black hole mass function and mass density based on galaxy/spheroid luminosity functions.

The bulges of the spiral galaxies trace a steeper *late-type sequence*, whose slope is less well constrained due to the smaller size of the subsample and, more importantly, to the smaller range in $M_{*,\text{sph}}$ that the subsample spans. For the bulges of spiral galaxies, the BCES code returns a log-linear relation with a slope $= 3.00 \pm 1.30$, while the modified FITEXY routine finds a shallower (but still consistent within the 1σ uncertainty) slope $= 2.28^{+1.67}_{-1.01}$. More data would be welcome to better constrain the slope of this *late-type sequence*, though we note that direct measurements of black hole masses below $10^6 M_{\odot}$ are extremely challenging to obtain with the current technological resources. In this regard, using a sample of ~ 140 low-redshift ($z \leq 0.35$, with a median redshift $\langle z \rangle = 0.085$) bulges hosting active galactic nuclei (AGNs) with virial black hole masses $10^5 \lesssim M_{\text{BH}}/M_{\odot} \lesssim 2 \times 10^6$ (Jiang et al. 2011), Graham & Scott (2015) showed that they roughly follow the quadratic $M_{\text{BH}}-M_{*,\text{sph}}$ relation defined by their Sérsic bulges. The majority of our spiral galaxies host an AGN²⁰ and we anticipate here that the correlation traced by our spiral galaxy bulges may track the location of these lower mass AGNs in the $M_{\text{BH}}-M_{*,\text{sph}}$ diagram. That is, the AGNs appear to be the low-mass continuations of our tentative *late-type sequence* shown in Figure 5 and this will be explored with more rigour in a forthcoming paper.

As a final remark, we comment on the work by Reines & Volonteri (2015), who investigated the relationship between black hole mass and total galaxy stellar mass, $M_{*,\text{gal}}$. Their

²⁰ According to the nuclear classification reported on NED (NASA Extragalactic Database), among our 17 spiral galaxies, at least 12 host a Seyfert AGN and one hosts a LINER AGN.

Figure 8 presents the $M_{\text{BH}} - M_{*,\text{gal}}$ distribution for a sample of ≈ 260 local AGNs with virial black hole masses and for ≈ 80 galaxies with dynamical black hole masses. They concluded that the AGN sample and the early-type galaxies with quiescent black holes define two distinct sequences in their $M_{\text{BH}} - M_{*,\text{gal}}$ diagram; these two sequences have similar slopes, but have normalization factors that are different by more than one order of magnitude. Since we noted that the Jiang et al. (2011) AGN sample follows the steeper $M_{\text{BH}} - M_{*,\text{sph}}$ correlation traced by our spiral galaxy bulges (the majority of which host an AGN), it would be interesting to recover the $M_{\text{BH}} - M_{*,\text{sph}}$ distribution also for the AGN sample of Reines & Volonteri (2015). However, we do note that there is emerging evidence (e.g., Busch et al. 2015; Subramanian et al. 2016) for a population of bulges with black hole masses residing below (or to the right of) the red and blue $M_{\text{BH}} - M_{*,\text{sph}}$ sequences constructed here using samples with directly measured black hole masses, as speculated by Batcheldor (2010).

5. CONCLUSIONS

Using $3.6 \mu\text{m}$ *Spitzer* images, we have performed accurate multicomponent decompositions (i.e., bulge, disks, bars, spiral arms, rings, halo, nucleus, depleted core, etc.), which were checked to be consistent with the two-dimensional galaxy kinematics, for 66 nearby galaxies with a dynamical measurement of their black hole mass. We have derived galaxy luminosities, spheroid luminosities, and spheroid stellar masses. Our galaxy sample, besides being to date the largest sample with reliable bulge masses used to investigate black hole mass scaling relations, contains 17 spiral galaxies, half of which have $M_{\text{BH}} < 10^7 M_{\odot}$. This constitutes a significant improvement over past studies whose samples were biased toward high-mass, early-type galaxies.

Using our state-of-the-art data set, we have investigated substructure in the $M_{\text{BH}} - L_{\text{gal}}$, $M_{\text{BH}} - L_{\text{sph}}$ and $M_{\text{BH}} - M_{*,\text{sph}}$ diagrams. Our principal conclusions are as follows.

1. The logarithmic $M_{\text{BH}} - M_{*,\text{sph}}$ relation for the spheroidal components of early-type (elliptical + lenticular) galaxies has a slope of 1.04 ± 0.10 and intrinsic scatter of $\epsilon_{(Y|X)} = 0.43 \pm 0.06$ dex. We call this tight correlation an *early-type sequence*. The $M_{\text{BH}} - M_{*,\text{sph}}$ log-relation for the bulges of late-type (spiral) galaxies has a slope of 2–3, which is less well constrained due to the smaller size of the subsample and, more importantly, the smaller range in spheroid stellar mass ($3 \times 10^9 \lesssim M_{*,\text{sph}}/M_{\odot} \lesssim 3 \times 10^{10}$) that the subsample spans. We refer to this correlation as a *late-type sequence*. In (gas-poor) early-type galaxies, the black hole and the stellar content of the spheroidal component grow at the same pace, following a linear $M_{\text{BH}} - M_{*,\text{sph}}$ relation. In (gas-rich) spiral galaxies, the black hole grows faster than its host bulge, following a quadratic/cubic $M_{\text{BH}} - M_{*,\text{sph}}$ relation. Unsurprisingly, in a color–magnitude diagram²¹, our early- and late-type galaxies occupy the two distinct regions of the red sequence and the blue cloud, respectively. Analogous with this, we refer to our *early-type sequence* as a *red sequence* and to our *late-type sequence* as a *blue sequence*.

²¹ Total $B - V$ colors, corrected for inclination, Galactic extinction and K -correction, were taken from the HyperLEDA online database (Makarov et al. 2014).

2. The median $M_{\text{BH}}/M_{*,\text{sph}}$ ratio for the early-type galaxies is $0.68 \pm 0.04\%$. This value is dramatically larger than what was previously reported (0.1%–0.2% for all galaxy types, e.g., Marconi & Hunt 2003), but in close agreement with the value of 0.49% reported by Graham & Scott (2013) for core-Sérsic spheroids.
3. The logarithmic $M_{\text{BH}} - M_{*,\text{sph}}$ relations for the core-Sérsic and Sérsic spheroids have slopes with overlapping uncertainties (1.19 ± 0.23 and 1.48 ± 0.20 , respectively). The Sérsic relation is less steep than, but also has overlapping uncertainties with, the slope of 2.22 ± 0.58 reported by Scott et al. (2013) for Sérsic spheroids. The distinction between core-Sérsic and Sérsic spheroids found by Scott et al. (2013) is thus less pronounced here.
4. In the $M_{\text{BH}} - L_{\text{sph}}$ (or $M_{\text{BH}} - M_{*,\text{sph}}$) diagram, for early-type galaxies, we did not observe the change in slope required for consistency with the log–linear $M_{\text{BH}} - \sigma$ and bent $L_{\text{sph}} - \sigma$ correlations. This issue of inconsistency, therefore, remains an open question. It might be that we are still not probing enough low-mass black holes ($M_{\text{BH}} < 10^7 M_{\odot}$) for the subsample of early-type galaxies, or that the transition from $L_{\text{sph}} \propto \sigma^2$ at low luminosities to $L_{\text{sph}} \propto \sigma^{(5–6)}$ at high luminosities is less sharp than previously thought. We intend to investigate this point in our future work.
5. It has been argued that pseudo-bulges (disk-like, rotation-supported systems, built from secular processes) do not follow the $M_{\text{BH}} - L_{\text{sph}}$ correlation defined by classical bulges (spheroidal, pressure-supported systems, formed through violent processes). The recent literature (e.g., Sani et al. 2011; Beifiori et al. 2012) has distinguished between pseudo- and classical bulges according to their Sérsic index, n_{sph} . Although we do not consider the Sérsic index a good indicator of the nature of a bulge (e.g., Graham & Worley 2008), we investigated this point and found that, within the current data set, spheroids with $n_{\text{sph}} < 2$ are not offset to lower M_{BH} from the $M_{\text{BH}} - L_{\text{sph}}$ correlation defined by spheroids with $n_{\text{sph}} > 2$.
6. The $M_{\text{BH}} - L_{\text{gal}}$ and $M_{\text{BH}} - L_{\text{sph}}$ correlations have the same level of intrinsic scatter when considering early-type galaxies only. Once reasonable numbers of spiral galaxies are included, M_{BH} correlates better with L_{sph} than with L_{gal} (see also Beifiori et al. 2012; Erwin & Gadotti 2012).

Finally, we note that some of the literature-sourced black hole mass measurements used by Kormendy & Ho (2013) are different from those used here. While these differences are smaller than 18% for 78% of the galaxies, in three cases (NGC 0821, NGC 4291, and NGC 3393) they are larger than a factor of 2.3. We repeated our entire analysis using only the 58 galaxies that are in common between our sample and the sample of Kormendy & Ho (2013), assuming for these galaxies the black hole mass measurements published by Kormendy & Ho (2013). In doing so, we found that none of our conclusions changed.

G.S. warmly thanks Luca Cortese, Elisabete Lima Da Cunha, Duncan Forbes, and Gonzalo Diaz for useful discussion. We also thank the anonymous referee for useful comments and suggestions. This research was supported by Australian Research Council funding through grants DP110103509 and FT110100263. This work is based on observations made with the IRAC instrument (Fazio

et al. 2004) on board the *Spitzer Space Telescope*, which is operated by the Jet Propulsion Laboratory, California Institute of Technology under a contract with NASA. This research has made use of the GOLDMine database (Gavazzi et al. 2003) and the NASA/IPAC Extragalactic Database (NED) which is operated by the Jet Propulsion Laboratory, California Institute of Technology, under contract with the National Aeronautics and Space Administration. We acknowledge the usage of the HyperLeda database (<http://leda.univ-lyon1.fr>). The BCES routine (Akritas & Bershady 1996) was run via the python module written by Rodrigo Nemmen (Nemmen et al. 2012), which is available at <https://github.com/rsnemmen/BCES>.

REFERENCES

- Akritas, M. G., & Bershady, M. A. 1996, *ApJ*, **470**, 706
 Arnold, J. A., Romanowsky, A. J., Brodie, J. P., et al. 2014, *ApJ*, **791**, 80
 Athanassoula, E. 2005, *MNRAS*, **358**, 1477
 Balcells, M., Graham, A. W., & Peletier, R. F. 2007, *ApJ*, **665**, 1104
 Bardeen, J. M. 1975, in IAU Symp. 69, Dynamics of the Solar Systems, ed. A. Hayli, 297
 Batcheldor, D. 2010, *ApJL*, **711**, L108
 Beifiori, A., Courteau, S., Corsini, E. M., & Zhu, Y. 2012, *MNRAS*, **419**, 2497
 Bekki, K. 2010, *MNRAS*, **401**, L58
 Bender, R. 1990, *A&A*, **229**, 441
 Busch, G., Fazeli, N., Eckart, A., et al. 2015, arXiv:1511.00904
 Capaccioli, M. 1987, IAU Symp. 127, Structure and Dynamics of Elliptical Galaxies, ed. P. T. de Zeeuw, 47
 Cappellari, M., Emsellem, E., Krajnović, D., et al. 2011, *MNRAS*, **413**, 813
 Carter, D. 1987, *ApJ*, **312**, 514
 Chilingarian, I. V., Cayatte, V., Durret, F., et al. 2008, *A&A*, **486**, 85
 Cody, A. M., Carter, D., Bridges, T. J., Mobasher, B., & Poggianti, B. M. 2009, *MNRAS*, **396**, 1647
 Combes, F., Debbasch, F., Friedli, D., & Pfenniger, D. 1990, *A&A*, **233**, 82
 Combes, F., & Sanders, R. H. 1981, *A&A*, **96**, 164
 Davies, J. I., Phillipps, S., Cawson, M. G. M., Disney, M. J., & Kibblewhite, E. J. 1988, *MNRAS*, **232**, 239
 Davies, R. L., Efstathiou, G., Fall, S. M., Illingworth, G., & Schechter, P. L. 1983, *ApJ*, **266**, 41
 de Rijcke, S., Michielson, D., Dejonghe, H., Zeilinger, W. W., & Hau, G. K. T. 2005, *A&A*, **438**, 491
 dos Anjos, S., & da Silva, M. B. 2013, *MSAIS*, **25**, 33
 Dressler, A. 1989, in IAU Symp. 134, Active Galactic Nuclei, ed. D. E. Osterbrock & J. S. Miller, 217
 Eliche-Moral, M. C., González-García, A. C., Balcells, M., et al. 2011, *A&A*, **533**, A104
 Emsellem, E., Cappellari, M., Krajnović, D., et al. 2011, *MNRAS*, **414**, 888
 Erwin, P. 2010, arXiv:1002.1445
 Erwin, P., Beltrán, J. C. V., Graham, A. W., & Beckman, J. E. 2003, *ApJ*, **597**, 929
 Erwin, P., & Gadotti, D. A. 2012, *AdAst*, **2012**, 4
 Erwin, P., Saglia, R., Thomas, J., et al. 2015, in IAU Symp. 309, Using 3D Spectroscopy to Probe the Orbital Structure of Composite Bulges, ed. B. L. Ziegler et al., 359
 Fazio, G. G., Hora, J. L., Allen, L. E., et al. 2004, *ApJS*, **154**, 10
 Ferrarese, L., & Ford, H. 2005, *SSRv*, **116**, 523
 Ferrarese, L., & Merritt, D. 2000, *ApJL*, **539**, L9
 Forbes, D. A., Lasky, P., Graham, A. W., & Spitler, L. 2008, *MNRAS*, **389**, 1924
 Gadotti, D. A. 2009, *MNRAS*, **393**, 1531
 Gavazzi, G., Boselli, A., Donati, A., Franzetti, P., & Scoglio, M. 2003, *A&A*, **400**, 451
 Gebhardt, K., Bender, R., Bower, G., et al. 2000, *ApJL*, **539**, L13
 Graham, A. 2015, *H&A*, **16**, 360
 Graham, A. W. 2007, *MNRAS*, **379**, 711
 Graham, A. W. 2012, *ApJ*, **746**, 113
 Graham, A. W. 2013, in Elliptical and Disk Galaxy Structure and Modern Scaling, ed. T. D. Oswalt, & W. C. Keel, 91
 Graham, A. W. 2014, in ASP Conf. Ser. 480, Structure and Dynamics of Disk Galaxies, ed. M. S. Seigar & P. Treuthardt (San Francisco, CA: ASP), 185
 Graham, A. W. 2016, *Galactic Bulges*, **418**, 263
 Graham, A. W., Erwin, P., Trujillo, I., & Asensio Ramos, A. 2003, *AJ*, **125**, 2951
 Graham, A. W., Onken, C. A., Athanassoula, E., & Combes, F. 2011, *MNRAS*, **412**, 2211
 Graham, A. W., & Scott, N. 2013, *ApJ*, **764**, 151
 Graham, A. W., & Scott, N. 2015, *ApJ*, **798**, 54
 Graham, A. W., & Worley, C. C. 2008, *MNRAS*, **388**, 1708
 Gültekin, K., Richstone, D. O., Gebhardt, K., et al. 2009, *ApJ*, **698**, 198
 Häring, N., & Rix, H.-W. 2004, *ApJL*, **604**, L89
 Held, E. V., de Zeeuw, T., Mould, J., & Picard, A. 1992, in IAU Symp. 149, The Stellar Populations of Galaxies, ed. B. Barbuy & A. Renzini, **429**
 Hohl, F. 1975, in IAU Symp. 69, Dynamics of the Solar Systems ed. A. Hayli, 349
 Jerjen, H., Binggeli, B., & Freeman, K. C. 2000, *AJ*, **119**, 593
 Jiang, Y.-F., Greene, J. E., & Ho, L. C. 2011, *ApJL*, **737**, L45
 Kelly, B. C. 2007, *ApJ*, **665**, 1489
 Keselman, J. A., & Nusser, A. 2012, *MNRAS*, **424**, 1232
 Kormendy, J. 2015, arXiv:1504.03330
 Kormendy, J., & Ho, L. C. 2013, *ARA&A*, **51**, 511
 Kormendy, J., & Richstone, D. 1995, *ARA&A*, **33**, 581
 Kourkchi, E., Khosroshahi, H. G., Carter, D., et al. 2012, *MNRAS*, **420**, 2819
 Laor, A. 1998, *ApJL*, **505**, L83
 Laor, A. 2001, *ApJ*, **553**, 677
 Läsker, R., Ferrarese, L., & van de Ven, G. 2014a, *ApJ*, **780**, 69
 Läsker, R., Ferrarese, L., van de Ven, G., & Shankar, F. 2014b, *ApJ*, **780**, 70
 Lauer, T. R., Faber, S. M., Richstone, D., et al. 2007a, *ApJ*, **662**, 808
 Lauer, T. R., Faber, S. M., Richstone, D., et al. 2007b, *ApJ*, **662**, 808
 Liu, F. S., Xia, X. Y., Mao, S., Wu, H., & Deng, Z. G. 2008, *MNRAS*, **385**, 23
 MacArthur, L. A., González, J. J., & Courteau, S. 2009, *MNRAS*, **395**, 28
 Magorrian, J., Tremaine, S., Richstone, D., et al. 1998, *AJ*, **115**, 2285
 Makarov, D., Prugniel, P., Terekhova, N., Courtois, H., & Vauglin, I. 2014, *A&A*, **570**, A13
 Malumuth, E. M., & Kirshner, R. P. 1981, *ApJ*, **251**, 508
 Marconi, A., & Hunt, L. K. 2003, *ApJL*, **589**, L21
 Matković, A., & Guzmán, R. 2005, *MNRAS*, **362**, 289
 McConnell, N. J., & Ma, C.-P. 2013, *ApJ*, **764**, 184
 McConnell, N. J., Ma, C.-P., Gebhardt, K., et al. 2011, *Natur*, **480**, 215
 Meidt, S. E., Schinnerer, E., van de Ven, G., et al. 2014, *ApJ*, **788**, 144
 Montero-Dorta, A. D., Shu, Y., Bolton, A. S., Brownstein, J. R., & Weiner, B. J. 2015, arXiv:1505.03866
 Nemmen, R. S., Georganopoulos, M., Guirieic, S., et al. 2012, *Sci*, **338**, 1445
 Nieto, J.-L., Bender, R., Arnaud, J., & Surma, P. 1991, *A&A*, **244**, L25
 Peletier, R. F., Kutdemir, E., van der Wolk, G., et al. 2012, *MNRAS*, **419**, 2031
 Pfenniger, D., & Friedli, D. 1991, *A&A*, **252**, 75
 Press, W. H., Teukolsky, S. A., Vetterling, W. T., & Flannery, B. P. 1992, Numerical Recipes in FORTRAN. The Art of Scientific Computing (2nd ed.; Cambridge: Cambridge Univ. Press)
 Querejeta, M., Eliche-Moral, M. C., Tapia, T., et al. 2015, *A&A*, **573**, A78
 Reines, A. E., & Volonteri, M. 2015, *ApJ*, **813**, 82
 Rix, H.-W., & White, S. D. M. 1990, *ApJ*, **362**, 52
 Rix, H.-W., & White, S. D. M. 1992, *MNRAS*, **254**, 389
 Rusli, S. P., Thomas, J., Saglia, R. P., et al. 2013, *AJ*, **146**, 45
 Ryan, C. J., De Robertis, M. M., Virani, S., Laor, A., & Dawson, P. C. 2007, *ApJ*, **654**, 799
 Saha, K. 2015, *ApJL*, **806**, L29
 Saha, K., Martinez-Valpuesta, I., & Gerhard, O. 2012, *MNRAS*, **421**, 333
 Sani, E., Marconi, A., Hunt, L. K., & Risaliti, G. 2011, *MNRAS*, **413**, 1479
 Savorgnan, G. A. D., & Graham, A. W. 2015, *MNRAS*, **446**, 2330
 Scannapieco, C., White, S. D. M., Springel, V., & Tissera, P. B. 2011, *MNRAS*, **417**, 154
 Schechter, P. L. 1980, *AJ*, **85**, 801
 Scorza, C., & Bender, R. 1990, *A&A*, **235**, 49
 Scorza, C., & Bender, R. 1995, *A&A*, **293**, 20
 Scott, N., Davies, R. L., Houghton, R. C. W., et al. 2014, *MNRAS*, **441**, 274
 Scott, N., Graham, A. W., & Schombert, J. 2013, *ApJ*, **768**, 76
 Seidel, M. K., Cacho, R., Ruiz-Lara, T., et al. 2015, *MNRAS*, **446**, 2837
 Sheth, K., Regan, M., Hinz, J. L., et al. 2010, *PASP*, **122**, 1397
 Subramanian, S., Ramya, S., Das, M., et al. 2016, *MNRAS*, **455**, 3148
 Tortora, C., Napolitano, N. R., Romanowsky, A. J., Capaccioli, M., & Covone, G. 2009, *MNRAS*, **396**, 1132
 Tremaine, S., Gebhardt, K., Bender, R., et al. 2002, *ApJ*, **574**, 740
 Trujillo, I., Erwin, P., Asensio Ramos, A., & Graham, A. W. 2004, *AJ*, **127**, 1917
 van den Bosch, R. C. E., Gebhardt, K., Gültekin, K., et al. 2012, *Natur*, **491**, 729

- Vika, M., Driver, S. P., Cameron, E., Kelvin, L., & Robotham, A. 2012,
[MNRAS](#), **419**, 2264
- von der Linden, A., Best, P. N., Kauffmann, G., & White, S. D. M. 2007,
[MNRAS](#), **379**, 867
- Wandel, A. 1999, [ApJL](#), **519**, L39
- Yee, H. K. C. 1992, in ASP Conf. Ser. 31, Relationships Between Active
Galactic Nuclei and Starburst Galaxies, ed. A. V. Filippenko (San
Francisco, CA: ASP), [417](#)
- Young, C. K., & Currie, M. J. 1994, [MNRAS](#), **268**, L11

5

$$M_{\text{BH}} - n_{\text{sph}}$$

While the previous Chapter was dedicated to the study of the relations between black hole mass and galaxy or spheroid luminosity, in this Chapter we will perform an analogous analysis to explore the relation between black hole mass and spheroid Sérsic index ($M_{\text{BH}} - n_{\text{sph}}$). To address the issue of consistency between galaxy scaling relations that was outlined in Chapter 1, it is mandatory to include also an analysis of the relation between spheroid luminosity and spheroid Sérsic index ($L_{\text{sph}} - n_{\text{sph}}$). The reliability of the uncertainties associated with the Sérsic index measurements obtained from our 1D decompositions ensures a robust estimate of the intrinsic scatter in the $M_{\text{BH}} - n_{\text{sph}}$ diagram, which can be compared with that in the $M_{\text{BH}} - L_{\text{sph}}$ diagram.

The remainder of this chapter comprises the peer-reviewed version of the paper “Supermassive Black Holes and Their Host Spheroids. III. The $M_{\text{BH}} - n_{\text{sph}}$ correlation” by G. A. D. Savorgnan, accepted for publication in the *The Astrophysical Journal*.

SUPERMASSIVE BLACK HOLES AND THEIR HOST SPHEROIDS III. THE $M_{\text{BH}} - n_{\text{sph}}$ CORRELATION

GILIA A. D. SAVORGNA¹

Centre for Astrophysics and Supercomputing, Swinburne University of Technology, Hawthorn, Victoria 3122, Australia.

Draft version March 9, 2016

ABSTRACT

The Sérsic $R^{1/n}$ model is the best approximation known to date for describing the light distribution of stellar spheroidal and disk components, with the Sérsic index n providing a direct measure of the central radial concentration of stars. The Sérsic index of a galaxy's spheroidal component, n_{sph} , has been shown to tightly correlate with the mass of the central supermassive black hole, M_{BH} . The $M_{\text{BH}} - n_{\text{sph}}$ correlation is also expected from other two well known scaling relations involving the spheroid luminosity, L_{sph} : the $L_{\text{sph}} - n_{\text{sph}}$ and the $M_{\text{BH}} - L_{\text{sph}}$. Obtaining an accurate estimate of the spheroid Sérsic index requires a careful modelling of a galaxy's light distribution and some studies have failed to recover a statistically significant $M_{\text{BH}} - n_{\text{sph}}$ correlation. With the aim of re-investigating the $M_{\text{BH}} - n_{\text{sph}}$ and other black hole mass scaling relations, we performed a detailed (i.e. bulge, disks, bars, spiral arms, rings, halo, nucleus, etc.) decomposition of 66 galaxies, with directly measured black hole masses, that had been imaged at 3.6 μm with *Spitzer*. In this paper, the third of this series, we present an analysis of the $L_{\text{sph}} - n_{\text{sph}}$ and $M_{\text{BH}} - n_{\text{sph}}$ diagrams. While early-type (elliptical+lenticular) and late-type (spiral) galaxies split into two separate relations in the $L_{\text{sph}} - n_{\text{sph}}$ and $M_{\text{BH}} - L_{\text{sph}}$ diagrams, they reunite into a single $M_{\text{BH}} \propto n_{\text{sph}}^{3.39 \pm 0.15}$ sequence with relatively small intrinsic scatter ($\epsilon \simeq 0.25$ dex). The black hole mass appears to be closely related to the spheroid central concentration of stars, which mirrors the inner gradient of the spheroid gravitational potential.

Subject headings: black hole physics; galaxies: bulges; galaxies: elliptical and lenticular, cD; galaxies: evolution; galaxies: structure

1. INTRODUCTION

The empirical Sérsic (1963, 1968) $R^{1/n}$ model has been demonstrated to provide adequate description of the light distribution of the stellar spheroidal¹ and disk components of galaxies (e.g. Caon et al. 1993; Andredakis et al. 1995; Iodice et al. 1997, 1999; Seigar & James 1998; Khosroshahi et al. 2000), yet its physical origin has remained unexplained for decades. The Sérsic model parameterizes the intensity of light I as a function of the projected galactic radius R such that

$$I(R; I_e, R_e, n) = I_e \exp \left\{ -b_n \left[\left(\frac{R}{R_e} \right)^{1/n} - 1 \right] \right\},$$

where I_e indicates the intensity at the effective radius R_e that encloses half of the total light from the model, the Sérsic index n is the parameter that regulates the curvature of the radial light profile, and b_n is a constant defined in terms of the Sérsic index (see Graham & Driver 2005, and references therein). A large Sérsic index corresponds to a steep inner profile and a shallow outer profile, whereas a small Sérsic index corresponds to a shallow inner profile and a steep outer profile. This means that, for a stellar spheroidal system whose light distribution is well approximated by the Sérsic model, the larger the

Sérsic index is, the more centrally concentrated the stars are and the more extended the outer envelope is.

A compelling physical interpretation for the Sérsic profile family was recently theorized by Cen (2014) and later confirmed by Nipoti (2015) by means of *N*-body simulations. Cen (2014) conjectured that, when structures form within a standard cold dark matter model seeded by random Gaussian fluctuations, any centrally concentrated stellar structure always possesses an extended stellar envelope, and vice versa. Nipoti (2015) quantitatively explored Cen's hypothesis and showed that systems originated from several mergers have a large Sérsic index ($n \gtrsim 4$), whereas systems with a Sérsic index as small as $n \simeq 2$ can be produced by coherent dissipationless collapse, and exponential profiles ($n = 1$) can only be obtained through dissipative processes. This scenario sets the theoretical framework for the well known correlation between the spheroid luminosity, L_{sph} , and the spheroid Sérsic index, n_{sph} , (e.g. Young & Currie 1994; Jerjen et al. 2000; Graham & Guzmán 2003), although the numerical results of Nipoti (2015) seem to lack of spheroidal systems with Sérsic indices as large as 7–10, which are commonly observed in the local Universe.

Given the existence of the $L_{\text{sph}} - n_{\text{sph}}$ correlation and the relation between the central black hole mass, M_{BH} , and the spheroid luminosity (e.g. Kormendy & Richstone 1995; Magorrian et al. 1998; Marconi & Hunt 2003; Häring & Rix 2004), an $M_{\text{BH}} - n_{\text{sph}}$ relation must exist. After Graham (2001) showed that the black hole mass is tightly linked to the stellar light concentration of spheroids (measured through a parameter different from,

gsavorgn@astro.swin.edu.au

¹ Throughout the text, we use the term “spheroid” to indicate either a disk-less elliptical galaxy or the bulge component of a disk galaxy; we do not attempt at distinguishing between classical bulges and disk-like pseudo-bulges (see Graham 2015b or Graham 2015a).

but closely related to the Sérsic index), Graham & Driver (2007) presented for the first time the $M_{\text{BH}} - n_{\text{sph}}$ correlation using a sample of 27 elliptical and disk galaxies. Graham & Driver (2007) fit their data with a log-quadratic regression, finding that the $M_{\text{BH}} - n_{\text{sph}}$ log-relation is steeper for spheroids with small Sérsic indices and shallower for spheroids with large Sérsic indices, and measured a relatively small level of scatter². A few years later, Sani et al. (2011), Vika et al. (2012) and Beifiori et al. (2012) performed multi-component decompositions for samples of galaxies similar to that used by Graham & Driver (2007), but they failed to recover a strong $M_{\text{BH}} - n_{\text{sph}}$ relation. This issue was tackled by Savorgnan et al. (2013), who collected the Sérsic index measurements published by Graham & Driver (2007), Sani et al. (2011), Vika et al. (2012) and Beifiori et al. (2012) for a sample of 54 galaxies, and showed that, by rejecting the most discrepant measurements and averaging the remaining ones, a strong $M_{\text{BH}} - n_{\text{sph}}$ relation was retrieved. Remarkably, Savorgnan et al. (2013) repeated their analysis upon excluding the Sérsic index measurements of Graham & Driver (2007) and still regained a significant $M_{\text{BH}} - n_{\text{sph}}$ correlation. This was suggesting that the individual galaxy decompositions of Sani et al. (2011), Vika et al. (2012) and Beifiori et al. (2012) were not accurate, i.e. each individual study obtained “noisy” Sérsic index measurements which prevented the recovery of a strong $M_{\text{BH}} - n_{\text{sph}}$ relation.

Motivated by the need for more accurate galaxy decompositions to refine and re-investigate scaling relations between the black hole mass and several host spheroid structural parameters, we performed state-of-the-art modelling for the largest sample of galaxies to date (Savorgnan & Graham 2015b, hereafter *Paper I*) for which a dynamical measurement of the black hole mass was available. In doing so, we used 3.6 μm *Spitzer* satellite imagery, given its superb capability to trace the stellar mass (Sheth et al. 2010, and references therein). In Savorgnan et al. (2015, hereafter *Paper II*) we examined the correlations between the black hole mass and the total galaxy luminosity, the spheroid luminosity and the spheroid stellar mass. Here we focus on the $M_{\text{BH}} - n_{\text{sph}}$ relation.

2. DATA

We populated the $L_{\text{sph}} - n_{\text{sph}}$ and $M_{\text{BH}} - n_{\text{sph}}$ diagrams with the same galaxy sample used in *Paper II* (and presented here in Table 1), i.e. 66 galaxies for which a dynamical measurement of the black hole mass has been reported in the literature (by Graham & Scott 2013 or Rusli et al. 2013) and for which we were able to successfully model the light distribution and measure the spheroid structural parameters using 3.6 μm *Spitzer* satellite images. Our galaxy decompositions take into account bulge, disks, spiral arms, bars, rings, halo, extended or unresolved nuclear source and partially depleted core, and – for the first time – they were checked to be consistent with the galaxy kinematics (Emsellem et al. 2011; Scott et al. 2014; Arnold et al. 2014). Kinematical information was used to confirm the presence

² At the time, the $M_{\text{BH}} - \sigma$ relation (Ferrarese & Merritt 2000; Gebhardt et al. 2000) was reported to have the same level of scatter as the $M_{\text{BH}} - n_{\text{sph}}$ relation ($\simeq 0.3$ dex).

of disk components in the majority of early-type (elliptical + lenticular) galaxies and, more importantly, to establish the radial extent of these disks, which in most cases is not obvious from a visual inspection of the galaxy images. This enabled us to distinguish between intermediate-scale disks, that are fully embedded in the spheroid, and large-scale disks, that encase the bulge and dominate the light at large radii. Savorgnan & Graham (2015a) demonstrate that when an intermediate-scale disk is misclassified and modeled as a large-scale disk, the luminosity of the spheroid is underestimated, hence the galaxy incorrectly appears as a positive outlier (an “over-massive” black hole) in the $M_{\text{BH}} - L_{\text{sph}}$ diagram. A detailed description of the dataset used here, the data reduction process and the galaxy modelling technique that we developed can be found in *Paper I*, along with a discussion of how we estimated the uncertainties on the spheroid Sérsic indices³. For the present analysis, we elected to use the spheroid Sérsic indices obtained from the decomposition of the one-dimensional major-axis surface brightness profiles of our galaxies. The morphological classification (E = elliptical; E/S0 = elliptical/lenticular; S0 = lenticular; S0/Sp = lenticular/spiral; Sp = spiral; and “merger”) follows from the galaxy decompositions illustrated in *Paper I*. As in *Paper II*, we will refer to early-type galaxies (E+S0) and late-type galaxies (Sp). The early-type bin includes the two galaxies classified as E/S0, whereas the two galaxies classified as S0/Sp and the two galaxies classified as “mergers” are included in neither the early- nor the late-type bin.

3. ANALYSIS AND RESULTS

As in *Paper II*, a linear regression analysis of the $L_{\text{sph}} - n_{\text{sph}}$ (Table 3 and Figure 1) and $M_{\text{BH}} - n_{\text{sph}}$ (Table 4 and Figure 2) diagrams was performed using three different routines: the BCES code from Akritas & Bershady (1996), the FITEXY routine (Press et al. 1992), as modified by Tremaine et al. (2002), and the Bayesian estimator `linmix_err` (Kelly 2007). All of these three routines take into account the intrinsic scatter, but only the FITEXY and the `linmix_err` codes allow one to quantify it. Tremaine et al. (2002) cautioned that the BCES estimator becomes ineffective when the dataset contains at least one low-precision measurement – regardless of how many high-precision measurements are in the sample – and tends to be biased in case of low number statistics, or if the mean square of the uncertainties associated to the independent variable is comparable to the variance of the distribution of the independent variable. According to the results from the Monte Carlo Markov Chain simulations of Tremaine et al. (2002) and Novak et al. (2006), these problems can be overcome with the use of the modified FITEXY routine. Park et al. (2012) also concluded that the modified FITEXY routine performs better and returns less biased results than the BCES estimator, and noted that the the modified FITEXY routine is computationally less intensive than the Bayesian

³ The uncertainties associated with the spheroid Sérsic indices were estimated with a method that takes into account systematic errors. This method consists in comparing, for each of our galaxies, the measurements of the spheroid Sérsic index obtained by other studies with that obtained by us. Systematic errors are typically not considered by popular 2D fitting codes, which report only the statistical errors associated with their fitted parameters. Readers should refer to *Paper I* for a more detailed discussion on this topic.

TABLE 1
 GALAXY SAMPLE.

Galaxy	Type	Distance [Mpc]	M_{BH} $[10^8 M_{\odot}]$	MAG_{sph}	$n_{\text{sph}}^{\text{maj}}$
(1)	(2)	(3)	(4)	(5)	(6)
IC 1459	E	28.4	24^{+10}_{-10}	$-26.15^{+0.18}_{-0.11}$	$6.6^{+0.9}_{-0.8}$
IC 2560	Sp (bar)	40.7	$0.044^{+0.044}_{-0.022}$	$-22.27^{+0.66}_{-0.58}$	$0.8^{+0.4}_{-0.3}$
IC 4296	E	40.7	11^{+2}_{-2}	$-26.35^{+0.18}_{-0.11}$	$5.8^{+0.8}_{-0.7}$
M31	Sp (bar)	0.7	$1.4^{+0.9}_{-0.3}$	$-22.74^{+0.18}_{-0.11}$	$2.2^{+0.3}_{-0.3}$
M49	E	17.1	25^{+3}_{-1}	$-26.54^{+0.18}_{-0.11}$	$6.6^{+0.9}_{-0.8}$
M59	E	17.8	$3.9^{+0.4}_{-0.4}$	$-25.18^{+0.18}_{-0.11}$	$5.5^{+0.8}_{-0.7}$
M64	Sp	7.3	$0.016^{+0.004}_{-0.004}$	$-21.54^{+0.18}_{-0.11}$	$0.8^{+0.1}_{-0.1}$
M81	Sp (bar)	3.8	$0.74^{+0.21}_{-0.11}$	$-23.01^{+0.88}_{-0.66}$	$1.7^{+1.3}_{-0.7}$
M84	E	17.9	$9.0^{+0.9}_{-0.8}$	$-26.01^{+0.66}_{-0.58}$	$7.8^{+3.6}_{-2.5}$
M87	E	15.6	$58.0^{+3.5}_{-3.5}$	$-26.00^{+0.66}_{-0.58}$	$10.0^{+4.7}_{-3.2}$
M89	E	14.9	$4.7^{+0.5}_{-0.5}$	$-24.48^{+0.66}_{-0.58}$	$4.6^{+2.2}_{-1.5}$
M94	Sp (bar)	4.4	$0.060^{+0.014}_{-0.014}$	$-22.08^{+0.18}_{-0.11}$	$0.9^{+0.1}_{-0.1}$
M96	Sp (bar)	10.1	$0.073^{+0.015}_{-0.015}$	$-22.15^{+0.18}_{-0.11}$	$1.5^{+0.2}_{-0.2}$
M104	S0/Sp	9.5	$6.4^{+0.4}_{-0.4}$	$-23.91^{+0.66}_{-0.58}$	$5.8^{+2.7}_{-1.8}$
M105	E	10.3	4^{+1}_{-1}	$-24.29^{+0.66}_{-0.58}$	$5.2^{+2.4}_{-1.6}$
M106	Sp (bar)	7.2	$0.39^{+0.01}_{-0.01}$	$-21.11^{+0.18}_{-0.11}$	$2.0^{+0.3}_{-0.2}$
NGC 0524	S0	23.3	$8.3^{+2.7}_{-1.3}$	$-23.19^{+0.18}_{-0.11}$	$1.1^{+0.2}_{-0.1}$
NGC 0821	E	23.4	$0.39^{+0.26}_{-0.09}$	$-24.00^{+0.88}_{-0.66}$	$5.3^{+4.1}_{-2.3}$
NGC 1023	S0 (bar)	11.1	$0.42^{+0.04}_{-0.04}$	$-22.82^{+0.18}_{-0.11}$	$2.1^{+0.3}_{-0.3}$
NGC 1300	Sp (bar)	20.7	$0.73^{+0.69}_{-0.35}$	$-22.06^{+0.66}_{-0.58}$	$3.8^{+1.8}_{-1.2}$
NGC 1316	merger	18.6	$1.50^{+0.75}_{-0.80}$	$-24.89^{+0.66}_{-0.58}$	$2.0^{+1.0}_{-0.7}$
NGC 1332	E/S0	22.3	14^{+2}_{-2}	$-24.89^{+0.88}_{-0.66}$	$5.1^{+3.9}_{-2.2}$
NGC 1374	E	19.2	$5.8^{+0.5}_{-0.5}$	$-23.68^{+0.18}_{-0.11}$	$3.7^{+0.5}_{-0.5}$
NGC 1399	E	19.4	$4.7^{+0.6}_{-0.6}$	$-26.43^{+0.18}_{-0.11}$	$10.0^{+1.4}_{-1.2}$
NGC 2273	Sp (bar)	28.5	$0.083^{+0.004}_{-0.004}$	$-23.00^{+0.66}_{-0.58}$	$2.1^{+1.0}_{-0.7}$
NGC 2549	S0 (bar)	12.3	$0.14^{+0.02}_{-0.13}$	$-21.25^{+0.18}_{-0.11}$	$2.3^{+0.3}_{-0.3}$
NGC 2778	S0 (bar)	22.3	$0.15^{+0.09}_{-0.10}$	$-20.80^{+0.66}_{-0.58}$	$1.3^{+0.6}_{-0.4}$
NGC 2787	S0 (bar)	7.3	$0.40^{+0.04}_{-0.05}$	$-20.11^{+0.66}_{-0.58}$	$1.1^{+0.5}_{-0.4}$
NGC 2974	Sp (bar)	20.9	$1.7^{+0.2}_{-0.2}$	$-22.95^{+0.66}_{-0.58}$	$1.4^{+0.7}_{-0.5}$
NGC 3079	Sp (bar)	20.7	$0.024^{+0.024}_{-0.012}$	$-23.01^{+0.66}_{-0.58}$	$1.3^{+0.6}_{-0.4}$
NGC 3091	E	51.2	36^{+1}_{-2}	$-26.28^{+0.18}_{-0.11}$	$7.6^{+1.0}_{-0.9}$
NGC 3115	E/S0	9.4	$8.8^{+10.0}_{-2.7}$	$-24.22^{+0.18}_{-0.11}$	$4.4^{+0.6}_{-0.5}$
NGC 3227	Sp (bar)	20.3	$0.14^{+0.10}_{-0.06}$	$-21.76^{+0.66}_{-0.58}$	$1.7^{+0.8}_{-0.5}$
NGC 3245	S0 (bar)	20.3	$2.0^{+0.5}_{-0.5}$	$-22.43^{+0.18}_{-0.11}$	$2.9^{+0.4}_{-0.3}$
NGC 3377	E	10.9	$0.77^{+0.04}_{-0.06}$	$-23.49^{+0.66}_{-0.58}$	$7.7^{+3.6}_{-2.5}$
NGC 3384	S0 (bar)	11.3	$0.17^{+0.01}_{-0.02}$	$-22.43^{+0.18}_{-0.11}$	$1.6^{+0.2}_{-0.2}$
NGC 3393	Sp (bar)	55.2	$0.34^{+0.02}_{-0.02}$	$-23.48^{+0.66}_{-0.58}$	$3.4^{+1.6}_{-1.1}$
NGC 3414	E	24.5	$2.4^{+0.3}_{-0.3}$	$-24.35^{+0.18}_{-0.11}$	$4.8^{+0.7}_{-0.6}$
NGC 3489	S0/Sp (bar)	11.7	$0.058^{+0.008}_{-0.008}$	$-21.13^{+0.66}_{-0.58}$	$1.5^{+0.7}_{-0.5}$
NGC 3585	E	19.5	$3.1^{+1.4}_{-0.6}$	$-25.52^{+0.66}_{-0.58}$	$5.2^{+2.4}_{-1.7}$
NGC 3607	E	22.2	$1.3^{+0.5}_{-0.5}$	$-25.36^{+0.66}_{-0.58}$	$5.5^{+2.6}_{-1.7}$
NGC 3608	E	22.3	$2.0^{+1.1}_{-0.6}$	$-24.50^{+0.66}_{-0.58}$	$5.2^{+2.4}_{-1.7}$
NGC 3842	E	98.4	97^{+30}_{-26}	$-27.00^{+0.18}_{-0.11}$	$8.1^{+1.1}_{-1.0}$
NGC 3998	S0 (bar)	13.7	$8.1^{+2.0}_{-1.9}$	$-22.32^{+0.88}_{-0.66}$	$1.2^{+0.9}_{-0.5}$
NGC 4026	S0 (bar)	13.2	$1.8^{+0.6}_{-0.6}$	$-21.58^{+0.88}_{-0.66}$	$2.4^{+1.8}_{-1.0}$
NGC 4151	Sp (bar)	20.0	$0.65^{+0.07}_{-0.07}$	$-23.40^{+0.66}_{-0.58}$	$1.4^{+0.6}_{-0.6}$
NGC 4261	E	30.8	5^{+1}_{-1}	$-25.72^{+0.66}_{-0.58}$	$4.7^{+2.2}_{-1.5}$
NGC 4291	E	25.5	$3.3^{+0.9}_{-2.5}$	$-24.05^{+0.66}_{-0.58}$	$4.2^{+2.0}_{-1.4}$
NGC 4388	Sp (bar)	17.0	$0.075^{+0.002}_{-0.002}$	$-21.26^{+0.88}_{-0.66}$	$0.6^{+0.5}_{-0.3}$
NGC 4459	S0	15.7	$0.68^{+0.13}_{-0.13}$	$-23.48^{+0.66}_{-0.58}$	$3.1^{+1.5}_{-1.0}$
NGC 4473	E	15.3	$1.2^{+0.4}_{-0.9}$	$-23.88^{+0.66}_{-0.58}$	$2.3^{+1.1}_{-0.7}$
NGC 4564	S0	14.6	$0.60^{+0.03}_{-0.09}$	$-22.30^{+0.18}_{-0.11}$	$2.6^{+0.4}_{-0.3}$
NGC 4596	S0 (bar)	17.0	$0.79^{+0.38}_{-0.33}$	$-22.73^{+0.18}_{-0.11}$	$2.7^{+0.4}_{-0.3}$

Galaxy	Type	Distance	M_{BH}	MAG_{sph}	$n_{\text{sph}}^{\text{maj}}$
(1)	(2)	[Mpc]	[$10^8 M_{\odot}$]	[mag]	(6)
(3)	(4)	(5)			
NGC 4697	E	11.4	$1.8^{+0.2}_{-0.1}$	$-24.82^{+0.88}_{-0.66}$	$7.2^{+5.5}_{-3.1}$
NGC 4889	E	103.2	210^{+160}_{-160}	$-27.54^{+0.18}_{-0.11}$	$8.1^{+1.1}_{-1.0}$
NGC 4945	Sp (bar)	3.8	$0.014^{+0.014}_{-0.007}$	$-20.96^{+0.66}_{-0.58}$	$1.4^{+0.7}_{-0.5}$
NGC 5077	E	41.2	$7.4^{+4.7}_{-3.0}$	$-25.45^{+0.18}_{-0.11}$	$4.2^{+0.6}_{-0.5}$
NGC 5128	merger	3.8	$0.45^{+0.17}_{-0.10}$	$-23.89^{+0.88}_{-0.66}$	$1.2^{+0.9}_{-0.5}$
NGC 5576	E	24.8	$1.6^{+0.3}_{-0.4}$	$-24.44^{+0.18}_{-0.11}$	$3.3^{+0.5}_{-0.4}$
NGC 5845	S0	25.2	$2.6^{+0.4}_{-1.5}$	$-22.96^{+0.88}_{-0.66}$	$2.5^{+1.9}_{-1.1}$
NGC 5846	E	24.2	11^{+1}_{-1}	$-25.81^{+0.66}_{-0.58}$	$6.4^{+3.0}_{-2.1}$
NGC 6251	E	104.6	5^{+2}_{-2}	$-26.75^{+0.18}_{-0.11}$	$6.8^{+0.9}_{-0.8}$
NGC 7052	E	66.4	$3.7^{+2.6}_{-1.5}$	$-26.32^{+0.18}_{-0.11}$	$4.2^{+0.6}_{-0.5}$
NGC 7619	E	51.5	25^{+8}_{-3}	$-26.35^{+0.66}_{-0.58}$	$5.3^{+2.5}_{-1.7}$
NGC 7768	E	112.8	13^{+5}_{-4}	$-26.90^{+0.66}_{-0.58}$	$8.4^{+3.9}_{-2.7}$
UGC 03789	Sp (bar)	48.4	$0.108^{+0.005}_{-0.005}$	$-22.77^{+0.88}_{-0.66}$	$1.9^{+1.4}_{-0.8}$

NOTE. — *Column (1):* Galaxy name. *Column (2):* Morphological type (E=elliptical, S0=lenticular, Sp=spiral, merger). The morphological classification of four galaxies is uncertain (E/S0 or S0/Sp). The presence of a bar is indicated. *Column (3):* Distance. *Column (4):* Black hole mass. *Column (5):* Absolute 3.6 μm spheroid magnitude. *Column (6):* Spheroid major-axis Sérsic index. Spheroid magnitudes and Sérsic indices come from our state-of-the-art multicomponent galaxy decompositions (*Paper I*), which include bulge, disks, bars, spiral arms, rings, halo, extended or unresolved nuclear source and partially depleted core, and that – for the first time – were checked to be consistent with the galaxy kinematics. The uncertainties were estimated with a method that takes into account systematic errors, which are typically not considered by popular 2D fitting codes.

technique `linmix_err`. Given that at least one of our subsamples (the lenticular galaxies) has a small size and that the uncertainties associated to n_{sph} are relatively large compared to the range spanned by the n_{sph} values for most of our subsamples, we put more trust in the results obtained with the modified FITEXY routine and throughout the text we quote only those.

We report both symmetrical and nonsymmetrical linear regressions. Symmetrical regressions are meant to be compared with theoretical expectations, whereas nonsymmetrical forward ($Y|X$) regressions – which minimize the scatter in the Y direction – allow one to predict the value of the observable Y with the best possible precision.

We searched for extreme outliers in both the $L_{\text{sph}} - n_{\text{sph}}$ and $M_{\text{BH}} - n_{\text{sph}}$ diagrams, and found that in our $L_{\text{sph}} - n_{\text{sph}}$ plot there are no 3σ outliers, whereas in our $M_{\text{BH}} - n_{\text{sph}}$ plot the lenticular galaxies NGC 0524 and NGC 3998 reside more than 3σ from the bisector linear regression for all galaxies. These two galaxies have therefore been excluded from the rest of the analysis.

3.1. $L_{\text{sph}} - n_{\text{sph}}$

Following Graham (2001), who showed that the $L_{\text{sph}} - n_{\text{sph}}$ relation is different for elliptical galaxies and the bulges of disk galaxies (S0+Sp), Savorgnan et al. (2013) re-analyzed the data from Graham & Guzmán (2003) and Graham & Worley (2008) and obtained two separate $L_{\text{sph}} - n_{\text{sph}}$ linear regressions for elliptical galaxies and the bulges of disk galaxies (in the B- and K-band, respectively). At the time, the $L_{\text{sph}} - n_{\text{sph}}$ datasets from Graham & Guzmán (2003) and Graham & Worley (2008) were of the best quality available to investigate the $L_{\text{sph}} - n_{\text{sph}}$ relation for different galaxy morphological types. However, these datasets were not obtained from a homogeneous analysis, but they were a collection of results taken from various past bulge/disk decomposition studies. Here we re-investigate the $L_{\text{sph}} - n_{\text{sph}}$ diagram (Figure 1) using only our high-quality dataset. Our spheroid luminosities and Sérsic indices were obtained from accurate multicomponent decompositions, performed in a consistent manner using the $3.6 \mu\text{m}$ band, which is less affected by dust extinction than the K-band. Graham & Worley (2008) presented a single $L_{\text{sph}} - n_{\text{sph}}$ correlation for the bulges of disk galaxies (S0+Sp). However, using our dataset, we fit the $L_{\text{sph}} - n_{\text{sph}}$ relation for elliptical, lenticular and spiral galaxies separately, and found that the values of the slope and intercept for the lenticular galaxies are not consistent within the errors with those for the spiral galaxies, but are consistent within the errors with those for the elliptical galaxies. Given this, we conclude that in the $L_{\text{sph}} - n_{\text{sph}}$ diagram elliptical and lenticular galaxies form together a single (*early-type*) sequence, whereas the combination of lenticular and spiral galaxies do not. According to the modified FITEXY routine, early-type galaxies⁴ fol-

⁴ Using the BCES estimator, Savorgnan et al. (2013) re-analyzed the dataset from Graham & Guzmán (2003) and obtained $L_{\text{sph}} \propto n_{\text{sph}}^{3.60 \pm 0.19}$ for the elliptical galaxies only. This result is in excellent agreement with the BCES linear regression obtained here for the early-type galaxies ($L_{\text{sph}} \propto n_{\text{sph}}^{3.89 \pm 0.42}$) and, remarkably, it is exactly the same proportionality obtained here for the early-type galaxies with the modified FITEXY routine.

low $L_{\text{sph}} \propto n_{\text{sph}}^{3.60 \pm 0.19}$, whereas late-type galaxies follow a shallower $L_{\text{sph}} \propto n_{\text{sph}}^{1.44 \pm 0.52}$ sequence.

Because the log-slopes of the correlations for early- and late-type galaxies are not consistent with each other within their 1σ uncertainties, our quantitative linear regression analysis suggests that the $L_{\text{sph}} - n_{\text{sph}}$ diagram is better described with a four-parameter model (two separate power-laws) rather than with a two-parameter model (single power-law). In addition, the relative quality of these two statistical models can be independently assessed using the Akaike Information Criterion (*AIC*, Akaike 1974). *AIC* is a trade-off between the statistical significance of a fit and the complexity of the model used. It benefits from the goodness of a fit, but at the same time is also penalized by the number of parameters of the model, hence it discourages overfitting. The *AICc* is a variation of the *AIC* that takes into account a correction for finite sample sizes:

$$AICc = 2k - 2 \ln(\mathcal{L}) + \frac{2k(k+1)}{n-k-1}, \quad (1)$$

where k is the number of parameter of the model, n is the sample size, and \mathcal{L} is the maximum value of the likelihood function for the model. Within a set of candidate models for a given dataset, the best model has the smallest *AICc* value. Using our $L_{\text{sph}} - n_{\text{sph}}$ dataset, the *AICc* value for a double power-law model is a factor of 3/4 smaller than the *AICc* value for a single power-law model.

3.2. $M_{\text{BH}} - n_{\text{sph}}$

Graham & Scott (2013) presented two different $M_{\text{BH}} - L_{\text{sph}}$ relations for Sérsic and core-Sérsic spheroids⁵ (Graham et al. 2003; Trujillo et al. 2004). However, in *Paper II* we found that the slopes of the $M_{\text{BH}} - L_{\text{sph}}$ correlations for Sérsic and core-Sérsic spheroids are consistent with each other within their 1σ uncertainties, which prevented us from considering them as two separate sequences. On the other hand, our analysis showed that early- and late-type galaxies follow two different $M_{\text{BH}} - L_{\text{sph}}$ relations. Given that early- and late-type galaxies define two separate sequences in both the $L_{\text{sph}} - n_{\text{sph}}$ and $M_{\text{BH}} - L_{\text{sph}}$ diagrams, we investigate substructure in the $M_{\text{BH}} - n_{\text{sph}}$ diagram. Using the results from the modified FITEXY routine, we know that the early-type galaxies follow $M_{\text{BH}} \propto L_{\text{sph}}^{1.03 \pm 0.11}$ and $L_{\text{sph}} \propto n_{\text{sph}}^{3.60 \pm 0.19}$, therefore we expect to find $M_{\text{BH}} \propto n_{\text{sph}}^{3.69 \pm 0.44}$; this prediction is in excellent agreement with the observed log-slope of 3.58 ± 0.27 obtained here. On the other hand, late-type galaxies follow $M_{\text{BH}} \propto L_{\text{sph}}^{2.58 \pm 1.06}$ and $L_{\text{sph}} \propto n_{\text{sph}}^{1.44 \pm 0.52}$, from which one can predict $M_{\text{BH}} \propto n_{\text{sph}}^{3.72 \pm 2.03}$; this is consistent with the observed log-slope of 4.55 ± 0.66 . The Bayesian estimator `linmix_err` returns consistent results: a log-slope of 3.44 ± 0.33 for the early-type galaxies and a log-slope of 4.12 ± 1.07 for the late-type galaxies. Regardless of the linear regression routine used, the values of the slope and intercept for the early- and late-type galaxies are consistent with each other within their 1σ uncertainties⁶. Our

⁵ Core-Sérsic spheroids have partially depleted cores relative to their outer Sérsic light profile, whereas Sérsic spheroids have no central deficit of stars.

⁶ In effect, considering the results of the modified FITEXY routine, the slopes of the relations for early- and late-type galaxies are

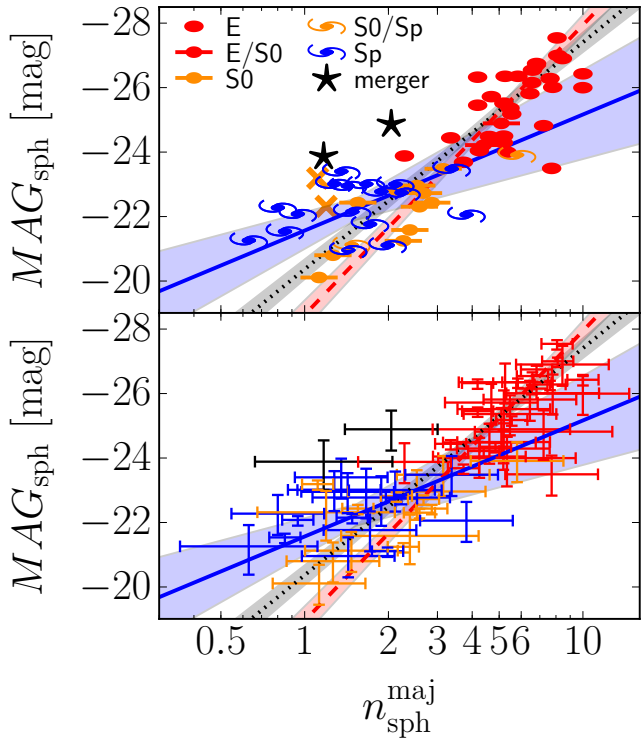


FIG. 1.— Spheroid absolute magnitude (at 3.6 μm) plotted against spheroid Sérsic index measured along the galaxy major-axis. The top and bottom panels show the data points and their error bars, respectively. Symbols are coded according to the galaxy morphological type (see legend in the top panel). The orange crosses denote two lenticular galaxies (NGC 0524 and NGC 3998) which were excluded from the linear regression analysis (see Section 3). The black dotted line is the FITEXY bisector linear regression for all (64) galaxies, with the gray shaded area denoting its 1σ uncertainty. The red dashed line is the FITEXY bisector linear regression for the $45 - 2 = 43$ early-type galaxies (E+S0), with the red shaded area denoting its 1σ uncertainty. The shallower blue solid line is the FITEXY bisector linear regression for the bulges of the 17 late-type (Sp) galaxies, with the blue shaded area denoting its 1σ uncertainty. The error bars in the bottom panel have the same color coding as the symbols in the top panel.

analysis shows that the early- and late-type galaxies do not follow two separate trends in the $M_{\text{BH}} - n_{\text{sph}}$ diagram, i.e. we do not identify any significant substructure based on the galaxy morphological type. The $AICc$ value for a single power-law model is a factor of 2/3 smaller than the $AICc$ value for a double power-law model. The symmetrical linear regression for all galaxies obtained with the modified FITEXY routine is:

$$\log\left(\frac{M_{\text{BH}}}{M_{\odot}}\right) = (8.15 \pm 0.06) + (3.37 \pm 0.15)(\log n_{\text{sph}} - 0.50).$$

We have seen that the early- and late-type galaxies in the $M_{\text{BH}} - n_{\text{sph}}$ diagram can be fit (together) with a

only marginally consistent with each other within their 1σ uncertainties. However, the same slopes obtained with Bayesian estimator `linmix_err` are fully consistent with each other within their 1σ uncertainties.

single power-law, whereas they follow two different correlations in the $M_{\text{BH}} - L_{\text{sph}}$ diagram (*Paper II*). We now want to compare the amount of intrinsic scatter in these two plots. In Table 5 we report the values of the intrinsic scatter in the $M_{\text{BH}} - n_{\text{sph}}$ and $M_{\text{BH}} - L_{\text{sph}}$ diagrams for all, early- and late-type galaxies, obtained with the modified FITEXY routine and the Bayesian estimator `linmix_err`. When considering all galaxies, irrespective of their morphological type, the intrinsic scatter of the $M_{\text{BH}} - n_{\text{sph}}$ relation is smaller than that of the $M_{\text{BH}} - L_{\text{sph}}$ relation. However, this is obviously not a fair comparison, because of the different nature of the $M_{\text{BH}} - n_{\text{sph}}$ and $M_{\text{BH}} - L_{\text{sph}}$ correlations (single and double power-law, respectively). One can obtain more informative results by considering early- and late-type galaxies separately. For the early-type galaxies, the intrinsic scatter of the $M_{\text{BH}} - n_{\text{sph}}$ relation is consistent⁷ with that of the $M_{\text{BH}} - L_{\text{sph}}$ relation (within their 1σ uncertainties). For the late-type galaxies, the intrinsic scatter of the $M_{\text{BH}} - n_{\text{sph}}$ relation is consistent with that of the $M_{\text{BH}} - L_{\text{sph}}$ relation, except for the inverse ($X|Y$) regression obtained with the modified FITEXY routine. In passing, we note that the values of the intrinsic scatter of the $M_{\text{BH}} - n_{\text{sph}}$ relation are systematically smaller – although consistent within the errors – than the corresponding values of the intrinsic scatter of the $M_{\text{BH}} - L_{\text{sph}}$ relation. In addition, the values of the intrinsic scatter returned by the modified FITEXY routine are systematically smaller than those output by the Bayesian estimator `linmix_err`.

4. CONCLUSIONS

The Sérsic index of a galaxy's spheroidal component, n_{sph} , constitutes a direct measure of its central radial concentration of stars. After Graham (2001) proved that the central black hole mass, M_{BH} , correlates with the stellar light concentration of a galaxy's spheroidal component, Graham & Driver (2007) presented and analyzed for the first time a tight $M_{\text{BH}} - n_{\text{sph}}$ correlation using a sample of 27 elliptical and disk galaxies for which they had performed photometric bulge/disk decomposition. The $M_{\text{BH}} - n_{\text{sph}}$ correlation can be predicted from the combination of two well known scaling relations involving the spheroid luminosity, L_{sph} : the $M_{\text{BH}} - L_{\text{sph}}$ (e.g. Kormendy & Richstone 1995; Magorrian et al. 1998; Marconi & Hunt 2003; Häring & Rix 2004) and the $L_{\text{sph}} - n_{\text{sph}}$ (e.g. Young & Currie 1994; Jerjen et al. 2000; Graham & Guzmán 2003). However, upon independently attempting photometric multicomponent decompositions for galaxy samples that were similar to that used by Graham & Driver (2007), three subsequent studies (Sani et al. 2011; Vika et al. 2012; Beifiori et al. 2012) failed to recover a statistically significant $M_{\text{BH}} - n_{\text{sph}}$ relation. Savorgnan et al. (2013) collected and compared the Sérsic index measurements obtained by Graham & Driver (2007), Sani et al. (2011), Vika et al. (2012) and Beifiori et al. (2012), and argued that the discrepancies were due to inaccurate galaxy decompositions.

Moved by a urgent need to re-investigate and refine

⁷ Looking at the results obtained with the modified FITEXY routine, the values of the intrinsic scatter are only marginally consistent with each other, but looking at the results obtained with the Bayesian estimator `linmix_err`, the values of the intrinsic scatter are fully consistent with each other.

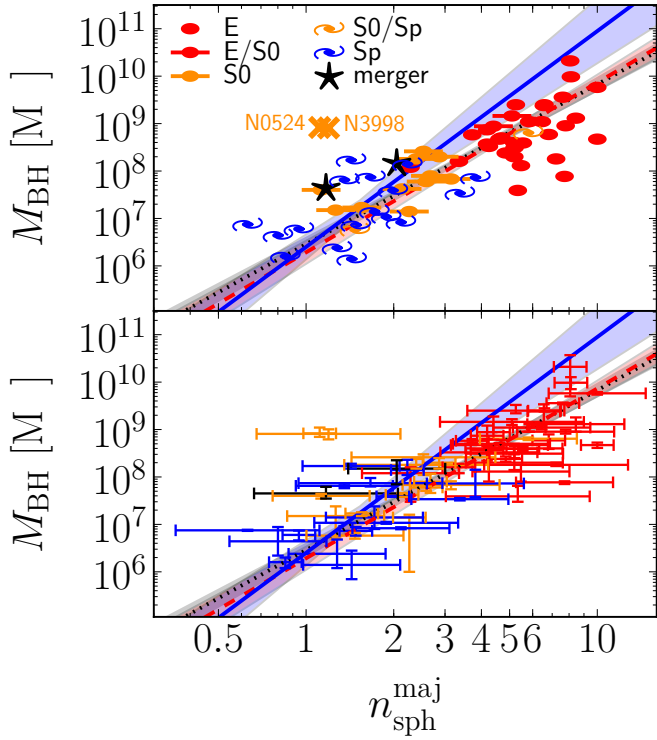


FIG. 2.— Black hole mass plotted against spheroid Sérsic index measured along the galaxy major-axis. The top and bottom panels show the data points and their error bars, respectively. Symbols are coded according to the galaxy morphological type (see legend). The orange crosses denote two lenticular galaxies (NGC 0524 and NGC 3998) which were excluded from the linear regression analysis (see Section 3). The black dotted line is the FITEXY bisector linear regression for all (64) galaxies, with the gray shaded area denoting its 1σ uncertainty. The red dashed line is the FITEXY bisector linear regression for the $45 - 2 = 43$ early-type galaxies (E+S0), with the red shaded area denoting its 1σ uncertainty. The blue solid line is the FITEXY bisector linear regression for the bulges of the 17 late-type (Sp) galaxies, with the blue shaded area denoting its 1σ uncertainty. The linear regressions for early- and late-type galaxies are consistent with each other within their 1σ uncertainties. The error bars in the bottom panel have the same color coding as the symbols in the top panel.

several black hole mass scaling relations, we performed state-of-the-art photometric multicomponent decompositions (i.e. bulge, disks, bars, spiral arms, rings, halo, nucleus, depleted core, etc.) for 66 galaxies with a dynamical measurement of their black hole mass (*Paper I*).

We carefully measured the Sérsic index of each galaxy’s spheroidal component and estimated its associated uncertainty with a method that takes into account statistical and systematic errors. Our analysis shows that early-(elliptical + lenticular) and late-type (spiral) galaxies define two different correlations in the $L_{\text{sph}} - n_{\text{sph}}$ diagram, whereas they reunite in a single sequence in the $M_{\text{BH}} - n_{\text{sph}}$ diagram. With the current dataset, we measured an amount of intrinsic scatter in the $M_{\text{BH}} - n_{\text{sph}}$ diagram systematically smaller, but still consistent within the errors, with that observed in the $M_{\text{BH}} - L_{\text{sph}}$ diagram (*Paper II*).

Our results suggest that the black hole mass is intimately connected to the spheroid central concentration of stars, which reflects the inner gradient of the spheroid gravitational potential. Besides conferring the spheroid Sérsic index a predictive power to infer the black hole mass from a galaxy’s image only (even photometrically uncalibrated), the $M_{\text{BH}} - n_{\text{sph}}$ correlation should become a fundamental ingredient in semi-analytic models and simulations of galaxy formation.

GS warmly thanks Chris Blake, Alister Graham and Carlo Nipoti for useful discussion. We also thank the anonymous referee for useful comments and suggestions. This research was supported by Australian Research Council funding through grants DP110103509 and FT110100263. This work is based on observations made with the IRAC instrument (Fazio et al. 2004) on-board the Spitzer Space Telescope, which is operated by the Jet Propulsion Laboratory, California Institute of Technology under a contract with NASA. This research has made use of the GOLDMine database (Gavazzi et al. 2003) and the NASA/IPAC Extragalactic Database (NED) which is operated by the Jet Propulsion Laboratory, California Institute of Technology, under contract with the National Aeronautics and Space Administration. We acknowledge the usage of the HyperLeda database (<http://leda.univ-lyon1.fr>). The BCES routine (Akritas & Bershady 1996) was run via the python module written by Rodrigo Nemmen (Nemmen et al. 2012), which is available at <https://github.com/rsnemmen/BCES>. The modified FITEXY linear regressions were performed using the IDL routine MPFITEXY (Williams et al. 2010), which is available at <http://purl.org/mike/mpfitexy>. The MPFITEXY routine depends on the MPFIT package (Markwardt 2009).

REFERENCES

- Akaike, H. 1974, Automatic Control, IEEE Transactions, 19, 716
 Akritas, M. G., & Bershady, M. A. 1996, ApJ, 470, 706
 Andredakis, Y. C., Peletier, R. F., & Balcells, M. 1995, MNRAS, 275, 874
 Arnold, J. A., Romanowsky, A. J., Brodie, J. P., et al. 2014, ApJ, 791, 80
 Beifiori, A., Courteau, S., Corsini, E. M., & Zhu, Y. 2012, MNRAS, 419, 2497
 Caon, N., Capaccioli, M., & D’Onofrio, M. 1993, MNRAS, 265, 1013
 Cen, R. 2014, ApJ, 790, L24
 Emsellem, E., Cappellari, M., Krajnović, D., et al. 2011, MNRAS, 414, 888
 Fazio, G. G., Hora, J. L., Allen, L. E., et al. 2004, ApJS, 154, 10
 Ferrarese, L., & Merritt, D. 2000, ApJ, 539, L9
 Gavazzi, G., Boselli, A., Donati, A., Franzetti, P., & Scodéglio, M. 2003, A&A, 400, 451
 Gebhardt, K., Bender, R., Bower, G., et al. 2000, ApJ, 539, L13
 Graham, A. 2015a, Highlights of Astronomy, 16, 360
 Graham, A. W. 2001, AJ, 121, 820
 —. 2015b, ArXiv e-prints, arXiv:1501.02937
 Graham, A. W., & Driver, S. P. 2005, PASA, 22, 118
 —. 2007, ApJ, 655, 77
 Graham, A. W., Erwin, P., Trujillo, I., & Asensio Ramos, A. 2003, AJ, 125, 2951
 Graham, A. W., & Guzmán, R. 2003, AJ, 125, 2936
 Graham, A. W., & Scott, N. 2013, ApJ, 764, 151
 Graham, A. W., & Worley, C. C. 2008, MNRAS, 388, 1708

TABLE 2
LINEAR REGRESSION ANALYSIS OF THE $L_{\text{sph}} - n_{\text{sph}}$ DIAGRAM.

Subsample (size)	Regression	α	β	$\langle \log n_{\text{sph}}^{\text{maj}} \rangle$	ϵ	Δ
$MAG_{\text{sph}}/[\text{mag}] = \alpha + \beta(\log n_{\text{sph}}^{\text{maj}} - \langle \log n_{\text{sph}}^{\text{maj}} \rangle)$						
All (64)	BCES ($Y X$)	-23.89 ± 0.15	-6.90 ± 0.74	0.50	—	1.22
	mFITEXY ($Y X$)	-23.91 ± 0.13	-6.63 ± 0.45	0.50	$0.59^{+0.16}_{-0.11}$	1.01
	linmix_err ($Y X$)	-23.89 ± 0.14	-6.34 ± 0.57	0.50	0.74 ± 0.13	1.14
	BCES ($X Y$)	-23.89 ± 0.15	-6.75 ± 0.52	0.50	—	1.20
	mFITEXY ($X Y$)	-23.89 ± 0.14	-7.49 ± 0.53	0.50	$0.62^{+0.18}_{-0.12}$	1.32
	linmix_err ($X Y$)	-23.90 ± 0.16	-7.49 ± 0.62	0.50	0.80 ± 0.16	1.32
	BCES Bisector	-23.89 ± 0.15	-6.83 ± 0.58	0.50	—	1.21
	mFITEXY Bisector	-23.90 ± 0.13	-7.04 ± 0.35	0.50	—	1.24
	linmix_err Bisector	-23.89 ± 0.15	-6.87 ± 0.42	0.50	—	1.21
Elliptical (E) (30)	BCES ($Y X$)	-25.46 ± 1.12	38.47 ± 114.45	0.76	—	6.37
	mFITEXY ($Y X$)	-25.74 ± 0.18	-9.74 ± 1.59	0.76	$0.24^{+0.32}_{-0.24}$	0.94
	linmix_err ($Y X$)	-25.65 ± 0.21	-7.87 ± 2.15	0.76	0.61 ± 0.22	1.06
	BCES ($X Y$)	-25.46 ± 0.23	-10.73 ± 3.21	0.76	—	1.29
	mFITEXY ($X Y$)	-25.74 ± 0.20	-10.42 ± 1.79	0.76	$0.22^{+0.38}_{-0.22}$	1.29
	linmix_err ($X Y$)	-25.72 ± 0.28	-10.92 ± 2.70	0.76	0.73 ± 0.34	1.33
	BCES Bisector	-25.46 ± 0.20	0.03 ± 0.05	0.76	—	1.14
	mFITEXY Bisector	-25.74 ± 0.19	-10.07 ± 1.19	0.76	—	1.26
	linmix_err Bisector	-25.68 ± 0.25	-9.15 ± 1.74	0.76	—	1.16
Lenticular (S0) (11)	BCES ($Y X$)	-22.08 ± 1.66	33.52 ± 98.87	0.33	—	6.09
	mFITEXY ($Y X$)	-22.11 ± 0.24	-6.31 ± 2.45	0.33	$0.42^{+0.28}_{-0.17}$	0.71
	linmix_err ($Y X$)			0.33		
	BCES ($X Y$)	-22.08 ± 0.19	-6.83 ± 1.16	0.33	—	0.71
	mFITEXY ($X Y$)	-21.94 ± 0.44	-13.16 ± 7.91	0.33	$0.61^{+0.60}_{-0.56}$	1.39
	linmix_err ($X Y$)			0.33		
	BCES Bisector	-22.08 ± 0.30	0.06 ± 0.05	0.33	—	1.09
	mFITEXY Bisector	-22.05 ± 0.35	-8.55 ± 2.79	0.33	—	0.84
	linmix_err Bisector			0.33		
Spiral (Sp) (17)	BCES ($Y X$)	-22.33 ± 0.26	-5.31 ± 5.83	0.18	—	1.15
	mFITEXY ($Y X$)	-22.22 ± 0.19	-2.17 ± 0.98	0.18	$0.53^{+0.24}_{-0.13}$	0.72
	linmix_err ($Y X$)	-22.26 ± 0.24	-1.53 ± 1.88	0.18	0.71 ± 0.22	0.78
	BCES ($X Y$)	-22.33 ± 0.26	-5.19 ± 3.77	0.18	—	1.13
	mFITEXY ($X Y$)	-22.28 ± 0.44	-9.08 ± 5.31	0.51	$1.12^{+0.54}_{-0.31}$	1.83
	linmix_err ($X Y$)	-22.24 ± 0.71	-11.12 ± 13.59	0.18	1.95 ± 2.47	2.24
	BCES Bisector	-22.33 ± 0.26	-5.25 ± 3.38	0.18	—	1.14
	mFITEXY Bisector	-22.23 ± 0.33	-3.60 ± 1.29	0.18	—	0.92
	linmix_err Bisector	-22.25 ± 0.53	-2.88 ± 2.66	0.18	—	0.84

- Häring, N., & Rix, H.-W. 2004, ApJ, 604, L89
- Iodice, E., D'Onofrio, M., & Capaccioli, M. 1997, in Astronomical Society of the Pacific Conference Series, Vol. 116, The Nature of Elliptical Galaxies; 2nd Stromlo Symposium, ed. M. Arnaboldi, G. S. Da Costa, & P. Saha, 84
- Iodice, E., D'Onofrio, M., & Capaccioli, M. 1999, in Astronomical Society of the Pacific Conference Series, Vol. 176, Observational Cosmology: The Development of Galaxy Systems, ed. G. Giuricin, M. Mezzetti, & P. Salucci, 402
- Jerjen, H., Binggeli, B., & Freeman, K. C. 2000, AJ, 119, 593
- Kelly, B. C. 2007, ApJ, 665, 1489
- Khosroshahi, H. G., Wadadekar, Y., & Kembhavi, A. 2000, ApJ, 533, 162
- Kormendy, J., & Richstone, D. 1995, ARA&A, 33, 581
- Magorrian, J., Tremaine, S., Richstone, D., et al. 1998, AJ, 115, 2285
- Marconi, A., & Hunt, L. K. 2003, ApJ, 589, L21
- Markwardt, C. B. 2009, in Astronomical Society of the Pacific Conference Series, Vol. 411, Astronomical Data Analysis Software and Systems XVIII, ed. D. A. Bohlender, D. Durand, & P. Dowler, 251
- Nemmen, R. S., Georgopoulos, M., Guiriec, S., et al. 2012, Science, 338, 1445
- Nipoti, C. 2015, ApJ, 805, L16
- Novak, G. S., Faber, S. M., & Dekel, A. 2006, ApJ, 637, 96
- Park, D., Kelly, B. C., Woo, J.-H., & Treu, T. 2012, ApJS, 203, 6
- Press, W. H., Teukolsky, S. A., Vetterling, W. T., & Flannery, B. P. 1992, Numerical recipes in FORTRAN. The art of scientific computing
- Rusli, S. P., Erwin, P., Saglia, R. P., et al. 2013, AJ, 146, 160
- Sani, E., Marconi, A., Hunt, L. K., & Risaliti, G. 2011, MNRAS, 413, 1479
- Savorgnan, G., Graham, A. W., Marconi, A., et al. 2013, MNRAS, 434, 387
- Savorgnan, G. A. D., & Graham, A. W. 2015a, ArXiv e-prints, arXiv:1511.05654
- . 2015b, ArXiv e-prints, arXiv:1511.07446
- Savorgnan, G. A. D., Graham, A. W., Marconi, A., & Sani, E. 2015, ArXiv e-prints, arXiv:1511.07437
- Scott, N., Davies, R. L., Houghton, R. C. W., et al. 2014, MNRAS, 441, 274
- Seigar, M. S., & James, P. A. 1998, MNRAS, 299, 672
- Sérsic, J. L. 1963, Boletín de la Asociación Argentina de Astronomía La Plata Argentina, 6, 41
- . 1968, Atlas de galaxias australes
- Sheth, K., Regan, M., Hinz, J. L., et al. 2010, PASP, 122, 1397
- Tremaine, S., Gebhardt, K., Bender, R., et al. 2002, ApJ, 574, 740
- Trujillo, I., Erwin, P., Asensio Ramos, A., & Graham, A. W. 2004, AJ, 127, 1917

TABLE 3
LINEAR REGRESSION ANALYSIS OF THE $L_{\text{sph}} - n_{\text{sph}}$ DIAGRAM.

Subsample (size)	Regression	α	β	$\langle \log n_{\text{sph}}^{\text{maj}} \rangle$	ϵ	Δ
Early-type (E+S0) (43)	BCES ($Y X$)	-24.55 ± 0.22	-11.84 ± 2.29	0.64	—	1.50
	mFITEXY ($Y X$)	-24.74 ± 0.14	-8.86 ± 0.66	0.51	$0.27^{+0.20}_{-0.27}$	0.87
	linmix_err ($Y X$)	-24.70 ± 0.17	-8.28 ± 0.87	0.64	0.58 ± 0.17	0.98
	BCES ($X Y$)	-24.55 ± 0.14	-8.25 ± 0.63	0.64	—	0.96
	mFITEXY ($X Y$)	-24.74 ± 0.14	-9.13 ± 0.68	0.64	$0.23^{+0.25}_{-0.23}$	1.08
	linmix_err ($X Y$)	-24.73 ± 0.18	-9.08 ± 0.87	0.64	0.60 ± 0.21	1.07
	BCES Bisector	-24.55 ± 0.17	-9.73 ± 1.05	0.64	—	1.14
	mFITEXY Bisector	-24.74 ± 0.14	-8.99 ± 0.48	0.64	—	1.06
	linmix_err Bisector	-24.72 ± 0.17	-8.66 ± 0.63	0.64	—	1.02
	BCES ($Y X$)	-22.25 ± 0.20	-5.88 ± 3.06	0.26	—	1.16
	mFITEXY ($Y X$)	-22.19 ± 0.14	-2.99 ± 0.73	0.26	$0.52^{+0.18}_{-0.10}$	0.75
	linmix_err ($Y X$)	-22.20 ± 0.17	-2.48 ± 1.21	0.26	0.67 ± 0.15	0.83
Bulge (S0+Sp) (30)	BCES ($X Y$)	-22.25 ± 0.20	-5.85 ± 1.83	0.26	—	1.15
	mFITEXY ($X Y$)	-22.17 ± 0.25	-7.65 ± 2.43	0.26	$0.87^{+0.30}_{-0.18}$	1.46
	linmix_err ($X Y$)	-22.16 ± 0.31	-7.80 ± 3.89	0.26	1.18 ± 0.65	1.48
	BCES Bisector	-22.25 ± 0.20	-5.87 ± 2.06	0.26	—	1.16
	mFITEXY Bisector	-22.18 ± 0.20	-4.34 ± 0.84	0.26	—	0.96
	linmix_err Bisector	-22.19 ± 0.25	-3.83 ± 1.39	0.26	—	0.91

NOTE. — For each subsample, we indicate $\langle \log n_{\text{sph}} \rangle$, its average value of spheroid Sérsic index. In the last two columns, we report ϵ , the intrinsic scatter, and Δ , the total rms scatter in the L_{sph} direction. The lenticular galaxies NGC 0524 and NGC 3998 were excluded from the linear regression analysis (see Section 3). Both the early- and late-type subsamples do not contain the two galaxies classified as S0/Sp and the two galaxies classified as mergers (45+17=66-2-2).

Vika, M., Driver, S. P., Cameron, E., Kelvin, L., & Robotham, A. 2012, MNRAS, 419, 2264

Williams, M. J., Bureau, M., & Cappellari, M. 2010, MNRAS, 409, 1330
Young, C. K., & Currie, M. J. 1994, MNRAS, 268, L11

TABLE 4
LINEAR REGRESSION ANALYSIS OF THE $M_{\text{BH}} - n_{\text{sph}}$ DIAGRAM.

Subsample (size)	Regression	α	β	$\langle \log n_{\text{sph}}^{\text{maj}} \rangle$	ϵ	Δ
$\log(M_{\text{BH}}/\text{M}_{\odot}) = \alpha + \beta(\log n_{\text{sph}}^{\text{maj}} - \langle \log n_{\text{sph}}^{\text{maj}} \rangle)$						
All (64)	BCES ($Y X$)	8.14 ± 0.07	3.49 ± 0.36	0.50	—	0.61
	mFITEXY ($Y X$)	8.15 ± 0.06	3.26 ± 0.21	0.50	$0.22^{+0.10}_{-0.07}$	0.46
	linmix_err ($Y X$)	8.15 ± 0.06	3.17 ± 0.24	0.50	0.28 ± 0.07	0.56
	BCES ($X Y$)	8.14 ± 0.08	3.52 ± 0.25	0.50	—	0.61
	mFITEXY ($X Y$)	8.15 ± 0.06	3.49 ± 0.23	0.50	$0.23^{+0.10}_{-0.07}$	0.61
	linmix_err ($X Y$)	8.15 ± 0.07	3.49 ± 0.26	0.50	0.29 ± 0.08	0.61
	BCES Bisector	8.14 ± 0.07	3.51 ± 0.28	0.50	—	0.61
	mFITEXY Bisector	8.15 ± 0.06	3.37 ± 0.15	0.50	—	0.59
	linmix_err Bisector	8.15 ± 0.07	3.32 ± 0.18	0.50	—	0.58
Early-type (E+S0) (43)	BCES ($Y X$)	8.54 ± 0.10	4.07 ± 0.87	0.64	—	0.65
	mFITEXY ($Y X$)	8.58 ± 0.07	3.32 ± 0.34	0.64	$0.24^{+0.10}_{-0.07}$	0.45
	linmix_err ($Y X$)	8.57 ± 0.08	3.12 ± 0.43	0.64	0.32 ± 0.08	0.53
	BCES ($X Y$)	8.54 ± 0.09	3.95 ± 0.55	0.64	—	0.63
	mFITEXY ($X Y$)	8.59 ± 0.08	3.88 ± 0.43	0.64	$0.26^{+0.11}_{-0.08}$	0.62
	linmix_err ($X Y$)	8.59 ± 0.09	3.82 ± 0.50	0.64	0.35 ± 0.10	0.61
	BCES Bisector	8.54 ± 0.10	4.01 ± 0.63	0.64	—	0.64
	mFITEXY Bisector	8.59 ± 0.07	3.58 ± 0.27	0.64	—	0.58
	linmix_err Bisector	8.58 ± 0.08	3.44 ± 0.33	0.64	—	0.56
Spiral (Sp) (17)	BCES ($Y X$)	7.18 ± 0.28	6.78 ± 6.62	0.18	—	1.23
	mFITEXY ($Y X$)	7.24 ± 0.13	4.48 ± 0.90	0.18	$0.13^{+0.42}_{-0.13}$	0.52
	linmix_err ($Y X$)	7.22 ± 0.16	3.57 ± 1.36	0.18	0.39 ± 0.19	0.70
	BCES ($X Y$)	7.18 ± 0.23	5.48 ± 1.93	0.18	—	0.99
	mFITEXY ($X Y$)	7.24 ± 0.14	4.62 ± 0.96	0.18	$0.13^{+0.43}_{-0.13}$	0.85
	linmix_err ($X Y$)	7.21 ± 0.21	4.86 ± 1.64	0.18	0.45 ± 0.31	0.89
	BCES Bisector	7.18 ± 0.25	6.06 ± 3.66	0.18	—	1.10
	mFITEXY Bisector	7.24 ± 0.14	4.55 ± 0.66	0.18	—	0.84
	linmix_err Bisector	7.22 ± 0.19	4.12 ± 1.07	0.18	—	0.77

NOTE. — For each subsample, we indicate $\langle \log n_{\text{sph}} \rangle$, its average value of spheroid Sérsic index. In the last two columns, we report ϵ , the intrinsic scatter, and Δ , the total rms scatter in the M_{BH} direction. The lenticular galaxies NGC 0524 and NGC 3998 were excluded from the linear regression analysis (see Section 3). Both the early- and late-type subsamples do not contain the two galaxies classified as S0/Sp and the two galaxies classified as mergers (45+17=66-2-2).

TABLE 5
INTRINSIC SCATTER ϵ OF THE $M_{\text{BH}} - n_{\text{sph}}$ AND $M_{\text{BH}} - L_{\text{sph}}$ RELATIONS.

Subsample	Regression	ϵ for $M_{\text{BH}} - n_{\text{sph}}$	ϵ for $M_{\text{BH}} - L_{\text{sph}}$
All	mFITEXY ($Y X$)	$0.22^{+0.10}_{-0.07}$	$0.49^{+0.06}_{-0.05}$
	linmix_err ($Y X$)	0.29 ± 0.07	0.51 ± 0.06
	mFITEXY ($X Y$)	$0.23^{+0.10}_{-0.07}$	$0.58^{+0.07}_{-0.06}$
	linmix_err ($X Y$)	0.30 ± 0.07	0.60 ± 0.09
Early-type	mFITEXY ($Y X$)	$0.24^{+0.10}_{-0.07}$	$0.40^{+0.06}_{-0.05}$
	linmix_err ($Y X$)	0.32 ± 0.08	0.41 ± 0.06
	mFITEXY ($X Y$)	$0.26^{+0.11}_{-0.08}$	$0.49^{+0.08}_{-0.06}$
	linmix_err ($X Y$)	0.35 ± 0.10	0.51 ± 0.10
Late-type	mFITEXY ($Y X$)	$0.13^{+0.42}_{-0.13}$	$0.55^{+0.15}_{-0.10}$
	linmix_err ($Y X$)	0.39 ± 0.19	0.63 ± 0.16
	mFITEXY ($X Y$)	$0.13^{+0.43}_{-0.13}$	$1.09^{+0.41}_{-0.24}$
	linmix_err ($X Y$)	0.45 ± 0.31	1.31 ± 0.97

6

Monster black holes in Central Cluster Galaxies

A precise measurement of the log-slope of the $M_{\text{BH}} - \sigma_*$ correlation is important to constrain theoretical models of AGN feedback. For example, energy driven outflows are expected to produce a scaling of $M_{\text{BH}} \propto \sigma_*^5$, whereas momentum driven outflows should result into a shallower $M_{\text{BH}} \propto \sigma_*^4$ relation (Silk & Rees, 1998; Fabian, 1999). Since the $M_{\text{BH}} - \sigma_*$ correlation was presented for the first time by Ferrarese & Merritt (2000) and Gebhardt et al. (2000), there has been an ongoing, lively debate about its log-slope, whose estimates differed by up to a few standard deviations depending on the choice of galaxy sample, the method used to measure the velocity dispersion, the assumed uncertainty associated with the velocity dispersion, and the linear regression algorithm (e.g. Tremaine et al. 2002).

Recent measurements of SMBH masses in Central Cluster Galaxies (CCGs) have added new data points at the high-mass end of the $M_{\text{BH}} - \sigma_*$ diagram (McConnell et al., 2011, 2012), which appear to be outlying (“over-massive”) with respect to the observed correlation. Volonteri & Ciotti (2013) explained the presence of over-massive black holes in CCGs (they included in this definition either central dominant galaxies or brightest cluster galaxies) as a natural consequence of the fact that these galaxies have experienced more dry mergers than any other early-type galaxy. Their semi-analytical models are based on the idea that parabolic dissipationless dry mergers increase a galaxy’s mass, luminosity and effective radius, but do not significantly change its velocity dispersion (e.g. Ciotti et al. 2007). Let an elliptical galaxy be a non rotating, isotropic and virialized spheroidal system with stellar mass M_* and gas mass $M_g = \alpha M_*$. The total energy E of this galaxy is the sum of its total kinetic energy K and its total gravitational energy W . The total kinetic energy is given by the sum of the stellar kinetic

energy K_* and the gas internal energy K_g , therefore the total energy can be expressed as:

$$E = K_* + K_g + W . \quad (6.1)$$

The stellar kinetic energy is

$$K_* = \frac{3}{2} M_* \sigma_*^2 , \quad (6.2)$$

where σ_* is the stellar velocity dispersion.

The gas internal energy is defined as

$$K_g = \frac{3 k_B}{2 \bar{m}} \int_{\mathcal{V}} \rho_g T d\mathcal{V} , \quad (6.3)$$

where k_B is the Boltzmann constant, \bar{m} is the gas mean molecular mass, and ρ_g and T are the density spatial distribution and the temperature of the gas, respectively, within the galaxy's volume \mathcal{V} .

The total gravitational energy is defined as

$$W = \frac{1}{2} \int_{\mathcal{V}} (\rho_* + \rho_g)(\phi_* + \phi_g) d\mathcal{V} , \quad (6.4)$$

where ρ_* is the density spatial distribution of stars, and ϕ_* and ϕ_g indicate the gravitational potential of stars and gas, respectively.

Under the assumption of gas in equilibrium in the total gravitational field, from the Jeans and hydrostatic equations one has that $T = \bar{m}\sigma_*^2/k_B$ and thus

$$K_g = \alpha K_* . \quad (6.5)$$

Assuming also that the spatial distribution of gas is proportional to that of stars (i.e. $\rho_g = \alpha\rho_*$ and $\phi_g = \alpha\phi_*$), the total gravitational energy can be written as

$$W = \frac{1}{2}(1 + \alpha)^2 \int_{\mathcal{V}} \rho_* \phi_* d\mathcal{V} = (1 + \alpha)^2 W_* , \quad (6.6)$$

where W_* is the gravitational energy of the stellar component only.

From the virial theorem (i.e. $E = K + W = W/2 = -2K$), the galaxy's total energy can be expressed as

$$E = \frac{1}{2}(1 + \alpha)^2 W_* = -(1 + \alpha) K_* . \quad (6.7)$$

We now consider the parabolic dissipationless merger of two galaxies (with stellar masses M_{*1} and M_{*2} , and total energies E_1 and E_2), i.e. a merger where both the total energy and the total

mass are conserved, and no gas is converted into stars.

The gas fraction α of the merger remnant is by definition

$$\alpha = \frac{M_g}{M_*} = \frac{M_{g1} + M_{g2}}{M_{*1} + M_{*2}} , \quad (6.8)$$

where the nomenclature is self-explanatory.

By imposing the conservation of total energy, we get

$$\begin{aligned} E &= E_1 + E_2 \\ -(1+\alpha)\frac{3}{2}M_*\sigma_*^2 &= -(1+\alpha_1)\frac{3}{2}M_{*1}\sigma_{*1}^2 - (1+\alpha_2)\frac{3}{2}M_{*2}\sigma_{*2}^2 \\ [(1+\alpha_1)M_{*1} + (1+\alpha_2)M_{*2}]\sigma_*^2 &= (1+\alpha_1)M_{*1}\sigma_{*1}^2 + (1+\alpha_2)M_{*2}\sigma_{*2}^2 \\ \sigma_*^2 &= \frac{(1+\alpha_1)M_{*1}\sigma_{*1}^2 + (1+\alpha_2)M_{*2}\sigma_{*2}^2}{[(1+\alpha_1)M_{*1} + (1+\alpha_2)M_{*2}]} . \end{aligned} \quad (6.9)$$

By defining $c_1 = (1+\alpha_1)M_{*1}/[(1+\alpha_1)M_{*1} + (1+\alpha_2)M_{*2}]$ and $c_2 = (1+\alpha_2)M_{*2}/[(1+\alpha_1)M_{*1} + (1+\alpha_2)M_{*2}]$, Equation 6.9 can be simplified as

$$\sigma_*^2 = c_1\sigma_{*1}^2 + c_2\sigma_{*2}^2 . \quad (6.10)$$

Finally, since $c_1 + c_2 = 1$, we have that

$$\min(\sigma_{*1}^2, \sigma_{*2}^2) \leq \sigma_*^2 \leq \max(\sigma_{*1}^2, \sigma_{*2}^2) , \quad (6.11)$$

that is, the velocity dispersion of the merger remnant cannot be larger than the maximum velocity dispersion of the progenitor galaxies. This conclusion is not true in case of a wet merger or non-parabolic (i.e. bound) orbits of the progenitors.

Whether or not considering the over-massive black holes as an “exception to the rule”, or in other words legitimately excluding them from the linear regression analysis of the $M_{\text{BH}} - \sigma_*$ diagram, obviously has an impact on the estimate of the log-slope of the correlation. Therefore, it is important to test the scenario proposed by Volonteri & Ciotti (2013) with empirical data.

The remainder of this chapter comprises the published version of the paper “Overmassive black holes in the $M_{\text{BH}} - \sigma$ diagram do not belong to over (dry) merged galaxies” by G. A. D. Savorgnan & A. W. Graham, as it appears in Volume 446 of *Monthly Notices of the Royal Astronomical Society*.



Overmassive black holes in the $M_{\text{BH}}-\sigma$ diagram do not belong to over (dry) merged galaxies

Giulia A. D. Savorgnan[★] and Alister W. Graham

Centre for Astrophysics and Supercomputing, Swinburne University of Technology, Hawthorn, VIC 3122, Australia

Accepted 2014 October 27. Received 2014 October 21; in original form 2014 July 9

ABSTRACT

Semi-analytical models in a Λ cold dark matter cosmology have predicted the presence of outlying, ‘overmassive’ black holes at the high-mass end of the (black hole mass–galaxy velocity dispersion) $M_{\text{BH}}-\sigma$ diagram (which we update here with a sample of 89 galaxies). They are a consequence of having experienced more dry mergers – thought not to increase a galaxy’s velocity dispersion – than the ‘main-sequence’ population. Wet mergers and gas-rich processes, on the other hand, preserve the main correlation. Due to the scouring action of binary supermassive black holes, the extent of these dry mergers (since the last significant wet merger) can be traced by the ratio between the central stellar mass deficit and the black hole mass ($M_{\text{def},*}/M_{\text{BH}}$). However, in a sample of 23 galaxies with partially depleted cores, including central cluster galaxies, we show that the ‘overmassive’ black holes are actually hosted by galaxies that appear to have undergone the lowest degree of such merging. In addition, the rotational kinematics of 37 galaxies in the $M_{\text{BH}}-\sigma$ diagram reveals that fast and slow rotators are not significantly offset from each other, also contrary to what is expected if these two populations were the product of wet and dry mergers, respectively. The observations are thus not in accordance with model predictions and further investigation is required.

Key words: black hole physics – galaxies: elliptical and lenticular, cD – galaxies: evolution – galaxies: formation.

1 INTRODUCTION

Our growing awareness of substructures and the actual relations within various black hole mass (M_{BH}) scaling diagrams is important because it provides us with clues into the joint evolution of black hole and host spheroid. For example, Graham (2012), Graham & Scott (2013) and Scott, Graham & Schombert (2013) have shown that the bent $M_{\text{BH}}-M_{\text{sph,dyn}}$ (spheroid dynamical mass), $M_{\text{BH}}-L_{\text{sph}}$ (spheroid luminosity) and $M_{\text{BH}}-M_{\text{sph,*}}$ (spheroid stellar mass) relations reveal that black holes grow roughly quadratically with their host spheroid until the onset of dry merging, as signalled by the presence of partially depleted galaxy cores and a linear scaling at the high-mass end of these diagrams. The clever many-merger model of Peng (2007), Hirschmann et al. (2010) and Jahnke & Macciò (2011) was therefore ruled out because it required convergence along a distribution in the $M_{\text{BH}}-M_{\text{sph,*}}$ diagram with a slope of unity, rather than the observed buildup (to higher masses) along the quadratic relation.

In addition, the demographics in the $M_{\text{BH}}-\sigma$ (stellar velocity dispersion) diagram (Ferrarese & Merritt 2000; Gebhardt et al. 2000) have disclosed a tendency for barred galaxies to be offset,

to higher velocity dispersions, than non-barred galaxies (Graham 2007, 2008a,b; Hu 2008; Graham & Li 2009). This may well be due to the elevated kinematics associated with bars (e.g. Graham et al. 2011; Brown et al. 2013; Hartmann et al. 2014). Speculation as to the role played by secular evolution and the possibility of ‘anaemic’ black holes in pseudo-bulges (e.g. Graham 2008b; Hu 2008) does however still remain an intriguing possibility (Kormendy, Bender & Cornell 2011), although their current lack of an offset about the bent $M_{\text{BH}}-M_{\text{sph,*}}$ relation (Graham & Scott 2013) argues against this.

An interesting suggestion for the presence of additional substructure in the $M_{\text{BH}}-\sigma$ diagram has recently been offered by Volonteri & Ciotti (2013), who investigated why central cluster galaxies tend to be outliers, hosting black holes that appear to be ‘overmassive’ compared to expectations from their velocity dispersion. On theoretical grounds it is well known that – as a consequence of the virial theorem and the conservation of the total energy – the mass, luminosity and size of a spheroidal galaxy increases more readily than its velocity dispersion when a galaxy undergoes (parabolic)¹

[★]E-mail: gsavorgn@astro.swin.edu.au

¹ In a parabolic dissipationless merger between two spheroidal galaxies, the virial velocity dispersion of the merger product cannot be larger than the maximum velocity dispersion of the progenitors. Therefore, when we say

dissipationless mergers with other spheroidal galaxies (e.g. Ciotti & van Albada 2001; Nipoti, Londrillo & Ciotti 2003; Ciotti, Lanzoni & Volonteri 2007; Naab, Johansson & Ostriker 2009). In this scenario, the supermassive black hole grows through black hole binary merger events, while the galaxy velocity dispersion remains unaffected, moving the black hole/galaxy pair upwards in the $M_{\text{BH}}-\sigma$ diagram. Using a combination of analytical and semi-analytical models, Volonteri & Ciotti (2013) show that central cluster galaxies can naturally become outliers in the $M_{\text{BH}}-\sigma$ diagram because they experience more mergers with spheroidal systems than any other galaxy and because these mergers are preferentially gas-poor.

Here we test this interesting idea with the latest observational data. In so doing, we update the $M_{\text{BH}}-\sigma$ diagram to include 89 galaxies now reported to have directly measured black hole masses.

2 RATIONALE

The high-mass end of the $M_{\text{BH}}-\sigma$ diagram, where a few ‘overmassive’ outliers have now been reported to exist, is mainly populated by core-Sérsic galaxies (Graham et al. 2003; Trujillo et al. 2004), i.e. galaxies (or bulges) with partially depleted cores relative to their outer Sérsic light profile. While these galaxies are also ‘core galaxies’, as given by the Nuker definition (Lauer et al. 2007), it should be noted that ~ 20 per cent of ‘core galaxies’ are not core-Sérsic galaxies (Dullo & Graham 2014, their appendix A.2), i.e. do not have depleted cores. Such Sérsic galaxies have no central deficit of stars. It has long been hypothesized that the presence of a partially depleted core indicates that the host galaxy has experienced one or more ‘dry’ major mergers (Begelman, Blandford & Rees 1980). During such dissipationless mergers, the progenitor supermassive black holes are expected to sink towards the centre of the remnant, form a bound pair and release their binding energy to the surrounding stars (Milosavljević & Merritt 2001; Merritt 2013b and references therein). Indeed, the latest high-resolution observations (e.g. Sillanpää et al. 1988; Komossa et al. 2003; Maness et al. 2004; Rodriguez et al. 2006; Dotti et al. 2009; Burke-Spolaor 2011; Fabbiano et al. 2011; Ju et al. 2013; U et al. 2013; Liu et al. 2014) are providing us with compelling evidence of tight black hole binary systems. The evacuation of stars takes place within the so-called loss-cone of the black hole binary and has the effect of lowering the galaxy’s central stellar density (e.g. Merritt 2006a, his fig. 5; Dotti, Sesana & Decarli 2012; Colpi 2014). Upon analysing the central stellar kinematics of a sample of core galaxies, Thomas et al. (2014) concluded that the homology of the distribution of the orbits matches the predictions from black hole binary theoretical models, and argued that the small values of central rotation velocities favour a sequence of several minor mergers rather than a few equal-mass mergers. Subsequent to the dry merging events, AGN feedback likely prevents further star formation in the spheroids of the core-Sérsic galaxies (e.g. Ciotti, Ostriker & Proga 2010, and references therein). High-accuracy N -body simulations (Merritt 2006b) have shown that, after \mathcal{N} (equivalent) major mergers, the magnitude of the stellar mass deficit $M_{\text{def},*}$ scales as \mathcal{N} times the final mass of the relic black hole ($M_{\text{def},*} \approx 0.5\mathcal{N} M_{\text{BH}}$). This result has been used to make inferences about the galaxy merger history (e.g. Graham 2004; Ferrarese et al. 2006; Hyde et al. 2008; Dullo & Graham 2014).

that, after such a merger, a galaxy experiences a growth of its black hole mass at a fixed velocity dispersion, we are referring to the progenitor galaxy with the highest velocity dispersion.

If one assumes that the ‘overmassive’ black holes belong to galaxies that have undergone a larger number of dry mergers compared to galaxies that obey the observed $M_{\text{BH}}-\sigma$ correlation (Graham & Scott 2013; McConnell & Ma 2013), it is a natural expectation that these $M_{\text{BH}}-\sigma$ outliers may also display a higher $M_{\text{def},*}/M_{\text{BH}}$ ratio when compared to the ‘main-sequence’ population. This argument motivates our first test.

A second test can be built by looking at the kinematics of the objects that populate the $M_{\text{BH}}-\sigma$ diagram. A galaxy’s velocity dispersion remains unaffected only in the case of a dissipationless merger (with another spheroidal galaxy), whereas it accordingly increases after a dissipational (gas-rich) merger, preserving the $M_{\text{BH}}-\sigma$ correlation (Volonteri & Ciotti 2013). Wet and dry mergers may produce remnants with different kinematical structures, classified as fast (disc) and slow rotators, respectively (e.g. Emsellem et al. 2008 and references therein). Therefore, an instinctive question is whether the populations of slow and fast rotators are significantly offset from each other in the $M_{\text{BH}}-\sigma$ diagram. This will be our second test.

3 DATA

Our galaxy sample (see Table 1) consists of 89 objects for which a dynamical detection of the black hole mass and a measure of the stellar velocity dispersion have been reported in the literature. We include in our sample all the 78 objects presented in the catalogue of Graham & Scott (2013), plus 10 objects taken from Rusli et al. (2013a) and 1 object from Greenhill et al. (2003). Partially depleted cores have been identified according to the same criteria used by Graham & Scott (2013). When no high-resolution image analysis was available from the literature, we inferred the presence of a partially depleted core based on the stellar velocity dispersion, σ : a galaxy is classified as core-Sérsic if $\sigma > 270 \text{ km s}^{-1}$, or as Sérsic if $\sigma \leq 166 \text{ km s}^{-1}$. This resulted in us assigning cores to just six galaxies, none of which were used in the following mass deficit analysis. We employ a 5 per cent uncertainty on σ in our regression analysis.

A kinematical classification (slow/fast rotator) is available for 34 of our 89 galaxies from the ATLAS^{3D} survey (Emsellem et al. 2011) and for 3 additional galaxies² from Scott et al. (2014). It is however beyond the scope of this paper to derive slow/fast rotator classifications for the remaining galaxies.

All galaxies are categorized as barred/unbarred objects according to the classification reported by Graham & Scott (2013), with the following updates. An isophotal analysis and unsharp masking of *Spitzer*/IRAC 3.6 μm images (Savorgnan et al., in preparation) has revealed the presence of a bar in the galaxies NGC 0224 (in agreement with Athanassoula & Beaton 2006; Beaton et al. 2007; Morrison et al. 2011), NGC 2974 (confirming the suggestion of Jeong et al. 2007), NGC 3031 (see also Elmegreen, Chromeley & Johnson 1995; Gutiérrez et al. 2011; Erwin & Debattista 2013), NGC 3245 (see also Laurikainen et al. 2010; Gutiérrez et al. 2011), NGC 3998 (as already noted by Gutiérrez et al. 2011), NGC 4026, NGC 4388 and NGC 4736 (see also Moellenhoff, Matthias & Gerhard 1995).

Although the fast rotator galaxy NGC 1316 has been frequently classified in the literature as an elliptical merger remnant, Graham & Scott (2013) identified this object as a barred lenticular galaxy. D’Onofrio (2001) found that a single-component model

² NGC 1316, NGC 1374 and NGC 1399.

Table 1. Galaxy sample. Column (1): galaxy names; for the 18 galaxies marked with a *, the black hole masses were estimated including in the modelling the effects of dark matter. Column (2): distances. Column (3): black hole masses; for the 10 measurements taken from Rusli et al. (2013a), we report in parenthesis also the measurements obtained without including in the modelling the effects of dark matter. Column (4): stellar velocity dispersions. Column (5): references of black hole mass and velocity dispersion measurements reported here (G+03 = Greenhill et al. 2003, R+13 = Rusli et al. 2013a, GS13 = Graham & Scott 2013). Column (6): presence of a partially depleted core. The question mark is used when the classification has come from the velocity dispersion criteria mentioned in Section 3. Column (7): presence of a bar. Column (8): central stellar mass deficits as measured by Rusli et al. (2013b). For seven galaxies we reconstructed the ‘no-dark-matter’ values (see Section 3.1), which are reported in parenthesis. Column (9): central stellar mass deficits as measured by Dullo & Graham (2014). Column (10): kinematical classification (fast/slow rotator).

Galaxy (1)	Dist Mpc (2)	M_{BH} $(10^8 M_{\odot})$ (3)	σ (km s^{-1}) (4)	Ref. (5)	Core (6)	Bar (7)	$M_{\text{def},*}^{R+13}$ $(10^8 M_{\odot})$ (8)	$M_{\text{def},*}^{\text{DG13}}$ $(10^8 M_{\odot})$ (9)	Kinematics (10)
A1836-BCG	158.0	39_{-5}^{+4}	309_{-15}^{+15}	GS13	yes?	no	–	–	–
A3565-BCG	40.7	11_{-2}^{+2}	335_{-17}^{+17}	GS13	yes?	no	–	–	–
Circinus	4.0	$0.017_{-0.003}^{+0.004}$	158_{-8}^{+8}	G+03	no?	no	–	–	–
CygnusA	232.0	25_{-7}^{+7}	270_{-13}^{+13}	GS13	yes?	no	–	–	–
IC 1459	28.4	24_{-10}^{+10}	306_{-15}^{+15}	GS13	yes	no	-16_{-7}^{+7}	–	–

Note. The full table is made available online in the electronic version.

cannot provide a good description of the light profile of this galaxy and de Souza, Gadotti & dos Anjos (2004) fitted NGC 1316 with a bulge + exponential disc model. Sani et al. (2011) adopted a three-component model, featuring a bulge, an exponential disc and a central Gaussian (attributed to non-stellar nuclear emission). Upon an analysis of the two-dimensional velocity field obtained from the kinematics of planetary nebulae, McNeil-Moylan et al. (2012) claimed that NGC 1316 represents a transition phase from a major-merger event to a bulge-dominated galaxy like the Sombrero galaxy (M104). We find evidence for the presence of a bar in NGC 1316 from an isophotal analysis and unsharp masking of its *Spitzer*/IRAC 3.6 μm image (Savorgnan et al., in preparation), but we exclude it for now to avoid any controversy.

Central stellar mass deficits (with individual uncertainties) have been estimated for 23 core-Sérsic galaxies – with directly measured black hole masses – by Rusli et al. (2013b). Briefly, they fit the surface brightness profiles of these galaxies with a core-Sérsic model and computed the light deficit as the difference between the luminosity of the Sérsic component of the best-fitting core-Sérsic model and the luminosity of the core-Sérsic model itself. Light deficits were then converted into stellar mass deficits through dynamically-determined, individual stellar mass-to-light ratios. Rusli et al. (2013b) used galaxy distances slightly different from those adopted in this work (see Table 1); therefore, we adjusted their stellar mass deficits (and uncertainties) accordingly.³ Among the 23 core-Sérsic galaxies whose stellar mass deficits have been computed by Rusli et al. (2013b), 10 were also analysed by Dullo & Graham (2014). Dullo & Graham (2014) measured light deficits with a method similar to that employed by Rusli et al. (2013b), but they converted light deficits into stellar mass deficits using stellar mass-to-light ratios derived from $V - I$ colours together with the colour-age-metallicity diagram (Graham & Spitler 2009). Their stellar mass deficits are accurate to 60 per cent (Dullo, private communication) and were rescaled according to the galaxy distances

³ Mass deficits and their uncertainties from Rusli et al. (2013b) were corrected by a factor of (D/D_{prev}) . Mass deficits from Dullo & Graham (2014) were corrected by a factor of $(D/D_{\text{prev}})^2$. Here, D are the galaxy distances adopted in this work and D_{prev} are the galaxy distances used in the original works.

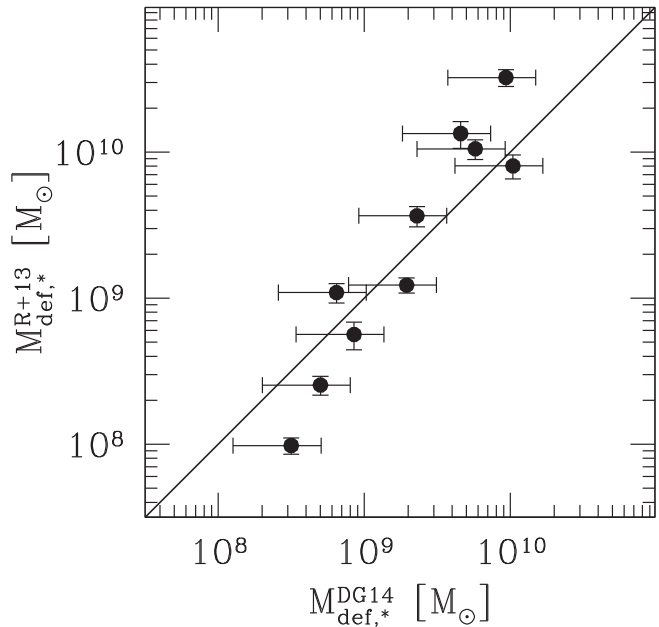


Figure 1. Comparison between the central stellar mass deficits estimated by Rusli et al. (2013b, R+13) and Dullo & Graham (2014, DG14) for 10 galaxies in common. The black solid line shows the 1:1 relation. As noted in the text, the small ‘apparent’ systematic difference is actually due to random causes.

adopted here. In Fig. 1, we compare these 10 common mass deficit estimates. The agreement is remarkably good, although a slight deviation from the 1:1 line can be noticed for the galaxies with the lowest or highest mass deficits, for which $M_{\text{def},*}$ reported by Dullo & Graham (2014) is larger or smaller than Rusli et al. (2013b), respectively. We checked and found that this effect actually depends in a random, i.e. non-systematic, way on the different choices to estimate the stellar mass-to-light ratios and/or their different galaxy data and modelling. We return to this point in the next section. For these individual 10 galaxies, we compute a weighted arithmetic mean of their two available stellar mass deficits.

3.1 Dark matter

The 10 black hole masses from Rusli et al. (2013a) – not to be confused with the different 10 galaxies with central mass deficits from Rusli et al. (2013b) that are in common with Dullo & Graham (2014) – were computed by taking into account the effects of dark matter. For these 10 galaxies, Rusli et al. (2013a) also published black hole masses estimated without the inclusion of dark matter haloes. Among the 78 black hole masses reported by Graham & Scott (2013), only 8 had dark matter included in their derivation, and no dark matter halo was included by Greenhill et al. (2003) in their black hole mass estimate.

The majority⁴ of the 23 stellar mass deficits from Rusli et al. (2013b) were derived from their analysis which incorporated dark matter to obtain the central mass-to-light ratios. However, Rusli et al. (2013b) did not publish the corresponding stellar mass deficits for the no-dark-matter case. Therefore, the sample of 89 galaxies that we use in our analysis contains 18 black hole masses estimated with the inclusion of a dark matter halo and the 23 stellar mass deficits published by Rusli et al. (2013b).

We have already shown in Section 3 that the stellar mass deficits measured by Dullo & Graham (2014), without accounting for dark matter, are in good agreement with the Rusli et al. (2013b) estimates which accounted for dark matter. The slight disagreement observed for the lowest and highest mass deficits (see Fig. 1) does not significantly affect the conclusions of our analysis. However, one could wonder whether our results change when using exclusively black hole masses and stellar mass deficits derived without the inclusion of dark matter. To address this question, we derived the no-dark-matter stellar mass deficits⁵ for 7 of the 10 galaxies whose black hole masses were measured by Rusli et al. (2013a). We repeated the analysis by (i) employing for these seven galaxies the no-dark-matter black hole masses (published by Rusli et al. 2013a) and the no-dark-matter stellar mass deficits (derived by us), and (ii) excluding the remaining black hole masses estimated with the inclusion of dark matter. We found that none of our conclusions was affected by this change.

4 RESULTS

In Fig. 2, we show the updated $M_{\text{BH}}-\sigma$ diagram for the 89 galaxies listed in Table 1. Core-Sérsic galaxies are colour coded according to their $M_{\text{def},*}/M_{\text{BH}}$ ratio (or, if no $M_{\text{def},*}$ estimate is available, they appear as empty symbols⁶). It is immediately evident that the ‘overmassive’ black holes are not hosted by galaxies with a high $M_{\text{def},*}/M_{\text{BH}}$ value.

NGC 4889, NGC 3842 and NGC 1407 are the three objects with the largest positive vertical offset from the $M_{\text{BH}}-\sigma$ correlation. Contrary to expectations, these three galaxies have a small

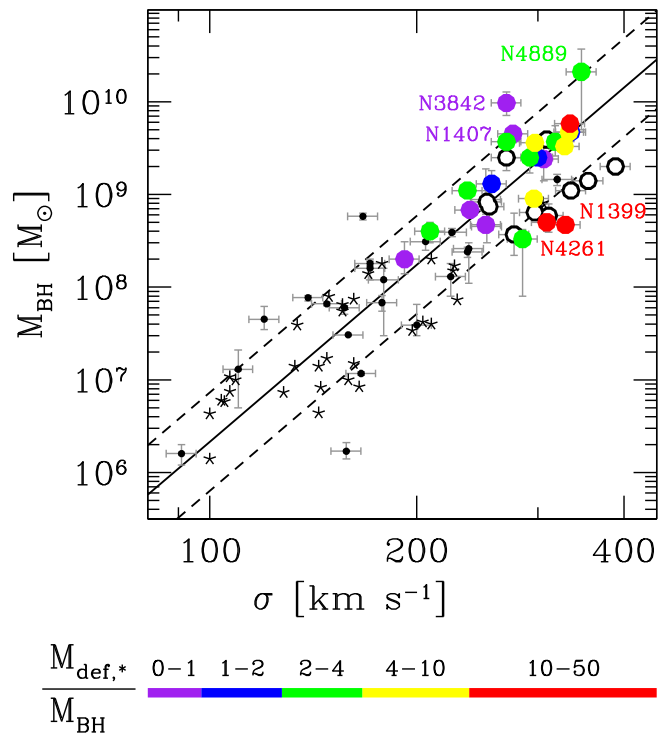


Figure 2. $M_{\text{BH}}-\sigma$ diagram for the 89 galaxies presented in Table 1. Core-Sérsic galaxies are colour coded according to their $M_{\text{def},*}/M_{\text{BH}}$ ratio. If no $M_{\text{def},*}$ estimate is available, they appear as open circles. Unbarred Sérsic galaxies are represented with (small) black dots and barred Sérsic galaxies with starred symbols. Error bars are reported only for unbarred galaxies used to derive equation (1). The black solid line shows the OLS($\sigma|M_{\text{BH}}$) linear regression for all non-barred galaxies and the black dashed lines mark the associated total rms scatter ($\Delta = 0.53$) in the log(M_{BH}) direction.

$M_{\text{def},*}/M_{\text{BH}}$ ratio, consistent with $\sim 1-2$ major dry merger events (Merritt 2006b).

Remarkably, NGC 4261 and NGC 1399 – the central galaxy in the Fornax cluster – which are two of the three galaxies with $M_{\text{def},*}/M_{\text{BH}} > 10$ (red symbols in Fig. 2), display a negative vertical offset from the correlation.⁷ While the offset of NGC 1399 and NGC 4261 is at odds with predictions from semi-analytical models (see Section 1), their large stellar deficits might be due to the effects of a recoiling black hole (see also Dullo & Graham 2014; Lena et al. 2014). A recoiling black hole is the final product of a coalesced black hole binary after the anisotropic emission of gravitational waves, which imparts a net impulse – a kick – to the remnant black hole (Bekenstein 1973; Fitchett & Detweiler 1984; Favata, Hughes & Holz 2004; Holley-Bockelmann et al. 2008; Batcheldor et al. 2010). The kicked black hole oscillates about the centre of the newly merged galaxy with decreasing amplitude, transferring kinetic energy to the stars and thus further lowering the core density (Redmount & Rees 1989; Merritt et al. 2004; Boylan-Kolchin, Ma & Quataert 2004). Kick-induced partially depleted cores can be as large as $M_{\text{def},*} \sim (4-5)M_{\text{BH}}$ (Gualandris & Merritt 2008) and could complicate the use of central mass deficits as a tracer of dry galaxy mergers. However, they do not explain the low $M_{\text{def},*}/M_{\text{BH}}$ ratios observed in the ‘overmassive’ black hole sample.

⁴ Stellar mass deficits for IC 1459, NGC 3379, NGC 4374 and NGC 4261 were estimated by Rusli et al. (2013b) with single-component dynamical modelling, i.e. without dark matter.

⁵ The no-dark-matter stellar mass deficits were calculated as $M_{\text{def},*}^{\text{noDM}} = M_{\text{def},*}^{\text{DM}} \cdot [(M/L)^{\text{DM}}]^{-1} \cdot (M/L)^{\text{noDM}}$, where $M_{\text{def},*}^{\text{DM}}$ are the mass deficits from Rusli et al. (2013b), which had dark matter incorporated in their derivation, and $(M/L)^{\text{DM}}$ and $(M/L)^{\text{noDM}}$ are the mass-to-light ratios from Rusli et al. (2013a) estimated with and without accounting for dark matter, respectively.

⁶ The 10 empty symbols refer to 6 suspected, plus 4 apparent core-Sérsic galaxies.

⁷ Although we have used the black hole mass for NGC 1399 from Gebhardt et al. (2007), we note that Houghton et al. (2006) had reported a value twice as large ($\sim 10^9 M_{\odot}$). Nevertheless, this is still too low to yield a positive offset for this galaxy in Fig. 2.

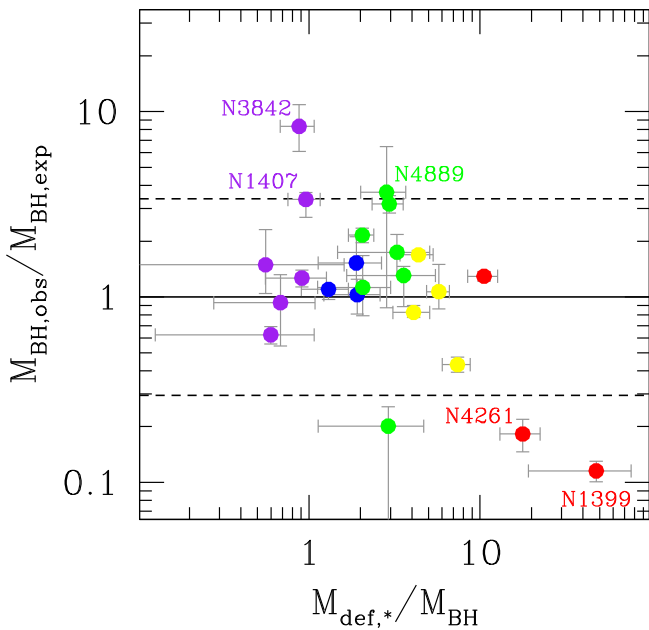


Figure 3. Vertical offset from the $M_{\text{BH}}-\sigma$ relation versus the $M_{\text{def},*}/M_{\text{BH}}$ ratio. Symbols are colour coded according to Fig. 2. The vertical error bars represent the uncertainty on M_{BH} . The horizontal solid line is equivalent to a zero vertical offset from the expected mass ($M_{\text{BH,obs}}/M_{\text{BH,exp}} = 1$) and the horizontal dashed lines show the total rms scatter ($\Delta = 0.53$) of the OLS($\sigma|M_{\text{BH}}$) linear regression in the log(M_{BH}) direction.

In Fig. 3, we plot the vertical offset from the $M_{\text{BH}}-\sigma$ relation versus the $M_{\text{def},*}/M_{\text{BH}}$ ratio. The vertical offset is defined as $\log(M_{\text{BH,obs}}/M_{\text{BH,exp}})$, where $M_{\text{BH,obs}}$ is the *observed* black hole mass and $M_{\text{BH,exp}}$ is the black hole mass *expected* from the galaxy velocity dispersion using an OLS($\sigma|M_{\text{BH}}$) linear regression⁸ for all non-barred⁹ galaxies:

$$\log \left(\frac{M_{\text{BH,exp}}}{M_{\odot}} \right) = (8.24 \pm 0.10) + (6.34 \pm 0.80) \times \log \left(\frac{\sigma}{200 \text{ km s}^{-1}} \right). \quad (1)$$

Clearly, there is no positive trend in Fig. 3. The significance of a correlation is rejected by a Spearman's test (Spearman's correlation coefficient $r_s = -0.33$, likelihood of the correlation occurring by chance $P > 5$ per cent). We conclude that no positive correlation is observed between the vertical offset from the $M_{\text{BH}}-\sigma$ relation and the $M_{\text{def},*}/M_{\text{BH}}$ ratio.

Repeating the analysis using only the Rusli et al. (2013b) mass deficits, i.e. without computing 10 weighted arithmetic means for the galaxies in common with Dullo & Graham (2014), gives the same conclusion. Similarly, the same conclusion is reached when using only the 10 Dullo & Graham (2014) derived mass deficits.

⁸ See Graham & Scott (2013, their section 3.1) for a discussion on the choice of an ordinary least-squares (OLS) regression of the abscissa on the ordinate. Their OLS($\sigma|M_{\text{BH}}$) linear regression for unbarred galaxies ($\log(M_{\text{BH,exp}}/M_{\odot}) = (8.22 \pm 0.05) + (5.53 \pm 0.34) \times \log(\sigma/200 \text{ km s}^{-1})$) is consistent within the overlapping 1σ uncertainties. It is however beyond the scope of this paper to repeat the same detailed analysis presented by Graham & Scott (2013).

⁹ As noted in Section 1, barred galaxies tend to be offset from non-barred galaxies in the $M_{\text{BH}}-\sigma$ diagram.

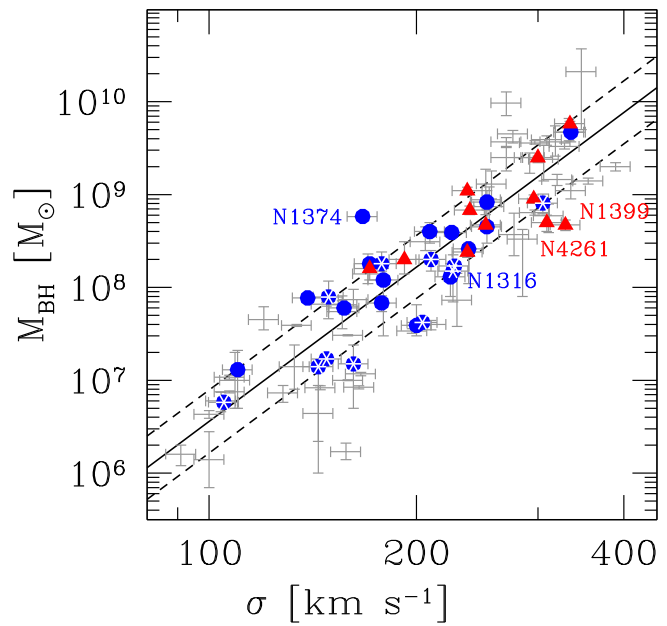


Figure 4. Fast (blue circles) and slow (red triangles) rotators in the $M_{\text{BH}}-\sigma$ diagram. Starred symbols mark barred galaxies. The black solid and dashed lines are the same as in Fig. 2.

In Fig. 4, we show the distribution of fast and slow rotators in the $M_{\text{BH}}-\sigma$ diagram. Our aim is to check whether the two populations are vertically offset from each other, in the sense that wet mergers can create fast rotating discs, while dry mergers can increase the black hole mass but not the velocity dispersion. Since the work of Graham (2008a,b), see also Hu (2008), we know that barred galaxies tend to be offset rightwards from the $M_{\text{BH}}-\sigma$ correlation defined by non-barred galaxies. It is therefore crucial to exclude the barred galaxies from the following analysis, to avoid biasing the results. We follow Graham & Scott (2013) in using the BCES code from Akritas & Bershady (1996) to obtain four different linear regressions for both the (unbarred) fast and slow rotators. The results are shown in the first part of Table 2. Regardless of the linear regression method used, the best-fitting slopes and intercepts of fast and slow rotators are consistent with each other within the 1σ uncertainty. To test the robustness of our results, we repeated the linear regression analysis excluding the most deviating data points: one fast rotator with a positive vertical offset (NGC 1374) and two slow rotators with a negative vertical offset (NGC 1399 and NGC 4261). The second

Table 2. Linear regression analysis for the populations of unbarred fast and slow rotators.

Regression	Slow rot.		Fast rot.	
	β	α	β	α
OLS($M_{\text{BH}} \sigma$)	3.7 ± 1.1	8.40 ± 0.08	4.4 ± 0.6	8.33 ± 0.09
OLS(σM_{BH})	6.8 ± 1.7	8.1 ± 0.3	5.9 ± 1.0	8.3 ± 0.1
Bisector	4.8 ± 1.0	8.3 ± 0.1	5.1 ± 0.5	8.33 ± 0.09
Orthogonal	6.7 ± 1.6	8.1 ± 0.3	5.8 ± 1.0	8.3 ± 0.1
<i>Excluding NGC 1374, NGC 1399 and NGC 4261.</i>				
OLS($M_{\text{BH}} \sigma$)	5.3 ± 0.8	8.36 ± 0.09	4.7 ± 0.6	8.27 ± 0.08
OLS(σM_{BH})	6.2 ± 0.9	8.3 ± 0.1	5.4 ± 0.8	8.28 ± 0.08
Bisector	5.7 ± 0.8	8.3 ± 0.1	5.0 ± 0.6	8.27 ± 0.08
Orthogonal	6.1 ± 0.9	8.3 ± 0.1	5.4 ± 0.8	8.28 ± 0.08

part of Table 2 reports the new values of the best-fitting slopes and intercepts, which remain consistent with each other.

5 DISCUSSION AND CONCLUSIONS

The presence of a central, supermassive black hole, coupled with the scarcity of binary supermassive black hole systems, suggests that the progenitor black holes have coalesced in most merged galaxies. They can do this by transferring their orbital angular momentum to the stars near the centre of their host galaxy and thereby evacuating the core. If a galaxy's $M_{\text{def},*}/M_{\text{BH}}$ ratio is a proxy for its equivalent number of major dry merger events since its last wet merger (e.g. Merritt 2006b), then our analysis (see Figs 2 and 3) reveals that the apparent ‘overmassive’ outliers at the high-mass end of the $M_{\text{BH}}-\sigma$ diagram are galaxies that have undergone the lowest degree of such recent dry merging. Although a final major wet merger may contribute to their low $M_{\text{def},*}/M_{\text{BH}}$ ratio, these galaxies are among the most massive early-type galaxies in the local Universe and they reside in the central regions of galaxy clusters, where wet major mergers are unlikely to occur (e.g. Fraser-McKelvie, Brown & Pimbblet 2014) due to prior ram pressure stripping of gas from infalling galaxies (Boselli & Gavazzi 2006; Haines et al. 2013; Boselli et al. 2014a,b). That is, the ‘overmassive’ black holes in central cluster galaxies cannot be explained by a large number of dissipationless mergers growing the black hole mass at a fixed galaxy velocity dispersion.

In addition to this, no significant offset is observed between the (unbarred) populations of fast and slow rotators in the $M_{\text{BH}}-\sigma$ diagram (see Table 2), contrary to what is expected if fast and slow rotators are, in general, the products of wet and dry mergers, respectively. This is because dry mergers will increase the black hole mass, but are said not to increase the velocity dispersion. This result is also in broad agreement with the observation that the (unbarred) Sérsic and core-Sérsic galaxies follow the same $M_{\text{BH}}-\sigma$ relation (Graham & Scott 2013). Our results appear consistent with studies of luminous elliptical galaxies which have shown that the galaxy luminosity scales with the velocity dispersion (Schechter 1980; Malumuth & Kirshner 1981; Bernardi et al. 2007; Lauer et al. 2007; von der Linden et al. 2007; Liu et al. 2008), i.e. the velocity dispersion appears not to completely saturate but rather still increases with increasing galaxy luminosity, contrary to what one would predict if these galaxies were built only by dry mergers on parabolic orbits.

An alternative possibility for the central cluster galaxies may be that they experience minor dry merger events that do not bring in a massive black hole but rather stars, and nuclear star clusters, which may partly or fully refill a depleted galaxy core. However, simulations are needed to verify whether, in a Λ cold dark matter cosmology, the extent of minor dry mergers experienced by a central cluster galaxy in late cosmic times can supply enough stellar mass ($\sim 10^9$ – $10^{10} M_{\odot}$) to replenish the galaxy's core.

Eventually, one should also consider the possibility that some of the overmassive black holes might have had their masses overestimated. Past studies have demonstrated the importance of resolving the black hole sphere-of-influence¹⁰ when measuring a black hole mass, to avoid systematic errors or even spurious detections (e.g. Ferrarese & Merritt 2000; Merritt & Ferrarese 2001a,b; Valluri, Merritt & Emsellem 2004; Ferrarese & Ford 2005). Merritt (2013a)

cautions against the use of black hole mass measurements obtained from stellar-dynamical data sets. His fig. 2.5 points out that no more than three galaxies – all belonging to the Local Group – have been observed with enough spatial resolution to exhibit a *prima facie* convincing Keplerian rise in their central stellar velocities. At the same time, gas kinematics can have motions not solely due to the gravitational potential of the black hole. For example, Mazzalay et al. (2014) showed that the gas dynamics in the innermost parsecs of spiral galaxies is typically far from simple circular motion. One possible example of such an overestimated black hole may be that reported by van den Bosch et al. (2012) for the galaxy NGC 1277 ($M_{\text{BH}} = 1.7 \times 10^{10} M_{\odot}$). In fact, upon re-analysing the same data, Emsellem (2013) showed that a model with a 2 times smaller black hole mass provides an equally good fit to the observed kinematics, and emphasized the need for higher spatial resolution spectroscopic data.

ACKNOWLEDGEMENTS

GS would like to acknowledge the valuable feedback provided by David Merritt and Luca Ciotti on an early version of the manuscript. GS thanks Gonzalo Díaz and Bililign Dullo for useful discussions. This research was supported by Australian Research Council funding through grants DP110103509 and FT110100263. This research has made use of the GOLDMine website (Gavazzi et al. 2003) and the NASA/IPAC Extragalactic Database (NED) which is operated by the Jet Propulsion Laboratory, California Institute of Technology, under contract with the National Aeronautics and Space Administration. We wish to thank an anonymous referee whose criticism helped improving the manuscript.

REFERENCES

- Akritas M. G., Bershady M. A., 1996, ApJ, 470, 706
- Athanassoula E., Beaton R. L., 2006, MNRAS, 370, 1499
- Batcheldor D., Robinson A., Axon D. J., Perlman E. S., Merritt D., 2010, ApJ, 717, L6
- Beaton R. L. et al., 2007, ApJ, 658, L91
- Begelman M. C., Blandford R. D., Rees M. J., 1980, Nature, 287, 307
- Bekenstein J. D., 1973, ApJ, 183, 657
- Bernardi M., Hyde J. B., Sheth R. K., Miller C. J., Nichol R. C., 2007, AJ, 133, 1741
- Boselli A., Gavazzi G., 2006, PASP, 118, 517
- Boselli A., Cortese L., Boquien M., Boissier S., Catinella B., Gavazzi G., Lagos C., Saintonge A., 2014a, A&A, 564, A67
- Boselli A. et al., 2014b, A&A, 570, A69
- Boylan-Kolchin M., Ma C.-P., Quataert E., 2004, ApJ, 613, L37
- Brown J. S., Valluri M., Shen J., Debattista V. P., 2013, ApJ, 778, 151
- Burke-Spolaor S., 2011, MNRAS, 410, 2113
- Ciotti L., van Albada T. S., 2001, ApJ, 552, L13
- Ciotti L., Lanzoni B., Volonteri M., 2007, ApJ, 658, 65
- Ciotti L., Ostriker J. P., Proga D., 2010, ApJ, 717, 708
- Colpi M., 2014, Space Sci. Rev., 183, 189
- D'Onofrio M., 2001, MNRAS, 326, 1517
- de Souza R. E., Gadotti D. A., dos Anjos S., 2004, ApJS, 153, 411
- Dotti M., Montuori C., Decarli R., Volonteri M., Colpi M., Haardt F., 2009, MNRAS, 398, L73
- Dotti M., Sesana A., Decarli R., 2012, Adv. Astron., 2012, 940568
- Dullo B. T., Graham A. W., 2014, MNRAS, 444, 2700
- Elmegreen D. M., Chromey F. R., Johnson C. O., 1995, AJ, 110, 2102
- Emsellem E., 2013, MNRAS, 433, 1862
- Emsellem E. et al., 2008, in Bureau M., Athanassoula E., Barbuy B., eds, Proc. IAU Symp. 245, Formation and Evolution of Galaxy Bulges. Cambridge Univ. Press, Cambridge, p. 11

¹⁰ The sphere-of-influence is the region of space within which the gravitational potential of the black hole dominates over that of the surrounding stars.

- Emsellem E. et al., 2011, MNRAS, 414, 888
 Erwin P., Debattista V. P., 2013, MNRAS, 431, 3060
 Fabbiano G., Wang J., Elvis M., Risaliti G., 2011, Nature, 477, 431
 Favata M., Hughes S. A., Holz D. E., 2004, ApJ, 607, L5
 Ferrarese L., Ford H., 2005, Space Sci. Rev., 116, 523
 Ferrarese L., Merritt D., 2000, ApJ, 539, L9
 Ferrarese L. et al., 2006, ApJS, 164, 334
 Fitchett M. J., Detweiler S., 1984, MNRAS, 211, 933
 Fraser-McKevie A., Brown M. J. I., Pimbblet K. A., 2014, MNRAS, 444, L63
 Gavazzi G., Boselli A., Donati A., Franzetti P., Scodéggi M., 2003, A&A, 400, 451
 Gebhardt K. et al., 2000, ApJ, 539, L13
 Gebhardt K. et al., 2007, ApJ, 671, 1321
 Graham A. W., 2004, ApJ, 613, L33
 Graham A., 2007, BAAS, 39, 759
 Graham A. W., 2008a, PASA, 25, 167
 Graham A. W., 2008b, ApJ, 680, 143
 Graham A. W., 2012, ApJ, 746, 113
 Graham A. W., Li I.-h., 2009, ApJ, 698, 812
 Graham A. W., Scott N., 2013, ApJ, 764, 151
 Graham A. W., Spitler L. R., 2009, MNRAS, 397, 2148
 Graham A. W., Erwin P., Trujillo I., Asensio Ramos A., 2003, AJ, 125, 2951
 Graham A. W., Onken C. A., Athanassoula E., Combes F., 2011, MNRAS, 412, 2211
 Greenhill L. J. et al., 2003, ApJ, 590, 162
 Gualandris A., Merritt D., 2008, ApJ, 678, 780
 Gutiérrez L., Erwin P., Aladro R., Beckman J. E., 2011, AJ, 142, 145
 Haines C. P. et al., 2013, ApJ, 775, 126
 Hartmann M., Debattista V. P., Cole D. R., Valluri M., Widrow L. M., Shen J., 2014, MNRAS, 441, 1243
 Hirschmann M., Khochfar S., Burkert A., Naab T., Genel S., Somerville R. S., 2010, MNRAS, 407, 1016
 Holley-Bockelmann K., Gültekin K., Shoemaker D., Yunes N., 2008, ApJ, 686, 829
 Houghton R. C. W., Magorrian J., Sarzi M., Thatte N., Davies R. L., Krajnović D., 2006, MNRAS, 367, 2
 Hu J., 2008, MNRAS, 386, 2242
 Hyde J. B., Bernardi M., Sheth R. K., Nichol R. C., 2008, MNRAS, 391, 1559
 Jahnke K., Macciò A. V., 2011, ApJ, 734, 92
 Jeong H., Bureau M., Yi S. K., Krajnović D., Davies R. L., 2007, MNRAS, 376, 1021
 Ju W., Greene J. E., Rafikov R. R., Bickerton S. J., Badenes C., 2013, ApJ, 777, 44
 Komossa S., Burwitz V., Hasinger G., Predehl P., Kaastra J. S., Ikebe Y., 2003, ApJ, 582, L15
 Kormendy J., Bender R., Cornell M. E., 2011, Nature, 469, 374
 Lauer T. R. et al., 2007, ApJ, 662, 808
 Laurikainen E., Salo H., Buta R., Knapen J. H., Comerón S., 2010, MNRAS, 405, 1089
 Lena D., Robinson A., Marconi A., Axon D. J., Capetti A., Merritt D., Batcheldor D., 2014, ApJ, 795, 146
 Liu F. S., Xia X. Y., Mao S., Wu H., Deng Z. G., 2008, MNRAS, 385, 23
 Liu X., Shen Y., Bian F., Loeb A., Tremaine S., 2014, ApJ, 789, 140
 McConnell N. J., Ma C.-P., 2013, ApJ, 764, 184
 McNeil-Moylan E. K., Freeman K. C., Arnaboldi M., Gerhard O. E., 2012, A&A, 539, A11
 Malumuth E. M., Kirshner R. P., 1981, ApJ, 251, 508
 Maness H. L., Taylor G. B., Zavala R. T., Peck A. B., Pollack L. K., 2004, ApJ, 602, 123
 Mazzalay X. et al., 2014, MNRAS, 438, 2036
 Merritt D., 2006a, Rep. Prog. Phys., 69, 2513
 Merritt D., 2006b, ApJ, 648, 976
 Merritt D., 2013a, Dynamics and Evolution of Galactic Nuclei. Princeton Univ. Press, Princeton, NJ
 Merritt D., 2013b, Class. Quantum Gravity, 30, 244005
 Merritt D., Ferrarese L., 2001a, in Knapen J. H., Beckman J. E., Shlosman I., Mahoney T. J., eds, ASP Conf. Ser. Vol. 249, The Central Kiloparsec of Starbursts and AGN: The La Palma Connection. Astron. Soc. Pac, San Francisco, p. 335
 Merritt D., Ferrarese L., 2001b, ApJ, 547, 140
 Merritt D., Milosavljević M., Favata M., Hughes S. A., Holz D. E., 2004, ApJ, 607, L9
 Milosavljević M., Merritt D., 2001, ApJ, 563, 34
 Moellenhoff C., Matthias M., Gerhard O. E., 1995, A&A, 301, 359
 Morrison H., Caldwell N., Schiavon R. P., Athanassoula E., Romanowsky A. J., Harding P., 2011, ApJ, 726, L9
 Naab T., Johansson P. H., Ostriker J. P., 2009, ApJ, 699, L178
 Nipoti C., Londrillo P., Ciotti L., 2003, MNRAS, 342, 501
 Peng C. Y., 2007, ApJ, 671, 1098
 Redmount I. H., Rees M. J., 1989, Comments Astrophys., 14, 165
 Rodriguez C., Taylor G. B., Zavala R. T., Peck A. B., Pollack L. K., Romani R. W., 2006, ApJ, 646, 49
 Rusli S. P. et al., 2013a, AJ, 146, 45
 Rusli S. P., Erwin P., Saglia R. P., Thomas J., Fabricius M., Bender R., Nowak N., 2013b, AJ, 146, 160
 Sani E., Marconi A., Hunt L. K., Risaliti G., 2011, MNRAS, 413, 1479
 Schechter P. L., 1980, AJ, 85, 801
 Scott N., Graham A. W., Schombert J., 2013, ApJ, 768, 76
 Scott N., Davies R. L., Houghton R. C. W., Cappellari M., Graham A. W., Pimbblet K. A., 2014, MNRAS, 441, 274
 Sillanpää A., Haarala S., Valtonen M. J., Sundelius B., Byrd G. G., 1988, ApJ, 325, 628
 Thomas J., Saglia R. P., Bender R., Erwin P., Fabricius M., 2014, ApJ, 782, 39
 Trujillo I., Erwin P., Asensio Ramos A., Graham A. W., 2004, AJ, 127, 1917
 U V. et al., 2013, ApJ, 775, 115
 Valluri M., Merritt D., Emsellem E., 2004, ApJ, 602, 66
 van den Bosch R. C. E., Gebhardt K., Gültekin K., van de Ven G., van der Wel A., Walsh J. L., 2012, Nature, 491, 729
 Volonteri M., Ciotti L., 2013, ApJ, 768, 29
 von der Linden A., Best P. N., Kauffmann G., White S. D. M., 2007, MNRAS, 379, 867

SUPPORTING INFORMATION

Additional Supporting Information may be found in the online version of this article:

Table 1. Galaxy sample (<http://mnras.oxfordjournals.org/lookup/suppl/doi:10.1093/mnras/stu2259/-DC1>).

Please note: Oxford University Press are not responsible for the content or functionality of any supporting materials supplied by the authors. Any queries (other than missing material) should be directed to the corresponding author for the paper.

This paper has been typeset from a TeX/LaTeX file prepared by the author.

Monster black holes in compact massive spheroids with intermediate scale discs

This Chapter brings together three “hot topics” of today’s astrophysical debate, that is, over-massive black holes in the $M_{\text{BH}} - L_{\text{sph}}$ diagram, the variety of bulge-to-disc ratios in local early-type galaxies, and the evolution of the mass-size relationship from $z = 2$ to $z = 0$. While an overview about the first two topics was given in Sections 1.1.8 and 1.2.1, no mention of the mass-size relation was made in Chapter 1 because not immediately related to SMBHs. Therefore, a more extensive introduction of this last point is given here.

It has been claimed that high-redshift passive galaxies were significantly more compact than their local counterparts. Daddi et al. (2005) reported on the observation of seven quiescent early-type galaxies at $z = 1.4 - 2.5$ with stellar masses $\gtrsim 10^{11} M_{\odot}$ and effective radii significantly smaller than those of local counterparts. Trujillo et al. (2006) analysed ten massive $\approx 5 \times 10^{11} M_{\odot}$ galaxies at $z = 1.2 - 1.7$ and measured for them sizes a factor of 4 smaller than $z = 0$ galaxies with similar stellar masses. From this, they concluded that the observed rapid evolution of the structural properties of massive quiescent galaxies over the last ≈ 10 Gyr cannot be reconciled with a monolithic formation scenario. Kriek et al. (2008) and van Dokkum et al. (2008) found that nearly half of $z \approx 2$ massive ($\approx 10^{11} M_{\odot}$) galaxies have old stellar populations, negligible star formation, and sizes a factor of 5 smaller than those of local descendants, and similar conclusions were reached by several other studies (e.g. Toft et al. 2007; Trujillo et al. 2007; Zirm et al. 2007; Buitrago et al. 2008; Damjanov et al. 2009). While some studies have pointed out that “progenitor bias”¹ (e.g. Carollo et al. 2014) might play an important role when

¹“Progenitor bias” refers to sample confusion of the local descendants of high-redshift massive quiescent galaxies.

tracking the evolution of massive quiescent galaxies, minor dry mergers have been commonly advocated to explain the size growth of these galaxies (e.g. Hopkins et al. 2009; Carrasco et al. 2010; Cimatti et al. 2012; Fan et al. 2013; De et al. 2014). However, not enough satellites have been found around massive galaxies to support the minor dry mergers scenario (e.g. Khochfar & Burkert 2006; Maller et al. 2006; Hopkins et al. 2009; Naab et al. 2009; McLure et al. 2013). A fascinating solution to the problem was proposed by Graham (2013), who suggested that the high-redshift compact massive spheroids have evolved into the bulges of today's massive early-type disc galaxies (see also Dullo & Graham 2013 and Driver et al. 2013). This view was confirmed by Graham et al. (2015), who used bulge/disc decomposition to unveil a large number of previously unnoticed local stellar spheroidal systems with the same structural properties, old stellar populations, and similar number density as the high-redshift compact massive spheroids. Graham et al. (2015) advocated the growth of two-dimensional stellar disks around the compact massive spheroids to explain the evolution of these objects.

The remainder of this chapter comprises the published version of the paper “Explaining the reportedly overmassive black holes in early-type galaxies with intermediate-scale discs” by G. A. D. Savorgnan & A. W. Graham, as it appears in Volume 457 of *Monthly Notices of the Royal Astronomical Society*.

While some of the $z = 0$ red-sequence galaxies might have had a passive evolution since $z \approx 2$, other $z = 0$ red-sequence galaxies might descend from $z \approx 2$ star-forming galaxies.



Explaining the reportedly overmassive black holes in early-type galaxies with intermediate-scale discs

Giulia A. D. Savorgnan[★] and Alister W. Graham

Centre for Astrophysics and Supercomputing, Swinburne University of Technology, Hawthorn, Victoria 3122, Australia

Accepted 2015 November 17. Received 2015 November 10; in original form 2015 September 22

ABSTRACT

The classification ‘early-type’ galaxy includes both elliptically and lenticular-shaped galaxies. Theoretically, the spheroid-to-disc flux ratio of an early-type galaxy can assume any positive value, but in practice studies often consider only spheroid/disc decompositions in which the disc neatly dominates over the spheroid at large galaxy radii, creating an inner ‘bulge’ as observed in most spiral galaxies. Here we show that decompositions in which the disc remains embedded within the spheroid, labelled by some as ‘unphysical’, correctly reproduce both the photometric and kinematic properties of early-type galaxies with intermediate-scale discs. Intermediate-scale discs have often been confused with large-scale discs and incorrectly modelled as such; when this happens, the spheroid luminosity is considerably underestimated. This has recently led to some surprising conclusions, such as the claim that a number of galaxies with intermediate-scale discs (Mrk 1216, NGC 1277, NGC 1271, and NGC 1332) host a central black hole whose mass is abnormally large compared to expectations from the (underestimated) spheroid luminosity. We show that when these galaxies are correctly modelled, they no longer appear as extreme outliers in the (black hole mass)–(spheroid mass) diagram. This not only nullifies the need for invoking different evolutionary scenarios for these galaxies but it strengthens the significance of the observed (black hole mass)–(spheroid mass) correlation and confirms its importance as a fundamental ingredient for theoretical and semi-analytic models used to describe the coevolution of spheroids and their central supermassive black holes.

Key words: black hole physics – galaxies: bulges – galaxies: elliptical and lenticular, cD – galaxies: evolution – galaxies: individual: Mrk 1216, NGC 1271, NGC 1277, NGC 1332, NGC 4291 – galaxies: structure.

1 INTRODUCTION

The awareness that *many* early-type galaxies contain previously overlooked stellar discs dates back half a century (Liller 1966; Strom & Strom 1978; Michard 1984; Djorgovski 1985; Bender & Moellenhoff 1987; Jedrzejewski 1987a; Capaccioli 1987; Carter 1987; Capaccioli, Piotto & Rampazzo 1988). It is well known that the identification of a stellar disc in an early-type galaxy, particularly when based on the galaxy’s photometric properties, is subject to inclination effects. As predicted by Carter (1987), this problem is largely overcome with kinematic analyses (e.g. Franx, Illingworth & Heckman 1989; Nieto et al. 1991; Rix & White 1992; Cinzano & van der Marel 1993; D’Onofrio et al. 1995; Graham et al. 1998, and the ATLAS^{3D} survey, Cappellari et al. 2011a), which allow one to determine the presence of a rotationally supported component

in a way nearly insensitive to projection effects (McElroy 1983; Cappellari et al. 2007; Emsellem et al. 2007). Yet, identifying the radial extent of an early-type galaxy’s disc with respect to the spheroidal component can still be subtle. Studying both the surface brightness profiles and the ellipticity profiles of early-type galaxies in the Virgo cluster – including those with elliptical (E), spindle and lenticular (S0) isophotes – Liller (1966) drew attention to the observation that many of the galaxies displayed ‘characteristics intermediate between those of type E and type S0’, and she classified them as ‘ES’ galaxies. Building on this and other investigations of ellipticity profiles (e.g. Strom & Strom 1978; di Tullio 1979), Michard (1984) used the classification ‘S0-like’ for these early-type galaxies with humped ellipticity profiles, dominated by a somewhat edge-on disc at intermediate radii. Nieto, Capaccioli & Held (1988) identified two dozen such spheroid-dominated early-type galaxies, whose discs do not prevail at large radii, and referred to them as ‘disk ellipticals’ (or ‘disky ellipticals’; Simien & Michard 1990). However, as noted by Nieto et al. (1988), unless the

* E-mail: gsavorgn@astro.swin.edu.au

orientation of the disc is favourable (i.e. somewhat edge-on), it can be missed. The same is true when searching for pointy isophotes that are shaped by the combination of the spheroid and a near edge-on disc (e.g. Carter 1978, 1987; Bender & Moellenhoff 1987; Ebneter et al. 1987; Jedrzejewski 1987a; Bender 1988; Bijaoui, Marchal & Michard 1989).

Today, most early-type galaxies are classified as ‘fast rotators’ (Emsellem et al. 2011; Scott et al. 2014), that is, they are rapidly rotating within their half-light radius. The exact definition of a fast rotator can be found in Emsellem et al. (2007), although the most recent literature (e.g. Arnold et al. 2011; Romanowsky & Fall 2012; Arnold et al. 2014) prefers the use of the term ‘central fast rotator’ to emphasize the fact that this classification pertains to the kinematic properties of a galaxy only within its half-light radius. Thanks to their more extended kinematic maps, Arnold et al. (2014) revealed that some of the central fast rotators continue to be fast rotating at large radii, whereas other central fast rotators become slow rotating in their outer regions.¹ Unfortunately, such extended kinematic maps are not yet available for large numbers of galaxies in the local Universe. Nevertheless, the ellipticity profile of a galaxy’s isophotes can help identify the extent of a stellar disc in an early-type galaxy.

In general, stellar discs are intrinsically flat and close to circular (e.g. Andersen et al. 2001; Andersen & Bershady 2002); their apparent ellipticity, dictated by their inclination to our line of sight, is fixed. Spheroids are often rounder than the observed projection on the sky of their associated discs, thus their average ellipticity is often lower than that of their disc. An ellipticity profile that increases with radius can be ascribed to an inclined disc that becomes progressively more important at large radii, whereas a radial decrease of ellipticity signifies the opposite case. This approach can be taken to the next level by inspecting the isophotes for discy structures (e.g. Carter 1978, 1987; Bender & Moellenhoff 1987; Capaccioli 1987; Jedrzejewski 1987a) and checking the velocity line profiles for asymmetry (e.g. Franx & Illingworth 1988; Bender 1990; Rix & White 1992; Scorsa & Bender 1995, and references therein; Scorsa 1998).

Building on the investigations in works such as Liller (1966), Jedrzejewski (1987a) and Rix & White (1990), the toy model shown in Fig. 1 illustrates the typical ellipticity profile ($\epsilon = 1 - b/a$, where b/a is the ratio of minor-to-major axis length) and the specific angular momentum profile ($\lambda = \langle R|V| \rangle / (R\sqrt{V^2 + \sigma^2})$, where R is the semimajor-axis radius, V is the mean velocity and σ is the velocity dispersion; Emsellem et al. 2007) of: (1) a lenticular galaxy, comprised of a large-scale disc which dominates the light at large radii over a relatively smaller encased bulge, i.e. a disc-dominated central fast rotator that continues to be fast rotating beyond one half-light radius; (2) a ‘discy elliptical’ galaxy (Michard 1984; Nieto et al. 1988) composed of an intermediate-scale disc embedded in a relatively larger spheroid which dominates the light at large radii, i.e. a spheroid-dominated central fast rotator that becomes slow rotating beyond 1–2 half-light radii; and (3) an elliptical galaxy with an additional nuclear stellar disc, i.e. a (spheroid-dominated) slow rotator. This sequence is analogue to that illustrated in fig. 2 of Cappellari et al. (2011b), although here we emphasize the correspondence

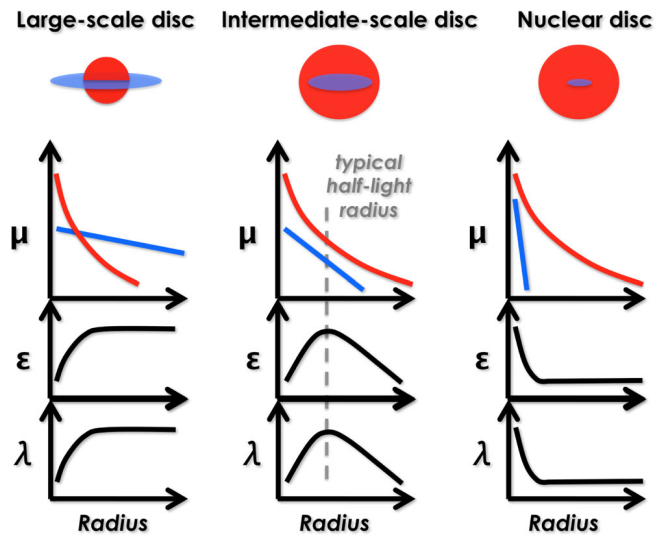


Figure 1. Illustration of the spheroid/disc decomposition of the one-dimensional surface brightness profile, μ , the ellipticity profile, ϵ , and the specific angular momentum profile, λ , for the three prototype early-type galaxy sub-classes. In the flux decompositions, the spheroid (or bulge) and the disc are shown with the red and blue colour, respectively. The left-hand panel shows a disc-dominated central fast rotator (lenticular galaxy), composed of a bulge encased in a large-scale disc. The right-hand panel displays a spheroid-dominated slow rotator (elliptical) with (an optional) nuclear stellar disc. The middle panel presents a spheroid-dominated central fast rotator with an intermediate-sized disc embedded in the spheroid.

between the spheroid/disc decomposition of the surface brightness profile and the ‘shape’ of the ellipticity profile (assuming that the disc inclination is not close to face-on) and also the specific angular momentum profiles.

While some recent studies have correctly distinguished between large- and intermediate-scale discs, and modelled them accordingly (e.g. Kormendy & Bender 2012; Krajnović et al. 2013), intermediate-scale discs have been missed by many galaxy modellers of late, who have labelled as ‘unphysical’ (Allen et al. 2006) those spheroid/disc decompositions in which the disc does not dominate over the spheroid at large radii as is observed with spiral galaxies. This has led to the rejection of many early-type galaxy decompositions similar to that illustrated in the top middle panel of Fig. 1. Unsurprisingly, studies affected by this bias have not obtained spheroid/disc decompositions with a spheroid-to-total ratio larger than 0.6–0.8 (e.g. Gadotti 2008; Head et al. 2014; Méndez-Abreu & CALIFA Team 2015; Querejeta et al. 2015).

As mentioned before, an isophotal analysis allows one to identify the presence and the radial extent of a disc in an early-type galaxy only when the disc has a certain level of inclination. On the other hand, a kinematic analysis has the advantage of being virtually insensitive to inclination effects, but cannot help one determine the radial extent of a disc if the kinematic data are limited within one half-light radius. Therefore, the best results are obtained when photometry and kinematics are combined together.

In this paper, we focus on the increasingly overlooked occurrence of intermediate-scale discs in galaxies with directly measured black hole masses. We report on the photometric and kinematical signatures of these intermediate-sized stellar discs, and the impact they have on the (black hole mass)-to-(spheroid stellar mass) ratio which is used to constrain galaxy evolution models. In Section 2, we present a detailed photometric analysis of three galaxies with intermediate-scale discs (Mrk 1216, NGC 1332, and NGC 3115)

¹ As pointed out by Cappellari et al. (2011a), while all of the disk ellipticals from Bender, Saglia & Gerhard (1994) are fast rotators, the complement is not true because weak discs only impact the isophotal shape if the discs have orientations close to edge-on, whereas their rotational signature can still be detected when they have a near face-on orientation. Of course if a disc is face-on, then the galaxy will not be classified as a fast rotator.

and we briefly describe another five galaxies with intermediate-scale discs (NGC 821, NGC 1271, NGC 1277, NGC 3377, and NGC 4697) already modelled by us elsewhere in the literature. We compare our photometric analysis with the kinematical information available from the literature, and explain the differences between our galaxy models and past decompositions. In Section 3, we explore the important implications this has for the (black hole mass)–(spheroid stellar mass) diagram. Finally, in Section 4 we briefly discuss our results in terms of galaxy evolution.

2 INTERMEDIATE-SCALE DISC GALAXIES

Three examples of galaxies with intermediate-scale discs are Mrk 1216, NGC 1332, and NGC 3115. In the following section, we present a photometric analysis of these three galaxies, and we compare our results with the kinematical analysis available from the literature for Mrk 1216 and NGC 3115. For the galaxies NGC 1332 and NGC 3115, we used $3.6\text{ }\mu\text{m}$ images obtained with the InfraRed Array Camera (IRAC) onboard the *Spitzer Space Telescope*. For the galaxy Mrk 1216, we used an archived *Hubble Space Telescope* (*HST*) image taken with the Wide Field Camera 3 (WFC3) and the near-infrared *F160W* filter (*H* band). Our galaxy decomposition technique is extensively described in Savorgnan & Graham (2015). Briefly, the galaxy images were background-subtracted, and masks for contaminating sources were created. The one-dimensional point spread function (PSF) was characterized using a Gaussian profile for the *HST* observation and a Moffat (1969) profile for the *Spitzer* observations. We performed an isophotal analysis of the galaxies using the *IRAF*² task *ellipse*³ (Jedrzejewski 1987b). The galaxy isophotes were modelled with a series of concentric ellipses, allowing the ellipticity, the position angle and the amplitude of the fourth harmonic to vary with radius. The decomposition of the surface brightness profiles was performed with software written by G. Savorgnan and described in Savorgnan & Graham (2015). We modelled the light profiles with a combination of PSF-convolved analytic functions, using one function per galaxy component.

2.1 NGC 3115

The presence of a disc in the central fast rotator NGC 3115 (e.g. Strom et al. 1977; Nieto et al. 1988; Scorsa & Bender 1995) is obvious due to its edge-on orientation (Fig. 2). Less obvious is the radial extent of this disc if one only relies on a visual inspection of the galaxy image. The ellipticity profile (Fig. 2) is consistent with the presence of an intermediate-scale disc. Moreover, the kinematics of NGC 3115 (Arnold et al. 2011) also disprove the presence of a large-scale disc, because the galaxy is rapidly rotating only

² *IRAF* is the Image Reduction and Analysis Facility, distributed by the National Optical Astronomy Observatory, which is operated by the Association of Universities for Research in Astronomy under cooperative agreement with the National Science Foundation.

³ Our analysis was performed before *isofit* (Ciambur 2015) was conceived or available. After *isofit* was recently developed and implemented in *IRAF*, we employed it to re-extract the surface brightness profiles of the galaxies NGC 1332 and NGC 3115. We then repeated the analysis and checked that this change does not significantly alter our results. In fact, although *isofit* provides a more accurate description of the isophotes in the presence of an inclined disc, the discs of NGC 1332 and NGC 3115 are relatively faint compared to the spheroidal components, therefore the differences between the light profile obtained with *ellipse* and that obtained with *isofit* are small for these two galaxies.

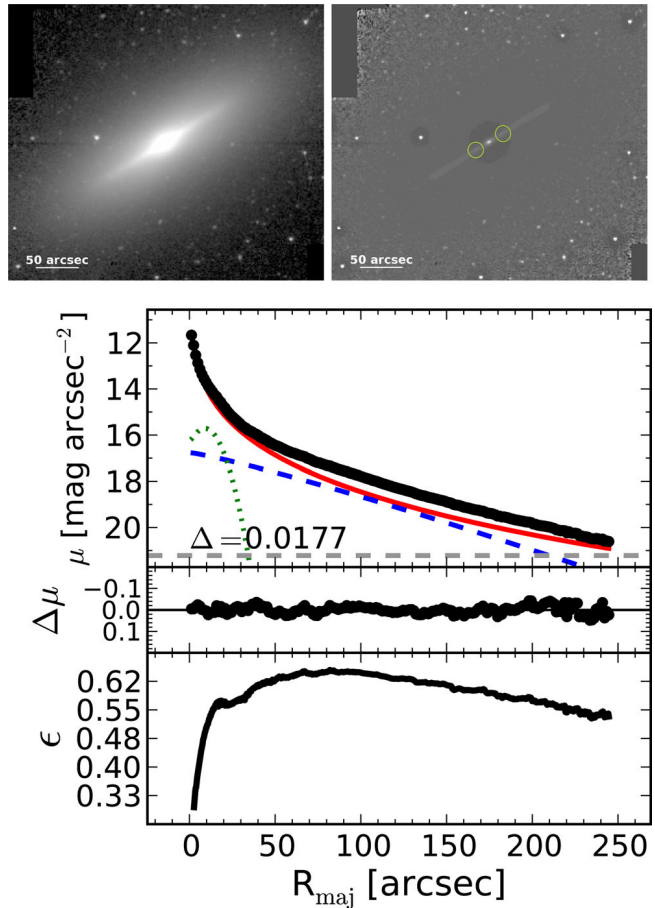


Figure 2. NGC 3115. The top panels are the *Spitzer*/IRAC $3.6\text{ }\mu\text{m}$ image (left) and its unsharp mask (right), obtained by dividing the image by a Gaussian-smoothed version of itself. In the unsharp mask, the green circles indicate the position of the two brighter spots associated with the edge-on nuclear ring. The bottom plots display the best-fitting model of the surface brightness profile, μ , and the ellipticity profile, ϵ , along the major axis, R_{maj} . The black points are the observed data, which extend out to five galaxy half-light radii ($\sim 5\text{ arcsec} \times 50\text{ arcsec}$). The colour lines represent the individual (PSF-convolved) model components: red solid = Sérsic (spheroid), blue dashed = Sérsic (disc), green dotted = Gaussian ring. The residual profile (data-model) is shown as $\Delta\mu$. The horizontal grey dashed line corresponds to an intensity equal to three times the root mean square of the sky background fluctuations. Δ denotes the root mean square scatter of the fit in units of mag arcsec^{-2} .

within two galaxy half-light radii ($\sim 2\text{ arcsec} \times 50\text{ arcsec}$), and the rotation significantly drops at larger radii. The unsharp mask of NGC 3115 (Fig. 2) betrays the presence of a faint edge-on nuclear ring, which can also be spotted as a small peak in the ellipticity profile (at semimajor-axis length $R_{\text{maj}} \sim 15\text{ arcsec}$). Such rings are common in early-type galaxies (e.g. Michard & Marchal 1993). The spheroidal component of NGC 3115 is well described with a Sérsic (1963) profile. The highly inclined intermediate-scale disc is better fitted with an $n < 1$ Sérsic profile (the Sérsic index n regulates the curvature of the Sérsic profile) rather than with an exponential function, as explained by Pastrav et al. (2013). The nuclear ring is modelled with a Gaussian function.

In comparison, Läsker, Ferrarese & van de Ven (2014a) fit NGC 3115 with a bulge + disc + envelope, and measured a bulge half-light radius of 3.9 arcsec and a bulge-to-total ratio of 0.12 . We describe this galaxy using a spheroid + intermediate-scale

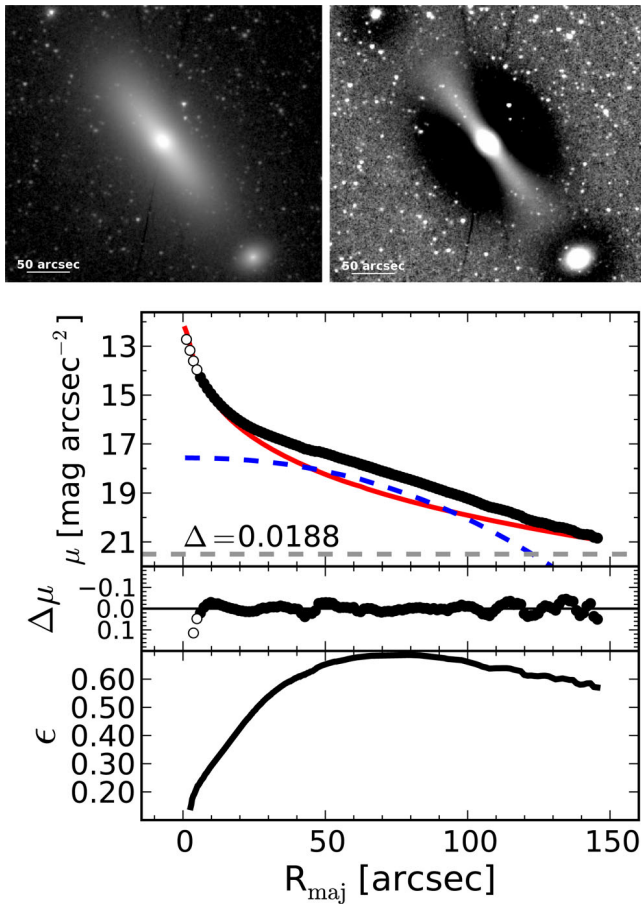


Figure 3. NGC 1332. Similar to Fig. 2. The surface brightness profile extends out to seven galaxy half-light radii ($\sim 7 \text{ arcsec} \times 20 \text{ arcsec}$). The empty points are data excluded from the fit.

disc + nuclear ring, and obtain a spheroid half-light radius of 43.6 arcsec and a spheroid-to-total ratio of 0.85. We have used both kinematical information and ellipticity profiles, together with the surface brightness profile, to obtain a physically consistent and meaningful model.

2.2 NGC 1332

The morphology of NGC 1332 (Fig. 3) is very similar to that of NGC 3115, with the ellipticity profile indicating the presence of an intermediate-scale disc, although in this case no nuclear component is evident. We were not able to find any extended kinematic profile or map for this galaxy in the literature. The data within the innermost 6 arcsec were excluded from the fit because, according to our galaxy decomposition, they are possibly affected by the presence of a partially depleted core. The surface brightness profile of NGC 1332 is well described with a Sérsic-spheroid plus an $n < 1$ Sérsic disc. Our galaxy decomposition suggests that NGC 1332 is a spheroid-dominated galaxy, with a spheroid-to-total ratio of 0.95.

Rusli et al. (2011) did not identify the restricted extent of the intermediate-scale disc, as revealed by the ellipticity profile, and proposed a model featuring a Sérsic bulge and a large-scale exponential disc, with a spheroid-to-total ratio of 0.43. Based on their bulge/disc decomposition, they concluded that NGC 1332 is a disc-dominated lenticular galaxy which is displaced from the (black hole mass)–(spheroid luminosity) correlation of Marconi & Hunt (2003) by an order of magnitude along the black hole mass direction. How-

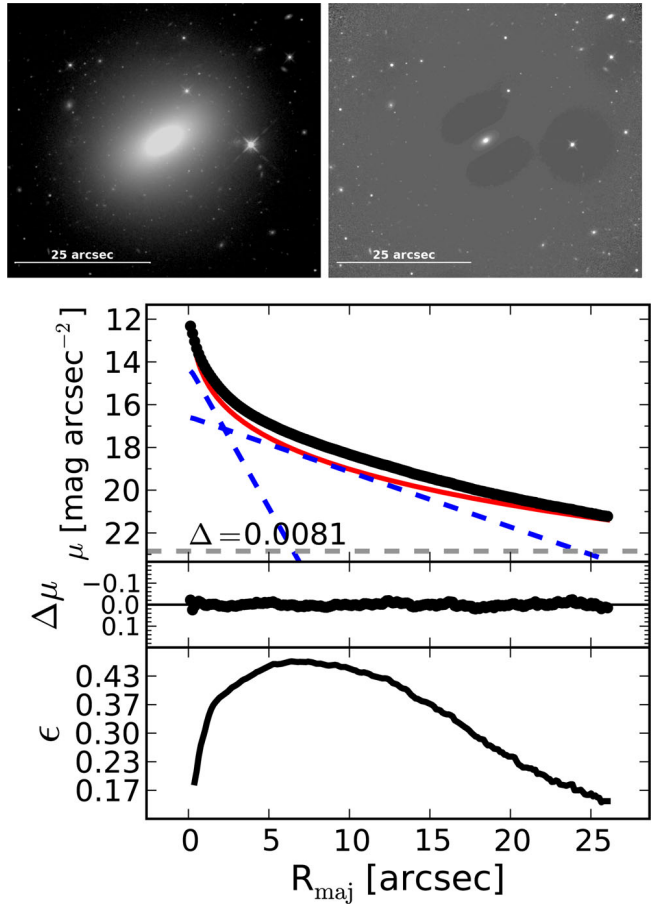


Figure 4. Mrk 1216. Similar to Fig. 2. The top panels are the *HST*/WFC3 *F160W* image (left) and its unsharp mask (right). The surface brightness profile extends out to five galaxy half-light radii ($\sim 5 \text{ arcsec} \times 5 \text{ arcsec}$). The colour lines represent the individual (PSF-convolved) model components: red solid = Sérsic (spheroid), blue dashed = exponential (nuclear and intermediate-scale disc).

ever, in Section 3 we show that, according to our decomposition, NGC 1332 lies within the 1σ scatter about the (black hole mass)–(spheroid stellar mass) correlation for early-type galaxies. We also note that the majority of galaxies with an elevated stellar velocity dispersion ($\sigma > 270 \text{ km s}^{-1}$) are core-Sérsic galaxies (Graham et al. 2003; Ferrarese et al. 2006; Dullo & Graham 2014), i.e. they have a partially depleted core which has been identified from high-resolution photometric data. NGC 1332 has $\sigma = 320 \text{ km s}^{-1}$, but, based on their decomposition of *HST* imaging, Rusli et al. (2011) did not find a core in this galaxy. However, our galaxy decomposition (Fig. 3) suggests that NGC 1332 is in fact a core-Sérsic galaxy. Since we did not use high-resolution photometric data, we refrain from a firm conclusion, but we caution that a re-analysis of the *HST* data – by taking into account the correct radial extent of the intermediate-scale disc – may indeed reveal the presence of a depleted core in this galaxy.

2.3 Mrk 1216

Although the disc in the central fast rotator Mrk 1216 is not immediately apparent from the image (Fig. 4), the velocity map (Yıldırım et al. 2015) reveals the presence of a fast rotating component within three galaxy half-light radii ($\sim 3 \text{ arcsec} \times 5 \text{ arcsec}$). The ellipticity

profile (Fig. 4), which extends out to five half-light radii, indicates the presence of an intermediate-scale disc. In addition, a nuclear disc is identified from the change in slope of the ellipticity profile ($R_{\text{maj}} \sim 1-2$ arcsec), from the unsharp mask, and from a clear feature in the $B4$ fourth harmonic profile (not shown here). We modelled the surface brightness profile of Mrk 1216 (Fig. 4) with a Sérsic-spheroid, an intermediate-sized exponential disc, and a nuclear exponential disc.

2.4 Other galaxies

Our models with an intermediate-sized disc embedded within a larger spheroidal component, plus an additional nuclear component when one is present, match the observed light distribution, and explain both the extended kinematic maps (when available; Arnold et al. 2014) and the ellipticity profiles, of five additional galaxies for which a direct measurement of their central supermassive black hole mass is available: NGC 821; NGC 1271; NGC 1277; NGC 3377; and NGC 4697. Our isophotal analysis and galaxy decompositions for NGC 1271 and NGC 1277 will be presented in Graham, Savorgnan & Ciambur (in preparation) and Graham et al. (2015a), respectively, while the galaxies NGC 821, NGC 3377, and NGC 4697 have been analysed in Savorgnan & Graham (2015).

2.4.1 NGC 1271

Walsh et al. (2015b) explored a three-component decomposition for the central fast rotator NGC 1271 and identified the galaxy bulge with the innermost of the three components, having a half-light radius of 0.61 arcsec and a bulge-to-total flux ratio of 0.23; our model features a spheroid + intermediate-scale disc, with a spheroid half-light radius of 3.3 arcsec and a spheroid-to-total flux ratio of 0.67.

2.4.2 NGC 1277

van den Bosch et al. (2012) proposed a model for the central fast rotator NGC 1277 with a bulge + disc + nuclear source + envelope, which gives a bulge half-light radius of 0.9 arcsec and a bulge-to-total flux ratio of 0.24; our model consists of a spheroid + intermediate-scale disc + nuclear component, and produces a spheroid half-light radius of 6.0 arcsec and a spheroid-to-total flux ratio of 0.79.

2.4.3 NGC 3377

Läsker et al. (2014a) modelled the central fast rotator NGC 3377 (e.g. Jedrzejewski 1987a; Scorsa & Bender 1995) with a bulge + nuclear disc + disc + envelope, and obtained a bulge half-light radius of 10.1 arcsec and a bulge-to-total flux ratio of 0.35; our model with a spheroid + intermediate-scale disc + nuclear disc returns a spheroid half-light radius of 61.8 arcsec and a spheroid-to-total flux ratio of 0.94.

2.4.4 NGC 821

Läsker et al. (2014a) decomposed the central fast rotator NGC 821 into a bulge + disc + envelope, and measured a bulge half-light radius of 3.8 arcsec and a bulge-to-total flux ratio of 0.19; our decomposition consists of a spheroid + intermediate-scale disc,

with a spheroid half-light radius of 36.5 arcsec and a spheroid-to-total flux ratio of 0.79.

2.4.5 NGC 4697

While NGC 4697 (e.g. Davies 1981; Carter 1987; Jedrzejewski, Davies & Illingworth 1987) was explicitly referred to as a ‘fast rotator’ by Capaccioli (1987) and Petrou (1981), it is only a central fast rotator and it represents an ‘extreme’ case. Läsker et al. (2014a) fit this galaxy with a bulge + nuclear source + disc + envelope, and obtained a bulge half-light radius of 6.3 arcsec and a bulge-to-total flux ratio of 0.08; we described NGC 4697 using a spheroid + intermediate-scale disc + nuclear disc model, and measured a spheroid half-light radius of 239.3 arcsec and a spheroid-to-total flux ratio of 0.89.

Past models that ‘forcedly’ described intermediate-scale disc galaxies using an inner bulge encased within a large-scale disc commonly required the addition of an extended envelope or halo to account for the outer portion of the spheroid. Such three-component models (bulge + disc + envelope) typically reduce the spheroid luminosity by a factor of 3–4, and underestimate the size of the spheroid by a factor of 6–10, although more ‘extreme’ cases can be found.

3 THE BLACK HOLE–SPHEROID CORRELATION

Inaccurate measurements of the spheroid-to-total ratio of galaxies can impact galaxy scaling relations. Recently, a handful of galaxies with intermediate-scale discs have been claimed to host overmassive black holes, i.e. the mass of their central supermassive black hole has been reported to be significantly larger than what is expected from the galaxy’s spheroid luminosity (or stellar mass). This is the case for the galaxies Mrk 1216 (for which only an upper limit on its black hole mass has been published; Yıldırım et al. 2015), NGC 1271 (Walsh et al. 2015b), NGC 1277 (van den Bosch et al. 2012; Walsh et al. 2015a; Yıldırım et al. 2015) and NGC 1332 (Rusli et al. 2011). In addition to these, the elliptical galaxy NGC 4291 has also been claimed to be an $\sim 3.6\sigma$ outlier above the (black hole mass)–(spheroid mass) scaling relation (Bogdán et al. 2012). Obviously, having both the black hole mass and the spheroid mass correct is important for placing systems in the (black hole mass)–(spheroid mass) diagram.

At present, for early-type galaxies, the spheroid luminosity and the galaxy luminosity can be used to predict the black hole mass with the same level of accuracy⁴ (Savorgnan et al. 2015). If a galaxy hosts a black hole that is overmassive compared to expectations from the spheroid luminosity, but whose mass is normal compared to expectations from the galaxy luminosity, one should wonder whether the spheroid luminosity might have been underestimated due to an inaccurate spheroid/disc decomposition. Indeed, none of the five galaxies just mentioned (Mrk 1216, NGC 1271, NGC 1277,

⁴ Note that Läsker et al. (2014b) reported that the spheroid luminosity and the galaxy luminosity are equally good tracers of the black hole mass irrespective of the galaxy morphological type, but their sample of 35 galaxies contained only 4 spiral galaxies. However, using a sample of 45 early-type and 17 spiral galaxies, Savorgnan et al. (2015) shows that, when considering all galaxies irrespective of their morphological type, the correlation of the black hole mass with the spheroid luminosity is better than that with the galaxy luminosity.

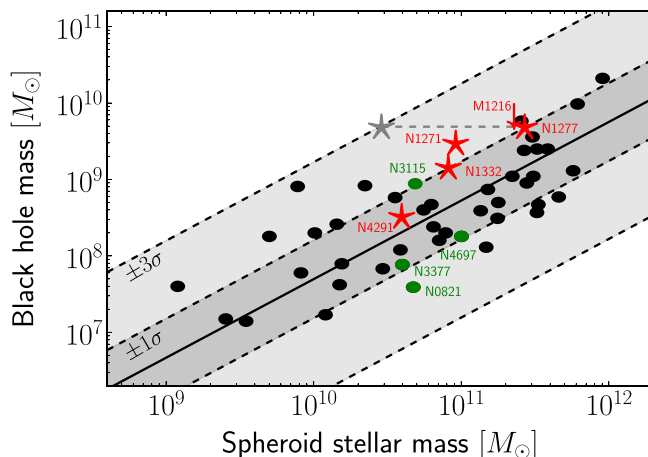


Figure 5. Black hole mass plotted against spheroid stellar mass for 45 + 3 early-type galaxies (from Savorgnan et al. 2015). The black solid line is the bisector linear regression for all galaxies except Mrk 1216, NGC 1271, and NGC 1277. The dashed lines mark the 1σ and 3σ deviations, where σ (0.51 dex) is the total rms scatter about the correlation in the black hole mass direction. The red symbols mark five galaxies that were claimed to be extreme outliers in this diagram: four intermediate-scale disc galaxies (Mrk 1216, NGC 1271, NGC 1277, and NGC 1332) and one elliptical galaxy (NGC 4291). All five reside well within a 3σ deviation from the correlation when using their correct spheroid mass. For NGC 1277, we show the previously reported spheroid stellar mass (van den Bosch et al. 2012) in grey. The green colour is used to show the location of four additional intermediate-scale disc galaxies mentioned in Section 2.

NGC 1332, and NGC 4291) is a noticeable outlier in the (black hole mass)–(galaxy luminosity) diagram. In Fig. 5, we show the location of these five galaxies in the updated (black hole mass)–(spheroid stellar mass) diagram for early-type galaxies from Savorgnan et al. (2015). Fig. 5 was populated using the galaxy decomposition technique shown here and extensively described in Savorgnan & Graham (2015). Briefly, we obtained *Spitzer*/IRAC 3.6 μ m images for 45 early-type galaxies which already had a dynamical detection of their black hole mass. We modelled their one-dimensional surface brightness profiles with a combination of analytic functions, using one function per galaxy component. Spheroid luminosities were converted into stellar masses using individual, but almost constant mass-to-light ratios (~ 0.6 ; Meidt et al. 2014).

In Fig. 5, we show the galaxies Mrk 1216, NGC 1271, and NGC 1277, which were not a part of the original sample of 45 early-type galaxies. For the galaxy NGC 1271, we use the black hole mass measurement and the stellar mass-to-light ratio obtained by Walsh et al. (2015b). For the galaxy NGC 1277, we use the black hole mass measurement obtained by Walsh et al. (2015a) and the stellar mass-to-light ratio obtained by Martín-Navarro et al. (2015). Note that for NGC 1277, we recover a spheroid stellar mass of $2.7 \times 10^{11} M_\odot$, in agreement with the value of $\approx 1.2 \times 10^{11} M_\odot$ obtained by Emsellem (2013) from his multi-Gaussian expansion models.⁵ For the galaxy Mrk 1216, we use the upper limit on the black hole mass and the stellar mass-to-light ratio obtained by Yıldırım et al. (2015). For the first time, Fig. 5 reveals that when the four intermediate-scale disc galaxies Mrk 1216, NGC 1271, NGC 1277, NGC 1332, and the

elliptical galaxy NGC 4291 are properly modelled, they no longer appear as extreme outliers above the (black hole mass)–(spheroid stellar mass) correlation for early-type galaxies, i.e. they all reside well within a 3σ deviation from the correlation.

4 ORIGIN OF COMPACT MASSIVE GALAXIES

Acknowledging the correct structure of galaxies with intermediate-scale discs is important to properly understand their origin. According to the current paradigm of cosmological structure evolution, the genesis of massive early-type galaxies is characterized by two distinct phases: ‘*in situ*’ and ‘*ex situ*’. The first phase takes place in a young Universe (within its first 4 Gyr), when cold gas inflows produced short and intense bursts of star formation that created compact and dense conglomerates of stars with high-velocity dispersion (e.g. Prieto, Jimenez & Haiman 2013). These naked and compact conglomerates, named ‘red nuggets’ (Damjanov et al. 2009), have been observed at high redshift with half-light sizes of 1–2 kpc (Daddi et al. 2005; Trujillo et al. 2006; van Dokkum et al. 2008). In the second phase (last 10 Gyr), discs and stellar envelopes were accreted around these primordial conglomerates and the external parts of today’s galaxies assembled on scales of 2–20 kpc (e.g. Driver et al. 2013).

Today’s Universe is populated by an abundance of compact, massive spheroids, with the same physical properties – mass and compactness – as the high-redshift red nuggets (Graham, Dullo & Savorgnan 2015b). Some of these local compact massive spheroids are encased within a large-scale disc, that is to say they are the bulges of some lenticular and spiral galaxies. Over the last 10 Gyr, their spheroids have evolved by growing a relatively flat disc (e.g. Pichon et al. 2011; Danovich et al. 2012; Stewart et al. 2013) – rather than a three-dimensional envelope – which has increased the galaxy size but preserved the bulge compactness. Of course, some lenticular/ES galaxies may have been built from mergers (e.g. Querejeta et al. 2015, and references therein). The other compact massive spheroids of today’s Universe belong to some galaxies with intermediate-scale discs. Indeed, Mrk 1216, NGC 1271, NGC 1277, NGC 1332, and NGC 3115 are all local compact intermediate-scale disc galaxies with purely old (> 10 Gyr) stellar populations. These galaxies have undergone the lowest degree of disc growth.

In addition to the observational clues as to the actual physical components in galaxies with intermediate-scale discs, one can reason on other grounds as to why these compact galaxies are not comprised of an inner bulge plus large-scale disc plus outer envelope. If they were such three-component systems, then one would have two possibilities. The first possibility is that these galaxies were already fully assembled 10 Gyr ago; this would explain their old stellar populations, but it would also imply that their discs and envelopes had already formed during the first 4 Gyr of the Universe, in disagreement with the current cosmological picture. The second possibility is that only their inner bulges (with sizes of 0.1–0.2 kpc, according to past decompositions) originated in the first 4 Gyr and they subsequently accreted a substantial disc and envelope. If this was correct, then we would observe high-redshift, star-like, naked bulges with stellar masses within a factor of a few times the currently observed red nuggets but sizes which are 10 times smaller. However, a dramatically different expectation is reached if one considers these galaxies today as spheroid-dominated systems with an intermediate-scale disc; in this case, both the galaxy size and the spheroid size are compact (1–2 kpc). This implies that, among the local descendants of the high-redshift red nuggets, the compact

⁵ In Emsellem (2013), readers will find a clever discussion of the problematics associated with the definition and the identification of the ‘bulge’ component in a galaxy.

intermediate-scale disc galaxies have undergone the lowest degree of disc growth. That is, the bulk of a compact intermediate-scale disc galaxy quickly assembled ‘*in situ*’ in a very young Universe and experienced very little evolution over the last 10 Gyr.

5 SUMMARY AND CONCLUSIONS

Early-type galaxies display a broad distribution of spheroid-to-total flux ratios (e.g. Cappellari et al. 2011b), going from disc-less, ‘pure’ elliptical galaxies (slow rotators) to disc-dominated lenticular galaxies (central fast rotators that continue to be fast rotating also beyond one half-light radius). In between these two extremes lie galaxies with intermediate-scale discs (spheroid-dominated central fast rotators that become slow rotating in their outer regions), i.e. discs of kiloparsec size that remain ‘embedded’ within the spheroidal component of the galaxy and do not dominate the galaxy light at large radii as large-scale discs do. While this is likely known to some readers, the surge of papers presenting galaxy decompositions which are not aware of this reality has created a pressing need for this reminder. We have shown that the light distribution of galaxies with intermediate-scale discs can be accurately described with a simple spheroid + disc (+optional nuclear component) model, without the need for the addition of a bright envelope component.

Our decompositions correctly reproduce both the photometric (surface brightness and ellipticity profiles) and kinematic (specific angular momentum profile) properties of nine intermediate-scale disc galaxies. Four of these nine galaxies (Mrk 1216, NGC 1271, NGC 1277, NGC 1332) and one additional elliptical galaxy (NGC 4291) had previously been claimed to be extreme outliers in the (black hole mass)–(spheroid mass) diagram. However, here we have demonstrated that, when correctly modelled, these five galaxies all reside well within the scatter of the correlation, i.e. they do not host overmassive black holes. This serves to strengthen the (black hole mass)–(spheroid mass) relation, and rules out the need for exotic formation scenarios.

ACKNOWLEDGEMENTS

This research was supported by Australian Research Council funding through grant FT110100263. GS is grateful to Matteo Fossati, Luca Cortese and Giuseppe Gavazzi for useful comments and discussion. The publication of this paper would not have been possible without the invaluable support of Chris Blake and Duncan Forbes. We warmly thank our anonymous referee for their very careful review of our paper, and for the comments, corrections and suggestions that ensued. This work is based on observations made with the IRAC instrument (Fazio et al. 2004) on-board the *Spitzer Space Telescope*, which is operated by the Jet Propulsion Laboratory, California Institute of Technology under a contract with NASA, and also on observations made with the NASA/ESA *HST*, and obtained from the Hubble Legacy Archive, which is a collaboration between the Space Telescope Science Institute (STScI/NASA), the Space Telescope European Coordinating Facility (ST-ECF/ESA) and the Canadian Astronomy Data Centre (CADC/NRC/CSA). This research has made use of the GOLDMine data base (Gavazzi et al. 2003) and the NASA/IPAC Extragalactic Database (NED) which is operated by the Jet Propulsion Laboratory, California Institute of Technology, under contract with the National Aeronautics and Space Administration.

REFERENCES

- Allen P. D., Driver S. P., Graham A. W., Cameron E., Liske J., de Propris R., 2006, MNRAS, 371, 2
 Andersen D., Bershady M. A., 2002, in Athanassoula E., Bosma A., Mujica R., eds, ASP Conf. Ser. Vol. 275, Disks of Galaxies: Kinematics, Dynamics and Peturbations. Astron. Soc. Pac., San Francisco, p. 39
 Andersen D. R., Bershady M. A., Sparke L. S., Gallagher J. S., III, Wilcots E. M., 2001, ApJ, 551, L131
 Arnold J. A., Romanowsky A. J., Brodie J. P., Chomiuk L., Spitler L. R., Strader J., Benson A. J., Forbes D. A., 2011, ApJ, 736, L26
 Arnold J. A. et al., 2014, ApJ, 791, 80
 Bender R., 1988, A&A, 193, L7
 Bender R., 1990, A&A, 229, 441
 Bender R., Moellenhoff C., 1987, A&A, 177, 71
 Bender R., Saglia R. P., Gerhard O. E., 1994, MNRAS, 269, 785
 Bijaoui A., Marchal J., Michard R., 1989, in Corwin H. G., Jr, Bottinelli L., eds, World of Galaxies (Le Monde des Galaxies), p. 250
 Bogdán Á. et al., 2012, ApJ, 753, 140
 Capaccioli M., 1987, in de Zeeuw P. T., ed., Proc. IAU Symp. 127, Structure and Dynamics of Elliptical Galaxies. Reidel, Dordrecht, p. 47
 Capaccioli M., Piotto G., Rampazzo R., 1988, AJ, 96, 487
 Cappellari M. et al., 2007, MNRAS, 379, 418
 Cappellari M. et al., 2011a, MNRAS, 413, 813
 Cappellari M. et al., 2011b, MNRAS, 416, 1680
 Carter D., 1978, MNRAS, 182, 797
 Carter D., 1987, ApJ, 312, 514
 Ciambur B. C., 2015, ApJ, 810, 120
 Cinzano P., van der Marel R. P., 1993, in Danziger I. J., Zeilinger W. W., Kjær K., eds, Eur. South. Obs. Conf. Workshop Proc. Vol. 45, Structure, Dynamics and Chemical Evolution of Elliptical Galaxies, p. 105
 D’Onofrio M., Zaggia S. R., Longo G., Caon N., Capaccioli M., 1995, A&A, 296, 319
 Daddi E. et al., 2005, ApJ, 626, 680
 Damjanov I. et al., 2009, ApJ, 695, 101
 Danovich M., Dekel A., Hahn O., Teyssier R., 2012, MNRAS, 422, 1732
 Davies R. L., 1981, MNRAS, 194, 879
 di Tullio G. A., 1979, A&AS, 37, 591
 Djorgovski S. B., 1985, PhD thesis, California Univ.
 Driver S. P., Robotham A. S. G., Bland-Hawthorn J., Brown M., Hopkins A., Liske J., Phillipps S., Wilkins S., 2013, MNRAS, 430, 2622
 Dullo B. T., Graham A. W., 2014, MNRAS, 444, 2700
 Ebneter K., Davis M., Jeske N., Stevens M., 1987, BAAS, 19, 681
 Emsellem E., 2013, MNRAS, 433, 1862
 Emsellem E. et al., 2007, MNRAS, 379, 401
 Emsellem E. et al., 2011, MNRAS, 414, 888
 Fazio G. G. et al., 2004, ApJS, 154, 10
 Ferrarese L. et al., 2006, ApJS, 164, 334
 Franx M., Illingworth G. D., 1988, ApJ, 327, L55
 Franx M., Illingworth G., Heckman T., 1989, ApJ, 344, 613
 Gadotti D. A., 2008, MNRAS, 384, 420
 Gavazzi G., Boselli A., Donati A., Franzetti P., Scodéglio M., 2003, A&A, 400, 451
 Graham A. W., Colless M. M., Busarello G., Zaggia S., Longo G., 1998, A&AS, 133, 325
 Graham A. W., Erwin P., Trujillo I., Asensio Ramos A., 2003, AJ, 125, 2951
 Graham A. W., Durrel M., Savorgnan G. A. D., Batcheldor D., Watson B., Medling A., Scott N., Marconi A., 2015a, ApJ, Submitted
 Graham A. W., Dullo B. T., Savorgnan G. A. D., 2015b, ApJ, 804, 32
 Head J. T. C. G., Lucey J. R., Hudson M. J., Smith R. J., 2014, MNRAS, 440, 1690
 Jedrzejewski R. I., 1987a, in de Zeeuw P. T., ed., Proc. IAU Symp. 127, Structure and Dynamics of Elliptical Galaxies. Reidel, Dordrecht, p. 37
 Jedrzejewski R. I., 1987b, MNRAS, 226, 747
 Jedrzejewski R. I., Davies R. L., Illingworth G. D., 1987, AJ, 94, 1508
 Kormendy J., Bender R., 2012, ApJS, 198, 2
 Krajnović D. et al., 2013, MNRAS, 432, 1768
 Läsker R., Ferrarese L., van de Ven G., 2014a, ApJ

- Läsker R., Ferrarese L., van de Ven G., Shankar F., 2014b, ApJ
Liller M. H., 1966, ApJ, 146, 28
McElroy D. B., 1983, ApJ, 270, 485
Marconi A., Hunt L. K., 2003, ApJ, 589, L21
Martín-Navarro I., La Barbera F., Vazdekis A., Ferré-Mateu A., Trujillo I., Beasley M. A., 2015, MNRAS, 451, 1081
Meidt S. E. et al., 2014, ApJ, 788, 144
Méndez-Abreu J., CALIFA Team 2015, in Cenarro A. J., Figueras F., Hernández-Monteagudo C., Trujillo Bueno J., Valdvielso L., eds, Proceedings of the XI Scientific Meeting of the Spanish Astronomical Society, Highlights of Spanish Astrophysics VIII. Teruel, p. 268
Michard R., 1984, A&A, 140, L39
Michard R., Marchal J., 1993, A&AS, 98, 29
Moffat A. F. J., 1969, A&A, 3, 455
Nieto J.-L., Capaccioli M., Held E. V., 1988, A&A, 195, L1
Nieto J.-L., Bender R., Arnaud J., Surma P., 1991, A&A, 244, L25
Pastrav B. A., Popescu C. C., Tuffs R. J., Sansom A. E., 2013, A&A, 553, A80
Petrou M., 1981, MNRAS, 196, 933
Pichon C., Pogosyan D., Kimm T., Slyz A., Devriendt J., Dubois Y., 2011, MNRAS, 418, 2493
Prieto J., Jimenez R., Haiman Z., 2013, MNRAS, 436, 2301
Querejeta M., Eliche-Moral M. C., Tapia T., Borlaff A., Rodríguez-Pérez C., Zamorano J., Gallego J., 2015, A&A, 573, A78
Rix H.-W., White S. D. M., 1990, ApJ, 362, 52
Rix H.-W., White S. D. M., 1992, MNRAS, 254, 389
Romanowsky A. J., Fall S. M., 2012, ApJS, 203, 17
Rusli S. P., Thomas J., Erwin P., Saglia R. P., Nowak N., Bender R., 2011, MNRAS, 410, 1223
Savorgnan G. A. D., Graham A. W., 2015, ApJ, preprint ([arXiv:1511.07446](https://arxiv.org/abs/1511.07446))
Savorgnan G. A. D., Graham A. W., Marconi A., Sani E., 2015, ApJ, preprint ([arXiv:1511.07437](https://arxiv.org/abs/1511.07437))
Scorza C., 1998, in Aguilar A., Carraminana A., eds, IX Latin American Regional IAU Meeting, Focal Points in Latin American Astronomy. p. 117
Scorza C., Bender R., 1995, A&A, 293, 20
Scott N., Davies R. L., Houghton R. C. W., Cappellari M., Graham A. W., Pimbblet K. A., 2014, MNRAS, 441, 274
Sérsic J. L., 1963, Bull. Argentina Assoc. Astron., 6, 41
Simien F., Michard R., 1990, A&A, 227, 11
Stewart K. R., Brooks A. M., Bullock J. S., Maller A. H., Diemand J., Wadsley J., Moustakas L. A., 2013, ApJ, 769, 74
Strom S. E., Strom K. M., 1978, AJ, 83, 732
Strom K. M., Strom S. E., Jensen E. B., Moller J., Thompson L. A., Thuan T. X., 1977, ApJ, 212, 335
Trujillo I. et al., 2006, MNRAS, 373, L36
van den Bosch R. C. E., Gebhardt K., Güttekin K., van de Ven G., van der Wel A., Walsh J. L., 2012, Nature, 491, 729
van Dokkum P. G. et al., 2008, ApJ, 677, L5
Walsh J. L., van den Bosch R. C. E., Gebhardt K., Yıldırım A., Richstone D. O., Güttekin K., Husemann B., 2015a, preprint ([arXiv:1511.04455](https://arxiv.org/abs/1511.04455))
Walsh J. L., van den Bosch R. C. E., Gebhardt K., Yıldırım A., Güttekin K., Husemann B., Richstone D. O., 2015b, ApJ, 808, 183
Yıldırım A., van den Bosch R. C. E., van de Ven G., Husemann B., Lyubanova M., Walsh J. L., Gebhardt K., Güttekin K., 2015, MNRAS, 452, 1792

This paper has been typeset from a TeX/LaTeX file prepared by the author.

Bibliography

- Abazajian K. N., et al., 2009, ApJS, 182, 543
- Akaike H., 1974, Automatic Control, IEEE Transactions, 19, 716
- Akritas M. G., Bershady M. A., 1996, ApJ, 470, 706
- Alexander T., Natarajan P., 2014, Science, 345, 1330
- Aller M. C., Richstone D. O., 2007, ApJ, 665, 120
- Andredakis Y. C., Peletier R. F., Balcells M., 1995, MNRAS, 275, 874
- Arnold J. A., et al., 2014, ApJ, 791, 80
- Bañados E., et al., 2014, AJ, 148, 14
- Baldassare V. F., Reines A. E., Gallo E., Greene J. E., 2015, ApJL, 809, L14
- Begelman M. C., Blandford R. D., Rees M. J., 1980, ??jnlNature, 287, 307
- Beifiori A., Courteau S., Corsini E. M., Zhu Y., 2012, MNRAS, 419, 2497
- Berrier J. C., et al., 2013, ApJ, 769, 132
- Bogdán Á., et al., 2012, ApJ, 753, 140
- Buitrago F., Trujillo I., Conselice C. J., Bouwens R. J., Dickinson M., Yan H., 2008, ApJL, 687, L61
- Burkert A., Tremaine S., 2010, ApJ, 720, 516

Caon N., Capaccioli M., D'Onofrio M., 1993, MNRAS, 265, 1013

Cappellari M., et al., 2011, MNRAS, 413, 813

Carollo C. M., et al., 2014, preprint, ([arXiv:1402.1172](https://arxiv.org/abs/1402.1172))

Carr B. J., Hawking S. W., 1974, MNRAS, 168, 399

Carrasco E. R., Conselice C. J., Trujillo I., 2010, MNRAS, 405, 2253

Carter D., 1987, ApJ, 312, 514

Ciambur B. C., 2015, preprint, ([arXiv:1507.02691](https://arxiv.org/abs/1507.02691))

Cimatti A., Nipoti C., Cassata P., 2012, MNRAS, 422, 62

Cinzano P., van der Marel R. P., 1993, in Danziger I. J., Zeilinger W. W., Kj  r K., eds, European Southern Observatory Conference and Workshop Proceedings Vol. 45, European Southern Observatory Conference and Workshop Proceedings. p. 105

Ciotti L., Lanzoni B., Volonteri M., 2007, ApJ, 658, 65

Clark P. C., Glover S. C. O., Klessen R. S., Bromm V., 2011, ApJ, 727, 110

Colpi M., 2014, Space Science Reviews,

Colpi M., Callegari S., Dotti M., Mayer L., 2009, Classical and Quantum Gravity, 26, 094029

Croom S. M., et al., 2012, MNRAS, 421, 872

Croton D. J., et al., 2006, MNRAS, 365, 11

D'Onofrio M., Capaccioli M., Caon N., 1994, MNRAS, 271, 523

D'Onofrio M., Zaggia S. R., Longo G., Caon N., Capaccioli M., 1995, A&A, 296, 319

Daddi E., et al., 2005, ApJ, 626, 680

Damjanov I., et al., 2009, ApJ, 695, 101

Davies R. L., Efstathiou G., Fall S. M., Illingworth G., Schechter P. L., 1983, ApJ, 266, 41

De T., Chattopadhyay T., Chattopadhyay A. K., 2014, PASA, 31, e047

- Dotti M., Sesana A., Decarli R., 2012, Advances in Astronomy, 2012
- Dressler A., 1989, in Osterbrock D. E., Miller J. S., eds, IAU Symposium Vol. 134, Active Galactic Nuclei. p. 217
- Driver S. P., Robotham A. S. G., Bland-Hawthorn J., Brown M., Hopkins A., Liske J., Phillipps S., Wilkins S., 2013, MNRAS, 430, 2622
- Dullo B. T., Graham A. W., 2013, preprint, ([arXiv:1310.5867](https://arxiv.org/abs/1310.5867))
- Dullo B. T., Graham A. W., 2014, MNRAS, 444, 2700
- Einstein A., 1915, Sitzungsberichte der Königlich Preußischen Akademie der Wissenschaften (Berlin), Seite 844-847.,
- Einstein A., 1939, Annals of Mathematics, 40, 922
- Emsellem E., 2013, MNRAS, 433, 1862
- Emsellem E., et al., 2007, MNRAS, 379, 401
- Emsellem E., et al., 2011, MNRAS, 414, 888
- Erwin P., 2015, ApJ, 799, 226
- Erwin P., Gadotti D. A., 2012, Advances in Astronomy, 2012, 4
- Erwin P., Sparke L. S., 2003, ApJS, 146, 299
- Faber S. M., Dressler A., Davies R. L., Burstein D., Lynden-Bell D., 1987, in Faber S. M., ed., Nearly Normal Galaxies. From the Planck Time to the Present. pp 175–183
- Fabian A. C., 1999, MNRAS, 308, L39
- Fabian A. C., 2012, ARAA, 50, 455
- Fabian A. C., Iwasawa K., Reynolds C. S., Young A. J., 2000, PASP, 112, 1145
- Fabricius M. H., et al., 2014, MNRAS, 441, 2212
- Fan X., et al., 2003, AJ, 125, 1649
- Fan L., Fang G., Chen Y., Pan Z., Lv X., Li J., Lin L., Kong X., 2013, ApJL, 771, L40

Feoli A., Mancini L., 2009, ApJ, 703, 1502

Feoli A., Mele D., 2005, International Journal of Modern Physics D, 14, 1861

Ferrarese L., 2002, ApJ, 578, 90

Ferrarese L., 2006, Observational Evidence for Supermassive Black Holes. pp 1–62,
doi:10.1201/9781420012095.ch1

Ferrarese L., Ford H., 2005, Space Science Reviews, 116, 523

Ferrarese L., Merritt D., 2000, ApJL, 539, L9

Ferré-Mateu A., Mezcua M., Trujillo I., Balcells M., van den Bosch R. C. E., 2015, ApJ, 808, 79

Franx M., Illingworth G., Heckman T., 1989, ApJ, 344, 613

Gadotti D. A., 2008, MNRAS, 384, 420

Gaskell C. M., 2010, in Whalen D. J., Bromm V., Yoshida N., eds, American Institute of Physics Conference Series Vol. 1294, American Institute of Physics Conference Series. pp 261–261
(arXiv:1004.1180), doi:10.1063/1.3518867

Gebhardt K., Thomas J., 2009, ApJ, 700, 1690

Gebhardt K., et al., 2000, ApJL, 539, L13

Genzel R., Eisenhauer F., Gillessen S., 2010, Reviews of Modern Physics, 82, 3121

Gerhard O. E., Binney J. J., 1996, MNRAS, 279, 993

Ghez A. M., et al., 2008, ApJ, 689, 1044

Graham A. W., 2007, MNRAS, 379, 711

Graham A. W., 2012, ApJ, 746, 113

Graham A. W., 2013, Elliptical and Disk Galaxy Structure and Modern Scaling Laws. p. 91,
doi:10.1007/978-94-007-5609-0_2

Graham A. W., 2016a, Galactic Bulges, 418, 263

- Graham A. W., 2016b, *Galactic Bulges*, 418, 263
- Graham A. W., Driver S. P., 2005, *PASA*, 22, 118
- Graham A. W., Driver S. P., 2007a, *MNRAS*, 380, L15
- Graham A. W., Driver S. P., 2007b, *ApJ*, 655, 77
- Graham A. W., Guzmán R., 2003, *AJ*, 125, 2936
- Graham A. W., Prieto M., 1999, *Ap&SS*, 269, 653
- Graham A. W., Scott N., 2013, *ApJ*, 764, 151
- Graham A. W., Scott N., 2015, *ApJ*, 798, 54
- Graham A. W., Worley C. C., 2008, *MNRAS*, 388, 1708
- Graham A. W., Colless M. M., Busarello G., Zaggia S., Longo G., 1998, *A&AS*, 133, 325
- Graham A. W., Erwin P., Caon N., Trujillo I., 2001, *ApJL*, 563, L11
- Graham A. W., Erwin P., Trujillo I., Asensio Ramos A., 2003, *AJ*, 125, 2951
- Graham A. W., Driver S. P., Allen P. D., Liske J., 2007, *MNRAS*, 378, 198
- Graham A. W., Dullo B. T., Savorgnan G. A. D., 2015, *ApJ*, 804, 32
- Graham A. W., Durré M., Savorgnan G. A. D., Medling A. M., Batcheldor D., Scott N., Watson B., Marconi A., 2016a, preprint, ([arXiv:1601.05151](https://arxiv.org/abs/1601.05151))
- Graham A. W., Ciambur B. C., Soria R., 2016b, *ApJ*, 818, 172
- Greif T. H., Springel V., White S. D. M., Glover S. C. O., Clark P. C., Smith R. J., Klessen R. S., Bromm V., 2011, *ApJ*, 737, 75
- Gültekin K., et al., 2009, *ApJ*, 698, 198
- Häring N., Rix H.-W., 2004, *ApJL*, 604, L89
- Heger A., Fryer C. L., Woosley S. E., Langer N., Hartmann D. H., 2003, *ApJ*, 591, 288
- Hirschmann M., Khochfar S., Burkert A., Naab T., Genel S., Somerville R. S., 2010, *MNRAS*, 407, 1016

- Ho L. C., Filippenko A. V., Sargent W. L. W., 1997, ApJS, 112, 315
- Hopkins P. F., Bundy K., Murray N., Quataert E., Lauer T. R., Ma C.-P., 2009, MNRAS, 398, 898
- Jahnke K., Macciò A. V., 2011, ApJ, 734, 92
- Jiang L., Fan X., Vestergaard M., Kurk J. D., Walter F., Kelly B. C., Strauss M. A., 2007, AJ, 134, 1150
- Jiang Y.-F., Greene J. E., Ho L. C., 2011, ApJL, 737, L45
- Kautsch S. J., Grebel E. K., Barazza F. D., Gallagher III J. S., 2006, A&A, 445, 765
- Kelly B. C., 2007, ApJ, 665, 1489
- Khochfar S., Burkert A., 2006, A&A, 445, 403
- Khosroshahi H. G., Wadadekar Y., Kembhavi A., 2000, ApJ, 533, 162
- Kormendy J., 1982, ApJ, 257, 75
- Kormendy J., Ho L. C., 2013, ARAA, 51, 511
- Kormendy J., Kennicutt Jr. R. C., 2004, ARAA, 42, 603
- Kormendy J., Richstone D., 1995, ARAA, 33, 581
- Krajnović D., 2015, in Cappellari M., Courteau S., eds, IAU Symposium Vol. 311, IAU Symposium. pp 45–48 ([arXiv:1410.2235](https://arxiv.org/abs/1410.2235)), doi:10.1017/S1743921315003361
- Krajnović D., Cappellari M., de Zeeuw P. T., Copin Y., 2006, MNRAS, 366, 787
- Krajnović D., et al., 2011, MNRAS, 414, 2923
- Krajnović D., et al., 2013, MNRAS, 432, 1768
- Kriek M., et al., 2008, ApJ, 677, 219
- Laor A., 1998, ApJL, 505, L83
- Laor A., 2001, ApJ, 553, 677

- Läsker R., Ferrarese L., van de Ven G., 2014a, ApJ, 780, 69
- Läsker R., Ferrarese L., van de Ven G., Shankar F., 2014b, ApJ, 780, 70
- Lauer T. R., et al., 2007, ApJ, 662, 808
- Laurikainen E., Salo H., Buta R., 2005, MNRAS, 362, 1319
- Laurikainen E., Salo H., Buta R., Knapen J. H., 2007, MNRAS, 381, 401
- Laurikainen E., Salo H., Buta R., Knapen J. H., Comerón S., 2010, MNRAS, 405, 1089
- Laurikainen E., Peletier R., Gadotti D., 2016, Galactic Bulges, 418
- Law D. R., MaNGA Team 2014, in American Astronomical Society Meeting Abstracts #223.
p. 254.31
- Lupi A., Haardt F., Dotti M., Fiacconi D., Mayer L., Madau P., 2015, preprint,
([arXiv:1512.02651](https://arxiv.org/abs/1512.02651))
- Lynden-Bell D., 1969, ??jnlNature, 223, 690
- Lynden-Bell D., 1978, ??jnlPhys. Scr, 17, 185
- Madau P., Haardt F., Dotti M., 2014, ApJL, 784, L38
- Magorrian J., et al., 1998, AJ, 115, 2285
- Malin D. F., Zealey W. J., 1979, Sky and Telescope, 57, 354
- Malkan M. A., 1983, ApJ, 268, 582
- Maller A. H., Katz N., Kereš D., Davé R., Weinberg D. H., 2006, ApJ, 647, 763
- Marconi A., Hunt L. K., 2003, ApJL, 589, L21
- Matković A., Guzmán R., 2005, MNRAS, 362, 289
- Mayer L., 2009, in APS April Meeting Abstracts.
- McConnell N. J., Ma C.-P., Gebhardt K., Wright S. A., Murphy J. D., Lauer T. R., Graham J. R., Richstone D. O., 2011, ??jnlNature, 480, 215

- McConnell N. J., Ma C.-P., Murphy J. D., Gebhardt K., Lauer T. R., Graham J. R., Wright S. A., Richstone D. O., 2012, ApJ, 756, 179
- McLure R. J., et al., 2013, MNRAS, 428, 1088
- McNamara B. R., Nulsen P. E. J., 2012, New Journal of Physics, 14, 055023
- Melia F., McClintock T. M., 2015, preprint, ([arXiv:1511.05494](https://arxiv.org/abs/1511.05494))
- Merritt D., 2006a, Reports on Progress in Physics, 69, 2513
- Merritt D., 2006b, ApJ, 648, 976
- Merritt D., 2013a, Dynamics and Evolution of Galactic Nuclei
- Merritt D., 2013b, Classical and Quantum Gravity, 30, 244005
- Michard R., 1984, A&A, 140, L39
- Miller M. C., Colbert E. J. M., 2004, International Journal of Modern Physics D, 13, 1
- Milosavljević M., Merritt D., 2001, ApJ, 563, 34
- Miyoshi M., Moran J., Herrnstein J., Greenhill L., Nakai N., Diamond P., Inoue M., 1995, ??jnlNature, 373, 127
- Montgomery C., Orchiston W., Whittingham I., 2009, Journal of Astronomical History and Heritage, 12, 90
- Moriondo G., Giovanardi C., Hunt L. K., 1998, A&AS, 130, 81
- Mortlock D. J., et al., 2011, ??jnlNature, 474, 616
- Naab T., Johansson P. H., Ostriker J. P., 2009, ApJL, 699, L178
- Nesvadba N. P. H., Lehnert M. D., Eisenhauer F., Gilbert A., Tecza M., Abuter R., 2006, ApJ, 650, 693
- Nieto J.-L., Capaccioli M., Held E. V., 1988, A&A, 195, L1
- Nieto J.-L., Bender R., Arnaud J., Surma P., 1991, A&A, 244, L25
- Novak G. S., Faber S. M., Dekel A., 2006, ApJ, 637, 96

- Ostriker J. P., Ciotti L., 2005, Royal Society of London Philosophical Transactions Series A, 363, 667
- Park D., Kelly B. C., Woo J.-H., Treu T., 2012, ApJS, 203, 6
- Pasham D. R., Strohmayer T. E., Mushotzky R. F., 2014, ??jnlNature, 513, 74
- Peng C. Y., 2007, ApJ, 671, 1098
- Peng C. Y., Ho L. C., Impey C. D., Rix H.-W., 2002, AJ, 124, 266
- Peng C. Y., Ho L. C., Impey C. D., Rix H.-W., 2010, AJ, 139, 2097
- Peterson B. M., 1993, PASP, 105, 247
- Pota V., Graham A. W., Forbes D. A., Romanowsky A. J., Brodie J. P., Strader J., 2013, MNRAS, 433, 235
- Press W. H., Teukolsky S. A., Vetterling W. T., Flannery B. P., 1992, Numerical recipes in FORTRAN. The art of scientific computing
- Reynolds C. S., Nowak M. A., 2003, Physics Reports, 377, 389
- Richstone D., et al., 1998, ??jnlNature, 395, A14
- Rix H.-W., White S. D. M., 1990, ApJ, 362, 52
- Rix H.-W., White S. D. M., 1992, MNRAS, 254, 389
- Rusli S. P., Thomas J., Erwin P., Saglia R. P., Nowak N., Bender R., 2011, MNRAS, 410, 1223
- Rusli S. P., et al., 2013, AJ, 146, 45
- Ryan C. J., De Robertis M. M., Virani S., Laor A., Dawson P. C., 2007, ApJ, 654, 799
- Sadoun R., Colin J., 2012, MNRAS, 426, L51
- Salo H., et al., 2015, ApJS, 219, 4
- Salpeter E. E., 1964, ApJ, 140, 796
- Salucci P., Szuszkiewicz E., Monaco P., Danese L., 1999, MNRAS, 307, 637

- Salucci P., Ratnam C., Monaco P., Danese L., 2000, MNRAS, 317, 488
- Sani E., Marconi A., Hunt L. K., Risaliti G., 2011, MNRAS, 413, 1479
- Saulder C., van den Bosch R. C. E., Mieske S., 2015, A&A, 578, A134
- Savorgnan G. A. D., Graham A. W., 2015, MNRAS, 446, 2330
- Savorgnan G. A. D., Graham A. W., 2016a, ApJS, 222, 10
- Savorgnan G. A. D., Graham A. W., 2016b, MNRAS, 457, 320
- Savorgnan G., Graham A. W., Marconi A., Sani E., Hunt L. K., Vika M., Driver S. P., 2013, MNRAS, 434, 387
- Savorgnan G. A. D., Graham A. W., Marconi A., Sani E., 2016, ApJ, 817, 21
- Scharwächter J., Combes F., Salomé P., Sun M., Krips M., 2015, preprint, ([arXiv:1507.02292](https://arxiv.org/abs/1507.02292))
- Scott N., Graham A. W., Schombert J., 2013, ApJ, 768, 76
- Scott N., Davies R. L., Houghton R. C. W., Cappellari M., Graham A. W., Pimbblet K. A., 2014, MNRAS, 441, 274
- Seigar M. S., Kennefick D., Kennefick J., Lacy C. H. S., 2008, ApJL, 678, L93
- Sérsic J. L., 1963, Boletin de la Asociacion Argentina de Astronomia La Plata Argentina, 6, 41
- Sérsic J. L., 1968, Atlas de galaxias australes
- Shahbaz T., 1999, Journal of Astrophysics and Astronomy, 20, 197
- Shankar F., et al., 2016, preprint, ([arXiv:1603.01276](https://arxiv.org/abs/1603.01276))
- Sheth K., et al., 2010, PASP, 122, 1397
- Shields G. A., 1978, ??jnlNature, 272, 706
- Silk J., Rees M. J., 1998, A&A, 331, L1
- Simard L., 1998, in Albrecht R., Hook R. N., Bushouse H. A., eds, Astronomical Society of the Pacific Conference Series Vol. 145, Astronomical Data Analysis Software and Systems VII. p. 108

- Simien F., de Vaucouleurs G., 1986, ApJ, 302, 564
- Snyder G. F., Hopkins P. F., Hernquist L., 2011, ApJL, 728, L24
- Soltan A., 1982, MNRAS, 200, 115
- Stacy A., Greif T. H., Bromm V., 2012, MNRAS, 422, 290
- Thorne K. S., 1994, Black holes and time warps: Einstein's outrageous legacy
- Toft S., et al., 2007, ApJ, 671, 285
- Tombesi F., Cappi M., Reeves J. N., Braito V., 2012, MNRAS, 422, L1
- Trakhtenbrot B., et al., 2015, Science, 349, 168
- Tremaine S., et al., 2002, ApJ, 574, 740
- Trujillo I., Erwin P., Asensio Ramos A., Graham A. W., 2004, AJ, 127, 1917
- Trujillo I., et al., 2006, MNRAS, 373, L36
- Trujillo I., Conselice C. J., Bundy K., Cooper M. C., Eisenhardt P., Ellis R. S., 2007, MNRAS, 382, 109
- Tundo E., Bernardi M., Hyde J. B., Sheth R. K., Pizzella A., 2007, ApJ, 663, 53
- Turk M. J., Abel T., O'Shea B., 2009, Science, 325, 601
- Valluri M., Merritt D., Emsellem E., 2004, ApJ, 602, 66
- Vika M., Driver S. P., Cameron E., Kelvin L., Robotham A., 2012, MNRAS, 419, 2264
- Volonteri M., Bellovary J., 2012, Reports on Progress in Physics, 75, 124901
- Volonteri M., Ciotti L., 2013, ApJ, 768, 29
- Walsh J. L., van den Bosch R. C. E., Gebhardt K., Yildirim A., Gültekin K., Husemann B., Richstone D. O., 2015, ApJ, 808, 183
- Wandel A., 1999, ApJL, 519, L39
- Wellons S., et al., 2016, MNRAS, 456, 1030

Wolfe A. M., Burbidge G. R., 1970, ApJ, 161, 419

Wu X.-B., et al., 2015, ??jnlNature, 518, 512

Yıldırım A., van den Bosch R. C. E., van de Ven G., Husemann B., Lyubenova M., Walsh J. L., Gebhardt K., Gültekin K., 2015, MNRAS, 452, 1792

Yıldırım A., et al., 2016, MNRAS, 456, 538

Zel'dovich Y. B., Novikov I. D., 1964, Doklady Akad. Nauk. SSSR, 158, 811

Zirm A. W., et al., 2007, ApJ, 656, 66

de Jong R. S., 1996, A&AS, 118, 557

de Souza R. E., Gadotti D. A., dos Anjos S., 2004, ApJS, 153, 411

de Vaucouleurs G., 1948, Annales d'Astrophysique, 11, 247

van Dokkum P. G., et al., 2008, ApJL, 677, L5

van den Bosch R. C. E., Gebhardt K., Gültekin K., van de Ven G., van der Wel A., Walsh J. L., 2012, ??jnlNature, 491, 729

van den Bosch R. C. E., Gebhardt K., Gültekin K., Yıldırım A., Walsh J. L., 2015, ApJS, 218, 10

van der Marel R. P., 2004, Coevolution of Black Holes and Galaxies, p. 37